

School of Molecular and Life Sciences

**Facet-resolved electrochemistry of monolayer-modified
silicon crystals**

Song Zhang

0000-0002-3387-4957

This thesis is presented for the Degree of

**Doctor of Philosophy
of
Curtin University**

December 2022

Declaration

To the best of my knowledge and belief, this thesis contains no material previously published by any other person except where due acknowledgment has been made.

This thesis contains no material which has been accepted for the award of any other degree or diploma in any university

Signature:

Date: 2023-02-06

*This doctoral dissertation is
dedicated to my father in heaven*

Abstract

Semiconductors play a vital role in our modern digital world, with applications ranging from microelectronics, electrocatalysis, biosensing to energy storage and conversion. Silicon still reigns as the main material in the semiconductor industry, because of its unique bulk and surface properties. The electrochemistry of silicon and its oxides has been actively researched for several decades but merging the richness of the organic chemistry world with the sturdiness and photoelectrochemistry of silicon is an area that is still rich of unanswered questions. Merging semiconductor electrochemistry with organic chemistry offers an avenue to expand the function of electronic and electrochemical devices. To explore and understand these areas, surface scientists can benefit from an expanding pool of reactions for the preparation of self-assembled monolayers (SAMs) on silicon electrodes.

The chief purpose of this thesis is to investigate the thermodynamics and kinetics of SAMs-modified silicon electrodes. The main analytical tools will be cyclic voltammetry (CV), atomic force microscopy (AFM, including conductive AFM), electrochemical impedance spectroscopy (EIS), alongside with surface-sensitive techniques (such as XPS, macroscopic electrical measurements and contact angle). The cornerstones include 1) photo effects, 2) facet-effects on surface conductivity and reactivity, and 3) a study of the relationship between facet-dependent electrical conductivity and charge transfer rates in monolayer-modified silicon crystals.

Chapter 2 explores photocurrent effects and revisits the origin of multiple non-ideal voltammetric peaks often observed and generally explained as molecular disorder in the adsorbate. This chapter concludes that heterogeneous photocurrents are a semiconductor effect, not strictly disorder.

The electrical (conductive AFM) data of Chapter 2 prompted us to re-assess the origin of another type of parasitic signal often encountered in silicon electrochemistry. Towards this end, Chapter 3 uses electrochemical and AFM methods to assign a near-ideal pair of CV waves often observed in the background of Si(111) electrodes. Data

presented in this chapter demonstrates that highly conductive Si(110) defects (the edges Si(111) terraces) are, surprisingly, the site where the silica–silicon conversion becomes electrochemically reversible at room temperature. Due to its insulating nature silica is not reducible to silicon by electrochemical methods (not at room temperature). The currently available electrochemical methods for silica reduction requires temperatures as high as 850 °C in molten CaCl₂. Chapter 3 describes a nanoscale reversible reaction at room temperature. Though it is not yet of any practical scale, it is still a key step forwards in the space of silica reduction research, and more importantly, data of this chapter redefine (restrict) the electrochemical potential window available for electrochemistry of silicon in water. It is an important result in the context of facet-resolved semiconductor electrochemistry.

The results of Chapter 3 led to the electrochemical kinetic studies of Chapter 4. The chapter performs systematic electrochemical and electrical analysis of Si(111), Si(110), and Si(211), and by constraining the surface coverage of redox probes to comparable levels between those samples it attempts to remove the influence of surface density on charge transfer rates. By measuring AFM I–V curves, this chapter unveils the conductivity to drop in the order of Si(211), Si(110) and Si(111), but the same trend is not followed by surface-confined (diffusionless) redox reactions occurring at a monolayer distal end.

Acknowledgements

The COVID-19 outbreak affected greatly my doctoral study, and the course my PhD took ended up being completely different from what I expected. The past few years have been full of ups and downs. Despite all the things that have happened, sad or happy, tears or laughs, my doctorate has been a prolonged process that has finally come to an end.

I would like to express my gratitude to all the people who have helped me in the last few years to finalize this dissertation.

Firstly, I would like to express my highest thanks to my supervisor Dr. Simone Ciampi. He has been the best mentor for this doctorate. He is full of wisdom, patience, and kindness. His meticulous care and earnest guidance have benefited me tremendously. His rigorous academic attitude, keen sensitive insight into scientific problems, and enthusiastic work style deeply impressed me. The infinite knowledge and subtle influence learned from him will profoundly play a vital role in my future scientific life. During the tough days, he offered constructive advice and endless encouragement with a perfect combination of kindness and firmness. He always had a sensible plan B. His support and plenty of knowledge in electrochemistry and semiconductor chemistry helped me in understanding the fundamental knowledge and guiding me through the publication progress. With immense help from him in revising my manuscripts, I managed to publish my research in selective journals. Remembering the first time I met him in his office, it was interesting and surprising that at our first encounter he offered me a box of papers with many hand-written notes with an advice that all that was in those papers would become a hot topic in the next few years. During the epidemic days far from Perth, I always remember that image. “Electrostatic catalysis is a blossoming field, and it will lead to a Nobel Prize for someone at some point. We just need to be on the front of that wave.” I am remembering those words again and again. Due to the

pandemic the research ended up taking a different direction, but it was nonetheless a very formative experience. In the beginning, Simone explained to me that the main research would have focused on the modification of silicon surface, not silica with silanes, however ironically my probably single most important contribution was in shining some light on the reversible conversion of silicon and silica at room temperature. Science is full of surprises. Simone opened to me the doors of electrochemistry and semiconductors science. I'm so proud of, and so grateful for this.

I would like to thank my co-supervisor Dr. Nadim Darwish. His immense knowledge of AFM and STM has impressed me from the start. His discussions were always full of encouragements. He over and over helped me when I met difficulties and his enthusiasm for basketball gave me a lot of happiness in my spare time.

I would like to thank Dr. Franca Jones for the help in submitting the candidacy and paperwork related to my studies.

I would like to thank Dr. Yan B. Vogel. He taught me how to perform hydrosilylation reactions on the surface of silicon, how to measure cyclic voltammetry, and how to analyze electrochemical data. He is an interesting and smart guy, full of enthusiasm and kindness.

I would like to thank my other colleagues in our group, Stuart P. Ferrie, Xin Lyu, Chandramalika Peiris, Carlos H. Torres, thanks a lot guys for your help in AFM, XPS and contact angle measurements. Also, sincere thanks to all the other groups members, including Jinyang Zhang, Tiexin Li, Mattia Belotti, Essam Dief, and Soraya Rahpeima – thanks for your discussions and for those happy and enjoyable times together.

I would like to thank other colleagues in Building 500, Peter Chapman, Grant Cope and Ching Goh. Thank you for your helps and assistances in the daily university life.

I would like to thank Prof. Zhenbo Wang at Harbin Institute of Technology. Thanks for helping me in purchasing reagents and offering me the lab for working in HIT. I would like to thank Mr. Yunfei Xia for his help in measuring XRD and thank Miss Yi Han and Mr. Wang Ke, I've really appreciated the lunch breaks we enjoyed together.

I would like to thank A/Prof. Josh Lipton-Duffin, Queensland University of Technology, for assistance with the XPS analysis.

I would like to thank my classmate, Dr. Ling Yang, for her major help in contacting the lab and help in daily life at Harbin Institute of Technology. I would like to thank Dr. Wentao Wang, Dalian Institute of Chemical Physics, for his continuous encouragements and help in those 'dark' days when borders were closed.

My most special appreciation goes to my mother. Thank you, mom, greatest gratitude to you for your raising me up and all of understandings in those difficult dates. Life is full of all kinds of hardships. Without your support and love, I could have not done much. From kindergarten to finishing a PhD course, you have been always supporting me, especially in the pandemic period for the financial support in those days without any earning. Lots of things occurred during this long march, no matter it is happiness or misery. Considerable endorse to me from you, the "thanks" is not enough to express the thanks.

The darkest days were obviously when my father passed away, suddenly in the middle of this doctoral journey, though I think you are always watching our family from another world. We are missing you every day deeply.

I would like to express appreciate to the special one in my life, although there were so many affairs disturbing the daily life between us in these years. I am quite sure about

that there must be a happy ending for the whole story of our lives. Everything happens for the best.

I have to say something to the SARS-CoV-2 and the COVID 19, you are the most unexpected accidents, and have added an extra level of difficulty to the PhD and shaped my future in an unexpected direction.

Finally, I would like to thank Curtin University for the CIPRS and Research Stipend Scholarship, for the financial support towards my doctorate, and the Australian Research Council (ARC) for the generous financial support.

SONG ZHANG

Lists of Abbreviations

AC	Alternating current
AFM	Atomic force microscopy
CA	Contact angle
C–AFM	Conductive atomic force microscopy
CuAAC	Copper-catalyzed azide–alkyne cycloaddition
CV	Cyclic voltammetry
CZ	Czochralski process
DC	Direct current
DCM	Dichloromethane
E_c	Energy level at lowest conduction band edge
E_F	Energy level at Fermi level
E_{fb}	Flat band potential
E_g	Band gap energy
EIS	Electrochemical impedance spectroscopy
E_{redox}	Energy level defined by the redox solution
E_v	Energy level of the valence band edge
FWHM	Full width at half maximum
HD	Highly doped
LD	Lowly doped
M–S	Mott–Schottky
OCP	Open circuit potential
PF-TUNA	Peak Force tunnelling AFM
SAMs	Self-assembled monolayers
TUNA	Tunnelling AFM
XPS	X-ray photoelectron spectroscopy

List of Publications

List of publications included as part of this thesis.

- 1 **Song Zhang**, and Simone Ciampi, Facet-resolved Electrochemistry: From Single Particles to Macroscopic Crystals. *Curr. Opin. Electrochem.* 2022, 35:101085. 10.1016/j.coelec.2022.101085

This paper is included in Chapter 1.

Affiliations:

S.Z. and S.C.

School of Molecular and Life Sciences, Curtin University, Bentley, Western Australia 6102, Australia.

- 2 **Song Zhang**, Xin Lyu, Carlos Hurtado Torres, Nadim Darwish, and Simone Ciampi. Non-Ideal Cyclic Voltammetry of Redox Monolayers on Silicon Electrodes: Peak Splitting is Caused by Heterogeneous Photocurrents and Not by Molecular Disorder. *Langmuir* 2022;38(2):743–750.

This paper is included in Chapter 2.

Affiliations:

S.Z., X.L., C.T., N.D., and S.C.

School of Molecular and Life Sciences, Curtin University, Bentley, Western Australia 6102, Australia.

- 3 **Song Zhang**, Stuart Ferrie, Chandramalika R. Peiris, Xin Lyu, Yan B. Vogel, Nadim Darwish, and Simone Ciampi. Common Background Signals in Voltammograms of Crystalline Silicon Electrodes are Reversible Silica-Silicon Redox Chemistry at Highly Conductive Surface Sites. *J. Am. Chem. Soc.* 2021;143(3):1267–1272.

This paper is included in Chapter 3.

Affiliations:

S.Z., S.F., C.P., X.L., Y.V., N.D., and S.C.

School of Molecular and Life Sciences, Curtin University, Bentley, Western Australia 6102, Australia.

- 4 **Song Zhang**, Stuart Ferrie, Xin Lyu, Yunfei Xia, Nadim Darwish, Zhenbo Wang, and Simone Ciampi* Absence of a Relationship between Surface Conductivity and Electrochemical Rates: Redox-Active Monolayers on Si(211), Si(111), and Si(110). *J. Phys. Chem. C.* 2021;125(33):18197–18203.

This paper is included in Chapter 4.

Affiliations:

S.Z., S.F., X.L., N.D., and S.C.

School of Molecular and Life Sciences, Curtin University, Bentley, Western Australia 6102, Australia.

Y.X., and Z.W.

MIT Key Laboratory of Critical Materials Technology for New Energy Conversion and Storage, State Key Laboratory of Urban Water Resources and Environment, School of Chemistry and Chemical Engineering, Harbin Institute of Technology, Harbin 150001, China

Copyright statement

I have obtained permission from the copyright owners to use any third-party copyright material reproduced in the thesis (e.g., questionnaires, artwork, unpublished letters), or to use any of my own published work (e.g., journal articles) in which the copyright is held by another party (e.g., publisher, co-author).

Statement of contribution of others

I, Song Zhang, as the author of this thesis, conduct most of the experimental works and data analysis, all under supervision of my principal supervisor, A/Prof. Simone Ciampi. Contribution statements for each of the four published papers presented in this thesis are provided separately in the appendix section. The skills and input of several senior scientists and junior colleagues have been pivotal, and these are specified below:

Dr. Simone Ciampi provided project supervision, data analysis and manuscript editing.

Dr. Nadim Darwish provided project supervision, data analysis and manuscript editing.

Stuart P. Ferrie, Xin Lyu and Chandramalika Peiris helped very generously with the AFM measurements.

Xin Lyu helped greatly with the XPS measurements.

Dr. Yan B. Vogel helped with the analysis of electrochemical data.

Carlos H. Torres helped with contact angle measurements.

Yunfei Xia and Dr. Zhenbo Wang helped with the XRD measurements.

List of Figures

Figure 1.1. Schematic illustration of the energy band diagram in an intrinsic semiconductor (without doping). E_C represents the conduction band edge, which is the lowest unoccupied band, and E_V represents the valence band edge, which is the highest occupied band, the Fermi level (E_F) is in the middle of E_C and E_V . The E_g is the forbidden band gap, restricting electron movement..... 5

Figure 1.2. Schematic of energy band in a) n-type semiconductor, as well as b) p-type semiconductor. When the concentration of donors is increased, E_F shifts nearer to E_C in an n-type semiconductor, conversely, the E_F in a p-type semiconductor moves nearer to E_V as the level of acceptors is increased. 7

Figure 1.3. Schematics illustrating the band bending at an equilibrated interface between a n-type semiconductor and a metal contact (an analogous situation can be reached for a liquid contact where a redox species is dissolved). a) When the work function in the isolated semiconductor phase is smaller than it in the metal phase, the direction of net electron transfer (leading to equilibrium) is towards the metal. A depletion layer with upward band bending forms in the semiconductor phase. b) When the work function of the semiconductor is larger than that of the metal phase, the direction of electron transfer points towards the semiconductor, forming an accumulation layer in the semiconductor phase (downward band bending)..... 8

Figure 1.4. Depiction of band bending for a) n-type semiconductor, and b) for a p-type semiconductor, before (left) and after (right) being brought in contact with a redox electrolyte solution. Equilibrium is then reached between E_F and E_{redox} . Where E_C is conduction band, E_V is valence band, E_F is Fermi level, and E_{redox} is the electrochemical potential of the redox electrolytic solution. 9

Figure 1.5. Band diagram and the associated electric field in a) n-type semiconductor and in a b) p-type semiconductor upon illumination with light of energy greater than the band gap. The minority charge carriers [electrons (-) in the n-type, and holes (+) in the p-type] sense the in-built electric field of the depletion region (the band bending direction depends on the doping type). After irradiation the concentration of minority charge carriers will change significantly. 11

Figure 1.6. Schematic of relative crystal orientations on commercial wafer Si(111). A lapped Si(110) edge marks an internal reference orientation, selected by the commercial wafer supplier. It often marks the Si(110) facet, therefore cutting the Si(111) wafer on a direction perpendicular to this edge it will expose the Si(211) facet..... 14

Figure 1.7. Schematic illustration for the hydrosilylation of the silicon wafer. Chemical scheme is employed for showing the passivation of silicon [i.e., schematic representation of the different substrates, Si(111), and α -Si] Assisted by UV irradiation, hydrosilylation of 1,8-nonadiene (**1**) on Si-H generates an alkyne modified substrate (**S-1**), which is then reacted with a redox head group (i.e., azidomethylferrocene (**2**) is representative here, but the reaction is amenable to many azides) through a click reaction (copper-catalyzed azide-alkyne cycloaddition (CuAAC), generating a self-assembled monolayer (**S-2**) in this example a redox-active sample for electrochemical research. Reprinted from the study by Vogel et al ref.^[82] Springer Nature.(2017) <https://www.nature.com/articles/s41467-017-02091-1>, under the terms of the CC BY 4.0 license, <http://creativecommons.org/licenses/by/4.0/>. 18

Figure 1.8. a) Schematic demonstration of two domains of monolayers which are composed of Fc-(CH₂)₁₂-SH and CH₃(CH₂)₉SH. Part I denotes isolated Fc-(CH₂)₁₂-S-Au molecules and part II denotes cluster-formed Fc-(CH₂)₁₂-S-Au molecules. b) Representative cyclic voltammograms of two components monolayers formed containing different ratios of Fc-(CH₂)₁₂-SH and CH₃-(CH₂)₉-SH. CVs were recorded versus Ag/AgCl as a reference electrode in HClO₄ (1.0 M aq) as electrolyte, and the scan rate was 20 mV/s. Panels a) and b) are adapted from the study of Lee et al. ref^[103] with permission from the American Chemical Society, copyright (2006). 21

Figure 1.9. In the upper row, a schematic demonstration of the SAMs of Fc-(CH₂)_n-S on Au, shows five different electrochemical microenvironments. In the lower row, four distinguish CV peaks, related to packing structures caused by different intermolecular interaction, are shown. Peak I' stands for interactions between Fc and Au, peak I stands for Fc group exposing to electrolyte solution, peak II stands for fractionally concealed Fc units, peak III stands for buried Fc groups, and peak IV stands for disorder in the monolayer. Gold is denoted by pale yellow circle, sulfur is denoted by dark yellow circle, and ferrocene is denoted by blue circle containing an orange sphere. The figure is reprinted from the study of Nerngchamnonng et al. ref^[96] with permission from the American Chemical Society, copyright

Figure 1.10. a) Molecule structure of $\text{Fc}-(\text{CH}_2)_{11}\text{-SH}$. b) Schematic illustration of structure alternating between Fe/Fc^+ redox process, black circles represented sulfur by the and green circles represented the electrolyte anions. c) Cyclic voltammograms of ferrocene- $(\text{CH}_2)_{11}$ -thiol monolayer on $\text{Au}(111)$ were recorded vs Ag/AgCl as reference electrode, performed in NaClO_4 (0.1 M) as electrolytes, the scan rates were 10 mV/s, 30 mV/s, and 50 mV/s (from inside to outside). Panels a), b), c) are adapted from the study by Wong et al. ref^[104] with permission from the American Chemical Society, copyright (2018). 24

Figure 1.11. Facet-dependent conductivity of silicon crystals. Current–potential (I – V) traces curves and SEM images (insets) obtained with microscopic tungsten probes contacting adjacent but different silicon crystal facets. (a) I – V curves recorded between two $\text{Si}(111)$ facets, (b) between two $\text{Si}(112)$ facets, and (c) between $\text{Si}(112)$ and $\text{Si}(111)$. Adapted from the study by Tan et al.^[11], copyright (2017), with permission from Wiley-VCH..... 30

Figure 1.12. Electrochemical signatures of reversible silica–silicon conversion on highly conductive silicon facets. (a) AFM topography image of a $\text{Si}(111)$ wafer. Data obtained ensuring a parallel alignment between the original wafer major flat, indicating the $[110]$ direction, and the x -direction of the AFM raster scan. Steps between terraces, here roughly parallel to the sample major flat, are $\langle 110 \rangle$ facets. The scale bar is 400 nm. (b) Schematics of a Pt–organic monolayer–Si junction in a C-AFM measurement and the corresponding I – V curves (average of 400 curves) for $\text{Si}(111)$, $\text{Si}(211)$ and $\text{Si}(110)$ samples. **S-I** indicates the substrate is coated with a protective monolayer of 1,8-nonadiyne. (c) Magnified view of the first three sequential cyclic voltammetry (CV) cycles (six segments) of freshly made **S-I** samples on $\text{Si}(111)$. The bias was ramped from an initial -0.5 V to an anodic vertex of 1.0 V (0.1 V/s, aqueous 1.0 M HClO_4). (d) Hanging meniscus configuration designed to wet exclusively the $\text{Si}(110)$ facet, exposed by cleaving a $\text{Si}(111)$ wafer along a direction parallel to the wafer’s lap. (e,f) CVs of anodically damaged monolayer-coated $\text{Si}(111)$ and $\text{Si}(110)$ electrodes (**S-I**, 0.1 V/s, aqueous 1.0 M HClO_4). The surface coverage of the Si/SiOx signal observed on $\text{Si}(110)$ is ~ 6.9 times larger than on $\text{Si}(111)$ while the measured (capacitance) area ratio between $\text{Si}(111)$ and $\text{Si}(110)$ is only 1.9. (a, c–f) Adapted from the study by Zhang et al.^[16], copyright (2021), with permission from the American Chemical Society. (b) Adapted from the study by Zhang et al. ^[151], copyright (2021), with permission

Figure 1.13. *Electrical conductivity and electrochemical rates are not strictly related: lesson learnt from imaging redox reactions. (a) Electrochemical image taken with a spatial light modulator (SLM) addressing sequentially square sections (46 μm pixels, 17 Hz) of a silicon photoanode coated with different Cu_2O crystals. Insets in (a) and the image in (b) are SEM data of the Cu_2O electrocatalytic “lines” under investigation for their ability to promote the electro-oxidation of methanol. (c) A single channel potentiostat synchronized with the SLM records a current–time trace as that in (c), and this trace is then reconstructed to give the 2D redox map of (a). The time 0 s corresponds with the bottom-left pixel of the electrochemical image in panel (a), and the time 59 s with the top-right pixel. The series of “spikes” in the current transient data correspond to the time when the projected light passes over a Cu_2O “line”. The alternate high and low intensity current “spikes” relates to different activities of cubic vs. polyhedral particles. Adapted from the study by Vogel et al. ^[159], <https://iopscience.iop.org/article/10.1149/2.0111804jes/meta>, under the terms of the CC BY 4.0 license, <http://creativecommons.org/licenses/by/4.0/>. 34*

Figure 1.14. *Tuning surface energy with bias-dependent anisotropic adsorption of charged species: scope in redox lithography. (a) SEM data showing the change of Cu_2O crystal shapes for a constant electrolysis potential but with changes to the bulk concentration of chloride ions. (b) Evolution of the crystal shape in response to an increased anodic bias under a fixed chloride ions concentration. (c) Plots of the “degree of cubicity” versus bias (or versus concentration, top x-axis) under constant illumination based on a Langmuir isotherm (solid line). (d) SEM image of a “Mona Lisa” pattern made of Cu_2O nanocrystals. Using localized changed to light intensity (micrometer scale lateral resolution) two sets of information can be encoded into the same unit area: control over the polyhedral shape of individual nanocrystals and their lateral spacing, hence enabling to harness facet-dependent halide electro-adsorption to hide cryptic polyhedral signatures. (a–c) Adapted from the study by Vogel et al. ^[152], copyright 2018, with permission from the American Chemical Society. (d) Adapted from the study by Vogel et al. ^[165], copyright 2018, with permission from Wiley-VCH. 35*

Figure 1.15. *Facet-dependent electro-grafting of organic films on textured silicon. (a) SEM image of a Si(100) electrode exposing an array of Si(111) pyramids. (b) AFM image of a single Si(111) pyramid*

protruding from a Si(100) surface. (c) Electrochemical reduction wave for a CV recorded on the sample whose SEM is presented in (a). The solution contained **bis-diazo** (1 mM *o*-dianisidine bis(diazotized) zinc double salt, with 0.1 M Bu₄NPF₆ in a 1:49 v/v DMSO/ACN mixture) and the CV scan rate was 50 mV/s. (d) Facet-resolved electrochemistry on transparent electrodes. Cathodic electrografting of an aryl diazonium salt (NBD, 2 mM in acetonitrile with 0.1 M [Bu₄N]BF₄) through a cyclic voltammetry experiment (50 mV/s) on either β-Ga₂O₃(201) (red trace) or β-Ga₂O₃(010) (blue trace). (a–c) Adapted from the study by Peiris et al.,^[79] copyright (2019), with permission from the American Chemical Society. (d) Adapted from the study by Carroll et al.,^[172] copyright (2021), with permission from the American Chemical Society. 37

Figure 2.1. a) Schematic representation of a heterogeneous (ordered/disordered regions) monolayer-coated gold electrode, and (right) a typical cyclic voltammogram recorded on a single-crystal gold electrode modified with a monolayer of 11-ferrocenyl-1-undecanethiol (Au(111); 100 mV/s, 1.0 M HClO₄). b) Schematic depiction of a monolayer-coated silicon electrode, and near-ideal cyclic voltammetry (right) acquired on a highly doped silicon electrode coated with a ferrocene monolayer (0.007–0.013 Ω cm, p-type, Si(111); 100 mV/s, 1.0 M HClO₄). c) Schematic depiction of heterogeneous photocurrents across a silicon photoanode (1.0 mW cm⁻²), and experimental evidence of peak-splitting in cyclic voltammetry (right) using a lowly doped silicon photocathode coated with a ferrocene monolayer (8–12 Ω cm, n-type, Si(111); 100 mV/s, 1.0 M HClO₄). d) Chemical strategy used for the passivation and derivatization of the hydrogen terminated silicon surface. The UV-assisted hydrosilylation of 1 on Si–H generates an alkyne-terminated surface (M-1), which is subsequently reacted with azidomethylferrocene (2) through a CuAAC reaction, yielding a redox-active monolayer (M-2)..... 61

Figure 2.2. Doping level and type and ideality of the redox response. a) Representative and close-to-ideal cyclic voltammogram (CV) recorded for a **M-2** sample prepared on HD, p-type Si(111) (100 mV/s, 1.0 M HClO₄, dark, $\Gamma = 1.64 \times 10^{-10}$ mol cm⁻²). b) Plot of current peak values (anodic waves) vs voltage scan rate (the error bars indicate the 95% confidence interval of the mean). c) A representative CV for a **M-2** monolayer grafted on a Si(111), n-type, LD photoanode, showing an evident non-ideal peak splitting (100 mV/s, 1.0 M HClO₄, electrode illuminated at a light intensity of 1.0 mW m⁻², $\Gamma = 1.95 \times$

$10^{-10} \text{ mol cm}^{-2}$)..... 62

Figure 2.3. Peak multiplicity on Si(111) photoanodes: experiments and simulations. a) Progressive disappearance with increasing light intensity of the peak multiplicity characteristic of voltammograms recorded on silicon photoanodes. The electrodes are LD, n-type Si(111) crystals modified with a M-2 monolayer. The level of electrode illumination is specified by labels to the CV traces. The electrolyte was 1.0 M HClO₄, and the scan rate 0.1 V/s. b) Simulation of the CV trace recorded at the lowest light intensity, demonstrating that the key feature of the experimental data, a 188 mV peak-to-peak separation, can be accounted for as surface domains with a 1,500 fold difference in photocurrent (larger photocurrent for the blue dashed trace). The self-interaction parameter, G, necessary to reproduce the experimental fwhm, is negative, indicating repulsive molecular interactions for ferrocenes in both domains (-1.4, red trace; -0.6, blue trace). Best fit parameters are 10 s⁻¹ for the electron transfer rate constant, 1 μA for the dark leakage current, unity for the diode quality factor, and 0.5 for α..... 65

Figure 2.4. Lateral electrical heterogeneity. Current–potential (I–V) curves acquired by C-AFM on M-1 samples (LD, n-type Si(111)) and measurement schematics of the platinum–monolayer–silicon junction. The bias routing is from the substrate to the AFM tip, so that the reverse current (leakage) of the junction appears in the positive quadrant (positive current, positive bias)..... 67

Figure 3.1. Cyclic voltammograms of 1,8-nonadiyne-modified Si(111) electrodes. The electrode voltage is ramped from an initial -0.5 V to an anodic vertex, set to either 0.0 V in (a), or to 1.0 V in (b). (c) Color-coded magnified views of the first three sequential voltammetric cycles (six segments) shown in (b). The voltage scan rate is 0.1 V/s, and the electrolyte is aqueous 1.0 M HClO₄..... 80

Figure 3.2. XPS narrow scans of the Si 2p region acquired (a) before, and (b–f) after having deliberately introduced an anodic damage to 1,8-nonadiyne-modified Si(111) n-type (7–13 ohm cm) electrodes. The anodic process consisted in cyclically ramping the potential of the working silicon electrode from an initial -0.5 V bias to an anodic vertex set to 1.0 V, and then back to -0.5 V (one cycle). Spectra in (b), one cycle; (c), two cycles; (d), three cycles; (e) five cycles; and (f), 10 cycles). The electrolyte was aqueous 1.0 M HClO₄. The black thick curves are the experimental XPS data (108–92 eV), while the four thin traces (105–95 eV) are the fitted contributions ascribed to Si⁽³⁾ & Si⁽⁴⁾, Si⁽¹⁾, and elemental silicon

(Si 2p_{1/2}, and Si 2p_{2/3}). The red trace is the sum of all refined peaks. The fraction of oxidized Si surface atoms is estimated to be 0 (a), 13.75% (b), 15.44% (c), 23.21% (d), 40.35% (e), and 65.07% (f). The distribution of silicon over its oxidation states is quite interesting, and for example as also observed by Cerofolini and co-workers,^[29] there is absolute absence of Si⁽²⁾ species and an anomalously high fraction of Si⁽¹⁾. It is therefore possible that the +0.95 eV (Si⁽¹⁾) shoulder on the high binding energy side of the main Si 2p peak also includes emissions from silicon bound to hydrogen.⁴ The quality of the fitting was improved by merging the Si⁽³⁾ and Si⁽⁴⁾ contributions into one single band of intermediate character between +2.48 eV (Si⁽³⁾) and +3.90 eV (Si⁽⁴⁾)..... 81

Figure 3.3. (a,b) Atomic force microscopy height images of monolayer-coated Si(111) wafers. Topography images were acquired paying attention to ensure a parallel alignment between the major flat, indicating the [110] direction, and the x-direction of the AFM raster scan. Steps between terraces are either roughly parallel to the sample major flat (a), or oriented 30° away from it (b). Scale bars in (a) and (b) are 400 and 220 nm, respectively. (c,d) Heat maps of current–potential (I–V) data for platinum–silicon junctions acquired by conductive AFM on Si(111) and Si(110) surfaces. I–V curves are sampled at 100 evenly spaced points and are recorded at a constant force of 2.5 μN with a 100 nA/V sensitivity. The sample-to-tip bias routing is such that forward currents appear in the negative quadrant, that is, when the n-type silicon is biased negative with respect to the platinum AFM tip 82

Figure 3.4. (a) Cyclic voltammograms of Si(111) electrodes indicating an anodic shift with progressive potential cycling (three cycles, black curves; 100 cycles, red curves) of the apparent formal potential of the silica/silicon redox couple. The scan rate is 0.1 V/s, and the electrolyte is 1.0 M HClO₄. b) I–V curves (AFM) of platinum–silicon junctions recorded on anodically damaged Si(111) electrodes, showing a significant increase in the leakage current (positive quadrant) compared to fresh samples (Figure 2c). (c,d) Changes to surface topography before (c) and after (d) three potential sweeps between –0.5 V and 1.0 V (0.1 V/s, 1.0 M HClO₄). Scale bars in (c) and (d) are 1 μm 84

Figure 3.5. (a,b) Cyclic voltammograms of anodically damaged Si(111) and Si(110). The surface coverage of the redox background signal observed on Si(110) is 12.73 × 10⁻¹² mol cm⁻², which is 6.9 times larger than on Si(111). The geometric area ratio of the two electrodes is approximately 1.9 ((111) to (110), estimated by capacitance measurements). Voltammograms were recorded at a scan rate of 0.1

V/s, in aqueous 1.0 M HClO₄, after three potential sweeps (0.1 V/s) between -0.5 V and 1.0 V. (c) Optical images of the hanging-meniscus configuration used to wet the (110) facet in a three-electrode experiment used to record the voltammograms in (b). A graphical depiction of the (211) and (110) crystal directions in commercial Si(111) wafer is in Figure B12 Appendix B. 86

Figure 3.6. AFM topography images of Si(100) samples etched with ammonium fluoride to expose Si(111) pyramids on the surface. Scale bars are 400 nm in (a), and 100 nm in (b). 87

Scheme 4.1. Passivation of hydrogen-terminated silicon electrodes on Si(111), Si(211), and Si(110), followed by UV-assisted hydrosilylation of 1,8-nonadiyne (**1**) to yield an alkyne-terminates silicon surface (**S-1**), and its reaction with azidomethylferrocene (**2**) via CuAAC “click” reactions generated a redox-active monolayer (**S-2**). 95

Figure 4.1. Representative cyclic voltammograms (CVs) for ferrocene monolayers (**S-2**) prepared on silicon substrates of different crystalline orientation [(a), Si(111); (b), Si(211); (c), Si(110)]. The potential sweep was started at 0 V (cathodic vertex). The voltage scan rate was 0.1 V/s, and the electrolyte was aqueous 1.0 M HClO₄. (d) CV-derived surface ferrocene coverage (Γ) for **S-2** samples prepared on Si(111), Si(211) and Si(110) electrodes. Error bars indicate the 99% confidence limit of the mean. 98

Figure 4.2. XRD patterns for Si(111), Si(110) and Si(211) substrates. Samples exposing a Si-H_x surface after NH₄F etching and stored in dichloromethane prior to XRD measurements. Note: The Si(111)-H surface is known to be a close to ideal, Si-monohydride terminated surface. However, even this near-ideal surface has dihydride edge sites. At present the average number of hydride terminations on NH₄F etched Si(211) and Si(110) is unknown. 99

Figure 4.3. Measurement schematic and current-potential (I-V) data for platinum-silicon junctions obtained by conductive mode (PF-TUNA) atomic force microscopy (AFM) on monolayer-modified (**S-1**) Si(111) (a), Si(211) (b), and Si(110) (c). Solid symbols indicate the mean value of 400 I-V sweeps obtained on four independently prepared and analyzed samples. The color-shaded areas represent the data standard deviation. 102

Figure 4.4. Representative EIS Bode plots for S-2 samples prepared on silicon crystals of different orientation ((a), Si(111); (b), Si(211); (c) Si(110)). The DC bias of the EIS measurement was set to the $E_{1/2}$ value obtained from CV measurements, and the amplitude of the AC perturbation was set to 15 mV. All experiments were performed in aqueous 1.0 M HClO₄. (d) Plot of the EIS-derived ket values..... 104

Figure A1. Representative CVs of a monolayer-modified gold electrode (11-ferrocenyl-1-undecanethiol monolayers self-assembled on Au(111)). The voltage sweep rate was changed between 100 and 2000 mV s⁻¹ and the data acquired in 1.0 M HClO₄, either under dark or under electrode illumination (solid line, dark; state, red empty symbols, light). Electrode illumination had no effect on the CV traces. (100 mV s⁻¹, dark coverage = 5.22×10^{-10} mol cm⁻², coverage under light = 5.17×10^{-10} mol cm⁻²; b) 250 mV s⁻¹, dark coverage = 5.19×10^{-10} mol cm⁻², coverage under light = 5.22×10^{-10} mol cm⁻²; c) 500 mV s⁻¹, dark coverage = 5.22×10^{-10} mol cm⁻², coverage under light = 5.17×10^{-10} mol cm⁻²; d) 750 mV s⁻¹, dark coverage = 5.06×10^{-10} mol cm⁻², coverage under light = 5.08×10^{-10} mol cm⁻²; e) 1000 mV s⁻¹, dark coverage = 5.12×10^{-10} mol cm⁻², v 5.11×10^{-10} mol cm⁻²; f) 2000 mV s⁻¹, dark coverage = 4.99×10^{-10} mol cm⁻², coverage under light = 4.97×10^{-10} mol cm⁻²)..... 119

Figure A2. Representative CVs of M-2 samples prepared on either (a) HD p-type Si(111), dark, and indicating a ferrocene coverage of $1.94 \pm 0.26 \times 10^{-10}$ mol cm⁻², (b) LD n-type Si(111) under light intensity 24.1 mW cm⁻², with a coverage of $1.99 \pm 0.84 \times 10^{-10}$ mol cm⁻², and (c) LD n-type Si(100) under light intensity 24.1 W cm⁻², showing a coverage of $1.44 \pm 0.23 \times 10$ mol cm⁻². The electrolyte was aqueous 1.0 M HClO₄ and the scan rate 100 mV s⁻¹. 120

Figure A3. Representative CVs of M-2 monolayers prepared on HD p-type Si(111) recorded under different light intensity (indicated in figure). The electrolyte was aqueous 1.0 M HClO₄ and the scan rate 100 mV s⁻¹. 121

Figure A4. Representative CVs of M-2 samples prepared HD p-type Si(111) under dark at different voltage scan rate (50 mV s⁻¹, 100 mV s⁻¹, 250 mV s⁻¹, 500 mV s⁻¹, 750 mV s⁻¹, 1.0 V s⁻¹, 2.0 V s⁻¹, 5.0 V s⁻¹, 7.5 V s⁻¹, 10.0 V s⁻¹ The electrolyte was aqueous 1.0 M HClO₄. 121

Figure A5. Representative CV of a M-2 sample prepared on LD n-type Si(111) and recorded under dark. The electrolyte was aqueous 1.0 M HClO₄ and the scan rate 100 mV s⁻¹. 122

Figure A6. a) In n-type electrodes, at potentials more positive than EFB, the Fermi level is lowered (i.e. further away from the zero AVS) and electrons are forced away from the space charge region and leave behind ionized positively charged donor centers. In depletion, and under illumination, holes generated in the valence band will migrate toward the interface under an electric field pointing outward (i.e. bands pointing upward) where this vacant state at the top of the valence band will consume available electrons. Depleted n-type electrodes under illumination can therefore act as photoanodes. In summary, the blocking effect of depleted dark silicon electrodes is efficiently reversed upon illumination with light of a frequency greater than 2.7×10^{14} Hz provided that inversion is not reached and electron-hole recombination events are minimized. Generated electron-hole (e^-/h^+) pairs at depleted n- electrodes under illumination. Minority charge carriers migrate under the space-charge region electric field toward the electrolyte and participate in redox reactions (i.e. photooxidations at n-type electrodes). Since valence band holes mediate the oxidation of surface species, the potential at which the rate of change of surface concentrations peaks (i.e. a peak in the CV of non-diffusive species) is less positive (i.e. closer to the zero of the AVS scale), or in other words contra-thermodynamic relative to the situation in a metal electrode. The situation of a metal electrode is depicted in b). Here The applied potential lifting or lowering EF above or below Eeq corresponds to electro-reduction (a) and electro-oxidation (b). c)The effect of increasing the light intensity is that of flattening the bands (i.e. shifting upward the E_F)..... 123

Figure A7 . Representative CVs of **M-2** samples prepared LD n-type Si(111) recorded under light intensity of 1.0 mW cm^{-2} by varying the voltage scan rate (0.1, 0.2, 0.5 and 1.0 V/s ; $\Gamma = 2.34 \times 10^{-10} \text{ mol cm}^{-2}$). The electrolyte was aqueous 1.0 M HClO_4 124

Figure A8. Electrochemical impedance spectroscopy (EIS) data for **M-2** monolayers (n-type, Si(111) dark) acquired between 10^5 Hz and 1 Hz , at an applied working electrode DC potential of 0.0 V versus Ag/AgCl and with an AC perturbation of 15 mV 124

Figure A9. Representative CV of **M-2** sample prepared by LD n-type Si(111) photoanodes under light intensity 1.0 mW cm^{-2} in aqueous 1.0 M HClO_4 . The scan rate is 0.1 V/s , and the ferrocene coverage (Γ) is $1.07 \times 10^{-10} \text{ mol cm}^{-2}$. Click reaction quenched after 5 min..... 125

Figure A10. Deconvolution of the anodic peaks from representative CVs of **M-2** monolayers prepared

on n-type LD, Si(111), recorded under variable light intensity. a) 1.0 mW cm⁻², cumulative coverage 2.40 × 10⁻¹⁰ mol cm⁻², fwhm of peak 1 = 122.2 mV, fwhm peak 2 = 161.7 mV; b) 2.9 mW cm⁻², cumulative coverage 2.43 × 10⁻¹⁰ mol cm⁻², fwhm of peak 1 = 99.7 mV, fwhm peak 2 = 152.2 mV; c) 4.7 mW cm⁻², cumulative coverage 2.45 × 10⁻¹⁰ mol cm⁻², fwhm of peak 1 = 97.8 mV, fwhm peak 2 = 130.3 mV. Curve refinement was done using the bi-Gaussian peak function in Origin 9. 126

Figure A11. Simulation of the CV trace recorded at the lowest light intensity, demonstrating that the key feature of the experimental data, a ~190 mV peak-to-peak separation, can be accounted for as surface domains with a 1,000 fold difference in the dark leakage current (1.0 × 10⁻⁹ A for the blue dashed trace, 1.1 × 10⁻⁶ A for the red dashed trace). The self-interaction parameter, G, necessary to reproduce the experimental fwhm, is negative, indicating repulsive molecular interactions for ferrocenes in both domains (-1.4, red trace; -0.6, blue trace). Best fit parameters are 10 s⁻¹ for the electron transfer rate constant, 750 μA for photocurrent (both peaks), unity for the diode quality factor, and 0.5 for α. 127

Figure A12. Representative AFM of current map at 0 V. The sampling area was of 2 × 2 μm². Individual I-V traces (from -2.0 V to +2.0 V) were collected in the center of each square shown in figure. 128

Figure A13. EIS Mott-Schottky (M-S) measurement of capacitance vs sample bias for M-2 samples prepared on LD n-type Si(111). The experiments were run in dark, with the AC frequency set to 40,000 Hz, the AC bias amplitude to 15 mV. The electrolyte was 1.0 M aqueous HClO₄. 128

Figure B1. Representative cyclic voltammograms recorded on anodically damaged monolayer-coated Si(111) samples of different doping level and type ((a), n-type, highly doped Si(111), 0.007–0.013 Ω cm; (b) Si(111), highly doped p-type Si(111), 0.007–0.013 Ω cm; (c) Si(111), lowly doped p-type Si(111), 8–12 Ω cm). The electrode voltage was first ramped three times from an initial bias of -0.5 V to an anodic vertex set to 1.0 V, and then back to -0.5 V (not shown). Cyclic voltammograms shown in figure were then sampled, after this oxidative procedure, between -0.4 V and 0.2 V. Scan rates were set to 0.1 V/s, and all experiments were performed in aqueous 1.0 M HClO₄ as the supporting electrolyte. 130

Figure B2. Representative consecutive cyclic voltammograms (ten cycles, scan rate 0.1 V/s) acquired on Si(111) electrodes previously subject to an electrochemical anodic damaging process. The electrode anodic damage was introduced by means of ramping the potential of the working silicon electrode from

an initial -0.5 V bias, to an anodic vertex set to 1.0 V (3 cycles). The electrolyte was aqueous 1.0 M HClO_4 . The surface coverage, estimated by integration of the first circle, was 2.50×10^{-12} mol cm^{-2} . From the second cycle onwards, the coverage remained approximately stable, changing from 2.33×10^{-12} mol cm^{-2} (second cycle), to 2.27×10^{-12} mol cm^{-2} (10^{th} cycle, equivalent to a drop smaller than 3%). 131

Figure B3. Stereographic projection of a Si(111) wafer. This is a graphical representation of crystal planes (3D features) in a 2D plane. The center of the circle indicates the direction of the (111), here meaning that sections parallel to the wafer will be (111) planes. The supplier marked a major lap to indicate the $\langle 110 \rangle$ direction. The stereographic projection depicts the angular relationships between crystal faces (defines the relative ϕ and ρ angles) and indicates that the terraces visible in the AFM images of Si(111), assuming they are normal to the wafer surface, are roughly either Si(110) or Si(211) facets..... 132

Figure B4. Estimation of the area ratio between Si(110) steps and Si(111) terraces. a) AFM topography image of a Si(111) sample showing a terraced structure. b–d) are height profiles measured along the three sampling lines (x, y and z) marked in panel (a). The three lines are drawn along a direction orthogonal to the terraces main direction, which by considering the major lap of the wafer indicates the surface of the steps is mainly Si(110). Quantitatively, data in b), pertinent to the line x drawn in (a) suggest a Si(111)/Si(11) area ratio of 0.18%, data in (c), pertinent to the line y in (a) suggest a 0.20% value, and data in (d), pertinent to line z indicate a 0.25% ratio. 133

Figure B5. Current output from (Pt–Si) contacts made by conductive AFM on lowly doped ($7\text{--}13$ Ω cm) CZ n-type Si(111). a) Representative (ca. 100) current–potential (I–V) curves acquired on oxide-free Si(111) sample coated with a monolayer of 1,8-nonadiyne. b) Average of the individual traces shown in panel (a). 134

Figure B6. Current output from (Pt–Si) contacts made by conductive AFM on lowly doped ($7\text{--}13$ Ω cm) CZ n-type Si(110). a) Representative (ca. 100) current–potential (I–V) curves acquired on oxide-free Si(110) sample coated with a monolayer of 1,8-nonadiyne. The Si(110) surface was first exposed by cutting a Si(111) wafer along a direction parallel to the lapped edge exposing the (110) plane, as marked

on commercial Si(111) wafers purchased from Siltronix. The sample was coated with a monolayer of 1,8-nonadiyne. Individual traces are in (a), and their average I–V values are in (b). 135

Figure B7. Cyclic voltammograms acquired on monolayer-coated Si(111) electrodes in different electrolyte systems. Data in figure show that for the entire range of electrolytes tested – from strongly coordinating sodium chloride to non-coordinating sodium tetrakis[3,5-bis(trifluoromethyl)phenyl]borate (NaBARF) – silicon anodic damage invariably leads to the appearance of the two redox waves centred at ca. -0.1 V, with no evidence of effects linked to the nature of the electrolyte anion. Experiments shown in figure were performed after having deliberately introduced an anodic damage to the electrode by means of ramping the voltage between -0.5 V and 1.0 V for three consecutive cycles. The electrolytic systems (electrolyte/solvent) are: a) 1.0 M NaCl/water, surface coverage 2.26×10^{-12} mol cm^{-2} ; b) 1.0 M TBABr/water, 1.22×10^{-12} mol cm^{-2} ; c) 1.0 M NaClO₄/water, 2.87×10^{-12} mol cm^{-2} ; d) 0.25 M TBAClO₄/acetonitrile, 4.60×10^{-13} mol cm^{-2} ; and e) 0.01 M NaBARF/isopropanol, 8.64×10^{-13} mol cm^{-2} . All scan rates were set to 0.1 V/s. 136

Figure B8. a) One hundred current–potential (I–V) curves (conductive AFM) acquired on anodically damaged Si(111) sample. The anodic process consisted of three cyclic voltammetry cycles between -0.5 V and 1.0 V in aqueous 1.0 M HClO₄ and at a scan rate of 0.1 V/s. b) Average of the traces shown in panel (a). The sample was monolayer-coated (1,8-nonadiyne) poorly doped (7 – 13 Ω cm) CZ n-type Si(111) wafer. 137

Figure B9. AFM topography images of an anodically damaged Si(111) sample. The sample was coated with a monolayer of 1,8-nonadiyne and then ramped between -0.5 V to 1.0 V (100 cycles, 1.0 M HClO₄, scan rate 0.1 V/s). Scale bars are $2\mu\text{m}$ in (a) and 400 nm in (b). 138

Figure B10. Representative cyclic voltammograms for anodically damaged Si(111) electrodes under acidic conditions. The electrolyte varied between a) 1.0 M HClO₄, b) 0.1 M HClO₄, and c) 0.01 M HClO₄. The scan rate is 0.1 V/s. Data shown in figures are recorded after having deliberately introduced an anodic damage to the electrode by means of ramping the voltage between -0.5 V and 1.0 V for three consecutive cycles. All electrodes were initially monolayer coated. 139

Figure B11. Cyclic voltammetry data of glassy carbon (a) and amorphous silicon electrodes (b). Both

samples were analyzed after performing three voltammetric scans between -0.5 V and 1.0 V at the sweep rate of 0.1 V/s in 1.0 M HClO_4 140

Figure B12. Schematic depiction of the Si(110) lap in a commercial Si(111) wafer. 141

Figure C1. a) Stereographic projection of silicon representing the crystallographic orientation relationship of Si(111), Si(211), and Si(110) surfaces. These projections illustrate the relative orientation of crystal planes (a 3D feature) on a 2D plane. b) Schematic depiction of cutting directions that could be used to expose Si(110) and Si(211) facets starting from a commercial Si(111) wafer. For instance, a lapped edge in a commercial Si(111) wafer often marks the (110) surface. and can be used to perform surface chemistry and electrochemistry on this facet. Alternatively, cleaving the Si(111) wafer along a direction normal to the lapped edge will expose the Si(211) surface. 143

Figure C2. XPS narrow scans of the Si 2p and C 1s regions for 1,8-nonadiyne-modified samples prepared on either: Si(211), (a–b); Si(110), (c–d), and Si(111), (e–f). The substrate was p-type of $0.007\text{--}0.013\text{ ohm cm}$ resistivity. The black thick lines are the experimental XPS data ($108\text{--}92\text{ eV}$ for Si 2p, and $294\text{--}279\text{ eV}$ for C 1s), while thinner black traces indicate the fitted contributions ascribed to Si 2p_{3/2} at 99.5 eV (0.6 eV fwhm), Si 2p_{1/2} at 100.1 eV (0.6 eV fwhm)^[1], Si-bound to hydrogen (Si–H) at 100.75 eV (0.9 eV fwhm)^[2], methylene carbons (C–C) at 285.0 eV (1.4 eV fwhm), silicon-bound olefinic carbons (Si–C=C) at 283.6 eV (0.9 eV fwhm), and oxygen bond carbon (C–O) at 286.3 eV (1.4 eV fwhm)^[3]. The structure of the adventitious C–O bond is not fully elucidated, although the contamination has been reported in several works.^[4–6] 144

Figure C3. Equivalent electrical circuit used to fit the electrochemical impedance spectroscopy data. R_s stands for solution resistance, R_{ct} for charge transfer resistance, C_{dl} for double layer capacitance, and C_{ads} for adsorption pseudo-capacitance. 145

Figure C4. Atomic force microscopy topography (height sensor) data for 1,8-nonadiyne coated Si(111), Si(211), and Si(110), a–c respectively. All scale bars are 400 nm 146

Table of Contents

DECLARATION.....	I
ABSTRACT.....	III
ACKNOWLEDGEMENTS	V
LISTS OF ABBREVIATIONS	IX
LIST OF PUBLICATIONS	X
COPYRIGHT STATEMENT.....	XII
STATEMENT OF CONTRIBUTION OF OTHERS.....	XIII
LIST OF FIGURES	XIV
TABLE OF CONTENTS	XXVIII
CHAPTER 1. THESIS OUTLINE AND GENERAL INTRODUCTION.....	1
1.1 Preface	1
1.2 Thesis outline	1
1.3 Background on silicon electronics and electrochemistry	4
1.3.1 Band bending in semiconductors	8
1.3.2 Photocurrent effects at semiconductor–liquid interfaces	10
1.3.3 Electrochemical reduction of silica to silicon	11
1.3.4 Miller indices and stereographic projections of silicon.....	13
1.4 Self-assembled monolayers	14
1.5 Electrochemical and electric measurements	19
1.5.1 Cyclic voltammetry	19

1.5.1.1 Non-ideal voltammetric signals	20
1.5.2 Electrochemical impedance spectroscopy	24
1.5.3 Conductive atomic force microscopy	25
1.6 Introduction to facet-resolved electrochemistry	27
1.6.1 Facet resolved electrochemistry in semiconductors	28
1.6.1.1 Abstract	28
1.6.1.2 Introduction.....	29
1.6.1.3 Facet-dependent electrical conductivity links to electrochemical reactivity: the case of Si and Cu ₂ O	30
1.6.1.5 Facet-resolved transition metal phosphides and hydrogen evolution reaction.....	38
1.6.1.6 Summary and perspective.....	39
1.7 References	39

CHAPTER 2. HETEROGENEOUS PHOTOCURRENTS EXPLAIN NON-IDEAL CYCLIC VOLTAMMOGRAMS OF REDOX MONOLAYERS ON SILICON PHOTOANODES

2.1 Abstract.....	55
2.2 Introduction	55
2.3 Experimental section	57
2.3.1 Chemicals	57
2.3.2 Silicon and gold crystals	57
2.3.3 Silicon surface modification	58
2.3.4 Gold surface modification	59
2.3.5 Electrochemical measurements.....	59
2.3.6. Atomic force microscopy	60
2.3.7. Water contact angle	61
2.4. Results and discussion.....	62
2.5 Conclusions	68
2.6 References	68

CHAPTER 3. REVERSIBLE SILICA–SILICON REDOX CHEMISTRY AT HIGHLY CONDUCTIVE SI(110) DEFECTS.....

3.1 Abstract.....	75
3.2 Introduction	75

3.3 Experimental section	76
3.3.1 Materials	76
3.3.2 Electrochemical measurements	77
3.3.3 Atomic force microscopy measurements	78
3.3.4 X-ray photoelectron spectroscopy measurements	78
3.4 Result and discussion	79
3.5 Conclusions	87
3.6 Reference	87
CHAPTER 4. ON THE RELATIONSHIP BETWEEN SURFACE CONDUCTIVITY AND ELECTROCHEMICAL RATES.....	92
4.1 Abstract	93
4.2 Introduction	93
4.3 Methods	95
4.3.1 Silicon surface modification	95
4.3.2 Electrochemical measurements	96
4.3.3 Surface topography and electrical measurements	97
4.3.4 X-ray diffraction measurements (XRD)	100
4.3.5 X-ray photoelectron spectroscopy (XPS)	100
4.4 Results and discussion	100
4.5 Conclusions	105
4.6 References	105
CHAPTER 5. SUMMARY AND CONCLUSIONS.....	111
CHAPTER 6. PERSPECTIVE AND OUTLOOK.....	114
6.1 Outlook.....	114
6.2 References	116
APPENDIX A	118
APPENDIX B	129

B1. Control experiments on Si(111) wafers of different doping level and type.....	130
B2. Stability testing.....	131
B3. Stereographic projection of a commercial Si(111) wafer	132
B4. Estimates of the area-ratio between surface steps and Si(111) terraces.....	133
B5. Facet-resolved conductivity: average current–potential (conductive AFM) data for Si(111) and Si(110).....	134
B6. Control experiments in different electrolyte systems.....	136
B7. Electrical and topographical characterization of samples upon their oxidation.....	137
B8. pH effects	139
B9. Controls with carbon and amorphous silicon electrodes.....	140
B10. Exposing a Si(110) facet in a lapped Si(111) wafer	141
APPENDIX C	142
C1. Additional results and discussions.....	143
C2. References	147
APPENDIX D. STATEMENTS OF CONTRIBUTIONS OF OTHERS	148
APPENDIX E. RIGHTS AND PERMISSIONS	155
Rights and Permissions related to Chapter 1:.....	156
Rights and Permissions related to Chapter 2:.....	171
Rights and Permissions related to Chapter 3:.....	172
Rights and Permissions related to Chapter 4:.....	173

Chapter 1. Thesis outline and general introduction

1.1 Preface

This thesis deals with electrochemistry and electrical conductivity of a semiconductor substrate that is modified with an organic monolayer. Electrochemistry is the branch of chemistry that studies chemical reactions coupled to the flow of electricity, and more specifically, its general objective is that to predict, explain and ultimately to manipulate the thermodynamics and kinetics of chemical changes at an electrode interface. The electrode substrate employed in this thesis is silicon, which is the dominant material of our modern digital world. Modification of the silicon surface leads to substrates with potential applications in telecommunications, microelectronics, photovoltaics, energy storage and biosensing. With these applications in mind, a complete and correct understanding of surface conductivity, charge transfer rate and thermodynamics, and photocurrent effects are crucial. All these are surface-dominated phenomena, and therefore to investigate the above mentioned topics, surface scientists have often resorted to engineering the silicon surface with self-assembled monolayers. The monolayers strategy expands the functionalization of the surface electronic property and energy level in the intrinsic silicon. Recently, researchers have discovered that the energy level and conductivity on silicon are dramatically facets-dependent.^[1] these recent observations suggest that the electrochemistry of silicon wafers, which to date have always almost exclusively been performed on Si(111) or Si(100), can be complicated (or benefit) by other crystal facets inevitably present on a nominal single crystal silicon substrate.

1.2 Thesis outline

This thesis is organized as follow.

Chapter 1 begins by introducing a general background on semiconductors and silicon.

The first sections will illustrate the basic principles of silicon electronics and

electrochemistry, and the important concepts required for studying the electrochemical and reactivity features of silicon crystals at the core of this dissertation. These includes, but are not limited to, the doping of silicon, the energy bands at a silicon–electrolyte interface, the energy level distribution, the band bending and the photo effects of a depleted interface, their impact on the charge transfer behavior across the space charge layer. Electrochemical methods for the reduction of silica to silicon, and the facet characterization of silicon wafers are introduced in the following section. As a main part of this thesis, a discussion on self-assembled monolayers is also presented. In addition, the main background knowledge of the experimental methods and instrumentation for electrochemical measurements is also introduced here. The last section of Chapter 1 is the paper published in *Curr Opin Electrochem.* 2022, 101085, a review article focusing on facet resolved electrochemistry on semiconductors.

Chapter 2 is adapted from the paper published in *Langmuir* 2022, 38, 743–750. This paper explores the nature of non-ideal multiple peaks in cyclic voltammetry of silicon. Peak multiplicity in experimental voltammetry of surface-confined (diffusionless) systems is generally attributed to molecular disorder. This paper shows that this is not always the case. This is important as chemists and surface scientists routinely turn to dynamic electrochemical measurements of molecular films – primarily through cyclic voltammetry (CV) – to probe charge transfer kinetics and redox equilibria at interfaces. But while for platinum, gold and carbon it is generally agreed that the splitting of CV waves is “diagnostic” of disorder in the molecular film, herein this chapter demonstrate, unambiguously, that such inference can be grossly erroneous for semiconducting electrodes. With semiconductor electrodes this non-ideal voltammetric signature is not indicative of molecular disorder. Through conductive AFM and a suite of electrochemical techniques, this chapter indicates how to systematically reproduce and magnify non-ideal peak splitting in silicon. It demonstrates that this signal is the manifestation of heterogeneous photocurrents and not caused by heterogeneous molecular interactions (*i.e.*, disorder). The results of this chapter are an essential step towards understanding the reason of non-ideal electrochemical features in

semiconductor electrochemistry, as a result that those signals can be avoided, and the redox behavior of self-assembled monolayers to be employed as photocatalytic systems can be improved. The work extends the understanding of the links between electrochemical and electrical features of interfaces.

Chapter 3 is adapted from the paper published in *J. Am. Chem. Soc.* 2021, 143, 1267–1272. This study has observed and explained the reversible electrochemical conversion of silicon to silica at room temperature. This discovery contributes to the electrochemistry and surface chemistry knowledge of silicon and ultimately it redefines the potential range which is free from parasitic redox peaks, and which is consequently accessible to investigate silicon surface reactions via electroanalytical methods. This is important because whilst for metal and carbon electrodes most adventitious electrochemical signals have been identified and explained, parasitic signals encountered when using silicon electrodes are still controversial (but most often in fact ignored). For example, several published papers focusing on the surface chemistry of silicon substrates carries explicit evidence of adventitious redox peaks. These peaks are generally either disregarded as artifacts, or more often associated with adsorption some target molecules, hence erroneously used to make inferences on the outcome of a range of surface reactions. The results of this chapter define how to systematically repeat and magnify a commonly observed parasitic signal. The data in the chapter bring evidence of this signal being the reversible electrochemical redox conversion of silicon to silica, which occurs at the edge of crystalline terraces – ubiquitous crystal defects that are very conductive and always present, even on nominally single crystal substrates.

Chapter 4 includes work published in *J. Phys. Chem. C* 2021, 125, 18197–18203. Electrode kinetics is dictated by surface properties of the electrode, such as bond lengths, geometries and band structure, but the search for the optimal electrode material remains by large a semi-empirical and time-consuming screening process, often progressing through trials and errors. Recent research has that discussed in Chapter 1 that for several technologically relevant electrode materials, such as silicon, Cu₂O and PbS, there is a prominent facet-dependent electrical conductivity. This chapter

demonstrate that despite evidence of a prominent facet-dependent electrical conductivity, as inferred by conductive atomic force microscopy, rates of redox reactions occurring on different facets of silicon surface remains indistinguishable. Using covalent Si–C-bound organic monolayers – both to protect the substrate from anodic decomposition as well as to tether a conventional redox probe, ferrocene – the research presented in this chapter demonstrate that conductivity decrease drastically in the order Si(211) > Si(110) > Si(111). Electrochemical rates inferred by electrochemical impedance spectroscopy point out however that there is no relationship between redox kinetics and surface conductivity.

Chapter 5 & Chapter 6 present the conclusions of the whole dissertation and introduce the perspective and outlook of facet-resolved electrochemistry future research, specifically towards electrostatic catalysis. Catalysis is the capability to speed up or control the rate of reactions using chemical entities that are not consumed in the process. This is one of the utmost effective fields of chemical industrial and science. Lack of a viable catalyst causes many reactions not to proceed at an appreciable rate. In 2016 scientists had demonstrated that an external and directional electric field can accelerate the rate of a chemical (non-redox) reaction.^[2] The external electric field can stabilize charge-separated contributors of the transition states, effectively acting as a non-chemical entity catalyst. In chapter 6 I will discuss facet resolved electrochemistry methodology combining with electric field stimulation to study and potentially accelerate (and perhaps control selectivity) of electrostatics catalysis to a chemical reaction, potentially to remodel catalysis by eliminating today's viewpoint that the specific chemical entity is suitable for specific chemical process.

1.3 Background on silicon electronics and electrochemistry

Silicon, whose abundance in the earth's crust is only second to oxygen, still reigns as the key material of our modern digitized society, largely owing to its unique bandgap (matching the solar spectrum), surface crystalline structure, electrical conductivity,

photoresponsivity, and stability.^[3-5] These features render it being the platform for the microelectronics and semiconductor industries. Pure silicon is almost an insulator, and

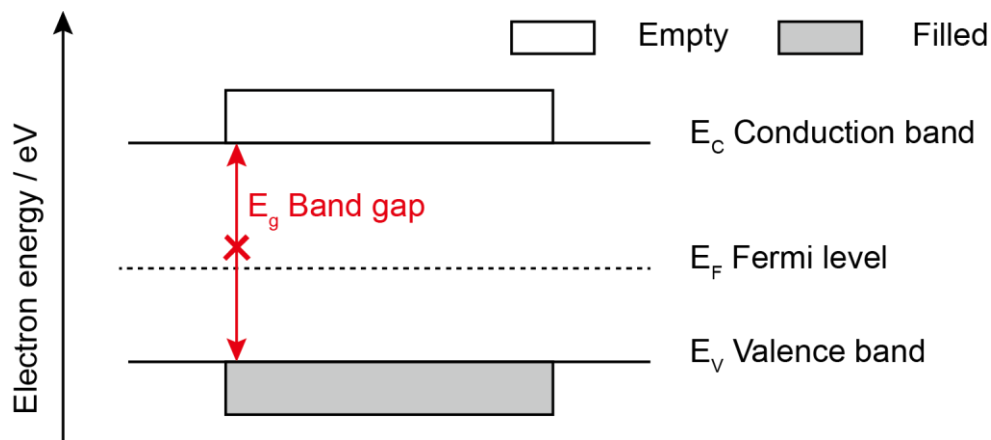


Figure 1.1. Schematic illustration of the energy band diagram in an intrinsic semiconductor (without doping). E_C represents the conduction band edge, which is the lowest unoccupied band, and E_V represents the valence band edge, which is the highest occupied band, the Fermi level (E_F) is in the middle of E_C and E_V . The E_g is the forbidden band gap, restricting electron movement.

its conductivity can be tuned by incorporating with other materials, *i.e.*, doping it with electron donor elements to form a negative carrier type of semiconductor [*i.e.*, phosphorus, n-type, electrons as the majority carrier], or doping it with electron acceptors to form a positive carrier type one [*i.e.*, boron, p-type, holes (+) as the majority carrier]. The conductivity of semiconductor is determined by the electron energy distribution from the surface to the bulk. The electron energy level distributed in semiconductor is classified as an allowed bands which exist at energy level and not allowed bands which exist without energy levels. Further, in allowed bands there are 1) conduction band (E_C) which is the lowest unoccupied band for electron, and 2) valence band (E_V) which is the highest energy occupied band for electron. In a semiconductor or in an insulator, E_C and E_V are separated by a band gap (E_g), which restricts the transfer of electrons from E_V to E_C , forming one clear forbidden band within which there exist no energy levels (in silicon the E_g is 1.12 V at 300 K). In metals, E_C and E_V overlaps, rendering its conductivity stronger comparing to semiconductors or insulators. Further, there is an important parameter which is in terms of Fermi level (E_F) represents the equilibrium distribution of carriers' energy level in semiconductor, the E_F is usually

located in middle of the band gap. Figure 1.1 show the energy level diagram of intrinsic semiconductor.

E_F can be altered by dopant, applied electric fields, and light. The electron can transfer from E_V to E_C , because it can be stimulated or excited by these mentioned functions to generate or move the electrons (-) and holes (+) carriers across the band gap. The electron density arrangement in the semiconductor is described by the Fermi-Dirac equation. $P_{Fermi-Dirac}(E)$ represents the probability of occupancy of an electron at the energy level (E) relative to the E_F as described by the following equation:

$$P_{Fermi-Dirac}(E) = 1/[1 + \exp(\frac{E - E_F}{kT})] \quad (1)$$

where k is the Boltzmann constant and T is the temperature on the Kelvin scale. It is easily seen from equation (1) that E_F is the energy level where the probability of occupancy by an electron is 1/2. Note that this does not imply that there are energy levels at E_F , but only what would be the probability of occupancy if there were an accessible level. It is implied from this distribution, that electrons [(-), negative charge carriers] are concentrated (i.e., the lower energy an electron can have, or in other words electrons would lose energy by moving towards the bottom of the page) at lowest edge of E_C above E_F , and holes [(+), positive charge carriers] are concentrated at highest edge of E_V below E_F . The distribution differences between the negative and the positive charge carriers in the energy band explain why electrons are excited from E_V to E_C . When the semiconductor is illuminated with light of enough energy (greater than the band gap) electrons are excited to E_C leaving a positive charge carrier in E_V (a hole (+) would be formed there). Besides traditional stimulation method as heat or light, the excitation of charge carriers also be achieved in response to friction.^[6-9] The concentration distribution of negative charge carriers in E_C and positive ones in E_V is approximated by the Boltzmann distribution as below:

$$n = N_C \exp\left(-\frac{E_C - E_F}{kT}\right) \quad (2)$$

$$p = N_V \exp\left(-\frac{E_F - E_V}{kT}\right) \quad (3)$$

where N_C is the *effective density of states* of negative charge carriers in the energy level at E_C , and N_V is the *effective density of states* of positive charge carriers in the energy level at E_V , k is the Boltzmann constant and T is the temperature on the Kelvin scale. Equations (2) and (3) indicate that the E_F is located nearer to E_C in an n-type

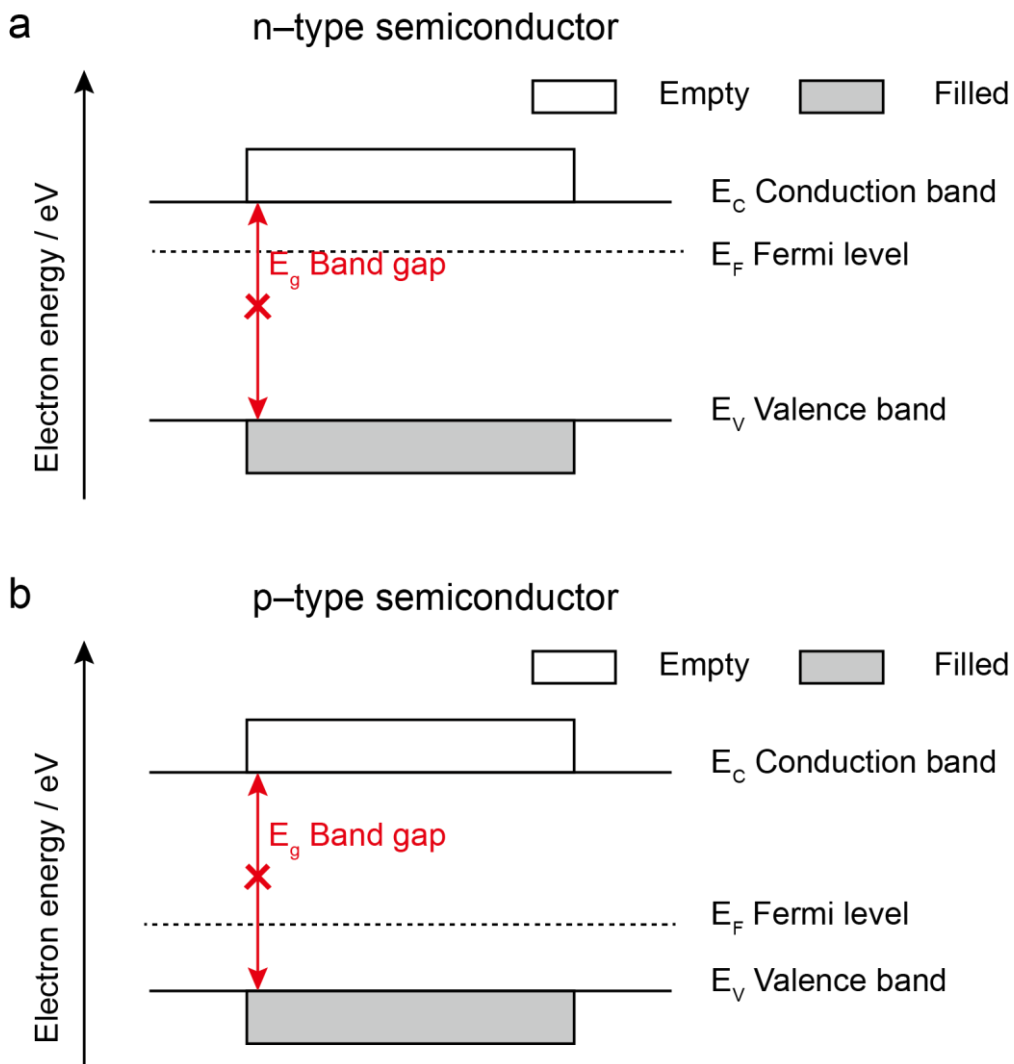


Figure 1.2. Schematic of energy band in a) n-type semiconductor, as well as b) p-type semiconductor. When the concentration of donors is increased, E_F shifts nearer to E_C in an n-type semiconductor, conversely, the E_F in a p-type semiconductor moves nearer to E_V as the level of acceptors is increased.

semiconductor, conversely, the E_F in a p-type semiconductor is located nearer to E_V , as

illustrated in Figure 1.2.

1.3.1 Band bending in semiconductors

In an electrochemical and electrical measurement involving semiconductor electrodes there are a couple of key interfaces, these are the interface between the semiconductor and a metal contact,^[6-8] and the interface between the semiconductor and the ionic conductor – the electrolyte.^[10, 11] Due to the intrinsic electron energy level differences between the two phases, an electric field will form at the interface. This generated field poorly screened by the free electron exchanging through the interface, the energy level changes in this contact volume are such to balance the energy difference between the two phases, and this is what causes the band bending phenomenon (at the interface of two different materials, the electronic energy band would be bending up and down).^[12, 13]

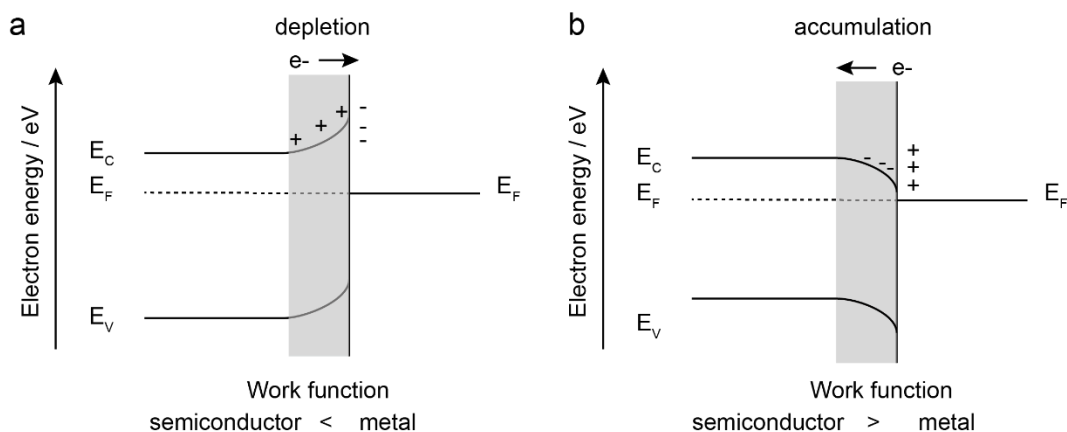


Figure 1.3. Schematics illustrating the band bending at an equilibrated interface between a n-type semiconductor and a metal contact (an analogous situation can be reached for a liquid contact where a redox species is dissolved). a) When the work function in the isolated semiconductor phase is smaller than it in the metal phase, the direction of net electron transfer (leading to equilibrium) is towards the metal. A depletion layer with upward band bending forms in the semiconductor phase. b) When the work function of the semiconductor is larger than that of the metal phase, the direction of electron transfer points towards the semiconductor, forming an accumulation layer in the semiconductor phase (downward band bending).

When a semiconductor is contacting a metal, the work function (defined as the minimum energy removing an electron out of solid surface to the vacuum point^[14])

difference between these two phases leads to an interfacial rearrangement of the electron energy distribution.^[12] If the work function of the semiconductor phase is lower than that of the metal phase, electrons will move from the semiconductor side to the metal side until the E_F of both phases equalize. Due to the direction of electron transfer pointing towards the metal, the semiconductor surface will gain an excess of positive charge carriers, and the metal surface an excess of negative charges. Because of this, in the n-type semiconductor, see Figure 1.3, the density of electrons is lower in the near-surface region of the semiconductor rather than it in its bulk, forming a depletion layer. On the contrary, if the work function of the semiconductor is higher than that of the metal phase, electrons will migrate from the metal side to the semiconductor side, forming an accumulation layer in the semiconductor.^[12]

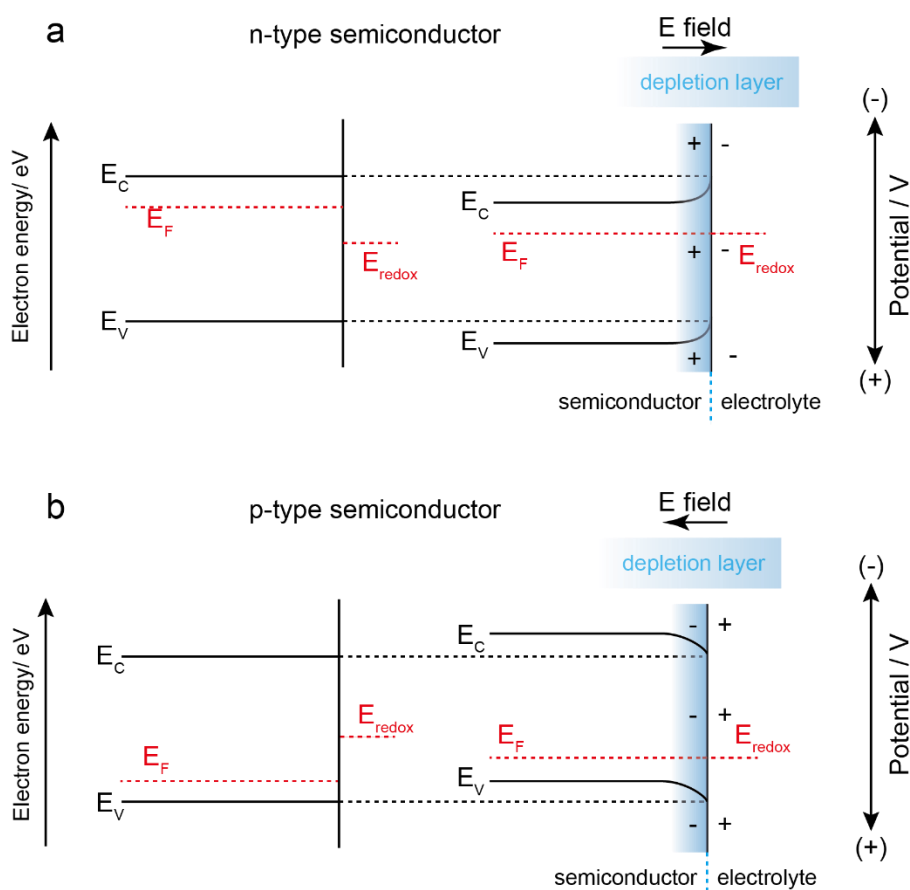


Figure 1.4. Depiction of band bending for a) n-type semiconductor, and b) for a p-type semiconductor, before (left) and after (right) being brought in contact with a redox electrolyte solution. Equilibrium is then reached between E_F and E_{redox} . Where E_C is conduction band, E_V is valence band, E_F is Fermi level, and E_{redox} is the electrochemical potential of the redox electrolytic solution.

Figure 1.4 illustrates the band bending at the semiconductor–electrolyte interface. The semiconductor is contacting the electrolyte, and as long as electrochemical potential level is different between the two, there will be an electronic redistribution (which manifests mainly in the semiconductor). Electrons will transfer through the interface to equalize the energy level and the electrochemical potential between the two phases, that is, until E_F in the semiconductor will match to the redox potential (E_{redox}) of the electrolyte species in solution. For the n-type semiconductor, if E_F is higher than the E_{redox} of the electrolytic solution, electrons will move from the semiconductor side to the solution side. As a result of this a positive charge appears in the space charge layer to form an electric field, the E_F moving down and the E_{redox} moving up to reach an equilibrium at the same energy level. Consequently, the majority carries form a depletion region layer from the surface to the bulk of semiconductor. For the p-type case the band bending is reversed.

1.3.2 Photocurrent effects at semiconductor–liquid interfaces

Photoeffects in semiconductors are more marked for depleted electrodes (as discussed in the previous section). A photocurrent is generated when a silicon wafer is irradiated with light, especially for doped and depleted interfaces. Electrons (-) are excited to E_C leaving an equal amount of holes (+) in E_V . In an intrinsic semiconductor, the concentration of charge carriers both for majority and minority are dominated by the density of the dopants. In an n-type semiconductor the majority of charge carrier is negative, while in a p-type is positive. Upon irradiation, the concentration of the majority charge carriers changes little, while the minority charge carriers concentration will change tremendously. Therefore, the ramification of the light irradiation is more remarkable in the depletion region, the formed minority charge carrier will move to the semiconductor surface to play a vital role as charge carrier in charge transfer.^[15] Figure 1.5 depicts this.

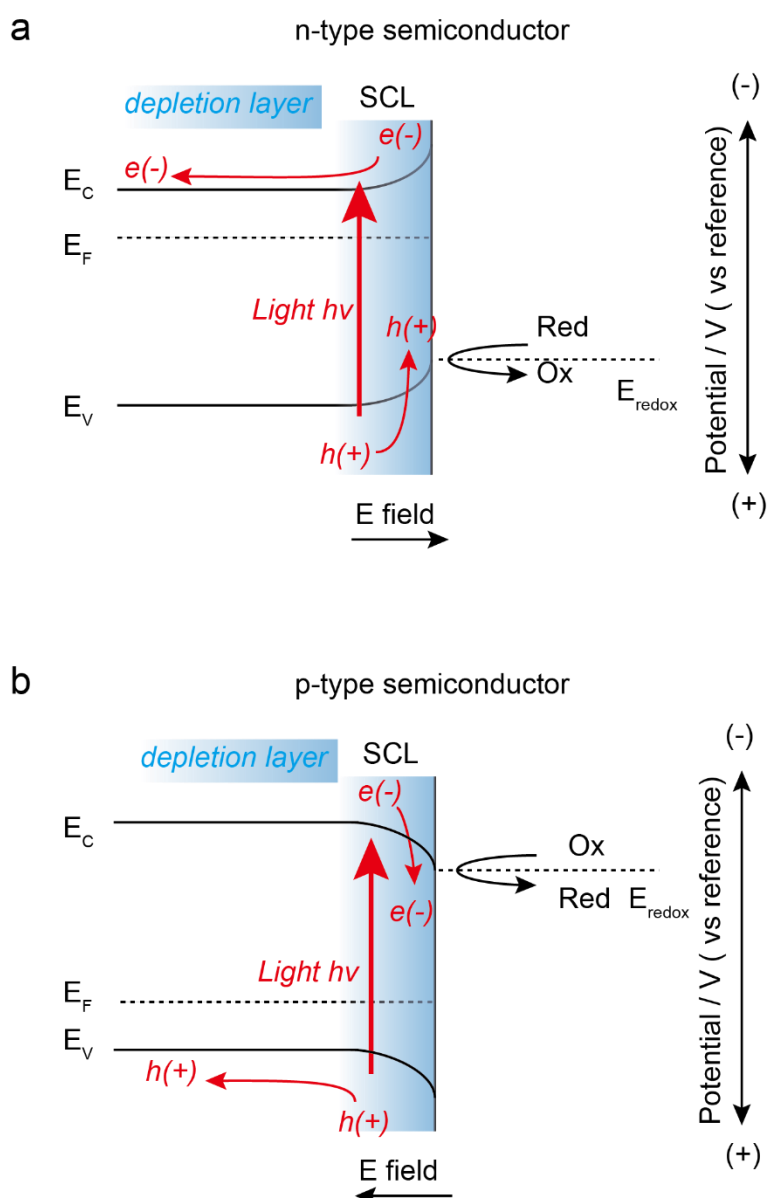


Figure 1.5. Band diagram and the associated electric field in a) *n*-type semiconductor and in a b) *p*-type semiconductor upon illumination with light of energy greater than the band gap. The minority charge carriers [electrons (-) in the *n*-type, and holes (+) in the *p*-type] sense the in-built electric field of the depletion region (the band bending direction depends on the doping type). After irradiation the concentration of minority charge carriers will change significantly.

1.3.3 Electrochemical reduction of silica to silicon

It has been mentioned above that unlike in a metal, a semiconductor can “hold” a certain

potential difference in its near-surface space charge layer. This field can assist or impede the migration of charged species. It has also been mentioned, and will be discussed in more details in the thesis, that a thin oxidation film forms spontaneously on the surface of silicon.^[3, 16] Silicon is the building block of all microelectronics devices, but it is not found in nature in a suitably pure form. Most silicon-based raw materials exist in the mineral form of silicates or silica, hence their reduction and transformation to silicon crystals is the first step in the semiconductor industry. Conventionally, silica is usually reduced by the carbothermal process to achieve pure silicon.^[17] The limitation of this traditional reduction is that it requires very harsh conditions and temperatures as high as 1700 °C.^[18] To decrease the reduction temperature (and associated costs), an electrochemical method may be a valuable option, nevertheless it is immediately appreciated by scientists and engineers that silica is an electrical insulator and not an ideal material on which to conduct electrochemical reductions. In 2003, Nohira *et al.* reported a contacting-electrode mode reduction capable of converting SiO₂ to Si within a molten CaCl₂ salt, succeeding in decreasing the harsh temperature requirements to 850 °C.^[18] The authors suggest that the reduction is proceeding at a three-phases contact point, that is at the point where the insulator, the molten electrolyte salt and the conductive electrode (an molybdenum wire bonding to a quartz plate) meet. The molybdenum wire contacts the SiO₂ surface, and when its reduction potential reaches sufficiently negative voltages, the oxygen fugacity at the electrode interface aids the reduction of SiO₂. Oxygen atoms can move from the bulk (inside) to the interface (outside), with ease, as oxygen atoms in SiO₂ will readily transfer diffusively at 850 °C.^[18] With the reduction continuum, the formed Si exhibited more conductive areas at the three phase contacting point helping the reduction to progress. This molten salt method is still a somewhat a harsh and energy intensive method, even though it is an effective way to realize the electrochemical reduction of silica. It remains an unmet challenge to achieve the electrochemical conversion of SiO₂ to Si at room temperature. An option forward in this context is discussed in Chapter 3 where it will be demonstrated that a thin oxide layer on highly conductive Si facets and

the field of the space charge can promote the nanoscale reversible silica/silicon redox chemistry.

1.3.4 Miller indices and stereographic projections of silicon

Commercial silicon ingots are usually made through either the Czochralski or through the Float zone crystallization process. Large ingots are then cut along specific crystal orientations, and the resulting wafers have well defined bulk resistances, thickness, and doping levels. As this thesis is broadly focused on facet-resolved electrochemistry of silicon, the orientation characterization needs to be introduced briefly here. Miller indices are a conventional method to describe the orientation, the lattice plane and the projection of a crystal structure (such as silicon). The Miller indices are always denoted by an array with three integers numbers h , k , and l , those three ones are the reciprocals of axis of x , y , and z value of the intercepts of the cartesian coordinates system. For example, when the intercepts are $x = 1$, $y = 1$, and $z = 1$, then it means $h = 1$, $k = 1$, $l = 1$, and the plane orientation would be (111). While the plane is parallel to one axis, like when $x = 1$, $y = 1$ and the plane is parallel to z -axis, then the integers array representing the plane are $h = 1$, $k = 1$, and $z = 0$, and the plane orientation is (110), in the same way, when $x = 1/2$, $y = 1$, $z = 1$, then $h = 2$, $k = 1$, $l = 1$, the plane orientation is (211).

To visualize the relative direction and orientation of the crystal facets in a commercial silicon wafer, stereographic projections are the required tool. Such projections render the analysis of a crystal structure effortless. For example, as shown in Figure 1.6, a commercial silicon wafer Si(111) is normally marked by the producer with a lapped edge, which indicates for example in the case of Siltronix wafers (those used in this thesis) the Si(110) as reference orientation. When the wafer is cut in parallel direction to this labelled edge, the fresh cut will obviously expose two Si(110) facets. On the other hand, when the wafer is cut along a vertical direction relative to this labelled edge, the cut will expose two new Si(211) facets.

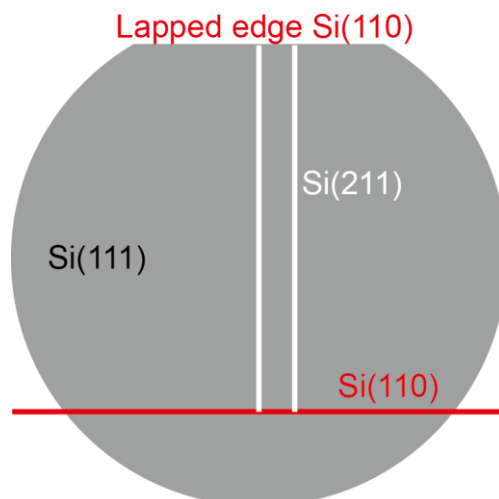


Figure 1.6. Schematic of relative crystal orientations on commercial wafer Si(111). A lapped Si(110) edge marks an internal reference orientation, selected by the commercial wafer supplier. It often marks the Si(110) facet, therefore cutting the Si(111) wafer on a direction perpendicular to this edge it will expose the Si(211) facet.

1.4 Self-assembled monolayers

It has been mentioned previously that the semiconductor industry plays a crucial role in our modern digitized society. The size of semiconductors and microelectronics devices is decreasing to the nanoscale, and this miniaturization has prompted extensive research in trying to merge molecular electronics with silicon technologies. For example it is feasible to tune electrical and electrochemical properties of semiconductor surfaces by tethering self-assembled monolayers (SAMs).^[19] Functionalized silicon surfaces can lead to specific electrochemical properties.^[5, 20, 21] SAMs offer advantages for example of tuning the conductivity,^[22-25] the adhesion,^[26, 27] the roughness,^[28-30] wettability^[31, 32] and friction^[33, 34] to trigger specific interaction with substrates to understand the chemical thermodynamic and kinetics process through interface for scientific and engineering purposes.^[35-37] Surface modification expands the chemical selectivity and controls the electronic energy levels in the semiconductor substrate leading the research of surface science to the molecular scale resolution.^[38-40] In order to achieve the above mentioned purposes, the first step is to fabricate the monolayer

structure. SAMs structure often contains three main components, which are 1), the headgroups that are attached on the substrate surface (metal or semiconductor), 2) the linker groups that are usually composed of alkyl chains (to impart flexibility) or aromatic groups (to impart rigidity), and 3) terminal groups that can exhibit the desired function, such as chemical or electrochemical properties at the distal end.^[39, 41]

The simplest method to form SAMs on the substrate is adsorbing molecule from a solution of the active adsorbate. Gold is the most popular substrate for such experiments, owing to it is easy for preparation of SAMs (although the main substrate in this thesis is silicon, the brief introduction of gold substrates here is needed). As a main platform, thiolate–gold SAMs remain the main experimental model, which are ubiquitously used as molecular devices or biosensors,^[42] being employed to investigate charge transfer, rectification, and thermodynamic electrochemical properties of the surface.^[42-45] SAMs on Au generally present supramolecular structures which are of value in molecular electronic research.^[45-50] In 2019 Wang et al. reported that the rectification ratio of the molecule junctions can be affected by the disorder of the supramolecular structures in the monolayers on the substrate.^[51] The rectification at junctions was sensitive to the defect site where the disorder structures existed in the monolayers. The leakage current flowing through the defect site changed drastically, and the best performing samples have rectification ratios 10 times larger than for the worst samples. There are many events leading to disordered structures in the monolayers, for instances, the different linker groups (aliphatic or aromatic chains) and different synthesis procedures (i.e., preparing from different solvent, polar or nonpolar).^[51-54] Also, a disordered structure can affect the electrochemical behavior, and this will be expanded later in the section 1.5. The advantages of thiolate–gold SAMs is the ease of incorporating functionalities at the distal end, and that such functional molecules can be prepared through organic synthesis to expand versatile applications of the gold monolayers. Nevertheless, the thiolate–gold monolayers face stability problems due to the weak bond energy of the thiolate–gold bond, which was readily to be oxidized in air limiting long term stability.

[55, 56]

Relative to SAMs formed by non-covalent bonding, covalently bound SAMs are obviously more stable.^[20, 25] As this thesis pertains with covalent SAMs on silicon, a small digression on covalent SAMs is necessary. In 1980, Sagiv reported the foremost paper that the covalent bond monolayers on the glass substrate were prepared from the reaction of chlorosilanes and alkoxy silanes with hydroxyl-terminated oxidized substrates.^[31] SAMs of this seminal study were originally intended as an experimental tool for mimicking biological membranes. The paper offered a novel tool for scientists to modify surfaces with molecular control, but the Si–O–Si bonds formed on the surface in this case were susceptible to hydrolysis and readily degraded by heat. The need of overcoming these stability issues prompted research to modify silicon surfaces with stable SAMs with stronger chemical bonding to their substrates.

One of such approaches was the hydrosilylation of unsaturated molecules on hydrogen-terminated silicon.^[57-62] Hydrosilylation refers to the insertion of hydrogen and silicon in alkenes and alkynes. To perform this kind of reaction, silicon is first etched in fluoride solutions (HF(aq) or NH₄F(aq)) in order to generate a Si–H surface.^[63, 64] The advantage of the Si–H surface is its ease of preparation and its stability in common solvents in laboratory (i.e., dichloromethane, acetonitrile, toluene).^[65-67] The hydrosilylation is compatible with several functionalities, so that SAMs with a reactive distal end can be formed.^[64, 68] That is, after forming a Si–C bond, the grafted monolayer can be further derivatized.^[27, 39, 69]

The Si–C bond resist hydrolysis and the first report on hydrosilylation on Si(111)–H by Chidsey and co-researchers relied on pyrolysis of a diacyl peroxide initiator.^[60, 61] They proposed a radical-intermediate mechanism. It was hypothesized that the peroxide initiator generates a silyl radical center on the substrate by dissociating the Si–H bond, and then the α -C of the olefin part would add to this silyl radical site (dangling bond) forming a second radical center at β -C of the olefin chain, then the second carbon radical site in the olefin part abstracted the H from the neighbor Si–H to generate a new silyl radical site for the next addition of another olefin molecule. The monolayer formed by this method was very stable because of the strong Si–C bond.

Organometallic chemistry is another choice to provide Si–C bond to link SAMs and silicon substrate, i.e. employing Grignard or organolithium reagents. Bansal et al. reported that a two-step chlorination/alkylation reaction on Si–H surfaces could produce an electrically and chemically well-passivated silicon surface.^[70] Firstly, the Si–H surface was chlorinated by PCl_5 , and then the Si–Cl surface was alkylated with organometallic reagents to yield the desired functionalities. This two-step reaction enables the formation of unprecedented functionalities, such as a methyl distal end to prevent oxidation, exhibiting a reasonable stability in air and exceptional electrical performances.

The homolytic dissociation of Si–H bonds can also be promoted by light, same as it is induced by heat.^[59, 71] Light can assist hydrosilylation on the silicon surface to provide well densely packed SAMs with good surface coverage.^[72, 73] The mechanism is similar to the thermal procedure (formation of silyl radicals), while comparing to harsh condition such as the thermal and organometallic chemistry, the light irradiated method was less detrimental to silicon substrates and tethered groups especially utilizing in semiconductor biosensors on which were attached tiny and sensitive biocompatible molecules.^[62, 74]

The diazonium salts is another interesting approach to form stable Si–C bonds SAMs.^[75-77] Unlike the above-mentioned olefin- and alkynyl-derived SAMs, diazonium-based approaches lead to robust SAMs with aromatic derivatives directly attached onto the silicon substrate.^[78-80] Stewart et al. reported a directly one step route to attach rigid π -conjugate moiety onto the silicon surface forming robust Si–C bonds.^[81] The diazonium salts is reduced to form a diazenyl radical even at open circuit potential, and then the diazenyl radical loose N_2 to form an aryl radical intermediate that rapidly reacts with the Si–H bond starting a chain reaction on the substrate. This spontaneous diazonium radical reaction provided an appealing route to generate strong Si–C bonds with distal desire rigid functionalities.^[79]

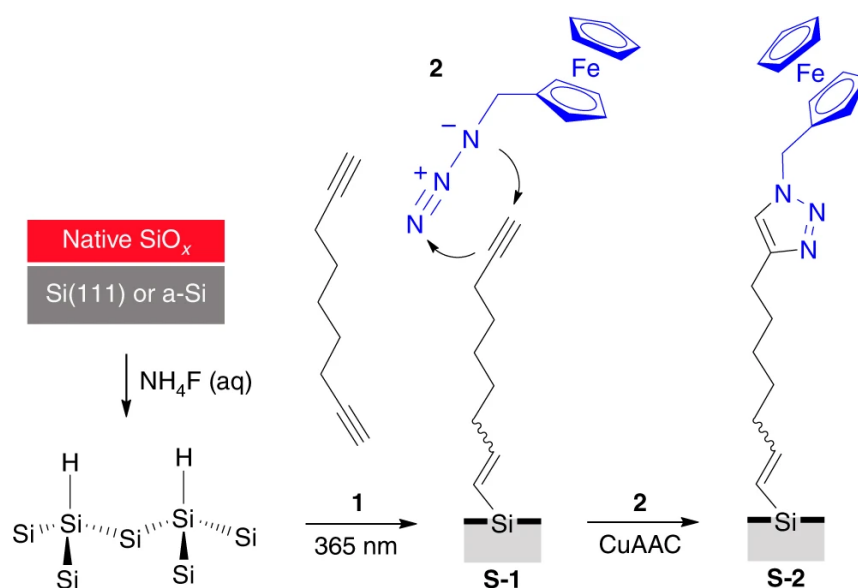


Figure 1.7. Schematic illustration for the hydrosilylation of the silicon wafer. Chemical scheme is employed for showing the passivation of silicon [i.e., schematic representation of the different substrates, Si(111), and a-Si] Assisted by UV irradiation, hydrosilylation of 1,8-nonadiene (**1**) on Si–H generates an alkyne modified substrate (**S-1**), which is then reacted with a redox head group (i.e., azidomethylferrocene (**2**) is representative here, but the reaction is amenable to many azides) through a click reaction (copper-catalyzed azide–alkyne cycloaddition (CuAAC), generating a self-assembled monolayer (**S-2**) in this example a redox-active sample for electrochemical research. Reprinted from the study by Vogel et al ref.^[82] Springer Nature.(2017) <https://www.nature.com/articles/s41467-017-02091-1>, under the terms of the CC BY 4.0 license, <http://creativecommons.org/licenses/by/4.0/>.

The “click” reaction shown for example in Figure 1.7 (passivation of silicon by a two-step modification employing a copper(I)-catalyzed alkyne–azide cycloaddition (CuAAC) is an attractive coupling approach for adding additional functionalities to the substrate. The merits of the click reaction are the easy minor purification requirements, no need of protection and deprotection procedures, high yields and high selectivity, compatibility with a wide range of solvents, and inertness towards other functional groups, the latter being especially important in biological applications.^[64, 69, 83, 84] Noticeably, this chemistry enabled the stepwise constructions of redox SAMs (i.e., ferrocene derivatives) on substrates with almost ideal electrochemical behavior, demonstrating the benefits of this click reaction, such as the lack of side effects and

good conversion yields.^[68] Due to the robust electrochemical properties demonstrated by ferrocene (Fc), the formed redox SAMs are often employed as redox model system. In this section we briefly introduce how to produce SAMs on metal/semiconductor surfaces. Since this thesis is focused on facet dependent electrochemical behavior it was essential to form stable covalent bonds linking monolayers with the substrate. Attempts to achieve high quality SAMs was a prerequisite to prevent the formation of silicon oxides on the substrate, which will introduce considerable and irreproducible effects on the electrochemical kinetics. Further, electrochemical kinetics of ferrocene SAMs is impacted by the surface coverage of the monolayer,^[85] by dipole effects, by the length of alkyl chain between the distal molecule and the substrate,^[29] and by the doping level in the substrate.^[86] In order to understand and explore these points it is necessary to introduce in the following section the principal electrochemical and electric measurements employed in this dissertation.

1.5 Electrochemical and electric measurements

1.5.1 Cyclic voltammetry

Cyclic voltammetry (CV) is a prime measurement for obtaining kinetic and thermodynamic electrochemical data of any electrode material, including semiconductor interfaces.^[87, 88] It is a simple technique that is widely employed in analyzing electrochemical reactions on semiconductor electrodes modified with organic monolayers.^[89] By varying the potential and recording the current flow of a redox reaction, this technique is suitable for the analysis of electron transfer behavior through an interface.^[27, 90, 91] CVs are a primary tool for scientists and surface scientists. By analyzing the shape of voltammograms, the full width at half-maximum (FWHM), the height of the peak current, peak currents ratio, the position of peak potential, the charge that passed, scientists can extract a lot of information on redox interfaces. For instance the shape of a voltammogram is related to the homogeneity of the monolayer.^[92] By acquiring the peak potential it is possible to understand thermodynamic properties. The separation of peak potentials of anodic vertex and

cathodic vertex can afford the kinetics process of the electrochemical reaction.^[93] The ratio between the anodic and cathodic current maxima can relate to the reversibility of redox reaction, and approaches unity for reversible reactions. The profile data of peak height versus scan rate can understand the electroactive species is attached on the substrate electrode or not.^[94] The redox peak of CVs can manage to understand the interaction existed in the molecular in monolayers. The advantage of CVs is in their simplicity, convenient and sensitive, nevertheless, it is not always easy to obtain perfect data, and often researchers record adventitious signals or non-ideal behaviors. These will be (for silicon) discussed and clarified by the experiments presented in this dissertation.

1.5.1.1 Non-ideal voltammetric signals

Electroactive species can exhibit perfect or nearly perfect symmetric peaks in voltammograms (i.e., the redox peak is symmetric and the FWHM is nearly 90.6 mV for one-electron processes).^[82, 95] Nevertheless, over the past few years several reports have illustrated that non-ideal CV shapes are not uncommon.^[50, 89, 96] These non-ideal shapes are usually broadened, split, and even multiple waves. For SAMs non-ideal behavior generally is linked to heterogeneous molecular interactions. Disorder, odd-even effect of the linker between headgroup and substrate, the repulsion function of headgroup, and the interaction between redox species with electrolyte are not uncommon.^[86, 97-102]

For example, Lee et al. reported a typically non-ideal cyclic voltammetry and explained it as a disordered structure. It has been mentioned previously, the thiolate-gold SAMs are generally employed in studying the electrochemical behavior due to their ease of formation.^[103] As shown in Figure 1.8a for a binary component monolayer prepared from Fc-(CH₂)₁₂-SH and CH₃(CH₂)₉SH on Au there can be two phases', domains of ferrocene moieties on the substrate, one phase has ferrocene groups isolated by surrounding alkyl thiolate, and the density of ferrocene molecules was diluted in this domain. In the other phase, the ferrocene molecules are forming clustered domains, in

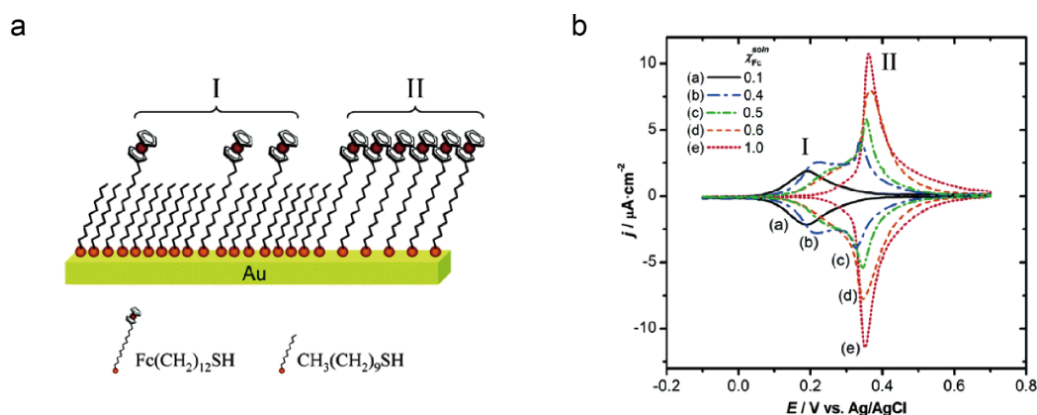


Figure 1.8. a) Schematic demonstration of two domains of monolayers which are composed of $\text{Fc}-(\text{CH}_2)_{12}\text{-SH}$ and $\text{CH}_3(\text{CH}_2)_9\text{SH}$. Part I denotes isolated $\text{Fc}-(\text{CH}_2)_{12}\text{-S-Au}$ molecules and part II denotes cluster-formed $\text{Fc}-(\text{CH}_2)_{12}\text{S-Au}$ molecules. b) Representative cyclic voltammograms of two components monolayers formed containing different ratios of $\text{Fc}-(\text{CH}_2)_{12}\text{-SH}$ and $\text{CH}_3(\text{CH}_2)_9\text{-SH}$. CVs were recorded versus Ag/AgCl as a reference electrode in HClO_4 (1.0 M aq) as electrolyte, and the scan rate was 20 mV/s. Panels a) and b) are adapted from the study of Lee et al. ref ^[103] with permission from the American Chemical Society, copyright (2006).

which the ferrocene is surrounded by neighbor ferrocenes. Two types of ferrocene domains would show phase separation on substrate, and it leads to the disorder structure environment that manifests in electrochemical measurements. Two couples of redox peaks are found in the relative CVs (Figure 1.8b). CVs acquired from samples prepared with the binary $\text{Fc}-(\text{CH}_2)_{12}\text{-SH}$ (FcS) and $\text{CH}_3(\text{CH}_2)_9\text{SH}$, (AS) mixture on Au at various ratio of FcS to AS, ranging from 0.1 to 1.0, are very different. The dominating peak is peak I at a mole ratio of FcS of 0.1, but interestingly, when the mole ratio is 0.4 a new redox signal peak II appears at 0.34 V. Increasing the ratio the dominating peak would almost entirely change to peak II. It can be inferred from CVs that at different density of ferrocene groups the phase separation would lead to huge changes in the average electrochemical environment.

Moreover, Nerngchamng et al. reported a different kind of non-ideal electrochemical behavior,^[96] and it is not like the above mentioned non-ideal peak in CVs which is caused by disordered structures. In this case the non-ideal electrochemical behavior, like peak splitting and broadening, results from the accumulation strain generated by

the size mismatch between the ferrocene terminal groups and the alkyl linkers in SAMs

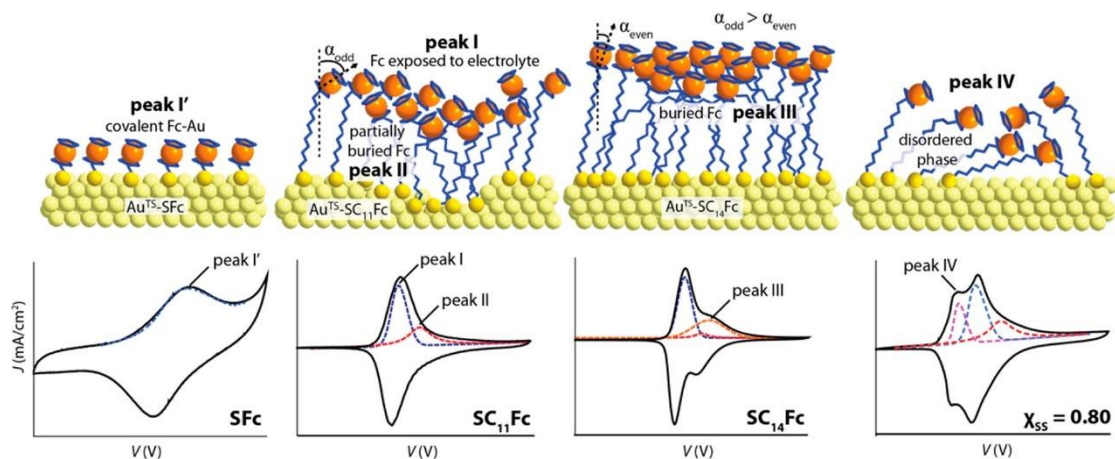


Figure 1.9. In the upper row, a schematic demonstration of the SAMs of $\text{Fc}-(\text{CH}_2)_n\text{-S}$ on Au, shows five different electrochemical microenvironments. In the lower row, four distinguish CV peaks, related to packing structures caused by different intermolecular interaction, are shown. Peak I' stands for interactions between Fc and Au, peak I stands for Fc group exposing to electrolyte solution, peak II stands for fractionally concealed Fc units, peak III stands for buried Fc groups, and peak IV stands for disorder in the monolayer. Gold is denoted by pale yellow circle, sulfur is denoted by dark yellow circle, and ferrocene is denoted by blue circle containing an orange sphere. The figure is reprinted from the study of Nerngchamnonng et al. ref [96] with permission from the American Chemical Society, copyright (2015)

on Au. See in Figure 1.9, the lengths of the alkyl chains were systematically changed by increasing the number of methylene (n) from 0 to 15. While n is larger than 2, multiple peaks gradually appeared in CVs, this non-ideal behavior was related to the packing interactions of molecules. Peak I' in CVs was assigned to the interaction between Fc and Au which was dominated by covalent bond (length of alkyl chain was short). With increasing the number of n , the interaction between Fc and Au would be weaken, owing to the interaction was gradually dominated by noncovalent bond (length of the alkyl chain increased). Peak I was generated by the Fc exposed to the electrolyte and interacting with another Fc directly. At higher anodic potentials peak II would appear alongside with peak I. Peak II originates from parts of Fc moieties marginally concealed in the monolayers and screened from the electrolyte solution. Because the size mismatch between Fc units and alkyl chains, some parts of Fc groups would be positioning lower or farther to other Fc groups, resulting orientations of Fc groups not all positioning at the same flat, meaning some of them were more screened and not

exposed to the electrolyte adequately. When the length of the alkyl chain increased to 14 and 15, the interaction between alkyl chain packing (alkyl chain interacted with alkyl chain) would play more fiercely, some parts of Fc groups would be screened from the solution deeply, there would exist peak III, same situation also happened in monolayers when the number of n is even integer (packing stronger than odd integer). The peak IV was obtained from disorder structures in the monolayer which were causing by two domains (chemisorption of some disulfide precursors).^[96] The research demonstrated the supramolecular structures could affect the electrochemical environment leading to non-ideal electrochemical behavior.

In addition, Wong et al reported another type of non-ideal electrochemical behavior generated from ion pair effects.^[104] The electronic structures and chemical environments of the molecular groups in the monolayers on substrate can influence the relative redox reaction behavior. The Fc-(CH₂)₁₁-S-Au monolayer is the classical electrochemical model to investigate the charge transfer process of redox reaction. See in Figure 1.10 a), b) after losing electron in the electrochemical reaction, the generated ferrocenium would form ion pairs with counterion in the electrolyte due to the charge compensation. By incorporating with the counterion, it led to a steric effect causing the electrostatic repulsion in the monolayer. Consequently, the electrochemical microenvironment was changed, and then CVs exhibited non-ideal wave. See in Figure 1.10 c) CVs were broaden and multiplied as double peaks, it indicated the electronic state change by forming ion pairs can cause effects to the charge transfer redox reaction in the monolayer. To understand the reason leading to non-ideal electrochemical behavior (broaden, split CVs peaks) would benefit optimizing the design of semiconductor microelectronics.

The non-ideal electrochemical behaviors of CVs measured on Au substrates have been briefly listed above, more or less, these examples are related to the heterogenous microenvironment of the monolayer. Nonetheless in semiconductor substrate like silicon, even when the environment of monolayer was homogenous, there still found multiple peaks for a one electron transfer redox reaction measured in CVs which is not

caused by molecular disorder but by different photocurrents generated from the substrate, ^[105] as will be introduced in Chapter 2.

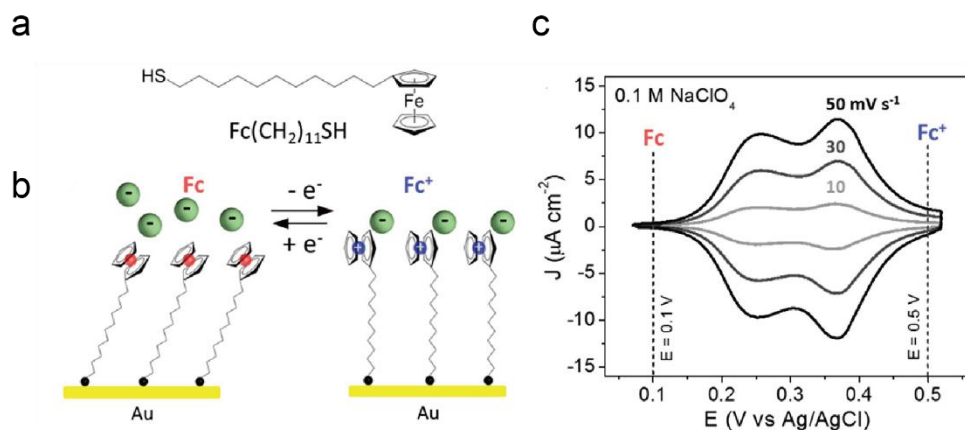


Figure 1.10. a) Molecule structure of $\text{Fc}-(\text{CH}_2)_{11}\text{-SH}$. b) Schematic illustration of structure alternating between Fe/Fc^+ redox process, black circles represented sulfur by the and green circles represented the electrolyte anions. c) Cyclic voltammograms of ferrocene- $(\text{CH}_2)_{11}$ -thiol monolayer on Au(111) were recorded vs Ag/AgCl as reference electrode, performed in NaClO_4 (0.1 M) as electrolytes, the scan rates were 10 mV/s, 30 mV/s, and 50 mV/s (from inside to outside). Panels a), b), c) are adapted from the study by Wong et al. ref ^[104] with permission from the American Chemical Society, copyright (2018).

1.5.2 Electrochemical impedance spectroscopy

Electrochemical impedance spectroscopy (EIS) is an effective and powerful method for measuring impedance/resistance of an electrical circuit. It is used for evaluating the diffusion state of solution, the electrolyte transfer to the electrode, and the charge transfer in the monolayer on the substrate.^[92, 106-108] The advantage of EIS is to acquire information of electrochemical reaction at a steady state in a vast range of frequencies. Differences in time constants between electrochemical reactions can be more easily detected at lower frequencies rather than at high frequencies. In an EIS measurement, the system under scrutiny is generally perturbed with an alternated voltage of small amplitude. The EIS is composing by a real part (Z_r) (which is frequency independent)

and an imaginary part (Z_i) (which is frequency dependent). To profile the EIS, it is usually used “Nyquist plot” and “Bode plot”. In a Nyquist plot, the X-axis is the Z_r and the Y-axis is the Z_i . The point of curves in Nyquist plot represents the impedance, which is record versus a relative frequency point. And the impedance can be denoted as the vector value (arrow direction pointing from the original zero of coordinates to the impedance point) in Nyquist plot. In a Bode plot, the X-axis represent the logarithmic value of the frequency. There are always double Y axes plotted versus X axis which is frequency in Bode plot, one Y axis is the logarithmic value of magnitude of impedance and the other Y axis is the phase angle. Usually, the Nyquist plot is employed to access the resistance parameter, and the Bode plot is utilized to estimate the capacitance parameter.^[109] In this thesis, the Bode plot and the formalism developed by Laviron is employed to estimate the charge transfer rate.^[110, 111] It will be mentioned in Chapter 4 (paper published in *J. Phys. Chem. C* 2021, 125, 18197–18203).

1.5.3 Conductive atomic force microscopy

Atomic force microscopy (AFM) is powerful technique to study surfaces by using a sharp tip to scan over the sample.^[112] By contacting the surface with a tip to achieve the interaction parameter, it can present the high resolution image of the sample surface at nanometer level. Detecting the repulsion and attracting interaction between the sample surface and the tip, it can create a three-dimensional morphological topography in high resolution to analyze the surface structure. The probe of AFM is composing of a sharp tip (like a “sharp finger”) and a flexible cantilever (like an “arm”). When it works, the image of the sample's surface can be created at a high resolution by the tip scanning across the surface of the sample and simultaneously measuring the deflection of the cantilever when the probe contacts the morphological features located on the surface. The deflection of the cantilever can be detected by a sensitive photodetector receiving a laser beam reflected at the back side of the cantilever.

There are couples of imaging modes of AFM accessible to check the measured samples. The contact mode is the simplest mode to achieve surface image. During the measuring

period, the tip is always contacting the sample surface. It is easy to operate and mostly used in measuring very hard and flat samples in the measurement. Though it is easy, there are some drawbacks of this mode. When the tip moves cross the lateral edge of samples, there would generate lateral force, adhesion force or friction force which can do damage the tip or samples. The contact mode is not employing in measuring soft samples which are easy deformation.^[112]

If researchers want to measure soft samples, the dynamic mode which are specialized as tapping mode and non-contact mode are preferable. In the tapping mode, the cantilever is oscillating nearly to its resonance frequency, and the tip is approaching and departing to the sample surface. In this mode, the oscillation decreases the impact of the lateral force. In the non-contact mode, the cantilever is also oscillating but the amplitude of the oscillation is much smaller comparing to the tapping mode. The non-contact mode is sensitive to environment, especially when there is water in air, it will decrease the resolution.^[112]

In this thesis, it is mostly focused on the conductive mode. The conductive mode AFM (C-AFM) is utilized to measure feature of the surface electrical conductivity at nanoscale.^[113, 114] With contacting on the tiny location on the measured sample surface, the tunnelling AFM can provide the current-voltage curves (I–V) to describe surface conductivity. The predominance of C-AFM is that it can achieve topography and current maps concurrently.^[115] The resolution and sensitivity of the spatialized electric features are dependent on material composition, morphology, crystal orientation, and thickness of monolayer.^[114] Alongside with analysis of topography AFM model, the C-AFM which can accurately pinpoint the conductive section on the surface where there is local defect, leakage current, or recombination phenomenon. The C-AFM can detect the charge transport information that is not only related to the formation of the molecule junctions, but also the molecular monolayer within electron contacting steadily.^[41] It can measure the surface resistance, detecting adsorption of molecule on the substrate and the current through the tip and substrate.^[116, 117] This advantage of C-AFM enables it to detect tiny area (i.e. nanoscale, sub-nanoscale) which is surrounding by an insulator

and yield the distribution of dopant concentration on the semiconductor surface. With the variation of bias voltages applied on the C-AFM tip, the generated current through the tip and sample can define the lateral resolution of current maps in high quality and can achieve the charge transfer properties.^[114, 118]

1.6 Introduction to facet-resolved electrochemistry

After general introduction of background of material and measurement, this section starts to introduce key content of the thesis. Electrostatics catalysis has attracted many scientists' attentions since the first reported electric field catalyzed the Diels-Alder reaction.^[2] Inspired by the electrostatics catalysis, at the beginning, we have an initial idea to perform electric field to catalyze the click reaction which there were only few theoretical reports about that without an experimental evidence.^[119] While during the research process, we found the crystal orientation of silicon wafer exhibit a huge effect on the electrochemical reaction on the surface, then we turned to a new world of electrochemistry, the facet resolved electrochemistry.

Recently, facet-dependent research has received extensive attentions owing to its fascinating physical properties and widely applications, especially in the fields of nanocrystal synthesis, nanowires, semiconductors, and photocatalytic.^[120-123] These studies obtained data by measuring distinguish chemical and physical interfacial characteristics. Even in the same material, there still exist different electrochemical behaviors due to the disparities of surface crystal structures. Facet dependent functions in a catalyst or in a reaction are resulting from the morphological or geometrical differences of surfaces, which may generate special electric density on the diverse surfaces of metallic oxides or semiconductors.^[40, 124-127] Within using distinct surface properties, scientists can control various physical parameters to present varieties of stimulations to promote the development of microdevices and the semiconductor industry. Huang et al have reported a method to measure the surface conductivity on single nanocrystals resulting from different facet-dependent effects.^[1] They employed the measurement to detect large different surface electric conductivity achieved by

contacting different facets on different sides of silicon wafer with tungsten probes. Although many researchers have focused on synthesizing diverse nanoparticles to achieve different well-defined structures for achieving photo-oxidation and electrical conductivity properties, the research on the surface current result in different reaction activities on surfaces is limited.

Previously it has been reported that the divergent crystal structure on nanoparticles will affect the electrochemical reaction rate.^[128] Herein, this background section presents experimental details to explore the influence of the facet-dependent effect related to the surface electrochemical kinetics. The summary of recently papers about facet-resolved chemistry is introduced in the following review paper section.

1.6.1 Facet resolved electrochemistry in semiconductors

This section is adapted from Elsevier, published in *Curr. Opin. Electrochem.* 2022:101085, titled “Facet-resolved electrochemistry: from single particles to macroscopic crystals”.

The paper is modified with minor changes in order to fit the general layout of this dissertation. Copyright permission of reprint with reusing in the doctoral thesis is attached in the appendix section.

Keywords: heterogeneous electrochemistry, interfaces, semiconductor electrochemistry, conductive atomic force microscopy, electrocatalysis

1.6.1.1 Abstract

Optimizing the kinetics and energy requirements of electrochemical reactions is central to the design of redox systems whose function ranges from energy conversion to chemical catalysis and sensing. This optimization takes often the form of a trial-and-error search for the optimal electrode material. Recent research has revealed pronounced facet-dependent electrical conductivity, redox reactivity and electro-

adsorption for a range of technologically relevant semiconductors, including silicon, Cu₂O, GaAs, InN, Ag₂O, and β -Ga₂O₃. We analyze selected recent reports, highlighting situations where testing alternative crystal cuts of the same material can be an effective electrode-optimization process. We discuss what is unambiguously known as well as what is emerging but still unclear, such as when and how electrical conductivity and electrochemical rates scale with each other (and when not), or the use of facet-dependent electro-adsorption to direct crystal growth and monolayer deposition. When there are contrasting or counterintuitive views, we explore the assumptions that underlie them.

1.6.1.2 Introduction

Electrochemistry is a broad and rapidly evolving discipline, but at its core remains the branch of chemistry combining the study of electronic conduction in solids with that of ionic conduction in electrolytes ^[129, 130]. Its ultimate aim is that of predicting and possibly engineering electrode kinetics and/or equilibrium positions of redox processes ^[131, 132]. It follows that most progresses in electrochemistry have resulted from improvements in the understanding of the physical and chemical properties of electrified interfaces ^[94, 133, 134]. From sensing to energy conversion, optimizing the kinetics of an electrode reaction and engineering its thermodynamics often begin a systematic change to the chemical nature of the electrode. For instance, volcano plots in hydrogen electrocatalysis are an excellent reminder that the nature of the electrode can dominate electrode kinetics ^[135]. However, the search for optimal electrode materials remains often a trial-and-error process.

Recent research has brought back attention to the scope of confining this search to a narrow range of alternative materials: alternative crystal cuts of the same material. Simply by selecting alternative crystal facets of a given material it is possible to substantially alter surface energies ^[136], electron trapping efficiencies ^[137], surface charges ^[138], electrode propensity to corrode ^[139], and adsorption selectivity ^[140]. Hence, facet-resolved electrochemical research is rapidly gaining momentum, especially in the

fields of nanocrystals sensing ^[141, 142], semiconductor electrochemistry ^[16, 143, 144], and electro- and photo-catalysis ^[145-148].

In this short review, we critically analyze recent research that has explored differences in electrochemical reactivity between different facets of the same semiconductor or metal. We highlight the most promising features of this emerging topic, as well as present systems where the scope of this approach is undoubtedly poor, or still unclear.

1.6.1.3 Facet-dependent electrical conductivity links to electrochemical reactivity: the case of Si and Cu₂O

Silicon continues to be the technologically most relevant material ^[149]. With only few exceptions ^[15, 150, 151], silicon electrochemical research has so far focused mainly on only two silicon orientations: $\langle 111 \rangle$ and $\langle 100 \rangle$. This changed in 2017 (Figure 1.11), when Huang and co-workers discovered the high electrical conductivity of Si(211) ^[1]. Similarly, remarkable differences between different facets of the same material are also emerging for other semiconducting materials, such as Cu₂O, GaAs, InN or Ag₂O ^[152-155]. Focusing on silicon and with the aid of conductive atomic force microscopy (C-AFM), it has been demonstrated that the conductivity of a junction between oxide-free silicon and a metal contact decreases in the order $\langle 211 \rangle \gg \langle 110 \rangle > \langle 111 \rangle$ ^[151]. One of

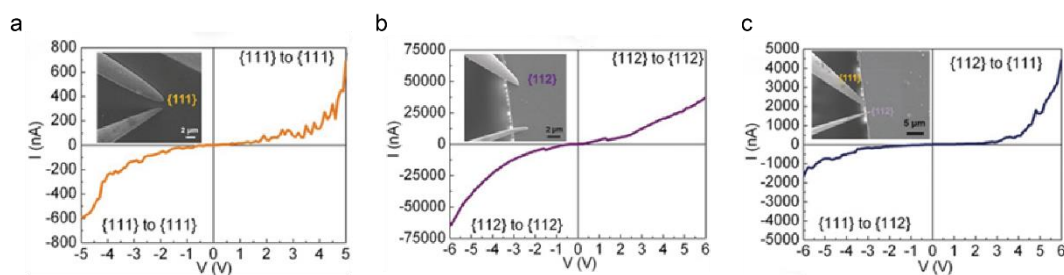


Figure 1.11. Facet-dependent conductivity of silicon crystals. Current–potential (I – V) traces curves and SEM images (insets) obtained with microscopic tungsten probes contacting adjacent but different silicon crystal facets. (a) I – V curves recorded between two Si(111) facets, (b) between two Si(112) facets, and (c) between Si(112) and Si(111). Adapted from the study by Tan et al.^[1], copyright (2017), with permission from Wiley-VCH.

the most notable, and unexpected, electrochemical consequences of this facet-dependent (electrical) conductivity is to allow the silica–silicon redox couple become reversible on highly conductive Si(110) defects, which are ubiquitous on a nominal Si(111) wafer ^[16].

This finding is surprising in several ways. Firstly, the notion that single crystals are an idealization is not sufficiently widespread, and its practical implications not entirely appreciated. Even a perfectly etched Si(111) wafer, of sub-nanometer roughness ^[156], exposes an array of vertical steps separating adjacent $\langle 111 \rangle$ terraces (Figure 1.12a). These steps are often aligned with the $\langle 211 \rangle$ and $\langle 110 \rangle$ directions ^[16]. Both Si(211) and Si(110) are more conductive than both Si(111) (Figure 1.12b) and Si(100), the other common silicon electrode material ^[21, 151]. On these steps, and for thin oxide films only, the electrochemical silica-to-silicon conversion occurs reversibly at room temperature (Figure 1.12c). Traces amount of OH^- and O_2^- migrate through the oxide layer covering highly conductive $\langle 110 \rangle$ and $\langle 211 \rangle$ terraces separating Si(111) planes, allowing the redox reaction to proceed reversibly ^[16]. In fact, deliberate anodic damaging of an initially oxide-free Si(111) electrode (Figure 1.12c) leads to the appearance of a surface-confined cathodic wave. This wave, labelled in Figure 1.12c as **1** in the return segment of the first cycle, is coupled to a new anodic signal (**2**) visible in the anodic segment of the second cycle ^[16].

In general, the electrochemical reduction of bulk silica, due to its high electrical resistance, is obviously of limited viability. It requires molten-salt reactors and temperatures in excess of 850 °C ^[18]. While these recent findings for Si (211) and Si (110) cannot immediately translate to a room-temperature bulk electrosynthesis of silicon from silica, they are however of practical importance as they explain the origin of recurrent parasitic signals often observed with silicon electrodes. Unlike for platinum, gold and carbon, where all common adventitious electrochemical signals have been satisfactorily assigned and explained, the origin of common parasitic signals has remained more elusive in silicon voltammetry ^[82, 157, 158]. In essence, highly conductive silicon defect defines for silicon the potential window free from redox parasitic signals,

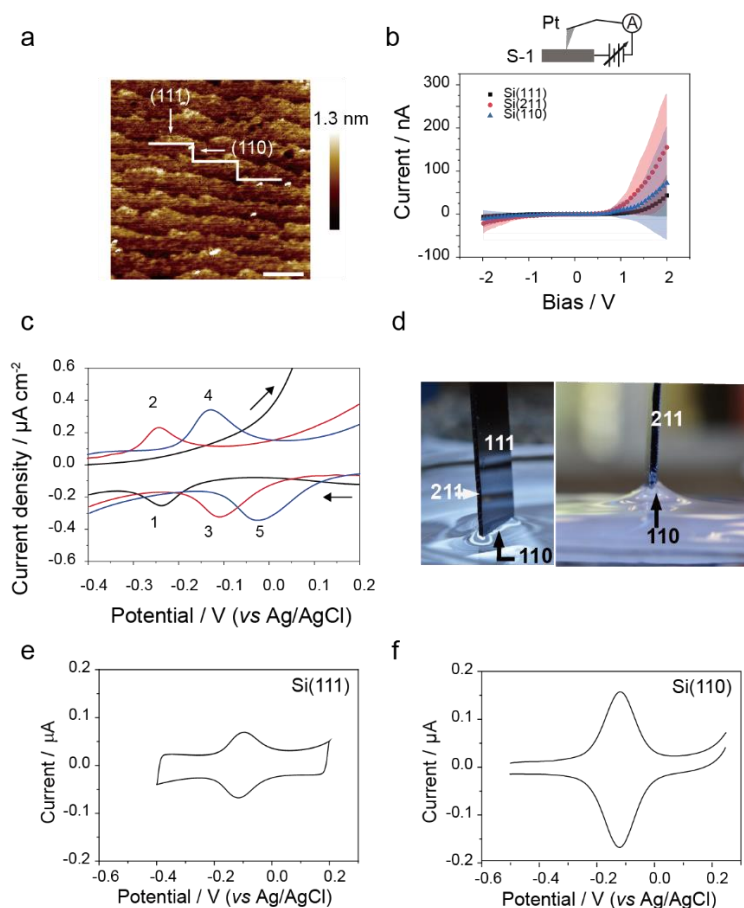


Figure 1.12. Electrochemical signatures of reversible silica-silicon conversion on highly conductive silicon facets. (a) AFM topography image of a Si(111) wafer. Data obtained ensuring a parallel alignment between the original wafer major flat, indicating the $[110]$ direction, and the x -direction of the AFM raster scan. Steps between terraces, here roughly parallel to the sample major flat, are $\langle 110 \rangle$ facets. The scale bar is 400 nm. (b) Schematics of a Pt-organic monolayer-Si junction in a C-AFM measurement and the corresponding I - V curves (average of 400 curves) for Si(111), Si(211) and Si(110) samples. S-1 indicates the substrate is coated with a protective monolayer of 1,8-nonadiyne. (c) Magnified view of the first three sequential cyclic voltammetry (CV) cycles (six segments) of freshly made S-1 samples on Si(111). The bias was ramped from an initial -0.5 V to an anodic vertex of 1.0 V (0.1 V/s, aqueous 1.0 M HClO_4). (d) Hanging meniscus configuration designed to wet exclusively the Si(110) facet, exposed by cleaving a Si(111) wafer along a direction parallel to the wafer's lap. (e, f) CVs of anodically damaged monolayer-coated Si(111) and Si(110) electrodes (S-1, 0.1 V/s, aqueous 1.0 M HClO_4). The surface coverage of the Si/SiO_x signal observed on Si(110) is ~ 6.9 times larger than on Si(111) while the measured (capacitance) area ratio between Si(111) and Si(110) is only 1.9. (a, c-f) Adapted from the study by Zhang et al.^[16], copyright (2021), with permission from the American Chemical Society. (b) Adapted from the study by Zhang et al.^[151], copyright (2021), with permission from the American Chemical Society.

and as such, suitable for the study of surface reactions by electroanalytical methods.

Furthermore, this example of nanoscopic facet-resolved electrochemistry can be scaled to relatively large electrodes (Figure 1.12d). It is customary for silicon manufacturers to mark wafers with a lapped edge. For Si(111) wafers this edge generally marks the $\langle 110 \rangle$ direction. In conjunction with readily available crystallographic stereographic projections, such lap helps in cleaving a commercial wafer to expose specific planes. For instance, cleaving the wafer in direction parallel to the lap will expose Si(110). Cyclic voltammetry in a hanging meniscus setup, such as to wet only the Si(110) facet (Figure 1.12d), leads to redox parasitic waves (the silica–silicon couple) significantly larger than what normally observed with Si(111) (Figure 1.12e,f).

Unlike for a redox reaction that requires migration of oxygenated species, like the one discussed above, or as for bias-dependent adsorptions as discussed in the next section, if the redox entity is held at some distance above the electrode, significant changes in substrate conductivity are not reflected by measurable changes in electrode kinetics. For example the charge-transfer rate constant for ferrocene molecules tethered on the top of a ~ 1 nm-thick organic monolayer are indistinguishable between Si(111), Si(211) and Si(110), despite these surfaces have very different surface conductivities (Figure 1.12b) ^[151].

Finally, it is extremely important to remember that electrical conductivity and electrochemical rate are not synonymous, and that increasing one is not necessarily leading to a similar change in the other. A notable example are Cu₂O crystals, where rates for methanol electro-oxidation are greater on (100) cubic particles than on octahedral (111) crystals, despite the electrical conductivity being larger in the latter ^[159]. A rigorous comparison between the electrochemical activity of differently shaped crystals is generally hindered by difficulties in exposing the materials under test to exactly the same leading to a similar change in the other electrolyte, same pH, if dealing with light-assisted reactions to the same illumination intensity, same active area and same cell geometry. Such difficulties highlight the need of further developing electrochemical imaging techniques to remove experimental ambiguity when attempting a comparison between different facets of the same material ^[160]. As shown

in Figure 1.13, specifically for the Cu_2O case described above, cubes and polyhedron can be simultaneously “imaged” electrochemically using a recently developed spatial light modulator for redox microscopy, but equally valuable are rapidly progressing SECM- and SECCM-based techniques [160, 161].

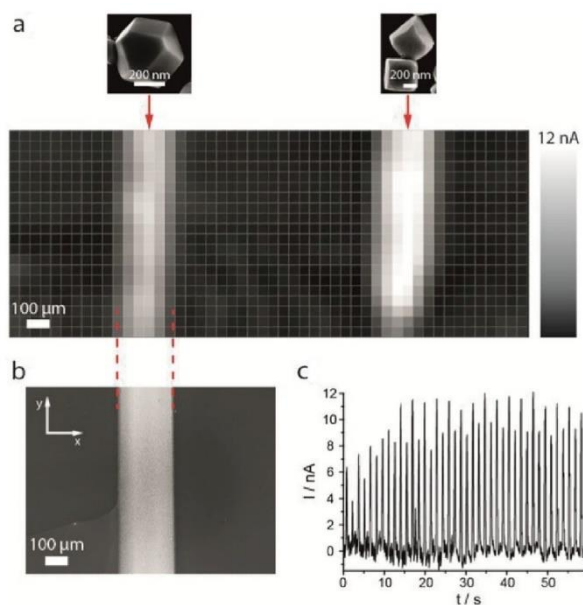


Figure 1.13. *Electrical conductivity and electrochemical rates are not strictly related: lesson learnt from imaging redox reactions. (a) Electrochemical image taken with a spatial light modulator (SLM) addressing sequentially square sections ($46\ \mu\text{m}$ pixels, $17\ \text{Hz}$) of a silicon photoanode coated with different Cu_2O crystals. Insets in (a) and the image in (b) are SEM data of the Cu_2O electrocatalytic “lines” under investigation for their ability to promote the electro-oxidation of methanol. (c) A single channel potentiostat synchronized with the SLM records a current–time trace as that in (c), and this trace is then reconstructed to give the 2D redox map of (a). The time $0\ \text{s}$ corresponds with the bottom-left pixel of the electrochemical image in panel (a), and the time $59\ \text{s}$ with the top-right pixel. The series of “spikes” in the current transient data correspond to the time when the projected light passes over a Cu_2O “line”. The alternate high and low intensity current “spikes” relates to different activities of cubic vs. polyhedral particles. Adapted from the study by Vogel et al. [159], <https://iopscience.iop.org/article/10.1149/2.0111804jes/meta>, under the terms of the CC BY 4.0 license, <http://creativecommons.org/licenses/by/4.0/>.*

1.6.1.4 Facet-dependent electro-adsorption reactions and crystal shapes

Chemists, material scientists and engineers appreciate that the shape and size of an inorganic particle can define its reactivity [148], its catalytic behaviour [162], its ability to

store or conduct charge ^[163], or its interactions with light ^[164]. Nonetheless, shape-control of nanoparticles is often serendipitous, and most generally achieved by chemical means (Figure 1.14a). Recently it was demonstrated that it is possible to use surface electric fields to modulate anisotropic interactions between additives and surfaces, hence predictably exploiting electrostatics to engineer the shape of nanocrystals ^[152, 165].

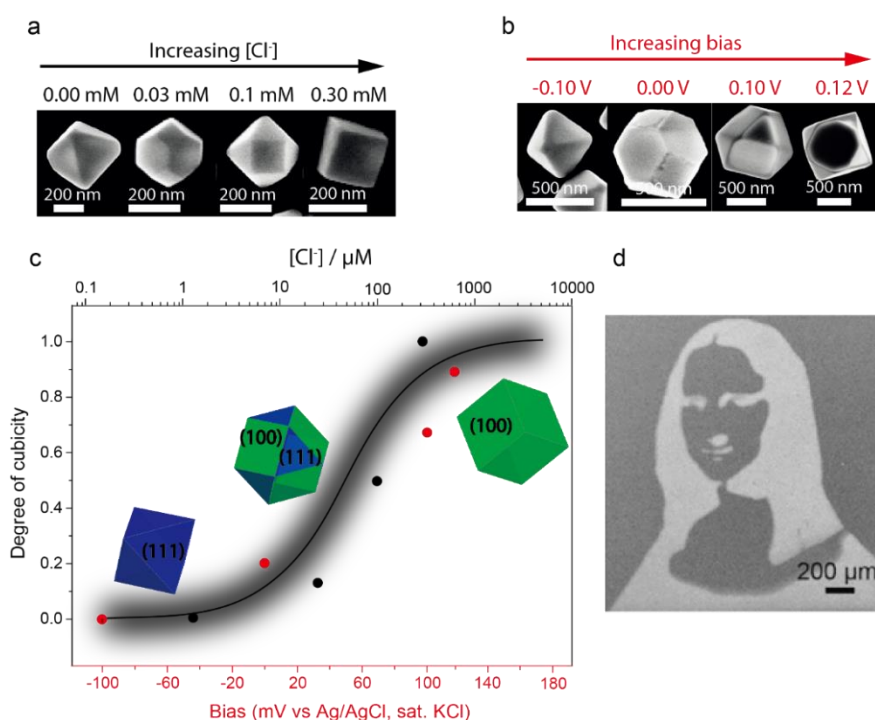


Figure 1.14. Tuning surface energy with bias-dependent anisotropic adsorption of charged species: scope in redox lithography. (a) SEM data showing the change of Cu₂O crystal shapes for a constant electrolysis potential but with changes to the bulk concentration of chloride ions. (b) Evolution of the crystal shape in response to an increased anodic bias under a fixed chloride ions concentration. (c) Plots of the “degree of cubicity” versus bias (or versus concentration, top x-axis) under constant illumination based on a Langmuir isotherm (solid line). (d) SEM image of a “Mona Lisa” pattern made of Cu₂O nanocrystals. Using localized changes to light intensity (micrometer scale lateral resolution) two sets of information can be encoded into the same unit area: control over the polyhedral shape of individual nanocrystals and their lateral spacing, hence enabling to harness facet-dependent halide electro-adsorption to hide cryptic polyhedral signatures. (a–c) Adapted from the study by Vogel et al.^[152], copyright 2018, with permission from the American Chemical Society. (d) Adapted from the study by Vogel et al.^[165], copyright 2018, with permission from Wiley-VCH.

There is a relationship between bias-dependent isothermal adsorption of halide ions and

changes to the surface energy of Cu₂O particles, hence their crystal shape (Figure 1.14b). Most importantly, the sigmoidal nature of adsorption isotherms means that exceedingly small changes to surface potentials can lead to drastic shape differences (Figure 1.14c). This finding can explain the high cubicity reported for particle growing when hydrogen permeates fuel cell membranes towards the cathode, as hydrogen preferentially adsorb on the Pt(100) face ^[166]. Further, as shown in Figure 1.14d, this knowledge was applied to develop a non-contact, non-moving part, mask-free redox printing technology that uses only simple assembly rules (voltages and local illumination density of a semiconductor electrode) for anti-counterfeiting applications ^[165].

It is a speculation, but not unreasonable, that as for the electrosynthesis of Cu₂O particles described above, differences in the electroadsorption bias of charged species, perhaps due to differences in the crystal's potential of zero charge (pzc) ^[167], could account for the remarkably different facet-specific rate in the electrografting of organic cations on metals and semiconductors ^[79]. As shown in Figure 1.15a, b, anisotropic etching of Si(100) wafers with hydroxide-containing solutions leads to a textured surface that exposes an array of Si(111) pyramids. In such a system, the presence or absence, as well as the number and density of <111> facets on a Si(100) crystal can be systematically adjusted. The reduction of a diazonium salt monolayer-forming molecule (o-dianisidine bis(diazotized) zinc double salt, **bis-diazo** in short), followed by its irreversible chemisorption, is favored on Si(111), with a ~200 mV separation between two clear reductive waves visible in Figure 1.15c. As both facets are simultaneously present on the same electrode, ambiguities potentially arising from a drifting reference electrode are prevented. The answer to the question of whether different rates are due to a favored adsorption of **bis-diazo** on Si(111) prior to the electrochemical step, perhaps due to differences in pzc between Si(100) and Si(111), or whether differences in surface conductivities are involved, will require further experiments but is undoubtedly an overlooked phenomenon. What is certain is that Si(111) pyramids are more conductive than the Si(100) plane from which the protrude ^[8], and that different facets of the same material can have significantly different pzc ^[167].

^{168]}. Furthermore, electrical conductivity peaks on the pyramid apex, perhaps because a relatively small amount of charge at the tip of an asperity leads to a large electric field outside the solid ^[169]. Whether electrochemical currents also peak at the convex pyramid apex, and/or in proximity of the (111)–(100) planes intersection, where a concave curvature should lead to a thinner space charge ^[170], as exploited in the formation of porous silicon ^[171], remain also to be experimentally determined.

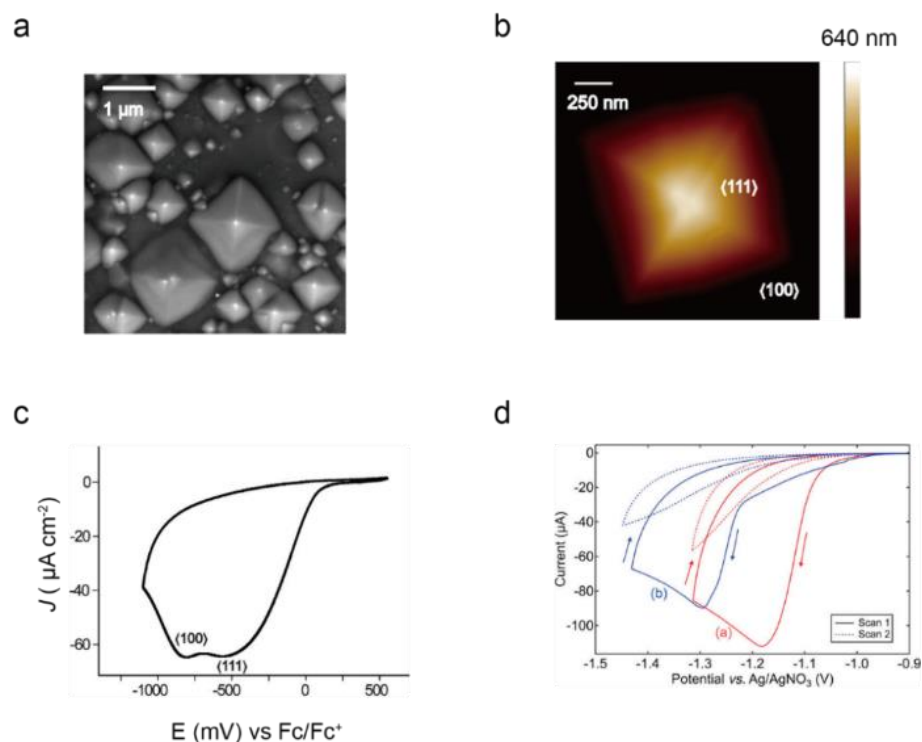


Figure 1.15. Facet-dependent electro-grafting of organic films on textured silicon. (a) SEM image of a Si(100) electrode exposing an array of Si(111) pyramids. (b) AFM image of a single Si(111) pyramid protruding from a Si(100) surface. (c) Electrochemical reduction wave for a CV recorded on the sample whose SEM is presented in (a). The solution contained **bis-diazo** (1 mM *o*-dianisidine bis(diazotized) zinc double salt, with 0.1 M Bu₄NPF₆ in a 1:49 v/v DMSO/ACN mixture) and the CV scan rate was 50 mV/s. (d) Facet-resolved electrochemistry on transparent electrodes. Cathodic electrografting of an aryl diazonium salt (NBD, 2 mM in acetonitrile with 0.1 M [Bu₄N]BF₄) through a cyclic voltammetry experiment (50 mV/s) on either β-Ga₂O₃(201) (red trace) or β-Ga₂O₃(010) (blue trace). (a–c) Adapted from the study by Peiris et al.,^[179] copyright (2019), with permission from the American Chemical Society. (d) Adapted from the study by Carroll et al.,^[172] copyright (2021), with permission from the American Chemical Society.

A similar scenario to the facet-dependent **bis-diazo** electroadsorption described above

has also been recently reported for a form of gallium(III) trioxide, β -Ga₂O₃. This is a semiconductor with an extremely high breakdown field, nearly 8 MV/cm, which is also transparent, hence an actively investigated alternative to the more commonly used and amorphous indium tin oxide ^[173]. The monoclinic crystal structure of β -Ga₂O₃ is highly anisotropic, to the point that for example its optical bandgap measured along the [010] direction is 4.57 eV, while it reaches 4.71 eV along the [201]. In a recent and very elegant study ^[172], Allen et al. have demonstrated that organic monolayers are a viable means to predictably tune the band bending of β -Ga₂O₃, to the point of achieving a downward band bending for a material that is normally strongly depleted in electrons. In this work there is clear implicit evidence of different crystal facets of β -Ga₂O₃ leading to very different electrografting rates. As shown in Figure 1.15d, the electrochemical grafting (reduction followed by chemisorption) of 4-nitrobenzenediazonium (NBD) [as tetrafluoroborate salt] is faster on the (210) facet. It remains to be explored whether the slower rate observed on β -Ga₂O₃(010) may be due to its higher electron affinity, and/or to the stronger upward band bending of the (010) compared to the (201) facet ^[174], or to differences in pzc between different facets controlling a pre-adsorption step.

1.6.1.5 Facet-resolved transition metal phosphides and hydrogen evolution reaction

Hydrogen is a clean and renewable energy source and its production by hydrogen evolution reaction (HER) during water electrolysis is perhaps one of the most actively researched electrochemical reactions. Both computations and experiments indicate that the HER can be strongly facet dependent ^[161, 175]. Transition metal phosphides (TMP) are non-precious metal compounds alternative to platinum. The relationship between crystal facets and HER rates has been investigated on alternative crystallographic facets of the same material: single crystals of iron-phosphide (FeP) and monoclinic nickel-diphosphide (m-NiP₂) ^[176]. Experimental results suggest that the anisotropy of the

catalytic activity is a feature for HER on TMPs. For FeP, a metallic material, the most active crystal facet was the $\langle 010 \rangle$, followed by $\langle 101 \rangle$, $\langle 111 \rangle$, and $\langle 011 \rangle$ is the least active facet. For m-NiP₂, a semiconductor, the $\langle 100 \rangle$ facet showed the highest activity, $\langle 121 \rangle$ and $\langle 101 \rangle$ were a little lower in activity, and $\langle 111 \rangle$ was the least active. These data agree well with DFT calculations, which indicate that the energy of H-binding is strongly facet-dependent. Further, the experiments–calculations correlation is particularly strong for H-binding energies on P on specific surface terminations, pointing to the need of improving our ability to perform and map electrochemistry on single crystals [176]. An interesting consequence of these results is that they weaken the generally held assumption, for transition-metal phosphides, of surface restructuring during the reaction. If this was the case the structure of the bulk catalysts would not particularly matter, as restructuring would occur in situ.

1.6.1.6 Summary and perspective

Assisted by recent developments in areas such as redox imaging [177, 178], spatially resolved electrochemistry [179], electrochemistry at the nanoscale [180, 181], and electrochemistry in confined spaces [182], there is a growing awareness of the anisotropic catalytic activity of alternative facets of technological materials such as silicon, boron-doped diamond, Cu₂O, GaAs, InN, Ag₂O, and β -Ga₂O₃ [1, 79, 152-155, 160, 165]. Facet-resolved electrochemistry is developing rapidly, and it has already had a fundamental and practical impact on semiconductor electrochemistry, redox lithography, electrocatalysis, particle and film growth. There are mature theoretical models that can explain the available experimental data, as well as guide the rational design of new materials and optimized electrode surfaces that will contribute to the global challenge of integrating renewable electricity into chemical manufacturing, that is, to progressively replace conventional molecular reactants with electricity towards a sustainable chemical industry.

1.7 References

- [1]. Tan, C.-S.; Hsieh, P.-L.; Chen, L.-J.; Huang, M. H., Silicon Wafers with Facet-

- Dependent Electrical Conductivity Properties. *Angew. Chem. Int. Ed.* **2017**, *56*, (48), 15339–15343.
- [2]. Aragonés, A. C.; Haworth, N. L.; Darwish, N.; Ciampi, S.; Bloomfield, N. J.; Wallace, G. G.; Diez-Perez, I.; Coote, M. L., Electrostatic catalysis of a Diels-Alder reaction. *Nature* **2016**, *531*, (7592), 88-91.
- [3]. Zhang, X. G., *Electrochemistry of Silicon and Its Oxide*. Kluwer Academic, New York,: 2001, <https://doi.org/10.1007/b100331>.
- [4]. Neergaard Waltenburg, H.; Yates, J., Surface Chemistry of Silicon. *Chem. Rev.* **1995**, *95*, (5), 1589-1673.
- [5]. Fabre, B., Ferrocene-Terminated Monolayers Covalently Bound to Hydrogen-Terminated Silicon Surfaces. Toward the Development of Charge Storage and Communication Devices. *Acc. Chem. Res.* **2010**, *43*, (12), 1509-1518.
- [6]. Lyu, X.; Ferrie, S.; Pivrikas, A.; MacGregor, M.; Ciampi, S., Sliding Schottky diode triboelectric nanogenerators with current output of 109 A/m² by molecular engineering of Si(211) surfaces. *Nano Energy* **2022**, *102*, 107658.
- [7]. Ferrie, S.; Le Brun, A. P.; Krishnan, G.; Andersson, G. G.; Darwish, N.; Ciampi, S., Sliding silicon-based Schottky diodes: Maximizing triboelectricity with surface chemistry. *Nano Energy* **2022**, *93*, 106861.
- [8]. Ferrie, S.; Darwish, N.; Gooding, J. J.; Ciampi, S., Harnessing silicon facet-dependent conductivity to enhance the direct-current produced by a sliding Schottky diode triboelectric nanogenerator. *Nano Energy* **2020**, *78*, 105210.
- [9]. Hurtado, C.; Lyu, X.; Ferrie, S.; Le Brun, A. P.; MacGregor, M.; Ciampi, S., Organic Monolayers on Si(211) for Triboelectricity Generation: Etching Optimization and Relationship between the Electrochemistry and Current Output. *ACS Appl. Nano Mater.* **2022**, *5*, (10), 14263-14274.
- [10]. Bard, A. J., Photoelectrochemistry. *Science* **1980**, *207*, (4427), 139-144.
- [11]. Zhao, Y.; Yu, J.; Xu, G.; Sojic, N.; Loget, G., Photoinduced Electrochemiluminescence at Silicon Electrodes in Water. *J. Am. Chem. Soc.* **2019**, *141*, (33), 13013-13016.
- [12]. Zhang, Z.; Yates, J. T., Band Bending in Semiconductors: Chemical and Physical Consequences at Surfaces and Interfaces. *Chem. Rev.* **2012**, *112*, (10), 5520-5551.
- [13]. Grätzel, M., Photoelectrochemical cells. *Nature* **2001**, *414*, (6861), 338-344.
- [14]. Lang, N. D.; Kohn, W., Theory of Metal Surfaces: Work Function. *Phys. Rev. B* **1971**, *3*, (4), 1215-1223.
- [15]. Vogel, Y. B.; Gooding, J. J.; Ciampi, S., Light-addressable electrochemistry at semiconductor electrodes: redox imaging, mask-free lithography and spatially resolved chemical and biological sensing. *Chem. Soc. Rev.* **2019**, *48*, (14), 3723–3739.
- [16]. Zhang, S.; Ferrie, S.; Peiris, C. R.; Lyu, X.; Vogel, Y. B.; Darwish, N.; Ciampi, S., Common Background Signals in Voltammograms of Crystalline Silicon Electrodes are Reversible Silica-Silicon Redox Chemistry at Highly Conductive Surface Sites. *J Am Chem Soc* **2021**, *143*, (3), 1267–1272.
- [17]. Filsinger, D. H.; Bourrie, D. B., Silica to Silicon: Key Carbothermic Reactions

- and Kinetics. *J. Am. Ceram. Soc.* **1990**, *73*, (6), 1726-1732.
- [18]. Nohira, T.; Yasuda, K.; Ito, Y., Pinpoint and bulk electrochemical reduction of insulating silicon dioxide to silicon. *Nat. Mater.* **2003**, *2*, (6), 397–401.
- [19]. Gonçalves, V. R.; Lian, J.; Gautam, S.; Tilley, R. D.; Gooding, J. J., Functionalized Silicon Electrodes in Electrochemistry. *Annu. Rev. Anal. Chem.* **2020**, *13*, (1), 135-158.
- [20]. Fabre, B.; Pujari, S. P.; Scheres, L.; Zuilhof, H., Micropatterned ferrocenyl monolayers covalently bound to hydrogen-terminated silicon surfaces: effects of pattern size on the cyclic voltammetry and capacitance characteristics. *Langmuir* **2014**, *30*, (24), 7235-43.
- [21]. Fabre, B., Functionalization of Oxide-Free Silicon Surfaces with Redox-Active Assemblies. *Chem Rev* **2016**, *116*, (8), 4808–4849.
- [22]. Austin, M. D.; Chou, S. Y., Fabrication of a Molecular Self-Assembled Monolayer Diode Using Nanoimprint Lithography. *Nano Letters* **2003**, *3*, (12), 1687-1690.
- [23]. Li, Q. L.; Mathur, G.; Homsy, M.; Surthi, S.; Misra, V.; Malinovskii, V.; Schweikart, K. H.; Yu, L. H.; Lindsey, J. S.; Liu, Z. M.; Dabke, R. B.; Yasseri, A.; Bocian, D. F.; Kuhr, W. G., Capacitance and conductance characterization of ferrocene-containing self-assembled monolayers on silicon surfaces for memory applications. *Appl. Phys. Lett.* **2002**, *81*, (8), 1494-1496.
- [24]. DiBenedetto, S. A.; Facchetti, A.; Ratner, M. A.; Marks, T. J., Charge Conduction and Breakdown Mechanisms in Self-Assembled Nanodielectrics. *J. Am. Chem. Soc.* **2009**, *131*, (20), 7158-7168.
- [25]. O’Leary, L. E.; Rose, M. J.; Ding, T. X.; Johansson, E.; Brunschwig, B. S.; Lewis, N. S., Heck Coupling of Olefins to Mixed Methyl/Thienyl Monolayers on Si(111) Surfaces. *J. Am. Chem. Soc.* **2013**, *135*, (27), 10081-10090.
- [26]. Wang, W.-Y.; Kala, K.; Wei, T.-C., Solvent-Dependent Adhesion Strength of Electroless Deposited Ni–P Layer on an Amino-Terminated Silane Compound-Modified Si Wafer. *Langmuir* **2018**, *34*, (45), 13597-13602.
- [27]. Ciampi, S.; James, M.; Le Saux, G.; Gaus, K.; Justin Gooding, J., Electrochemical "switching" of Si(100) modular assemblies. *J. Am. Chem. Soc.* **2012**, *134*, (2), 844-847.
- [28]. Wallart, X.; Henry de Villeneuve, C.; Allongue, P., Truly Quantitative XPS Characterization of Organic Monolayers on Silicon: Study of Alkyl and Alkoxy Monolayers on H–Si(111). *J. Am. Chem. Soc.* **2005**, *127*, (21), 7871-7878.
- [29]. Ahmad, S. A. A.; Ciampi, S.; Parker, S. G.; Goncales, V. R.; Gooding, J. J., Forming Ferrocenyl Self-Assembled Monolayers on Si(100) Electrodes with Different Alkyl Chain Lengths for Electron Transfer Studies. *Chemelectrochem* **2019**, *6*, (1), 211-220.
- [30]. Himpfel, F. J.; McFeely, F. R.; Taleb-Ibrahimi, A.; Yarmoff, J. A.; Hollinger, G., Microscopic structure of the SiO₂/Si interface. *Phys. Rev. B* **1988**, *38*, (9), 6084-6096.
- [31]. Sagiv, J., Organized monolayers by adsorption. 1. Formation and structure of oleophobic mixed monolayers on solid surfaces. *J. Am. Chem. Soc.* **1980**, *102*,

- (1), 92-98.
- [32]. Jia, X.; McCarthy, T. J., Controlled Growth of Silicon Dioxide from “Nanoholes” in Silicon-Supported Tris(trimethylsiloxy)silyl Monolayers: Rational Control of Surface Roughness at the Nanometer Length Scale. *Langmuir* **2003**, *19*, (6), 2449-2457.
- [33]. Pujari, S. P.; Spruijt, E.; Cohen Stuart, M. A.; van Rijn, C. J. M.; Paulusse, J. M. J.; Zuilhof, H., Ultralow Adhesion and Friction of Fluoro-Hydro Alkyne-Derived Self-Assembled Monolayers on H-Terminated Si(111). *Langmuir* **2012**, *28*, (51), 17690-17700.
- [34]. DePalma, V.; Tillman, N., Friction and wear of self-assembled trichlorosilane monolayer films on silicon. *Langmuir* **1989**, *5*, (3), 868-872.
- [35]. Ciampi, S.; Choudhury, M. H.; Ahmad, S. A. B. A.; Darwish, N.; Brun, A. L.; Gooding, J. J., The impact of surface coverage on the kinetics of electron transfer through redox monolayers on a silicon electrode surface. *Electrochim. Acta* **2015**, *186*, 216-222.
- [36]. Yang, Y.; Ciampi, S.; Choudhury, M. H.; Gooding, J. J., Light Activated Electrochemistry: Light Intensity and pH Dependence on Electrochemical Performance of Anthraquinone Derivatized Silicon. *J. Phys. Chem. C* **2016**, *120*, (5), 2874-2882.
- [37]. Sumner, J. J.; Creager, S. E., Redox Kinetics in Monolayers on Electrodes: Electron Transfer Is Sluggish for Ferrocene Groups Buried within the Monolayer Interior. *J. Phys. Chem. B* **2001**, *105*, (37), 8739-8745.
- [38]. Whitesides, G. M.; Kriebel, J. K.; Love, J. C., Molecular engineering of Surfaces Using Self-Assembled Monolayers. *Sci Prog.* **2005**, *88*, (1), 17-48.
- [39]. Gooding, J. J.; Ciampi, S., The molecular level modification of surfaces: from self-assembled monolayers to complex molecular assemblies. *Chem Soc Rev* **2011**, *40*, (5), 2704-2718.
- [40]. Vilan, A.; Cahen, D., Chemical Modification of Semiconductor Surfaces for Molecular Electronics. *Chem. Rev.* **2017**, *117*, (5), 4624-4666.
- [41]. Aswal, D. K.; Lenfant, S.; Guerin, D.; Yakhmi, J. V.; Vuillaume, D., Self assembled monolayers on silicon for molecular electronics. *Anal. Chim. Acta* **2006**, *568*, (1), 84-108.
- [42]. Devaraj, N. K.; Dinolfo, P. H.; Chidsey, C. E. D.; Collman, J. P., Selective Functionalization of Independently Addressed Microelectrodes by Electrochemical Activation and Deactivation of a Coupling Catalyst. *J. Am. Chem. Soc.* **2006**, *128*, (6), 1794-1795.
- [43]. Evans, D. H., One-Electron and Two-Electron Transfers in Electrochemistry and Homogeneous Solution Reactions. *J. Am. Chem. Soc.* **2008**, *108*, (7), 2113-2144.
- [44]. Creager, S. E.; Wooster, T. T., A New Way of Using ac Voltammetry To Study Redox Kinetics in Electroactive Monolayers. *Anal. Chem.* **1998**, *70*, (20), 4257-4263.
- [45]. Steentjes, T.; Jonkheijm, P.; Huskens, J., Electron Transfer Processes in Ferrocene-Modified Poly(ethylene glycol) Monolayers on Electrodes.

- Langmuir* **2017**, *33*, (43), 11878-11883.
- [46]. Love, J. C.; Estroff, L. A.; Kriebel, J. K.; Nuzzo, R. G.; Whitesides, G. M., Self-Assembled Monolayers of Thiolates on Metals as a Form of Nanotechnology. *Chem. Rev.* **2005**, *105*, (4), 1103-1170.
- [47]. Wong, R. A.; Yokota, Y.; Wakisaka, M.; Inukai, J.; Kim, Y., Probing consequences of anion-dictated electrochemistry on the electrode/monolayer/electrolyte interfacial properties. *Nat. Commun.* **2020**, *11*, (1), 4194.
- [48]. Liljeroth, P.; Quinn, B. M., Resolving Electron Transfer Kinetics at the Nanocrystal/Solution Interface. *J. Am. Chem. Soc.* **2006**, *128*, (15), 4922-4923.
- [49]. Norman, L. L.; Badia, A., Redox Actuation of a Microcantilever Driven by a Self-Assembled Ferrocenylundecanethiolate Monolayer: An Investigation of the Origin of the Micromechanical Motion and Surface Stress. *J. Am. Chem. Soc.* **2009**, *131*, (6), 2328-2337.
- [50]. Dionne, E. R.; Sultana, T.; Norman, L. L.; Toader, V.; Badia, A., Redox-Induced Ion Pairing of Anionic Surfactants with Ferrocene-Terminated Self-Assembled Monolayers: Faradaic Electrochemistry and Surfactant Aggregation at the Monolayer/Liquid Interface. *J. Am. Chem. Soc.* **2013**, *135*, (46), 17457-17468.
- [51]. Wang, L.; Yuan, L.; Jiang, L.; Yu, X.; Cao, L.; Nijhuis, C. A., Unraveling the Failure Modes of Molecular Diodes: The Importance of the Monolayer Formation Protocol and Anchoring Group to Minimize Leakage Currents. *J. Phys. Chem. C* **2019**, *123*, (32), 19759-19767.
- [52]. Bowers, C. M.; Rappoport, D.; Baghbanzadeh, M.; Simeone, F. C.; Liao, K.-C.; Semenov, S. N.; Žaba, T.; Cyganik, P.; Aspuru-Guzik, A.; Whitesides, G. M., Tunneling across SAMs Containing Oligophenyl Groups. *J. Phys. Chem. C* **2016**, *120*, (21), 11331-11337.
- [53]. Mamun, A. H. A.; Hahn, J. R., Effects of Solvent on the Formation of Octanethiol Self-Assembled Monolayers on Au(111) at High Temperatures in a Closed Vessel: A Scanning Tunneling Microscopy and X-ray Photoelectron Spectroscopy Study. *J. Phys. Chem. C* **2012**, *116*, (42), 22441-22448.
- [54]. Käfer, D.; Witte, G.; Cyganik, P.; Terfort, A.; Wöll, C., A Comprehensive Study of Self-Assembled Monolayers of Anthracenethiol on Gold: Solvent Effects, Structure, and Stability. *J. Am. Chem. Soc.* **2006**, *128*, (5), 1723-1732.
- [55]. English, R. D.; Van Stipdonk, M. J.; Sabapathy, R. C.; Crooks, R. M.; Schweikert, E. A., Characterization of Photooxidized Self-Assembled Monolayers and Bilayers by Spontaneous Desorption Mass Spectrometry. *Anal. Chem.* **2000**, *72*, (24), 5973-5980.
- [56]. Yang, G.; Amro, N. A.; Starkewolfe, Z. B.; Liu, G.-y., Molecular-Level Approach To Inhibit Degradations of Alkanethiol Self-Assembled Monolayers in Aqueous Media. *Langmuir* **2004**, *20*, (10), 3995-4003.
- [57]. Hurley, P. T.; Ribbe, A. E.; Buriak, J. M., Nanopatterning of Alkynes on Hydrogen-Terminated Silicon Surfaces by Scanning Probe-Induced Cathodic Electrografting. *J. Am. Chem. Soc.* **2003**, *125*, (37), 11334-11339.

- [58]. Uchida, K.; Yamanoi, Y.; Yonezawa, T.; Nishihara, H., Reversible On/Off Conductance Switching of Single Diarylethene Immobilized on a Silicon Surface. *J. Am. Chem. Soc.* **2011**, *133*, (24), 9239-9241.
- [59]. Cicero, R. L.; Linford, M. R.; Chidsey, C. E. D., Photoreactivity of Unsaturated Compounds with Hydrogen-Terminated Silicon(111). *Langmuir* **2000**, *16*, (13), 5688-5695.
- [60]. Linford, M. R.; Chidsey, C. E. D., Alkyl monolayers covalently bonded to silicon surfaces. *J. Am. Chem. Soc.* **1993**, *115*, (26), 12631-12632.
- [61]. Linford, M. R.; Fenter, P.; Eisenberger, P. M.; Chidsey, C. E. D., Alkyl Monolayers on Silicon Prepared from 1-Alkenes and Hydrogen-Terminated Silicon. *J. Am. Chem. Soc.* **1995**, *117*, (11), 3145-3155.
- [62]. Qin, G.; Santos, C.; Zhang, W.; Li, Y.; Kumar, A.; Erasquin, U. J.; Liu, K.; Muradov, P.; Trautner, B. W.; Cai, C., Biofunctionalization on Alkylated Silicon Substrate Surfaces via "Click" Chemistry. *J. Am. Chem. Soc.* **2010**, *132*, (46), 16432-16441.
- [63]. Ciampi, S.; Harper, J. B.; Gooding, J. J., Wet chemical routes to the assembly of organic monolayers on silicon surfaces via the formation of Si-C bonds: surface preparation, passivation and functionalization. *Chem. Soc. Rev.* **2010**, *39*, (6), 2158-2183.
- [64]. Ciampi, S.; James, M.; Michaels, P.; Gooding, J. J., Tandem "click" reactions at acetylene-terminated Si(100) monolayers. *Langmuir* **2011**, *27*, (11), 6940-6949.
- [65]. Bateman, J. E.; Eagling, R. D.; Worrall, D. R.; Horrocks, B. R.; Houlton, A., Alkylation of Porous Silicon by Direct Reaction with Alkenes and Alkynes. *Angew. Chem., Int. Ed.* **1998**, *37*, (19), 2683-2685.
- [66]. Sieval, A. B.; Vleeming, V.; Zuilhof, H.; Sudhölter, E. J. R., An Improved Method for the Preparation of Organic Monolayers of 1-Alkenes on Hydrogen-Terminated Silicon Surfaces. *Langmuir* **1999**, *15*, (23), 8288-8291.
- [67]. Sieval, A. B.; Linke, R.; Heij, G.; Meijer, G.; Zuilhof, H.; Sudhölter, E. J. R., Amino-Terminated Organic Monolayers on Hydrogen-Terminated Silicon Surfaces. *Langmuir* **2001**, *17*, (24), 7554-7559.
- [68]. Ciampi, S.; Eggers, P. K.; Le Saux, G.; James, M.; Harper, J. B.; Gooding, J. J., Silicon (100) electrodes resistant to oxidation in aqueous solutions: an unexpected benefit of surface acetylene moieties. *Langmuir* **2009**, *25*, (4), 2530-2539.
- [69]. Ciampi, S.; Guan, B.; Darwish, N.; Reece, P. J.; Gooding, J. J., Redox-Active Monolayers in Mesoporous Silicon. *J. Phys. Chem. C* **2012**, *116*, (30), 16080-16088.
- [70]. Bansal, A.; Li, X.; Lauermann, I.; Lewis, N. S.; Yi, S. I.; Weinberg, W. H., Alkylation of Si Surfaces Using a Two-Step Halogenation/Grignard Route. *J. Am. Chem. Soc.* **1996**, *118*, (30), 7225-7226.
- [71]. Boukherroub, R.; Wayner, D. D. M., Controlled Functionalization and Multistep Chemical Manipulation of Covalently Modified Si(111) Surfaces. *J. Am. Chem. Soc.* **1999**, *121*, (49), 11513-11515.

- [72]. Sun, Q.-Y.; de Smet, L. C. P. M.; van Lagen, B.; Giesbers, M.; Thüne, P. C.; van Engelenburg, J.; de Wolf, F. A.; Zuilhof, H.; Sudhölter, E. J. R., Covalently Attached Monolayers on Crystalline Hydrogen-Terminated Silicon: Extremely Mild Attachment by Visible Light. *J. Am. Chem. Soc.* **2005**, *127*, (8), 2514-2523.
- [73]. Effenberger, F.; Götz, G.; Bidlingmaier, B.; Wezstein, M., Photoactivated Preparation and Patterning of Self-Assembled Monolayers with 1-Alkenes and Aldehydes on Silicon Hydride Surfaces. *Angew. Chem., Int. Ed.* **1998**, *37*, (18), 2462-2464.
- [74]. Howland, M. C.; Sapuri-Butti, A. R.; Dixit, S. S.; Dattelbaum, A. M.; Shreve, A. P.; Parikh, A. N., Phospholipid Morphologies on Photochemically Patterned Silane Monolayers. *J. Am. Chem. Soc.* **2005**, *127*, (18), 6752-6765.
- [75]. Chen, B.; Flatt, A. K.; Jian, H.; Hudson, J. L.; Tour, J. M., Molecular Grafting to Silicon Surfaces in Air Using Organic Triazenes as Stable Diazonium Sources and HF as a Constant Hydride-Passivation Source. *Chem. Mater.* **2005**, *17*, (19), 4832-4836.
- [76]. Flatt, A. K.; Chen, B.; Taylor, P. G.; Chen, M.; Tour, J. M., Attaching Electronically Active Oligoanilines to Silicon Surfaces. *Chem. Mater.* **2006**, *18*, (18), 4513-4518.
- [77]. Combellas, C.; Kanoufi, F.; Pinson, J.; Podvorica, F. I., Sterically Hindered Diazonium Salts for the Grafting of a Monolayer on Metals. *J. Am. Chem. Soc.* **2008**, *130*, (27), 8576-8577.
- [78]. de Villeneuve, C. H.; Pinson, J.; Bernard, M. C.; Allongue, P., Electrochemical Formation of Close-Packed Phenyl Layers on Si(111). *J. Phys. Chem. B* **1997**, *101*, (14), 2415-2420.
- [79]. Peiris, C. R.; Vogel, Y. B.; Le Brun, A. P.; Aragonès, A. C.; Coote, M. L.; Díez-Pérez, I.; Ciampi, S.; Darwish, N., Metal–Single-Molecule–Semiconductor Junctions Formed by a Radical Reaction Bridging Gold and Silicon Electrodes. *J. Am. Chem. Soc.* **2019**, *141*, (37), 14788–14797.
- [80]. Pandey, D.; Zemlyanov, D. Y.; Bevan, K.; Reifenberger, R. G.; Dirk, S. M.; Howell, S. W.; Wheeler, D. R., UHV STM I(V) and XPS Studies of Aryl Diazonium Molecules Assembled on Si(111). *Langmuir* **2007**, *23*, (9), 4700-4708.
- [81]. Stewart, M. P.; Maya, F.; Kosynkin, D. V.; Dirk, S. M.; Stapleton, J. J.; McGuinness, C. L.; Allara, D. L.; Tour, J. M., Direct Covalent Grafting of Conjugated Molecules onto Si, GaAs, and Pd Surfaces from Aryldiazonium Salts. *J. Am. Chem. Soc.* **2004**, *126*, (1), 370-378.
- [82]. Vogel, Y. B.; Zhang, L.; Darwish, N.; Gonçalves, V. R.; Le Brun, A.; Gooding, J. J.; Molina, A.; Wallace, G. G.; Coote, M. L.; Gonzalez, J.; Ciampi, S., Reproducible flaws unveil electrostatic aspects of semiconductor electrochemistry. *Nat. Commun.* **2017**, *8*, (1), 2066.
- [83]. Ciampi, S.; Bocking, T.; Kilian, K. A.; James, M.; Harper, J. B.; Gooding, J. J., Functionalization of acetylene-terminated monolayers on Si(100) surfaces: a click chemistry approach. *Langmuir* **2007**, *23*, (18), 9320-9329.
- [84]. Zarei, L.; Tavallaie, R.; Choudhury, M. H.; Parker, S. G.; Bakthavathsalam,

- P.; Ciampi, S.; Goncales, V. R.; Gooding, J. J., DNA-Hybridization Detection on Si(100) Surfaces Using Light-Activated Electrochemistry: A Comparative Study between Bovine Serum Albumin and Hexaethylene Glycol as Antifouling Layers. *Langmuir* **2018**, *34*, (49), 14817-14824.
- [85]. Ciampi, S.; Choudhury, M. H.; Ahmad, S. A. B. A.; Darwish, N.; Le Brun, A.; Gooding, J. J., The impact of surface coverage on the kinetics of electron transfer through redox monolayers on a silicon electrode surface. *Electrochim. Acta* **2015**, *186*, 216-222.
- [86]. Veerbeek, J.; Méndez-Ardoy, A.; Huskens, J., Electrochemistry of Redox-Active Guest Molecules at β -Cyclodextrin-Functionalized Silicon Electrodes. *Chemelectrochem* **2017**, *4*, (6), 1470-1477.
- [87]. Heinze, J., Cyclic Voltammetry—"Electrochemical Spectroscopy". *New Analytical Methods* (25). *Angew. Chem. Int. Ed.* **1984**, *23*, (11), 831-847.
- [88]. Nicholson, R. S., Theory and Application of Cyclic Voltammetry for Measurement of Electrode Reaction Kinetics. *Anal. Chem.* **1965**, *37*, (11), 1351-1355.
- [89]. Vogel, Y. B.; Molina, A.; Gonzalez, J.; Ciampi, S., Quantitative Analysis of Cyclic Voltammetry of Redox Monolayers Adsorbed on Semiconductors: Isolating Electrode Kinetics, Lateral Interactions, and Diode Currents. *Anal. Chem.* **2019**, *91*, (9), 5929-5937.
- [90]. Yang, Y.; Ciampi, S.; Gooding, J. J., Coupled Thermodynamic and Kinetic Changes in the Electrochemistry of Ferrocenyl Monolayers Induced by Light. *Langmuir* **2017**, *33*, (10), 2497-2503.
- [91]. Gonzalez, J.; Sequí-Castellano, J. A., Electrochemical determination of kinetic parameters of surface confined redox probes in presence of intermolecular interactions by means of Cyclic Voltammetry. Application to TEMPO monolayers in gold and platinum electrodes. *Electrochim. Acta* **2021**, *365*, 137331.
- [92]. Eckermann, A. L.; Feld, D. J.; Shaw, J. A.; Meade, T. J., Electrochemistry of redox-active self-assembled monolayers. *Coord Chem Rev* **2010**, *254*, (15), 1769-1802.
- [93]. Randviir, E. P., A cross examination of electron transfer rate constants for carbon screen-printed electrodes using Electrochemical Impedance Spectroscopy and cyclic voltammetry. *Electrochim. Acta* **2018**, *286*, 179-186.
- [94]. Darwish, N.; Eggers, P. K.; Ciampi, S.; Tong, Y.; Ye, S.; Paddon-Row, M. N.; Gooding, J. J., Probing the Effect of the Solution Environment around Redox-Active Moieties Using Rigid Anthraquinone Terminated Molecular Rulers. *J. Am. Chem. Soc.* **2012**, *134*, (44), 18401-18409.
- [95]. Brown, A. P.; Anson, F. C., Cyclic and differential pulse voltammetric behavior of reactants confined to the electrode surface. *Anal. Chem.* **1977**, *49*, (11), 1589-1595.
- [96]. Nerngchamnon, N.; Thompson, D.; Cao, L.; Yuan, L.; Jiang, L.; Roemer, M.; Nijhuis, C. A., Nonideal Electrochemical Behavior of Ferrocenyl-Alkanethiolate SAMs Maps the Microenvironment of the Redox Unit. *J. Phys.*

- Chem. C* **2015**, *119*, (38), 21978-21991.
- [97]. Ruther, R. E.; Cui, Q.; Hamers, R. J., Conformational Disorder Enhances Electron Transfer Through Alkyl Monolayers: Ferrocene on Conductive Diamond. *J. Am. Chem. Soc.* **2013**, *135*, (15), 5751-5761.
- [98]. Rudnev, A. V.; Yoshida, K.; Wandlowski, T., Electrochemical characterization of self-assembled ferrocene-terminated alkanethiol monolayers on low-index gold single crystal electrodes. *Electrochim Acta.* **2013**, *87*, 770-778.
- [99]. Patel, D. A.; Chevalier, R. B.; Weller, A. M.; Shakespeare, C. C.; Soares, E. J.; Landis, E. C., Porosity Effects on the Ordering and Stability of Self-Assembled Monolayers on Nanoporous Gold. *J. Phys. Chem. C* **2020**, *124*, (49), 26851-26863.
- [100]. Dhar, D.; McKenas, C. G.; Huang, C.-W.; Atkin, J. M.; Dempsey, J. L.; Lockett, M. R., Quantitative Effects of Disorder on Chemically Modified Amorphous Carbon Electrodes. *ACS Appl. Energy Mater.* **2020**, *3*, (8), 8038-8047.
- [101]. Green, K.; Gauthier, N.; Sahnoune, H.; Halet, J.-F.; Paul, F.; Fabre, B., Covalent Immobilization of Redox-Active Fe(κ 2-dppe)(η 5-C5Me5)-Based π -Conjugated Wires on Oxide-Free Hydrogen-Terminated Silicon Surfaces. *Organometallics* **2013**, *32*, (19), 5333-5342.
- [102]. Song, P.; Thompson, D.; Annadata, H. V.; Guerin, S.; Loh, K. P.; Nijhuis, C. A., Supramolecular Structure of the Monolayer Triggers Odd–Even Effects in the Tunneling Rates across Noncovalent Junctions on Graphene. *J. Phys. Chem. C* **2017**, *121*, (8), 4172-4180.
- [103]. Lee, L. Y. S.; Sutherland, T. C.; Rucareanu, S.; Lennox, R. B., Ferrocenylalkylthiolates as a Probe of Heterogeneity in Binary Self-Assembled Monolayers on Gold. *Langmuir* **2006**, *22*, (9), 4438-4444.
- [104]. Wong, R. A.; Yokota, Y.; Wakisaka, M.; Inukai, J.; Kim, Y., Discerning the Redox-Dependent Electronic and Interfacial Structures in Electroactive Self-Assembled Monolayers. *J. Am. Chem. Soc.* **2018**, *140*, (42), 13672-13679.
- [105]. Zhang, S.; Lyu, X.; Hurtado Torres, C.; Darwish, N.; Ciampi, S., Non-Ideal Cyclic Voltammetry of Redox Monolayers on Silicon Electrodes: Peak Splitting is Caused by Heterogeneous Photocurrents and Not by Molecular Disorder. *Langmuir* **2022**, *38*, (2), 743-750.
- [106]. Chang, B.-Y.; Park, S.-M., Electrochemical Impedance Spectroscopy. *Annu. Rev. Anal. Chem.* **2010**, *3*, (1), 207-229.
- [107]. Pajkossy, T.; Jurczakowski, R., Electrochemical impedance spectroscopy in interfacial studies. *Curr. Opin. Electrochem.* **2017**, *1*, (1), 53-58.
- [108]. Macdonald, D. D., Reflections on the history of electrochemical impedance spectroscopy. *Electrochim. Acta* **2006**, *51*, (8), 1376-1388.
- [109]. Magar, H. S.; Hassan, R. Y. A.; Mulchandani, A., Electrochemical Impedance Spectroscopy (EIS): Principles, Construction, and Biosensing Applications. *Sensors* **2021**, *21*, (19), 6578.
- [110]. Laviron, E., A.C. polarography and faradaic impedance of strongly adsorbed electroactive species: Part I. Theoretical and experimental study of a quasi-

- reversible reaction in the case of a Langmuir isotherm. *Journal of Electroanalytical Chemistry and Interfacial Electrochemistry* **1979**, *97*, (2), 135-149.
- [111]. Laviron, E., A.C. Polarography and faradaic impedance of strongly adsorbed electroactive species: Part III. Theoretical complex plane analysis for a surface redox reaction. *Journal of Electroanalytical Chemistry and Interfacial Electrochemistry* **1979**, *105*, (1), 35-42.
- [112]. Bowen, R.; Hilal, N., *Atomic force microscopy in process engineering: An introduction to AFM for improved processes and products*. Butterworth-Heinemann: 2009.
- [113]. Shin, C.; Kim, K.; Kim, J.; Ko, W.; Yang, Y.; Lee, S.; Jun, C. S.; Kim, Y. S., Fast, exact and non-destructive diagnoses of contact failures in nano-scale semiconductor device using conductive AFM. *Sci Rep* **2013**, *3*, (1), 2088.
- [114]. Yanev, V.; Erlbacher, T.; Rommel, M.; Bauer, A. J.; Frey, L., Comparative study between conventional macroscopic IV techniques and advanced AFM based methods for electrical characterization of dielectrics at the nanoscale. *Microelectron. Eng.* **2009**, *86*, (7), 1911-1914.
- [115]. Andolfi, L.; Cannistraro, S., Conductive atomic force microscopy study of plastocyanin molecules adsorbed on gold electrode. *Surf. Sci.* **2005**, *598*, (1), 68-77.
- [116]. Si, H.; Zhang, S.; Ma, S.; Xiong, Z.; Kausar, A.; Liao, Q.; Zhang, Z.; Sattar, A.; Kang, Z.; Zhang, Y., Emerging Conductive Atomic Force Microscopy for Metal Halide Perovskite Materials and Solar Cells. *Adv. Energy Mater.* **2020**, *10*, (10), 1903922.
- [117]. Ulgut, B.; Abruña, H. D., Electron Transfer through Molecules and Assemblies at Electrode Surfaces. *Chem. Rev.* **2008**, *108*, (7), 2721-2736.
- [118]. Desbief, S.; Hergué, N.; Douhéret, O.; Surin, M.; Dubois, P.; Geerts, Y.; Lazzaroni, R.; Leclère, P., Nanoscale investigation of the electrical properties in semiconductor polymer-carbon nanotube hybrid materials. *Nanoscale* **2012**, *4*, (8), 2705-2712.
- [119]. Bhattacharyya, K.; Karmakar, S.; Datta, A., External electric field control: driving the reactivity of metal-free azide-alkyne click reactions. *Phys Chem Chem Phys* **2017**, *19*, (33), 22482-22486.
- [120]. Hsieh, P. L.; Lee, A. T.; Chen, L. J.; Huang, M. H., Germanium Wafers Possessing Facet-Dependent Electrical Conductivity Properties. *Angew Chem Int Ed* **2018**, *57*, (49), 16162-16165.
- [121]. Ke, W. H.; Hsia, C. F.; Chen, Y. J.; Huang, M. H., Synthesis of Ultrasmall Cu₂O Nanocubes and Octahedra with Tunable Sizes for Facet-Dependent Optical Property Examination. *Small* **2016**, *12*, (26), 3530-3534.
- [122]. Liu, G.; Yin, L. C.; Pan, J.; Li, F.; Wen, L.; Zhen, C.; Cheng, H. M., Greatly Enhanced Electronic Conduction and Lithium Storage of Faceted TiO₂ Crystals Supported on Metallic Substrates by Tuning Crystallographic Orientation of TiO₂. *Adv Mater* **2015**, *27*, (23), 3507-3512.
- [123]. Tan, C. S.; Hsu, S. C.; Ke, W. H.; Chen, L. J.; Huang, M. H., Facet-dependent electrical conductivity properties of Cu₂O crystals. *Nano Lett* **2015**, *15*, (3),

2155-2160.

- [124]. Zhu, C.; Chen, D.; Cao, W.; Lai, R.; Pu, C.; Li, J.; Kong, X.; Peng, X., Facet-Dependent On-Surface Reactions in the Growth of CdSe Nanoplatelets. *Angew. Chem. Int. Ed.* **2019**, *58*, (49), 17764-17770.
- [125]. Xiao, J.; Liu, S.; Tian, N.; Zhou, Z.-Y.; Liu, H.-X.; Xu, B.-B.; Sun, S.-G., Synthesis of Convex Hexoctahedral Pt Micro/Nanocrystals with High-Index Facets and Electrochemistry-Mediated Shape Evolution. *J. Am. Chem. Soc.* **2013**, *135*, (50), 18754-18757.
- [126]. Karan, K., Interesting Facets of Surface, Interfacial, and Bulk Characteristics of Perfluorinated Ionomer Films. *Langmuir* **2019**, *35*, (42), 13489-13520.
- [127]. Li, H.; Baldelli, S., Influence of Microcrystallinity on the CO/Pt(poly) Electrode Surface Using Sum Frequency Generation Microscopy Combined With Electrochemistry. *J Phys Chem C* **2021**, *125*, (24), 13560-13571.
- [128]. Chen, M.; Zhao, E.; Yan, Q.; Hu, Z.; Xiao, X.; Chen, D., The Effect of Crystal Face of Fe₂O₃ on the Electrochemical Performance for Lithium-ion Batteries. *Sci. Rep.* **2016**, *6*, (1), 29381.
- [129]. Gileadi, E., *Electrode Kinetics for Chemists, Chemical Engineers and Materials Scientists*. Wiley-VCH Verlag GmbH: New York, 1993, p 597.
- [130]. Bard, A. J.; Faulkner, L. R., *Electrochemical methods : Fundamentals and applications*. John Wiley & Sons: Hoboken, 2007.
- [131]. Bangle, R. E.; Schneider, J.; Conroy, D. T.; Aramburu-Trošelj, B. M.; Meyer, G. J., Kinetic Evidence That the Solvent Barrier for Electron Transfer Is Absent in the Electric Double Layer. *J. Am. Chem. Soc.* **2020**, *142*, (35), 14940–14946.
- [132]. Gonçalves, V. R.; Lian, J.; Gautam, S.; Hagness, D.; Yang, Y.; Tilley, R. D.; Ciampi, S.; Gooding, J. J., Heterojunctions Based on Amorphous Silicon: A Versatile Surface Engineering Strategy To Tune Peak Position of Redox Monolayers on Photoelectrodes. *J. Phys. Chem. C* **2020**, *124*, (1), 836–844.
- [133]. Hurth, C.; Li, C.; Bard, A. J., Direct Probing of Electrical Double Layers by Scanning Electrochemical Potential Microscopy. *J. Phys. Chem. C* **2007**, *111*, (12), 4620–4627.
- [134]. Favaro, M.; Jeong, B.; Ross, P. N.; Yano, J.; Hussain, Z.; Liu, Z.; Crumlin, E. J., Unravelling the electrochemical double layer by direct probing of the solid/liquid interface. *Nat. Commun.* **2016**, *7*, (1), 12695.
- [135]. Quaino, P.; Juarez, F.; Santos, E.; Schmickler, W., Volcano plots in hydrogen electrocatalysis - uses and abuses. *Beilstein J Nanotechnol* **2014**, *5*, 846–854.
- [136]. Roy, N.; Sohn, Y.; Pradhan, D., Synergy of Low-Energy {101} and High-Energy {001} TiO₂ Crystal Facets for Enhanced Photocatalysis. *ACS Nano* **2013**, *7*, (3), 2532–2540.
- [137]. Wallace, S. K.; McKenna, K. P., Facet-Dependent Electron Trapping in TiO₂ Nanocrystals. *J. Phys. Chem. C* **2015**, *119*, (4), 1913–1920.
- [138]. Asif, A. H.; Rafique, N.; Hirani, R. A. K.; Wu, H.; Shi, L.; Zhang, S.; Wang, S.; Yin, Y.; Saunders, M.; Sun, H., Morphology/facet-dependent photo-Fenton-like degradation of pharmaceuticals and personal care products over hematite nanocrystals. *Chem. Eng. J.* **2022**, *432*, 134429.

- [139]. Luo, Y.; Deng, Y.; Guan, L.; Ye, L.; Guo, X.; Luo, A., Effect of grain size and crystal orientation on the corrosion behavior of as-extruded Mg-6Gd-2Y-0.2Zr alloy. *Corros. Sci.* **2020**, *164*, 108338.
- [140]. Toyoda, T.; Yindeesuk, W.; Kamiyama, K.; Hayase, S.; Shen, Q., Adsorption and Electronic Structure of CdSe Quantum Dots on Single Crystal ZnO: A Basic Study of Quantum Dot-Sensitization System. *J. Phys. Chem. C* **2016**, *120*, (30), 16367–16376.
- [141]. Yang, Y.; Zeng, J.; Shu, Y.; Gao, Q., Revealing Facet Effects of Palladium Nanocrystals on Electrochemical Biosensing. *ACS Appl. Mater. Interfaces* **2020**, *12*, (13), 15622–15630.
- [142]. Yu, X.-Y.; Meng, Q.-Q.; Luo, T.; Jia, Y.; Sun, B.; Li, Q.-X.; Liu, J.-H.; Huang, X.-J., Facet-dependent electrochemical properties of Co₃O₄ nanocrystals toward heavy metal ions. *Sci. Rep.* **2013**, *3*, (1), 2886.
- [143]. Mankin, M. N.; Day, R. W.; Gao, R.; No, Y.-S.; Kim, S.-K.; McClelland, A. A.; Bell, D. C.; Park, H.-G.; Lieber, C. M., Facet-Selective Epitaxy of Compound Semiconductors on Faceted Silicon Nanowires. *Nano Lett.* **2015**, *15*, (7), 4776–4782.
- [144]. Tan, C.-S.; Zhao, Y.; Guo, R.-H.; Chuang, W.-T.; Chen, L.-J.; Huang, M. H., Facet-Dependent Surface Trap States and Carrier Lifetimes of Silicon. *Nano Lett.* **2020**, *20*, (3), 1952–1958.
- [145]. Kuo, C. H.; Yang, Y. C.; Gwo, S.; Huang, M. H., Facet-dependent and au nanocrystal-enhanced electrical and photocatalytic properties of Au-Cu₂O core-shell heterostructures. *J. Am. Chem. Soc.* **2011**, *133*, (4), 1052–1057.
- [146]. Tachikawa, T.; Yamashita, S.; Majima, T., Evidence for crystal-face-dependent TiO₂ photocatalysis from single-molecule imaging and kinetic analysis. *J. Am. Chem. Soc.* **2011**, *133*, (18), 7197–7204.
- [147]. Judd, C. J.; Haddow, S. L.; Champness, N. R.; Saywell, A., Ullmann Coupling Reactions on Ag(111) and Ag(110); Substrate Influence on the Formation of Covalently Coupled Products and Intermediate Metal-Organic Structures. *Sci. Rep.* **2017**, *7*, (1), 14541.
- [148]. Torquato, L. D. M.; Pastrian, F. A. C.; Perini, J. A. L.; Irikura, K.; de L. Batista, A. P.; de Oliveira-Filho, A. G. S.; Córdoba de Torresi, S. I.; Zanoni, M. V. B., Relation between the nature of the surface facets and the reactivity of Cu₂O nanostructures anchored on TiO₂NT@PDA electrodes in the photoelectrocatalytic conversion of CO₂ to methanol. *Appl. Catal., B* **2020**, *261*, 118221.
- [149]. Ball, P., Silicon still supreme. *Nat. Mater.* **2005**, *4*, (2), 119–119.
- [150]. Pharr, M.; Zhao, K.; Wang, X.; Suo, Z.; Vlassak, J. J., Kinetics of Initial Lithiation of Crystalline Silicon Electrodes of Lithium-Ion Batteries. *Nano Lett.* **2012**, *12*, (9), 5039–5047.
- [151]. Zhang, S.; Ferrie, S.; Lyu, X.; Xia, Y.; Darwish, N.; Wang, Z.; Ciampi, S., Absence of a Relationship between Surface Conductivity and Electrochemical Rates: Redox-Active Monolayers on Si(211), Si(111), and Si(110). *J. Phys. Chem. C* **2021**, *125*, (33), 18197–18203.

- [152]. Vogel, Y. B.; Zhang, J.; Darwish, N.; Ciampi, S., Switching of Current Rectification Ratios within a Single Nanocrystal by Facet-Resolved Electrical Wiring. *Acs Nano* **2018**, *12*, (8), 8071–8080.
- [153]. Tan, C.-S.; Chen, L.-J.; Huang, M. H., Large Facet-Specific Built-in Potential Differences Affecting Trap State Densities and Carrier Lifetimes of GaAs Wafers. *J. Phys. Chem. C* **2020**, *124*, (39), 21577–21582.
- [154]. Liu, H.; Ma, X.; Chen, Z.; Li, Q.; Lin, Z.; Liu, H.; Zhao, L.; Chu, S., Controllable Synthesis of [11–2–2] Faceted InN Nanopyramids on ZnO for Photoelectrochemical Water Splitting. *Small* **2018**, *14*, (17), 1703623.
- [155]. Chen, Y.-J.; Chiang, Y.-W.; Huang, M. H., Synthesis of Diverse Ag₂O Crystals and Their Facet-Dependent Photocatalytic Activity Examination. *ACS Appl. Mater. Interfaces* **2016**, *8*, (30), 19672–19679.
- [156]. Allongue, P.; Henry de Villeneuve, C.; Morin, S.; Boukherroub, R.; Wayner, D. D. M., The preparation of flat H–Si(111) surfaces in 40% NH₄F revisited. *Electrochim. Acta* **2000**, *45*, (28), 4591–4598.
- [157]. Wu, Y. F.; Kashi, M. B.; Yang, Y.; Goncales, V. R.; Ciampi, S.; Tilley, R. D.; Gooding, J. J., Light-activated electrochemistry on alkyne-terminated Si(100) surfaces towards solution-based redox probes. *Electrochim. Acta* **2016**, *213*, 540–546.
- [158]. Zhang, L.; Vogel, Y. B.; Noble, B. B.; Goncales, V. R.; Darwish, N.; Brun, A. L.; Gooding, J. J.; Wallace, G. G.; Coote, M. L.; Ciampi, S., TEMPO Monolayers on Si(100) Electrodes: Electrostatic Effects by the Electrolyte and Semiconductor Space-Charge on the Electroactivity of a Persistent Radical. *J. Am. Chem. Soc.* **2016**, *138*, (30), 9611–9619.
- [159]. Vogel, Y. B.; Gonçales, V. R.; Gooding, J. J.; Ciampi, S., Electrochemical Microscopy Based on Spatial Light Modulators: A Projection System to Spatially Address Electrochemical Reactions at Semiconductors. *J. Electrochem. Soc.* **2017**, *165*, (4), H3085–H3092.
- [160]. Liu, D.-Q.; Chen, C.-H.; Perry, D.; West, G.; Cobb, S. J.; Macpherson, J. V.; Unwin, P. R., Facet-Resolved Electrochemistry of Polycrystalline Boron-Doped Diamond Electrodes: Microscopic Factors Determining the Solvent Window in Aqueous Potassium Chloride Solutions. *Chemelectrochem* **2018**, *5*, (20), 3028–3035.
- [161]. Choi, M.; Siepser, N. P.; Jeong, S.; Wang, Y.; Jagdale, G.; Ye, X. C.; Baker, L. A., Probing single-particle electrocatalytic activity at facet-controlled gold nanocrystals. *Nano Lett.* **2020**, *20*, (2), 1233–1239.
- [162]. Huang, L.; Zhang, X.; Wang, Q.; Han, Y.; Fang, Y.; Dong, S., Shape-Control of Pt-Ru Nanocrystals: Tuning Surface Structure for Enhanced Electrocatalytic Methanol Oxidation. *J. Am. Chem. Soc.* **2018**, *140*, (3), 1142–1147.
- [163]. Li, B.; Yan, Y.; Shen, C.; Yu, Y.; Wang, Q.; Liu, M., Extraordinary lithium ion storage capability achieved by SnO₂ nanocrystals with exposed {221} facets. *Nanoscale* **2018**, *10*, (34), 16217–16230.
- [164]. Anwer, S.; Bharath, G.; Iqbal, S.; Qian, H.; Masood, T.; Liao, K.; Cantwell, W. J.; Zhang, J.; Zheng, L., Synthesis of edge-site selectively deposited Au

- nanocrystals on TiO₂ nanosheets: An efficient heterogeneous catalyst with enhanced visible-light photoactivity. *Electrochim. Acta* **2018**, *283*, 1095–1104.
- [165]. Vogel, Y. B.; Gonçalves, V. R.; Al-Obaidi, L.; Gooding, J. J.; Darwish, N.; Ciampi, S., Nanocrystal Inks: Photoelectrochemical Printing of Cu₂O Nanocrystals on Silicon with 2D Control on Polyhedral Shapes. *Adv. Funct. Mater.* **2018**, *28*, (51), 1804791.
- [166]. Ferreira, P. J.; Shao-Horn, Y., Formation Mechanism of Pt Single-Crystal Nanoparticles in Proton Exchange Membrane Fuel Cells. *Electrochem. Solid-State Lett.* **2007**, *10*, (3), B60-B63.
- [167]. Su, S.; Siretanu, I.; van den Ende, D.; Mei, B.; Mul, G.; Mugele, F., Facet-Dependent Surface Charge and Hydration of Semiconducting Nanoparticles at Variable pH. *Adv. Mater.* **2021**, *33*, (52), 2106229.
- [168]. Łukomska, A.; Sobkowski, J., Potential of zero charge of monocrystalline copper electrodes in perchlorate solutions. *J. Electroanal. Chem.* **2004**, *567*, (1), 95–102.
- [169]. Lazić, P.; Persson, B. N. J., Surface-Roughness-Induced Electric-Field Enhancement and Triboluminescence. *EPL* **2010**, *91*, (4), 46003–46007.
- [170]. Zhang, X. G., Mechanism of pore formation on n-type silicon. *J. Electrochem. Soc.* **1991**, *138*, (12), 3750–3756.
- [171]. Zhang, X. G.; Collins, S. D.; Smith, R. L., Porous silicon formation and electropolishing of silicon by anodic polarization in HF solution. *J. Electrochem. Soc.* **1989**, *136*, (5), 1561–1565.
- [172]. Carroll, L. R.; Martinez-Gazoni, R. F.; Gaston, N.; Reeves, R. J.; Downard, A. J.; Allen, M. W., Bidirectional Control of the Band Bending at the (201) and (010) Surfaces of β-Ga₂O₃ Using Aryldiazonium Ion and Phosphonic Acid Grafting. *ACS Appl. Electron. Mater.* **2021**, *3*, (12), 5608–5620.
- [173]. Vogel, Y. B.; Evans, C.; Belotti, M.; Xu, L.; Russell, I.; Yu, L.-J.; Fung, A.; Hill, N.; Darwish, N.; Gonçalves, V.; Coote, M. L.; Iyer, S.; Ciampi, S., The Corona of a Surface Bubble Promotes Electrochemical Reactions. *Nat. Commun.* **2020**, *11*, 6323.
- [174]. Hou, C.; Gazoni, R. M.; Reeves, R. J.; Allen, M. W., Direct comparison of plain and oxidized metal Schottky contacts on β-Ga₂O₃. *Appl. Phys. Lett.* **2019**, *114*, (3), 033502.
- [175]. Hu, H. X.; Chang, B.; Sun, X. C.; Huo, Q.; Zhang, B. G.; Li, Y. L.; Shao, Y. L.; Zhang, L.; Wu, Y. Z.; Hao, X. P., Intrinsic Properties of Macroscopically Tuned Gallium Nitride Single-Crystalline Facets for Electrocatalytic Hydrogen Evolution. *Chem. Eur. J.* **2019**, *25*, (44), 10420–10426.
- [176]. Owens-Baird, B.; Sousa, J. P. S.; Ziouani, Y.; Petrovykh, D. Y.; Zarkevich, N.; Johnson, D. D.; Kolen'ko, Y. V.; Kovnir, K., Crystallographic facet selective HER catalysis: exemplified in FeP and NiP₂ single crystals. *Chem. Sci.* **2020**, *11*, (19), 5007–5016.
- [177]. Vogel, Y. B.; Darwish, N.; Ciampi, S., Spatiotemporal Control of Electrochemiluminescence Guided by a Visible Light Stimulus. *Cell. Rep. Phys. Sci.* **2020**, *1*, (7), 100107.

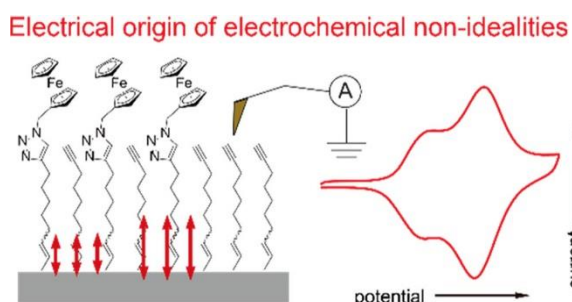
- [178]. Rapino, S.; Treossi, E.; Palermo, V.; Marcaccio, M.; Paolucci, F.; Zerbetto, F., Playing peekaboo with graphene oxide: a scanning electrochemical microscopy investigation. *Chem. Commun.* **2014**, *50*, (86), 13117–13120.
- [179]. Fiorani, A.; Han, D.; Jiang, D.; Fang, D.; Paolucci, F.; Sojic, N.; Valenti, G., Spatially resolved electrochemiluminescence through a chemical lens. *Chem. Sci.* **2020**, *11*, (38), 10496–10500.
- [180]. Zhao, Y.; Bouffier, L.; Xu, G.; Loget, G.; Sojic, N., Electrochemiluminescence with semiconductor (nano)materials. *Chem. Sci.* **2022**, *13*, (9), 2528–2550.
- [181]. Verlato, E.; Barison, S.; Einaga, Y.; Fasolin, S.; Musiani, M.; Nasi, L.; Natsui, K.; Paolucci, F.; Valenti, G., CO₂ reduction to formic acid at low overpotential on BDD electrodes modified with nanostructured CeO₂. *J. Mater. Chem. A* **2019**, *7*, (30), 17896–17905.
- [182]. Andronescu, C.; Masa, J.; Tilley, R. D.; Gooding, J. J.; Schuhmann, W., Electrocatalysis in confined space. *Curr. Opin. Electrochem.* **2021**, *25*, 100644.

Every reasonable effort has been made to acknowledge the owners of copyright material. I would be pleased to hear from any copyright owner who has been omitted or incorrectly acknowledged.

Chapter 2. Heterogeneous photocurrents explain non-ideal cyclic voltammograms of redox monolayers on silicon photoanodes

The content of this chapter is adapted from the paper published by the American Chemical Society in *Langmuir* 2022, 38, 743–750, titled “Non-Ideal cyclic voltammetry of redox monolayers on silicon electrodes: Peak splitting is caused by heterogeneous photocurrents and not by molecular disorder”.

The paper is modified with minor changes in order to fit the general layout of this dissertation. Copyright permissions for the use of this published material in the doctoral thesis is found in the appendix section (Appendix A).



Chapter 1 has described how, over the past few years, research on redox active SAMs has demonstrated and consolidated their fundamental and applied scopes. Chapter 1 has explained the analytical power of voltammetry in the study of charge transfer reactions. For mainstream diffusionless redox monolayer systems, such as thiolate-based gold SAMs, disordered domains often lead to multiple CV waves. With almost no exception the appearance of peak multiplicities is taken as diagnostic sign of disorder in the molecular adsorbate. The experiments and results of this chapter demonstrate that contrary to simpler metallic systems (such as gold) in illuminated photoconductors peak multiplicity is more likely to be the manifestation generated of heterogeneous photocurrents across the interface.

2.1 Abstract

Over the last three decades, research on redox-active monolayers has consolidated their importance as advanced functional material. For widespread monolayer systems, such as alkanethiols on gold, non-ideal multiple peaks in cyclic voltammetry are generally taken as indication of heterogeneous intermolecular interactions – namely disorder in the monolayer. Our findings show that, contrary to metals, peak multiplicity in silicon photoelectrodes is not diagnostic of heterogeneous intermolecular microenvironments but is more likely caused by photocurrent being heterogeneous across the monolayer. This work is an important step to understand the cause of electrochemical non-idealities in semiconductor electrodes, so that these can be prevented and the redox behavior of molecular monolayers, as photocatalytic systems, can be optimized.

2.2 Introduction

Chemical reactions that are coupled to charge transfer events – the realm of redox chemistry – have wide-ranging ramifications across nature and are broadly exploited in technology.^[1, 2] The physical and chemical properties of the interface where a redox reaction takes place govern both its thermodynamics and kinetics.^[3-5] Gaining control of the molecular features of electrode surfaces has therefore been pivotal in advancing our understanding of heterogeneous redox reactivity.^[6] Prompted by the 1980 work of Sagiv on irreversible adsorption reactions of organic molecules on solids,^[7] molecular self-assembly on solid electrodes remains one of the principal laboratory resources in the study of redox chemistry.^[8, 9] Redox reactivity can for instance, be controlled by i) engineering changes to the density of surface redox molecules, hence to intermolecular interactions,^[10-13] interfacial bonding^[14] and surface conductivity,^[15] ii) by controlling monolayer order,^[16] and iii) by adjusting ion-pairing between redox entity and electrolyte ions.^[17] Research on the latter – the engineering of ion-pair interactions – such as electrostatic interactions between surface ferrocenium molecules and soluble anions (e.g. $\text{Fc} + \text{X}^- \rightleftharpoons \text{Fc}^+-\text{X}^- + \text{e}^-$),^[4, 17-20] is at the centre of the emerging electrochemistry sub-field of “electrolyte engineering”. These interactions can be

probed by dynamic electrochemical measurements – primarily cyclic voltammetry (CV)^[21] – during the process of studying kinetics and thermodynamics of an electrode reaction.^[22-25] Through a CV measurement the magnitude and degree of such interactions are often gauged by an analysis of the full-width-at-half-maximum (fwhm hereafter) of oxidation and reduction current peaks, of peak positions, and of peak-to-peak separation.^[11, 16, 19] The common appearance of multiple waves is generally taken as indication of these interactions being highly heterogeneous due to different causes, being disorder one of the most frequent.

Herein we demonstrate that unlike for metallic electrodes (Figure 2.1a) in the technologically relevant case of semiconductor photoelectrodes, it is not advisable to make inferences on the heterogeneity of the redox environment, such as disorder and local differences in Fc^+-X^- vs $\text{Fc}-\text{Fc}$ interactions,^[17] based solely on the appearance of multiple CV waves. We show that, in semiconductors the appearance of this non-ideal CV feature – multiple waves for a one-electron redox reaction – does not require molecular disorder across the monolayer, but is more likely caused by heterogeneous photocurrent across the surface (Figures 2.1b and 2.1c). This is important because while most of the research on interfacial redox reactivity still relies on alkanethiol chemistry and gold substrates,^[26] the field is rapidly expanding towards silicon electrodes.^[9] Silicon remains the technologically most relevant material,^[27-31] and silicon surfaces that are functionalized with organic monolayers have applications ranging from sensing,^[32-36] chemical catalysis,^[37] microscopy,^[38, 39] molecular electronics,^[40-42] and data storage.^[9, 43, 44]

All silicon electrodes used in this study were protected against major oxidation by an hydrosilylation procedure,^[45] through which hydrogen terminated silicon was reacted with a symmetrical α,ω -diyne (1,8-nonadiyne **1**, Figure 2.1d).^[46] The hydrosilylation of diyne **1** with an hydrogen-terminated silicon surface results in an exceedingly stable alkenyl linkage ($\text{Si}-\text{C}=\text{C}-$)^[47] in an ordered monolayer (**M-1**).^[48] The distal end of this monolayer is an acetylene function, which permits the attachment of an azide-tagged

ferrocene molecule (**2**, Figure 2.1d) via a copper-(I) catalyzed alkyne–azide cycloaddition (CuAAC) reaction.^[49, 50] The electrode doping type and level (p- and n-type, highly and lowly doped, HD and LD hereafter), and the level of substrate illumination (or lack of it) during the CV measurements were adjusted so to demonstrate that multiple oxidation and reduction waves for surface confined redox units are not linked to poor solvation and/or monolayer disorder, but instead caused by heterogeneity in the substrate photocurrent.

2.3 Experimental section

2.3.1 Chemicals

Unless specified otherwise, all chemicals were of analytical grade and used as received. 1,8-Nonadiyne (**1**, Figure 2.1), 11-(ferrocenyl)undecanethiol (95%), H₂O₂ (aqueous hydrogen peroxide, 30% w/w), H₂SO₄ (sulfuric acid, 95–97%), NH₄F (aqueous ammonium fluoride, 40%), (NH₄)₂SO₃·H₂O (ammonium sulfite monohydrate, 92%), HCl (hydrochloric acid, 35–37%) were purchased from Sigma-Aldrich and used for cleaning, etching, and modifying silicon wafers. Redistilled dichloromethane (DCM), propan-2-ol and ethanol were utilized for substrate cleaning and monolayer-forming procedures. Milli-Q water (>18 MΩ cm) was used for substrate cleaning and modification and to prepare electrolytic solutions. Azidomethylferrocene (**2**, Figure 2.1d) was synthesized following a previously reported procedure.^[46]

2.3.2 Silicon and gold crystals

Silicon wafers were of prime grade, single-side polished, prepared through the Czochralski process and purchased from Siltronic, S.A.S. (Archamps, France). Highly doped n-type Si(111), referred to as HD, was $\langle 111 \rangle \pm 0.5^\circ$ phosphorous-doped, with a thickness of $500 \pm 25 \mu\text{m}$ and with a resistivity of 0.007–0.013 Ω cm. Lowly doped

Si(111), referred to as LD, was $\langle 111 \rangle \pm 0.5^\circ$, 7–13 Ω cm, phosphorous-doped, 500 ± 25 μm . Highly doped p-type Si(111) was $\langle 111 \rangle \pm 0.5^\circ$, boron-doped, 500 ± 25 μm . Lowly doped n-type Si(100) was $\langle 100 \rangle \pm 0.5^\circ$, phosphorous-doped, 500 ± 25 μm and 8–12 Ω cm. Gold single crystal electrodes (Au(111), 99.999%) were polished on one side to 1 μm or better, flame-annealed prior to use, and purchased from Goodfellow (Huntingdon, England).

2.3.3 Silicon surface modification

Before any chemical modification, samples were cut into squares of 1×1 cm, rinsed with DCM, propan-2-ol, and water. Samples were then immersed for at least 30 min in hot piranha solution [100 °C, a 3:1 mixture (v/v) of concentrated sulphuric acid (95–97%) and hydrogen peroxide (30%)]. Samples were then rinsed with water and immediately transferred to a degassed (by means of bubbling argon gas for more than 30 minutes) aqueous 40% solution of NH_4F . This etching solution contained a trace amount of ammonium sulphite (ca. 2 mg) added as oxygen scavenger. The silicon etching in the NH_4F solution for 9 min, rinsed with copious Milli-Q water and DCM and then immediately reacted with 1,8-nonadiyne (which is degassed with nitrogen for 30min). The liquid sample of α , ω -diyne (ca. 50 μl) was dropped on the hydrogen-terminated silicon surface and then irradiated under UV light for 2 hours under nitrogen atmosphere ($\lambda = 312$ nm, purchased from Vilber, VL-215.M, nominal power output of 30W, set approximately 20 cm away from the silicon sample). The silicon substrates modified with monolayers of 1,8-nonadiyne were then rinsed three times with propan-2-ol and kept for 12 h in a reaction vial under DCM before the CuAAC surface modification step. The CuAAC reaction was performed as follows: to a reaction vial containing the alkyne-terminated substrate were added 5 mL of azidomethylferrocene solution (**2**, 0.5 mM in in a propan-2-ol and water mixture, 1:1, v/v), sodium ascorbate (100 mol % relative to the azide) and then copper (II) sulphate pentahydrate (20 mol % relative to the azide). The reaction was carried out at room temperature in dark and

quenched by decanting the reaction solution after 40 min (unless specified otherwise). The electrodes tethered with ferrocene molecules (**M-2**, Figure 2.1d) were immediately rinsed with copious amounts of propan-2-ol, water, 0.5 M aqueous hydrochloric acid, water, propan-2-ol, dichloromethane, blown dry under nitrogen and kept under DCM before analysis.

2.3.4 Gold surface modification

Au(111) crystals were annealed in a butane gas flame to yellow color and then quenched in DCM. The crystals were then transferred to an ethanolic 1.0 mM solution of 11-(ferrocenyl)undecanethiol, and rested in this monolayer-forming solution for 24 h. The modified electrodes were then rinsed with copious ethanol and immediately analyzed.

2.3.5 Electrochemical measurements

Cyclic voltammetry (CV) experiments were carried out with a CHI650D potentiostat (CH Instruments, Austin, Texas) using a three-electrode and single-compartment polytetrafluoroethylene custom cell. The modified silicon substrate (**M-2**) or the Au(111) crystal coated with a self-assembled monolayer of 11-(ferrocenyl)undecanethiol served as the working electrode, a platinum mesh as the counter electrode, and a Ag/AgCl (3.0 M NaCl) electrode as the reference electrode. A circular Viton gasket defined the geometric area of the working electrode to be 0.28 cm², and Ohmic contact between the back of the silicon sample and a copper plate was obtained by gently scribing the back of the electrode with emery paper before applying on it a small amount of the gallium–indium eutectic. Unless specified otherwise, the electrolyte was aqueous 1.0 M perchloric acid (HClO₄). All measurements were carried out in air at room temperature (22 ± 2°C) and under either dark or red light. The red light was a collimated deep red LED (660 nm, nominal power output 1050 mW,

Thorlabs part M660L4 coupled to a SM1P25-A collimator adapter) illuminating the silicon electrode through the electrolyte. The collimator–sample distance was approximately 7 cm. The LED current was adjusted in six levels (LEDD1B, Thorlabs) to yield the following light intensities measured at the silicon surface: level 1, 1.0 mW cm⁻²; level 2, 2.9 mW cm⁻²; level 3, 4.7 mW cm⁻²; level 4, 11.1 mW cm⁻²; level 5, 24.1 mW cm⁻²; level 6, 29.9 mW cm⁻² (the illuminance was measured with a light meter from Amprobe, IC-LM-200 and the lx output was subsequently converted to mW cm⁻² assuming 1 lx = 0.0024 mW cm⁻²). Simulations of the voltammograms were performed in Wolfram Mathematica (Version 11) using a previously reported model.^[23] All reported potentials are relative to the reference electrode. Surface coverages (Γ) of ferrocene molecules on silicon substrate were reported in mol cm⁻² and calculated from the faradaic charge taken as the background-subtracted integrated current from the anodic scan of the voltammograms.^[51, 52] Electrochemical impedance spectroscopy (EIS) data were collected between 10⁵ Hz and 10⁻¹ Hz, at an applied working electrode DC potential, E_{dc} , equal to -0.5 V and with an AC perturbation of 15 mV.

2.3.6. Atomic force microscopy

Current–potential curves (I–Vs) for the monolayer-modified silicon samples were recorded using a ParkNX10 atomic force microscope (AFM) (Park Systems Corporation, Suwon, Korea), operated in conductive mode. The AFM tips were made of solid platinum (12 Pt300B, Rocky Mountain Nanotechnology, Holladay, UT) and had a nominal resonance frequency of 9 kHz and a nominal spring constant of 0.8 N/m. All the AFM data were analyzed with image processing software XEI 4.3.4 developed by Park Systems Corporation. The I–V traces were sampled at 100 separate locations. When comparing leakage current differences, we neglected traces that reached current saturation.

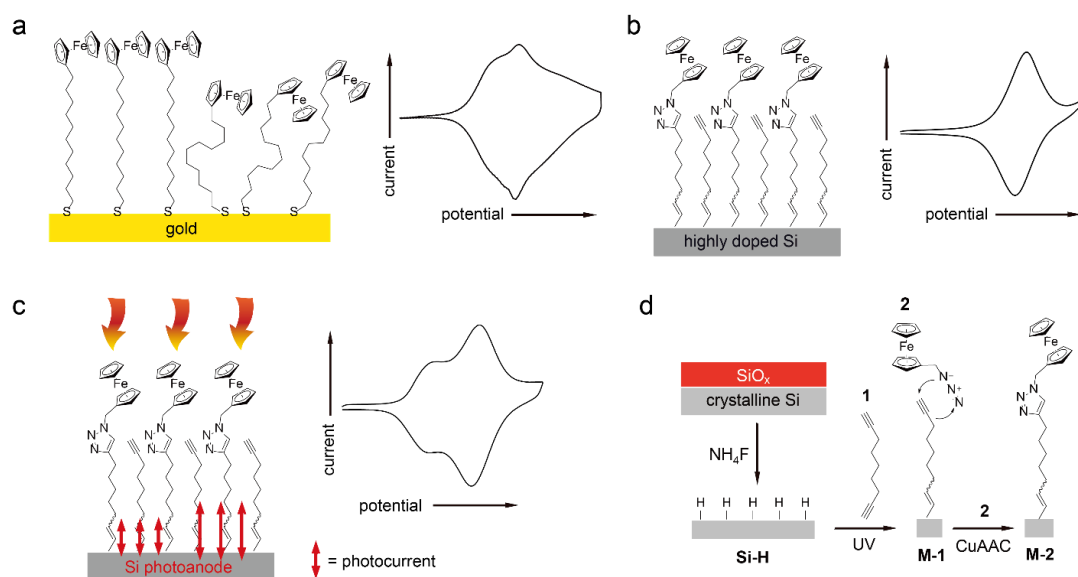


Figure 2.1. a) Schematic representation of a heterogeneous (ordered/disordered regions) monolayer-coated gold electrode, and (right) a typical cyclic voltammogram recorded on a single-crystal gold electrode modified with a monolayer of 11-ferrocenyl-1-undecanethiol (Au(111); 100 mV/s, 1.0 M HClO₄). b) Schematic depiction of a monolayer-coated silicon electrode, and near-ideal cyclic voltammetry (right) acquired on a highly doped silicon electrode coated with a ferrocene monolayer (0.007–0.013 Ω cm, p-type, Si(111); 100 mV/s, 1.0 M HClO₄). c) Schematic depiction of heterogeneous photocurrents across a silicon photoanode (1.0 mW cm⁻²), and experimental evidence of peak-splitting in cyclic voltammetry (right) using a lowly doped silicon photocathode coated with a ferrocene monolayer (8–12 Ω cm, n-type, Si(111); 100 mV/s, 1.0 M HClO₄). d) Chemical strategy used for the passivation and derivatization of the hydrogen terminated silicon surface. The UV-assisted hydrosilylation of 1 on Si–H generates an alkyne-terminated surface (M-1), which is subsequently reacted with azidomethylferrocene (2) through a CuAAC reaction, yielding a redox-active monolayer (M-2).

2.3.7. Water contact angle

Measurements of the sessile water contact angle were performed on a CAM 101 optical contact angle meter (KSV Instruments Ltd., Finland). Measurements were conducted on three independently prepared and analyzed samples of each doping level, with four separate spots measured on each sample. The reported value is the arithmetic average

of the 12 measurements. Data were analyzed using the KSV CAM Pendant Drop Surface Tension software (3.81).

2.4. Results and discussion

The appearance of multiple CV waves when single-crystal metallic electrodes are derivatized with redox monolayers is a relatively common observation.^[17] This non-ideal electrochemical behavior is caused by disorder and heterogeneity of the redox environment,^[53] but as expected when dealing with a metal, these are not linked to any photoeffect (Figure A1, Appendix). Because peak multiplicity in gold manifests generally only for high surface densities of the redox molecule under study,^[20, 24] before exploring the conditions necessary for the systematic appearance of multiple redox waves in silicon, we first tested to which degree the surface coverage of ferrocene units is reproducible as well as independent on the silicon crystal orientation and doping. As shown for example in Figure A2 (Appendix A), the faradaic charge obtained by integrating CV curves for **M-2** samples prepared on either Si(111) or Si(100) was not affected by doping level and type [$(1.99 \pm 0.84) \times 10^{-10}$ mol cm⁻², Si(111), LD, n-type;

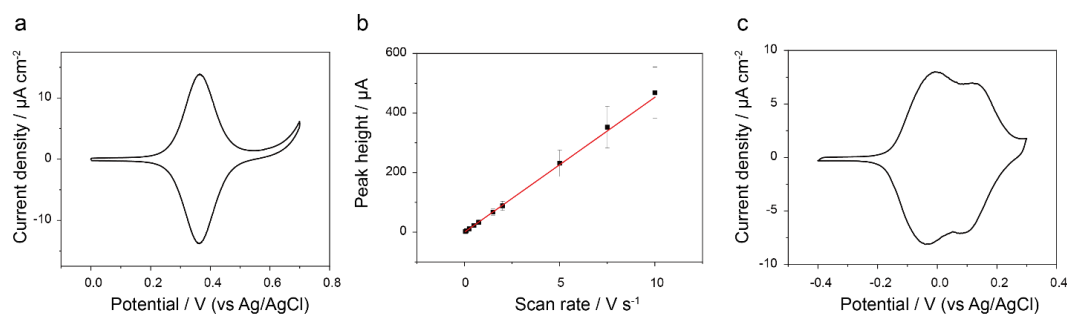


Figure 2.2. Doping level and type and ideality of the redox response. a) Representative and close-to-ideal cyclic voltammogram (CV) recorded for a **M-2** sample prepared on HD, p-type Si(111) (100 mV/s, 1.0 M HClO₄, dark, $\Gamma = 1.64 \times 10^{-10}$ mol cm⁻²). b) Plot of current peak values (anodic waves) vs voltage scan rate (the error bars indicate the 95% confidence interval of the mean). c) A representative CV for a **M-2** monolayer grafted on a Si(111), n-type, LD photoanode, showing an evident non-ideal peak splitting (100 mV/s, 1.0 M HClO₄, electrode illuminated at a light intensity of 1.0 mW m⁻², $\Gamma = 1.95 \times 10^{-10}$ mol cm⁻²).

$(1.44 \pm 0.23) \times 10^{-10}$ mol cm⁻² Si(100), LD, n-type; $(1.94 \pm 0.26) \times 10^{-10}$ mol cm⁻², Si(111), HD, p-type].

Furthermore, as can be seen from the data in Figure 2.2a, the current response from **M-2** samples upon cyclic bias ramping is of very good quality. Voltametric data presented in Figure 2.2a are obtained on p-type HD silicon operating in accumulation, so to prevent space-charge effects.^[54] The CV waves had a fwhm of 115 ± 3 mV, and the presence and absence of illumination had no effect on the peak broadness (Figure A3, Appendix A). The ideal fwhm expected from the Langmuir isotherm of a Nernstian process should be 90.6 mV, hence our experimental values are larger than ideal, which is not unusual,^[55] and often explained as repulsive interactions between the electroactive species.^[56] The peak current varied linearly with the voltage sweep rate, which confirms a surface-confined process (Figure 2.2b and Figure A4, Appendix A). The exact same monolayer system (**M-2**) when prepared on n-type silicon of low doping [LD, Si(111)], showed however a far from ideal voltammetry (Figure 2.2c). As indicated above, surface coverages did not vary between substrates of different doping level and type, hence the **M-2** samples of Figure 2.2c are likely to have the same level of monolayer packing and order as the more ideal samples of Figure 2.2a. The only difference is that the system of Figure 2.2c is a photonanode. (LD, and n-type), requiring biasing of the silicon electrode–electrolyte interface into depletion to trigger the redox chemistry of ferrocene.^[22, 56, 57] This is because the ferrocene apparent formal potential lies anodic of the electrode’s flat band potential,^[54] and therefore electrode illumination is required to overcome the substantial kinetic barrier (Figure A5, Appendix A). These photoanodes showed, as expected, a “contra-thermodynamic” shift characteristic of a process mediated by valence-band holes (Figure A6, Appendix A), but more interestingly they can display a very pronounced voltametric peak splitting (Figure 2.2c) at low light intensity. As stressed above, this double-peak feature, absent in HD p-type (Figure 2.2a), is unlikely related or caused by monolayer disorder, or by heterogeneous ion-pairing. As a further proof of this last remark, the two peaks progressively merged into a single band upon a simple increase in light intensity (Figure

2.3a) despite illumination alone having no effect on the degree of monolayer order (Figure A1 Appendix A). Such an effect is partially masked at larger scan rates (Figure A7, Appendix A). To further reinforce on the order of the monolayer, electrochemical impedance data, acquired at an E_{dc} offset sufficiently different from the ferrocene apparent formal potential, showed that at low frequencies the phase angle approaches -90° , indicating that all samples are relatively free of imperfections (Figure A8, Appendix A). We also remark that the appearance of the double-peak feature is still evident in samples of lower coverage (Figure A9, Appendix A), where lateral interactions become even less likely. Furthermore, no significant difference in the water contact angle was found between **M-2** samples prepared on either n-type or p-type substrates ($68^\circ \pm 4^\circ$, LD n-type; $67^\circ \pm 2^\circ$, HD p-type), suggesting substrate doping is unlikely to have an effect on the monolayer structure.

As evident from the data in Figure 2.3a, two well resolved waves separated by approximately 190 mV at low light intensity (1.0 mW cm^{-2}), progressively merge into a single broad wave as the light intensity was increased (up to $\sim 24.1 \text{ mW m}^{-2}$). Peak deconvolutions shown in Figure A10 (Appendix A) indicate that the faradaic charge of the individual contributions did not vary with illumination, while peak positions shifted progressively cathodic with increased irradiation. The origin of this shift is well known, and is the result of a logarithmic dependence of the electrode open circuit potential (E_{OCP}) on dark leakage current and photocurrent.^[56] The $I-E$ relationship for a cyclic voltammetry experiment, when interactions of the attached redox species (in the oxidized, O, and reduced, R, forms) are not negligible, was developed by Laviron assuming a Frumkin isotherm.^[58, 59] The Frumkin self-interaction parameter G was adjusted in our model (Figure 2.3b),^[51, 59] as changes to G account for the imbalance in the electrostatic push/pull, forcing the voltammetric wave to broaden or narrow when the activities of the reduced and oxidized species do not follow their surface concentrations.^[23] Larger repulsive interactions (a more negative G , see Figure 2.3b) are probably experienced by surface ferrocene units sensing a smaller photocurrent (more anodic E_{OCP} , vide infra). The G parameter is purely phenomenological and no

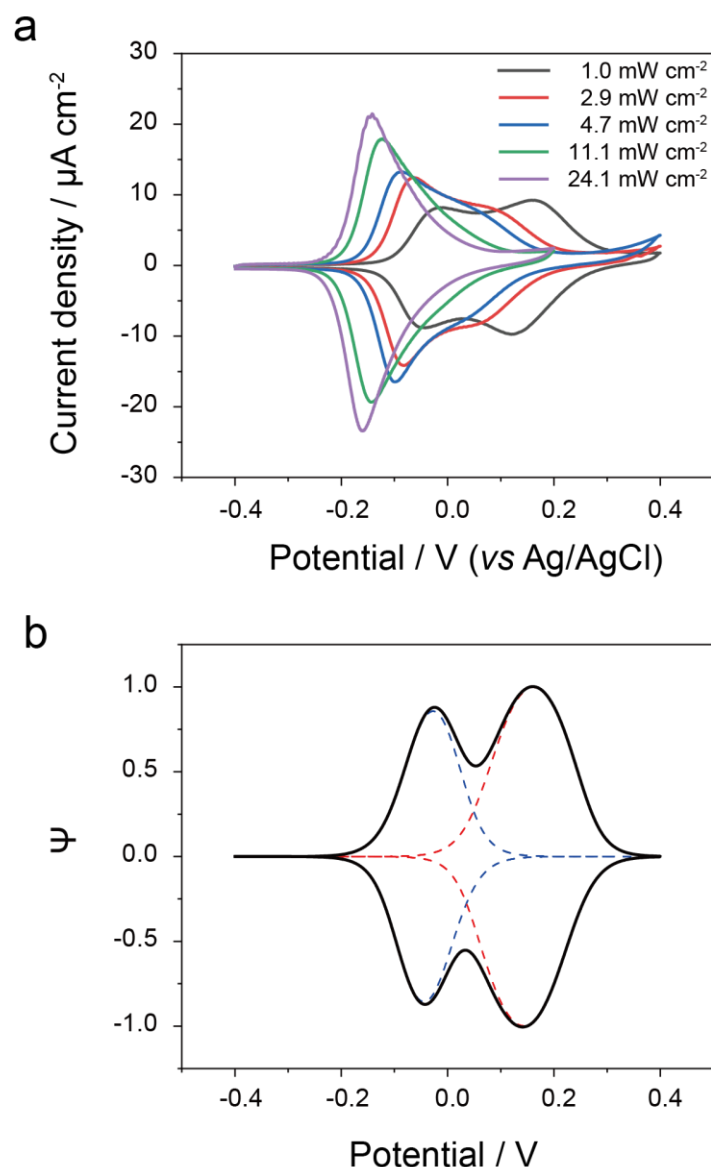


Figure 2.3. Peak multiplicity on Si(111) photoanodes: experiments and simulations. a) Progressive disappearance with increasing light intensity of the peak multiplicity characteristic of voltammograms recorded on silicon photoanodes. The electrodes are LD, n-type Si(111) crystals modified with a **M-2** monolayer. The level of electrode illumination is specified by labels to the CV traces. The electrolyte was 1.0 M HClO₄, and the scan rate 0.1 V/s. b) Simulation of the CV trace recorded at the lowest light intensity, demonstrating that the key feature of the experimental data, a 188 mV peak-to-peak separation, can be accounted for as surface domains with a 1,500 fold difference in photocurrent (larger photocurrent for the blue dashed trace). The self-interaction parameter, G , necessary to reproduce the experimental fwhm, is negative, indicating repulsive molecular interactions for ferrocenes in both domains (-1.4 , red trace; -0.6 , blue trace). Best fit parameters are 10 s^{-1} for the electron transfer rate constant, $1 \text{ } \mu\text{A}$ for the dark leakage current, unity for the diode quality factor, and 0.5 for α .

attempt is made to describe the nature of these interactions. Whether these interactions are a cause, an effect, or not linked to the magnitude of the surface photocurrent is at present unclear.

We therefore hypothesize that the two CV bands clearly visible at low levels of illumination on Si(111) photoanodes relate to a heterogeneous electrode E_{OCP} , most likely the result of differences in local photocurrents (Figure 2.3b). Shifts in the experimental “macroscopic” E_{OCP} with changes to the light intensity are well documented for both photoanodes and photocathodes,^[23, 57] but the possibility of a local heterogeneity of this shift within a given sample is generally neglected. Simulations where the photocurrent was varied by a factor close to 1,500 could reproduce the experimental peak-to-peak separation (Figure 2.3b). Surface defects introducing energy levels in the band gap are a possible cause of heterogeneous “wet” photocurrents, and such defects should manifest as a degree of heterogeneity in “dry” electrical leakage currents, that is, large local differences in the dark leakage current across the sample should parallel the appearance of CV peak multiplicity. On a photoanode, an increase in dark leakage (not necessarily an electrochemical process) causes a progressive anodic shift of E_{OCP} ^[23] (Figure A11, Appendix A) and electrical mapping of dry junctions did support the existence of a significant difference in leakage across a given sample. I–V data acquired by conductive atomic force microscopy (C-AFM), shown in Figure 2.4, highlight such heterogeneity in leakage current (which in turn affect the forward bias), with the largest experimental variation being ~400 folds at a bias of 0.6 V. I–Vs were sampled from 100 locations across the sample (Figure 2.4 and Figure A12, Appendix A) and it is probable that at forward biases larger than 1.6 V the scatter in the current leakage is even larger, but as can be seen in Figure 2.4 above this bias several traces are already beyond the range of the current amplifier. This current saturation is however not a serious shortcoming as a comparison between electrical and electrochemical experiments is meaningful at a significantly lower bias. To select the sample bias at which a comparison between the “dry” leakage current, sampled at different microscopic locations, becomes valuable in attempting to explain the

macroscopic “wet” CV response, we first assessed the “wet” flat-band potential, E_{FB} , of the electrode–electrolyte interface. E_{FB} was estimated from EIS Mott–Schottky (MS) measurements of capacitance vs sample bias. MS measurements shown in Figure A13 (Appendix A) suggest a E_{FB} of ~ -0.57 V vs Ag/AgCl. Considering that the apparent formal potential of the Fc/Fc⁺ couple in dark is ~ 0.35 V, there is therefore a ~ 0.92 V gap between the onset of accumulation and the apparent formal potential. In the electrical “dry” measurements (I–V) the magnitude of the leakage current scatter across a macroscopic sample (Figure 2.4) was therefore evaluated at a junction voltage of 0.92 V, being this the “dry” bias that best matches the 0.92 V “wet” gap described above (the flat-band of the silicon–platinum junction was estimated to be around 0 V, i.e., where the current generally starts its exponential rise). At this sampling point, the largest difference in leakage was 204 folds, which is smaller than the 1000 folds difference in dark reverse current suggested by the model as required to account for the experimental CV peak separations if the photocurrent is unchanged (Figure A11, Appendix A). It is therefore most likely that the experimental peak splitting is almost

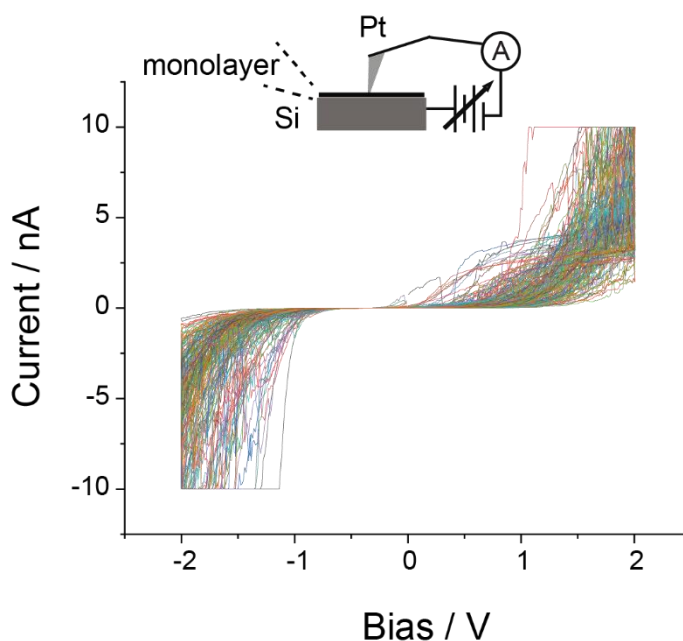


Figure 2.4. Lateral electrical heterogeneity. Current–potential (I–V) curves acquired by C-AFM on M-1 samples (LD, n-type Si(111)) and measurement schematics of the platinum–monolayer–silicon junction. The bias routing is from the substrate to the AFM tip, so that the reverse current (leakage) of the junction appears in the positive quadrant (positive current, positive bias).

entirely caused by a heterogeneous photocurrent across the macroscopic monolayer system as in fact changing the illumination intensity minimize the splitting (Figure 2.3). A dependency of photocurrent on the reverse dark leakage is not unprecedented,^[60] and therefore, the cause of photocurrent heterogeneity is probably rooted in the broad variability of the latter. Future measurements of lateral heterogeneity in the degree of Fermi-level pinning,^[61, 62] for instance, by harvesting the latest developments in light-addressed potentiometric sensors,^[31, 35] could be used to advance our understanding of the silicon–electrolyte interface.

2.5 Conclusions

A complete and correct understanding of the factors governing how charges are transferred across a semiconductor interface underpins the design of devices whose function span from converting light into electricity to sensing their environment. Among these factors, a key one is the apparent formal potential of surface confined redox reactions. When a scientist and engineer require an analytical tool for such measurement, cyclic voltammetry still reigns supreme. Chemists, material scientists and engineers encountering non-ideal shapes and positions in voltammograms of electrodes modified with molecules are often inclined to reject these features as disorder in the adsorbate layer. Here we have shown that at monolayer-modified crystalline silicon electrodes, multiple voltammetric waves are not necessarily diagnostic of molecular disorder, but instead caused by heterogeneous leakage (reverse bias) currents across the monolayer system. The leakage heterogeneity, probed by C-AFM, causes photocurrents to vary across the sample and hence brings about changes to the local E_{OCP} , which finally manifest as multiple redox bands.

2.6 References

- [1]. Blanco, D. E.; Modestino, M. A., Organic Electrosynthesis for Sustainable

- Chemical Manufacturing. *Trends Chem.* **2019**, *1*, (1), 8-10.
- [2]. Lisdat, F., Coupling biology to electrochemistry—future trends and needs. *J. Solid State Electrochem.* **2020**, *24*, (9), 2125-2127.
- [3]. Gileadi, E., *Electrode Kinetics for Chemists, Chemical Engineers and Materials Scientists*. Wiley-VCH Verlag GmbH: New York, 1993, p 597.
- [4]. Rowe, G. K.; Creager, S. E., Redox and ion-pairing thermodynamics in self-assembled monolayers. *Langmuir* **1991**, *7*, (10), 2307-2312.
- [5]. Vogel, Y. B.; Evans, C.; Belotti, M.; Xu, L.; Russell, I.; Yu, L.-J.; Fung, A.; Hill, N.; Darwish, N.; Gonçalves, V.; Coote, M. L.; Iyer, S.; Ciampi, S., The Corona of a Surface Bubble Promotes Electrochemical Reactions. *Nat. Commun.* **2020**, *11*, 6323.
- [6]. Eckermann, A. L.; Feld, D. J.; Shaw, J. A.; Meade, T. J., Electrochemistry of redox-active self-assembled monolayers. *Coord. Chem. Rev.* **2010**, *254*, (15–16), 1769-1802.
- [7]. Sagiv, J., Organized Monolayers by Adsorption. 1. Formation and Structure of Oleophobic Mixed Monolayers on Solid Surfaces. *J. Am. Chem. Soc.* **1980**, *102*, (1), 92–98.
- [8]. Gooding, J. J.; Ciampi, S., The Molecular Level Modification of Surfaces: From Self-Assembled Monolayers to Complex Molecular Assemblies. *Chem. Soc. Rev.* **2011**, *40*, 2704-2718.
- [9]. Fabre, B., Functionalization of Oxide-Free Silicon Surfaces with Redox-Active Assemblies. *Chem. Rev.* **2016**, *116*, (8), 4808–4849.
- [10]. Ciampi, S.; Choudhury, M. H.; Ahmad, S. A. B. A.; Darwish, N.; Brun, A. L.; Gooding, J. J., The impact of surface coverage on the kinetics of electron transfer through redox monolayers on a silicon electrode surface. *Electrochim. Acta* **2015**, *186*, 216-222.
- [11]. Gonzalez, J.; Sequí, J.-A., Kinetic Implications of the Presence of Intermolecular Interactions in the Response of Binary Self-Assembled Electroactive Monolayers. *ACS Omega* **2018**, *3*, (1), 1276-1292.
- [12]. Gonzalez, J.; Sequí-Castellano, J. A., Electrochemical determination of kinetic parameters of surface confined redox probes in presence of intermolecular interactions by means of Cyclic Voltammetry. Application to TEMPO monolayers in gold and platinum electrodes. *Electrochim. Acta* **2021**, *365*, 137331.
- [13]. Nerngchamnon, N.; Thompson, D.; Cao, L.; Yuan, L.; Jiang, L.; Roemer, M.; Nijhuis, C. A., Nonideal Electrochemical Behavior of Ferrocenyl–Alkanethiolate SAMs Maps the Microenvironment of the Redox Unit. *J. Phys. Chem. C* **2015**, *119*, (38), 21978-21991.
- [14]. Dief, E. M.; Darwish, N., Ultrasonic Generation of Thiyl Radicals: A General Method of Rapidly Connecting Molecules to a Range of Electrodes for Electrochemical and Molecular Electronics Applications. *ACS Sens.* **2021**, *6*, (2), 573–580.
- [15]. Zhang, S.; Ferrie, S.; Peiris, C. R.; Lyu, X.; Vogel, Y. B.; Darwish, N.; Ciampi, S., Common Background Signals in Voltammograms of Crystalline

- Silicon Electrodes are Reversible Silica–Silicon Redox Chemistry at Highly Conductive Surface Sites. *J. Am. Chem. Soc.* **2021**, *143*, (3), 1267–1272.
- [16]. Laborda, E.; González, J.; Molina, A., Analytical Theory for Ion Transfer–Electron Transfer Coupled Reactions at Redox Layer–Modified/Thick Film–Modified Electrodes. *Curr. Opin. Electrochem.* **2020**, *19*, 78–87.
- [17]. Wong, R. A.; Yokota, Y.; Wakisaka, M.; Inukai, J.; Kim, Y., Probing consequences of anion-dictated electrochemistry on the electrode/monolayer/electrolyte interfacial properties. *Nat. Commun.* **2020**, *11*, (1), 4194.
- [18]. Yokota, Y.; Yamada, T.; Kawai, M., Ion-Pair Formation between Ferrocene-Terminated Self-Assembled Monolayers and Counteranions Studied by Force Measurements. *J. Phys. Chem. C* **2011**, *115*, (14), 6775–6781.
- [19]. Zhang, L.; Vogel, Y. B.; Noble, B. B.; Goncales, V. R.; Darwish, N.; Brun, A. L.; Gooding, J. J.; Wallace, G. G.; Coote, M. L.; Ciampi, S., TEMPO Monolayers on Si(100) Electrodes: Electrostatic Effects by the Electrolyte and Semiconductor Space-Charge on the Electroactivity of a Persistent Radical. *J. Am. Chem. Soc.* **2016**, *138*, (30), 9611–9619.
- [20]. Darwish, N.; Eggers, P. K.; Ciampi, S.; Tong, Y.; Ye, S.; Paddon-Row, M. N.; Gooding, J. J., Probing the Effect of the Solution Environment around Redox-Active Moieties Using Rigid Anthraquinone Terminated Molecular Rulers. *J. Am. Chem. Soc.* **2012**, *134*, (44), 18401–18409.
- [21]. Heinze, J., Cyclic Voltammetry—“Electrochemical Spectroscopy”. *New Analytical Methods* (25). *Angew. Chem. Int. Ed.* **1984**, *23*, (11), 831–847.
- [22]. Santangelo, P. G.; Miskelly, G. M.; Lewis, N. S., Cyclic Voltammetry at Semiconductor Photoelectrodes. 1. Ideal Surface-Attached Redox Couples with Ideal Semiconductor Behavior. *J. Phys. Chem.* **1988**, *92*, (22), 6359–6367.
- [23]. Vogel, Y. B.; Zhang, L.; Darwish, N.; Gonçalves, V. R.; Le Brun, A.; Gooding, J. J.; Molina, A.; Wallace, G. G.; Coote, M. L.; Gonzalez, J.; Ciampi, S., Reproducible flaws unveil electrostatic aspects of semiconductor electrochemistry. *Nat Commun* **2017**, *8*, (1), 2066.
- [24]. Eggers, P. K.; Darwish, N.; Paddon-Row, M. N.; Gooding, J. J., Surface-Bound Molecular Rulers for Probing the Electrical Double Layer. *J. Am. Chem. Soc.* **2012**, *134*, (17), 7539–7544.
- [25]. Zhang, S.; Ferrie, S.; Lyu, X.; Xia, Y.; Darwish, N.; Wang, Z.; Ciampi, S., Absence of a Relationship between Surface Conductivity and Electrochemical Rates: Redox-Active Monolayers on Si(211), Si(111), and Si(110). *J. Phys. Chem. C* **2021**, *125*, (33), 18197–18203.
- [26]. Vericat, C.; Vela, M. E.; Benitez, G.; Carro, P.; Salvarezza, R. C., Self-Assembled Monolayers of Thiols and Dithiols on Gold: New Challenges for a Well-Known System. *Chem. Soc. Rev.* **2010**, *39*, (5), 1805–1834.
- [27]. Landman, U.; Barnett, R. N.; Scherbakov, A. G.; Avouris, P., Metal-Semiconductor Nanocontacts: Silicon Nanowires. *Phys. Rev. Lett.* **2000**, *85*, (9), 1958–1961.
- [28]. Lapano, J.; Brahlek, M.; Zhang, L.; Roth, J.; Pogrebnyakov, A.; Engel-

- Herbert, R., Scaling growth rates for perovskite oxide virtual substrates on silicon. *Nat. Commun.* **2019**, *10*, (1), 2464.
- [29]. Zhang, H.; Liu, H.; Wei, K.; Kurakevych, O. O.; Le Godec, Y.; Liu, Z.; Martin, J.; Guerrette, M.; Nolas, G. S.; Strobel, T. A., BC8 Silicon (Si-III) is a Narrow-Gap Semiconductor. *Phys. Rev. Lett.* **2017**, *118*, (14), 146601.
- [30]. Schmehl, A.; Vaithyanathan, V.; Herrnberger, A.; Thiel, S.; Richter, C.; Liberati, M.; Heeg, T.; Rockerath, M.; Kourkoutis, L. F.; Muhlbauer, S.; Boni, P.; Muller, D. A.; Barash, Y.; Schubert, J.; Idzerda, Y.; Mannhart, J.; Schlom, D. G., Epitaxial Integration of the Highly Spin-Polarized Ferromagnetic Semiconductor EuO with Silicon and GaN. *Nat. Mater.* **2007**, *6*, (11), 882–887.
- [31]. Wang, J.; Yang, Z.; Chen, W.; Du, L.; Jiao, B.; Krause, S.; Wang, P.; Wei, Q.; Zhang, D.-W.; Wu, C., Modulated Light-Activated Electrochemistry at Silicon Functionalized with Metal-Organic Frameworks Towards Addressable DNA Chips. *Biosens. Bioelectron.* **2019**, *146*, 111750.
- [32]. Qin, G.; Santos, C.; Zhang, W.; Li, Y.; Kumar, A.; Erasquin, U. J.; Liu, K.; Muradov, P.; Trautner, B. W.; Cai, C., Biofunctionalization on Alkylated Silicon Substrate Surfaces via “Click” Chemistry. *J. Am. Chem. Soc.* **2010**, *132*, (46), 16432–16441.
- [33]. Juan-Colás, J.; Parkin, A.; Dunn, K. E.; Scullion, M. G.; Krauss, T. F.; Johnson, S. D., The electrophotonic silicon biosensor. *Nat. Commun.* **2016**, *7*, (1), 12769.
- [34]. Terrero Rodríguez, I. M.; Borrill, A. J.; Schaffer, K. J.; Hernandez, J. B.; O’Neil, G. D., Light-Addressable Electrochemical Sensing with Electrodeposited n-Silicon/Gold Nanoparticle Schottky Junctions. *Anal. Chem.* **2020**, *92*, (16), 11444–11452.
- [35]. Chen, L.; Zhou, Y.; Jiang, S.; Kunze, J.; Schmuki, P.; Krause, S., High resolution LAPS and SPIM. *Electrochem. Commun.* **2010**, *12*, (6), 758–760
- [36]. Wang, J.; Zhou, Y.; Watkinson, M.; Gautrot, J.; Krause, S., High-sensitivity light-addressable potentiometric sensors using silicon on sapphire functionalized with self-assembled organic monolayers. *Sens. Actuators, B* **2015**, *209*, 230–236.
- [37]. Pekarek, R. T.; Kearney, K.; Simon, B. M.; Ertekin, E.; Rockett, A. A.; Rose, M. J., Identifying Charge Transfer Mechanisms across Semiconductor Heterostructures via Surface Dipole Modulation and Multiscale Modeling. *J. Am. Chem. Soc.* **2018**, *140*, (41), 13223–13232.
- [38]. Vogel, Y. B.; Darwish, N.; Ciampi, S., Spatiotemporal Control of Electrochemiluminescence Guided by a Visible Light Stimulus. *Cell Rep. Phys. Sci.* **2020**, *1*, (7), 100107.
- [39]. Ciampi, S.; James, M.; Le Saux, G.; Gaus, K.; Justin Gooding, J., Electrochemical "Switching" of Si(100) Modular Assemblies. *J. Am. Chem. Soc.* **2012**, *134*, (2), 844–847.
- [40]. Ciampi, S.; Gooding, J. J., Direct Electrochemistry of Cytochrome c at Modified Si(100) Electrodes. *Chem. Eur. J.* **2010**, *16*, (20), 5961–5968.
- [41]. Chen, X.; Park, Y. J.; Kang, M.; Kang, S.-K.; Koo, J.; Shinde, S. M.; Shin,

- J.; Jeon, S.; Park, G.; Yan, Y.; MacEwan, M. R.; Ray, W. Z.; Lee, K.-M.; Rogers, J. A.; Ahn, J.-H., CVD-grown monolayer MoS₂ in bioabsorbable electronics and biosensors. *Nat. Commun.* **2018**, *9*, (1), 1690.
- [42]. Aragonès, A. C.; Darwish, N.; Ciampi, S.; Sanz, F.; Gooding, J. J.; Díez-Pérez, I., Single-Molecule Electrical Contacts on Silicon Electrodes under Ambient Conditions. *Nat. Commun.* **2017**, *8*, 15056.
- [43]. Fabre, B., Ferrocene-Terminated Monolayers Covalently Bound to Hydrogen-Terminated Silicon Surfaces. Toward the Development of Charge Storage and Communication Devices. *Acc. Chem. Res.* **2010**, *43*, (12), 1509-1518.
- [44]. Fabre, B.; Pujari, S. P.; Scheres, L.; Zuilhof, H., Micropatterned Ferrocenyl Monolayers Covalently Bound to Hydrogen-Terminated Silicon Surfaces: Effects of Pattern Size on the Cyclic Voltammetry and Capacitance Characteristics. *Langmuir* **2014**, *30*, (24), 7235–7243.
- [45]. Linford, M. R.; Chidsey, C. E. D., Alkyl monolayers covalently bonded to silicon surfaces. *J. Am. Chem. Soc.* **1993**, *115*, (26), 12631-12632.
- [46]. Ciampi, S.; Böcking, T.; Kilian, K. A.; James, M.; Harper, J. B.; Gooding, J. J., Functionalization of Acetylene-Terminated Monolayers on Si(100) Surfaces: A Click Chemistry Approach. *Langmuir* **2007**, *23*, (18), 9320–9329.
- [47]. Ciampi, S.; Eggers, P. K.; Le Saux, G.; James, M.; Harper, J. B.; Gooding, J. J., Silicon (100) Electrodes Resistant to Oxidation in Aqueous Solutions: An Unexpected Benefit of Surface Acetylene Moieties. *Langmuir* **2009**, *25*, (4), 2530-2539.
- [48]. James, M.; Darwish, T. A.; Ciampi, S.; Sylvester, S. O.; Zhang, Z.; Ng, A.; Gooding, J. J.; Hanley, T. L., Nanoscale Condensation of Water on Self-Assembled Monolayers. *Soft Matter* **2011**, *7*, 5309-5318.
- [49]. Glaser, T.; Meinecke, J.; Länger, C.; Heep, J.; Koert, U.; Dürr, M., Solution-Based Alkyne–Azide Coupling on Functionalized Si(001) Prepared under UHV Conditions. *J. Phys. Chem. C* **2021**, *125*, (7), 4021-4026.
- [50]. Wu, F.; Zhang, D.-W.; Wang, J.; Watkinson, M.; Krause, S., Copper Contamination of Self-Assembled Organic Monolayer Modified Silicon Surfaces Following a “Click” Reaction Characterized with LAPS and SPIM. *Langmuir* **2017**, *33*, (13), 3170-3177.
- [51]. Laviron, E., Surface linear potential sweep voltammetry: Equation of the peaks for a reversible reaction when interactions between the adsorbed molecules are taken into account. *J. Electroanal. Chem. Interf. Electrochem.* **1974**, *52*, (3), 395–402.
- [52]. Laviron, E., The use of linear potential sweep voltammetry and of a.c. voltammetry for the study of the surface electrochemical reaction of strongly adsorbed systems and of redox modified electrodes. *J. Electroanal. Chem.* **1979**, *100*, (1–2), 263–270.
- [53]. Rudnev, A. V.; Yoshida, K.; Wandlowski, T., Electrochemical characterization of self-assembled ferrocene-terminated alkanethiol monolayers on low-index gold single crystal electrodes. *Electrochim Acta.* **2013**, *87*, 770-778.
- [54]. Choudhury, M. H.; Ciampi, S.; Yang, Y.; Tavallaie, R.; Zhu, Y.; Zarei, L.;

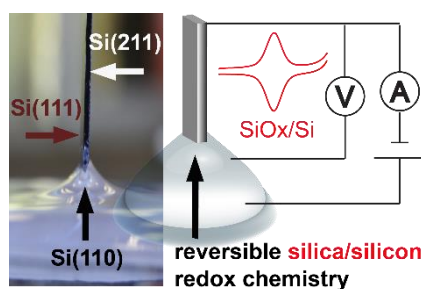
- Gonçales, V. R.; Gooding, J. J., Connecting Electrodes with Light: One Wire, Many Electrodes. *Chem. Sci.* **2015**, *6*, (12), 6769-6776.
- [55]. Paxton, W. F.; Kleinman, S. L.; Basuray, A. N.; Stoddart, J. F.; Van Duyne, R. P., Surface-Enhanced Raman Spectroelectrochemistry of TTF-Modified Self-Assembled Monolayers. *J. Phys. Chem. Lett.* **2011**, *2*, (10), 1145-1149.
- [56]. Vogel, Y. B.; Molina, A.; Gonzalez, J.; Ciampi, S., Quantitative Analysis of Cyclic Voltammetry of Redox Monolayers Adsorbed on Semiconductors: Isolating Electrode Kinetics, Lateral Interactions, and Diode Currents. *Anal. Chem.* **2019**, *91*, (9), 5929-5937.
- [57]. Yang, Y.; Ciampi, S.; Choudhury, M. H.; Gooding, J. J., Light Activated Electrochemistry: Light Intensity and pH Dependence on Electrochemical Performance of Anthraquinone Derivatized Silicon. *J. Phys. Chem. C* **2016**, *120*, (5), 2874-2882.
- [58]. Laviron, E., General Expression of the Linear Potential Sweep Voltammogram in the Case of Diffusionless Electrochemical Systems. *J. Electroanal. Chem. Interfacial Electrochem.* **1979**, *101*, (1), 19-28.
- [59]. Laviron, E.; Roullier, L., General Expression of the Linear Potential Sweep Voltammogram for a Surface Redox Reaction with Interactions between the Adsorbed Molecules: Applications to Modified Electrodes. *J. Electroanal. Chem. Interfacial Electrochem.* **1980**, *115*, (1), 65-74.
- [60]. Brenneis, A.; Overbeck, J.; Treu, J.; Hertenberger, S.; Morkötter, S.; Döblinger, M.; Finley, J. J.; Abstreiter, G.; Koblmüller, G.; Holleitner, A. W., Photocurrents in a Single InAs Nanowire/Silicon Heterojunction. *Acs Nano* **2015**, *9*, (10), 9849-9858.
- [61]. Bard, A. J.; Bocarsly, A. B.; Fan, F. R. F.; Walton, E. G.; Wrighton, M. S., The concept of Fermi level pinning at semiconductor/liquid junctions. Consequences for energy conversion efficiency and selection of useful solution redox couples in solar devices. *J. Am. Chem. Soc.* **1980**, *102*, (11), 3671-3677.
- [62]. Chazalviel, J. N.; Truong, T. B., Experimental study of the n-silicon/acetonitrile interface: Fermi level pinning and surface states investigation. *J. Am. Chem. Soc.* **1981**, *103*, (25), 7447-7451.

Every reasonable effort has been made to acknowledge the owners of copyright material. I would be pleased to hear from any copyright owner who has been omitted or incorrectly acknowledged.

Chapter 3. Reversible Silica–Silicon Redox Chemistry at Highly Conductive Si(110) Defects

This chapter is adapted from the paper published in *J. Am. Chem. Soc.* 2021, 143, 1267–1272, titled “Common Background Signals in Voltammograms of Crystalline Silicon Electrodes are Reversible Silica-Silicon Redox Chemistry at Highly Conductive Surface Sites”.

The paper is modified with minor changes in order to fit the general layout of this dissertation. Copyright permission of reprint with reusing in the doctoral thesis is attached in the appendix section.



Inspired by the results presented in Chapter 2, this chapter identifies the origin of a commonly found parasitic voltammetric signal. A minor but constantly present set of reversible waves are the reversible conversion of silicon to silica at room temperature on highly conductive crystal defects. This is important because whereas for metal and carbon electrode entire incidental voltammetric peaks have been elucidated and discerned, recurrent parasitic peaks in voltammograms of silicon electrodes are unaccounted for. The data of this chapter explain how to reproducibly obtain and magnify these parasitic peaks and give an explanation of their origin. The results of this chapter are a significant contribution towards a more complete understanding of the electrochemistry and surface chemistry of crystalline silicon electrodes and redefine (restrict) the potential range which is free from parasitic signals, and which is therefore of analytical value in the context of using voltammetry to study surface reactions on silicon.

3.1 Abstract

The electrochemical reduction of bulk silica, due to its high electrical resistance, is of limited viability, namely requiring temperatures in excess 850 °C. By means of electrochemical, and electrical measurements in atomic force microscopy, we demonstrate that at a buried interface, where silica has grown on highly conductive Si(110) crystal facets, the silica–silicon conversion becomes reversible at room temperature and accessible within a narrow potential window. We conclude that parasitic signals commonly observed in voltammograms of silicon electrodes originate from silica–silicon redox chemistry. While these findings do not remove the requirement of high temperature towards bulk silica electrochemical reduction, they however redefine for silicon the potential window free from parasitic signals, and as such, significantly restrict the conditions where electroanalytical methods can be applied to the study of silicon surface reactivity.

3.2 Introduction

Cyclic voltammetry still reigns as the main form of electrochemical spectroscopy.^[1] From electrocatalysis, to sensing and corrosion, this straightforward current–potential measurement is a widespread tool for studying redox reactions at solid–liquid interfaces.^[2] For both metals and semiconductors,^[3-6] and for diffusive and diffusion-less systems,^[7-9] kinetic, mass transport and thermodynamic parameters of redox reactions are readily obtained from the analysis of voltammetric currents (peak positions and intensities).^[10]

Owing to the simplicity of recording current magnitude against time (charges), chemists and surface scientists routinely turn to Coulomb values extracted from cyclic voltammograms to monitor the progress and estimate yields of surface reactions.^[9, 11-15] Even the chemisorption of just enough molecules to results in a fractional monolayer (e.g. $<0.1 \text{ ng cm}^{-2}$) generally leads to currents well above the noise of basic commercial potentiostats.^[16-18] This aspect makes voltammetry one of the most sensitive analytical techniques for studying the reactivity of surfaces.^[19]

Silicon remains the technologically most relevant semiconductor, and research is constantly expanding the pool of reactions targeting its surface.^[20, 21] However, the power of voltammetry, when applied to silicon surface science, hinges around a correct understanding of background current signals. While for platinum, gold and carbon, all common adventitious voltammetric signals have been explained and assigned,^[22] recurrent parasitic signals observed for silicon electrodes remain unexplained.

Several published reports, dealing with the surface reactivity of silicon crystals, carry clear evidence of a pair of adventitious redox waves, either disregarded, or tentatively associated with the adsorption of a target molecule.^[23-26] Herein we demonstrate how to systematically reproduce and amplify this parasitic signal. We bring evidence of this signal being the reversible electrochemical conversion of silica to silicon, taking place at the buried silicon–silica interface in correspondence of ubiquitous highly conductive crystal defects.

3.3 Experimental section

3.3.1 Materials

Unless noted otherwise, all reagents were of analytical grade and utilized without further purification. Sodium chloride (NaCl), sodium perchlorate (NaClO₄), tetrabutylammonium perchlorate (TBAClO₄), sodium tetrakis[3,5-bis(trifluoromethyl)phenyl] borate (NaBARF), perchloric acid (HClO₄) were purchased from Sigma Aldrich. Redistilled solvents and Milli-Q water (>18 MΩ cm) were used for substrate cleaning, surface modification procedures and to prepare electrolytic solutions. Prime grade single-side polished Si(111) wafers ((111)±0.5°, n-type, phosphorous-doped, 500–550 μm thick, 7–13 Ω cm) were purchased from Siltronix, S.A.S. (Archamps, France) and cut into squared samples of 1 × 1 cm in size. Samples were washed extensively with dichloromethane, isopropanol and water, then immersed for 20 min in hot piranha solution (100 °C, the solution is a 3:1 (v/v) mixture of concentrated sulphuric acid and 30% hydrogen peroxide). Samples were then rinsed with water and immediately transferred to an argon-saturated 40% aqueous ammonium

fluoride solution, to which traces of ammonium sulphite are added as oxygen scavenger. The silicon wafers were etched in the fluoride solution for 9 min, rinsed with copious water and dichloromethane, and then blown dry with argon before the dropping of a small deoxygenated sample of 1,8-nonadiyne (ca. 50 μl) on the wafer.^[5, 27] The liquid sample was contacted with a quartz slide to limit evaporation, rapidly transferred to an air-tight reaction chamber where a UV light source (Vilber, VL-215.M, $\lambda = 312$ nm, nominal power output of 30 W and positioned approx. 200 mm away from the silicon sample) illuminated the sample for 2 hours. The acetylene-functionalized samples were then removed from the reaction chamber, rinsed several times with dichloromethane and rested in a sealed vial under dichloromethane at 4 °C for 8 h. To expose (110) facets, Si (111) wafers were cleaved using as reference the (110) lap marked by the supplier, and then etched and reacted with 1,8-nonadiyne following the above procedure.

3.3.2 Electrochemical measurements

All electrochemical experiments were performed using a CHI650D electrochemical workstation (CH Instruments, Austin) and, unless specified otherwise, a three-electrode and single-compartment PTFE cell. In the cyclic voltammetry experiments, diyne-modified silicon wafers were used as the working electrode, a platinum mesh as the counter electrode, and an Ag/AgCl (in 3M NaCl) electrode served as the reference electrode. All potentials are reported against the reference electrode. A circular Viton gasket defined the geometric area of the working electrode to 0.28 cm². For the hanging-meniscus experiments in (Figure 3.5 in the main text), the active area of the (110) facet was determined by capacitance measurements. In all cases an ohmic contact between a copper plate and the working electrode was ensured by gently scribing with emery paper the electrode before applying a small amount of gallium–indium eutectic. Surface coverages are expressed in mol cm⁻² and are calculated from the faradaic charge taken as the background-subtracted integrated current from the anodic scan of the voltammograms. All electrochemical experiments were performed in air at room

temperature (22 ± 2 °C), and under ambient illumination. Control experiments shown in Figure B1 (Appendix B) were performed with monolayer-coated n- and p-type (phosphorous- and boron-doped) wafers of different level of doping (prime grade single-side polished Si(111) wafers ($\langle 111 \rangle \pm 0.5^\circ$), 500–550 μm thick, Siltronix). The resistivity specified by the manufacturer was 0.007–0.013 $\Omega\text{ cm}$ (referred to as highly doped, n- or p-type), and 8–12 $\Omega\text{ cm}$ (lowly doped p-type).

3.3.3 Atomic force microscopy measurements

Atomic force microscopy (AFM) experiments were conducted on a Bruker Dimension atomic force microscope, in air and at room temperature. The ICON head module was used for topography measurements, and the Bruker PeakForce Tunneling AFM (PF-TUNA) module was used to acquire current–voltage (I–V) data. AFM data were analyzed with Nano Scope 1.9. For topography measurements the resolution was set to 512 points/line, and the scan rate to 0.5 Hz. Silicon nitride AFM tips were used to probe sample topography (TESPA-Bruker AFM probes, with spring constant of 20 N m^{-1}), while conductive platinum tips from Rocky Mountain Nanotechnology (25Pt300B, with a spring constant of 18 N m^{-1}) were used to measure I–V characteristics. I–V curves were acquired with the peak force set to 2.5 nN and a current gain of either 10 nA/V or 100 nA/V. The bias routing is from the substrate to the tip, with the tip being grounded, so that in the figures and in the text the forward current of the junctions is appearing in the negative quadrant (negative current, negative bias). I–V curves were taken at a voltage sweep rate of 8.26 V/s.

3.3.4 X-ray photoelectron spectroscopy measurements

X-ray photoelectron spectroscopy (XPS) measurements were acquired by an AXIS Ultra DLD spectrometer (Kratos Analytical Ltd, Manchester, UK) with a monochromatic Al $K\alpha$ source (1486.7 eV), an hemispherical analyzer, and multichannel detector. Spectra were recorded in normal emission with pressure in the sample chamber below 9×10^{-9} Torr, and with a spot size of approximately 300×700

μm . The angle of incidence was set to 90° to the sample surface. All energies are reported as binding energies in electron volts (eV) and referenced to the Si $2p_{3/2}$ signal (corrected to 99.5 eV). The survey scans were conducted over 1100–0 eV range, with a step size of 1 eV, a dwell time of 100 ms, and an analyzer pass energy of 160 eV. High-resolution (narrow scans) data were collected with a step size of 0.1 eV, a dwell time of 1500 ms and an analyzer pass energy of 40 eV. XPS spectral analysis were processed in CasaXPS software (Casa Software Ltd., UK). Analysis of the spectra involved background subtraction using the Adjustable routine and nonlinear fittings with Gaussian-Lorentzian (GL) line shape functions. All peaks detected in the Si 2p narrow scans were fitted to functions having 95% Gaussian and 5% Lorentzian character. The Si $2p_{1/2}$ and Si $2p_{3/2}$ spin–orbit-split signals were best fitted by two bands located ~ 0.6 eV apart, and by setting their full width at half maximum (fwhm) to 0.6 eV. The Si $2p_{1/2}$ to Si $2p_{3/2}$ peak area ratio was fixed to 0.51.^[28] The shift towards larger binding energies for the spectral contributions arising from $\text{Si}^{(1)}$ – $\text{Si}^{(4)}$ oxides were set, relative to the bulk elemental silicon signal ($\text{Si}^{(0)}$, 99.8 eV, centre of the Si $2p_{1/2}$ and Si $2p_{3/2}$ peak positions) to +0.95 eV ($\text{Si}^{(1)}$, fwhm 0.9 eV), +1.75 eV ($\text{Si}^{(2)}$, fwhm 1.2 eV), +2.48 eV ($\text{Si}^{(3)}$, fwhm 1.3 eV), +3.90 eV ($\text{Si}^{(4)}$, fwhm 2.3 eV).^[29] The fractional coverage of SiO_n in the oxidized samples was estimated from the $\text{Si}^{(3)}/\text{Si}^{(4)}$ to Si 2p peak area ratio.^[28]

3.4 Result and discussion

Figure 3.1 illustrates the process of deliberately oxidizing a monolayer-coated, oxide-free,^[27] Si(111) surface in aqueous 1.0 M HClO_4 . This is an exceedingly common electrode–electrolyte system for silicon electrochemistry,^[30–32] and when we first ramped the voltage, from -0.5 V to a relatively low anodic vertex of 0.0 V, nothing unexpected appeared in the current trace (Figure 3.1a). Raising the anodic vertex from 0.0 to 1.0 V led again, at a first look, to a featureless voltammogram, with the only exception of a steep rise in current which is generally associated with the oxidation of either the substrate or the solvent (Figure 3.1b). However, a closer inspection of the trace in Figure 3.1b indicates the appearance of a surface-confined cathodic wave,

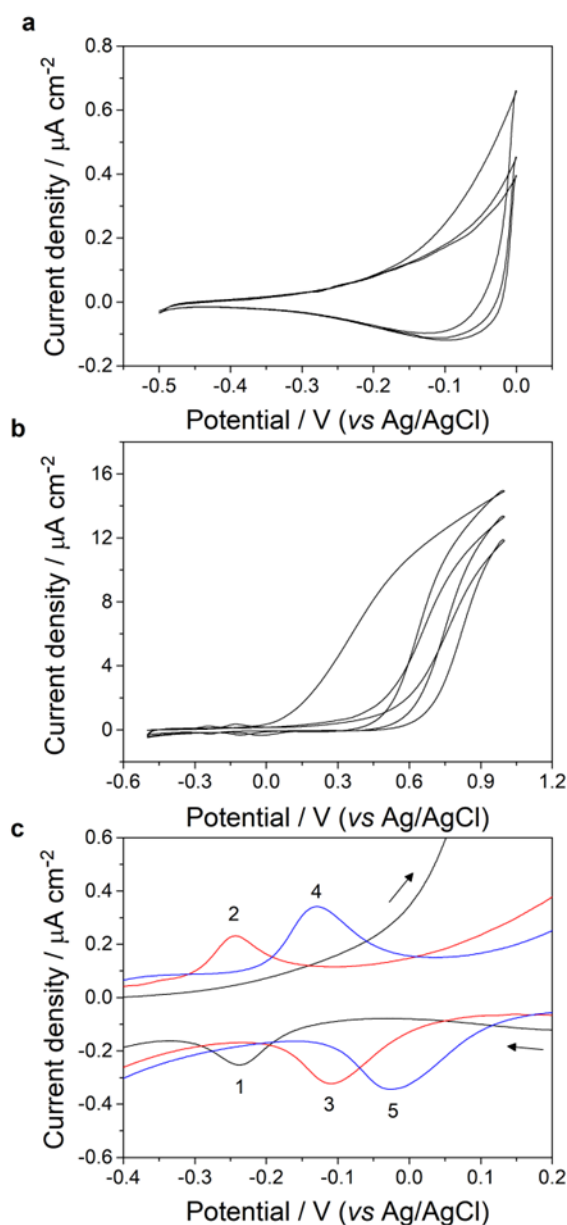


Figure 3.1. Cyclic voltammograms of 1,8-nonadiyne-modified Si(111) electrodes. The electrode voltage is ramped from an initial -0.5 V to an anodic vertex, set to either 0.0 V in (a), or to 1.0 V in (b). (c) Color-coded magnified views of the first three sequential voltammetric cycles (six segments) shown in (b). The voltage scan rate is 0.1 V/s, and the electrolyte is aqueous 1.0 M HClO_4 .

labelled as **1** in the return segment of the first cycle (Figure 3.1c). This wave is coupled to a new anodic signal, evident in the third segment (**2**). These new signals increase in size, and shift anodically, upon further cycling (waves labelled as **3–5** in Figure 3.1c). These waves are therefore associated with anodic damaging of the electrode, that is, the appearance of silica on its surface. Figure 3.2 shows the changes to the

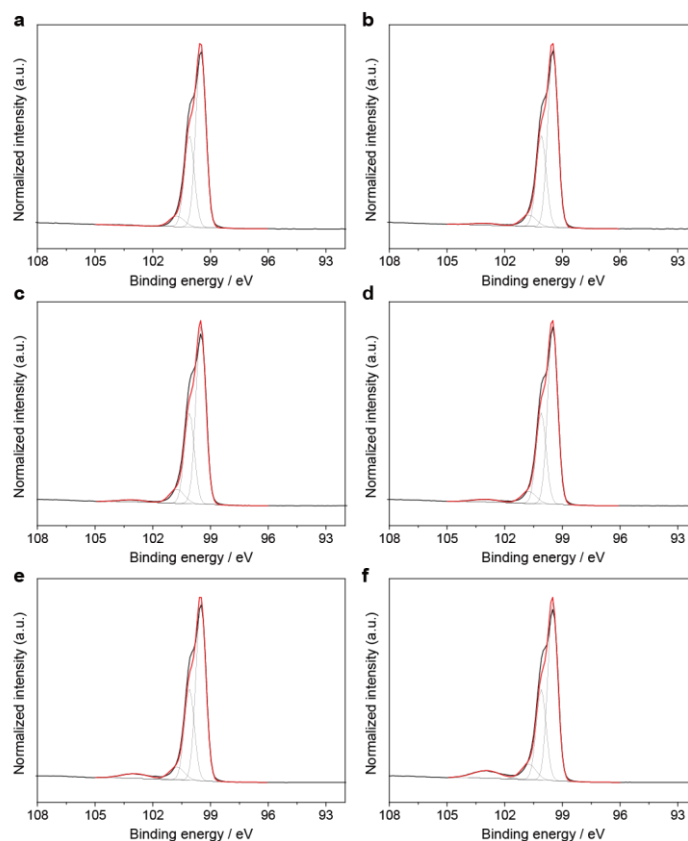


Figure 3.2. XPS narrow scans of the Si 2p region acquired (a) before, and (b–f) after having deliberately introduced an anodic damage to 1,8-nonadiyne-modified Si(111) *n*-type (7–13 ohm cm) electrodes. The anodic process consisted in cyclically ramping the potential of the working silicon electrode from an initial -0.5 V bias to an anodic vertex set to 1.0 V, and then back to -0.5 V (one cycle). Spectra in (b), one cycle; (c), two cycles; (d), three cycles; (e) five cycles; and (f), 10 cycles). The electrolyte was aqueous 1.0 M HClO_4 . The black thick curves are the experimental XPS data (108–92 eV), while the four thin traces (105–95 eV) are the fitted contributions ascribed to $\text{Si}^{(3)}$ & $\text{Si}^{(4)}$, $\text{Si}^{(1)}$, and elemental silicon ($\text{Si } 2p_{1/2}$, and $\text{Si } 2p_{2/3}$). The red trace is the sum of all refined peaks. The fraction of oxidized Si surface atoms is estimated to be 0 (a), 13.75% (b), 15.44% (c), 23.21% (d), 40.35% (e), and 65.07% (f). The distribution of silicon over its oxidation states is quite interesting, and for example as also observed by Cerofolini and co-workers,^[29] there is absolute absence of $\text{Si}^{(2)}$ species and an anomalously high fraction of $\text{Si}^{(1)}$. It is therefore possible that the $+0.95$ eV ($\text{Si}^{(1)}$) shoulder on the high binding energy side of the main Si 2p peak also includes emissions from silicon bound to hydrogen.⁴ The quality of the fitting was improved by merging the $\text{Si}^{(3)}$ and $\text{Si}^{(4)}$ contributions into one single band of intermediate character between $+2.48$ eV ($\text{Si}^{(3)}$) and $+3.90$ eV ($\text{Si}^{(4)}$).

XPS Si 2p region as the anodic process evolves, revealing the appearance of photoemissions at binding energies larger than ca. 100 eV, which are assigned to SiO_n species (silicon in the oxidation state n , $1 \leq n \leq 4$) using the spectral deconvolution

proposed by Himpsel.^[29, 33] From the above results we infer that the background reversible redox peaks, of which we are trying to define the origin, are most likely related to silicon oxides. This is surprising, since the reduction of silica requires normally very harsh conditions (high temperatures and molten salts electrolytes, *vide infra*).^[34-36] Further, these waves reflect an irreversible chemical change of the electrode, as opposed to a simple capacitive process. Data in Figure B2 (Appendix B) show that the surface-confined redox couple formed upon the anodic excursion to 1.0 V is remarkably stable to prolonged potential cycling. Its surface density, estimated under the assumption of a one-electron redox reaction,^[37, 38] is $(2.34 \pm 0.68) \times 10^{-12}$ mol cm^{-2} , which is equivalent to about 0.1% of the surface atoms density of an ideal Si(111) surface (15.66×10^{14} atoms cm^{-2}).

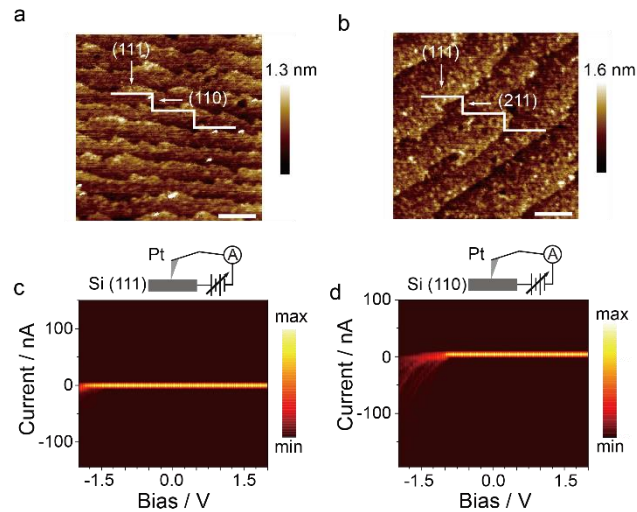


Figure 3.3. (a,b) Atomic force microscopy height images of monolayer-coated Si(111) wafers. Topography images were acquired paying attention to ensure a parallel alignment between the major flat, indicating the [110] direction, and the x -direction of the AFM raster scan. Steps between terraces are either roughly parallel to the sample major flat (a), or oriented 30° away from it (b). Scale bars in (a) and (b) are 400 and 220 nm, respectively. (c,d) Heat maps of current–potential (I – V) data for platinum–silicon junctions acquired by conductive AFM on Si(111) and Si(110) surfaces. I – V curves are sampled at 100 evenly spaced points and are recorded at a constant force of $2.5 \mu\text{N}$ with a 100 nA/V sensitivity. The sample-to-tip bias routing is such that forward currents appear in the negative quadrant, that is, when the n -type silicon is biased negative with respect to the platinum AFM tip

This last quantitative remark is important, since this fractional coverage is close to the ratio, expected for a Si(111) wafer, of atoms on step-edges to atoms on surface terraces. There is in fact a strong dependence between the electrical conductivity of a silicon surface and its crystal orientation.^[39] Recently published electrical measurements, performed with microscopic tungsten probes, have revealed that the electrical conductivity for common low-index silicon facets decrease in the order (110)>>(111)>(100).^[39] We have observed similar facet-dependent conductivity trends in small Cu₂O crystals.^[40] We therefore postulate that the electrical conductivity of the silicon–SiO_n interface is enhanced at sites where silica grows on surface defects of large conductivity.^[39] Under these circumstances the silica–silicon redox couple may become reversible within a moderate potential window, therefore explaining the origin of the parasitic signals ubiquitous to oxidized silicon electrodes (Figure 3.1).

We therefore investigated the existence of highly conductive defects on nominal single-crystal silicon wafers. Atomically flat electrodes are an idealization, and well-prepared and nominally flat semiconductor electrodes are a continuous of flat terraces separated by small vertical steps.^[5,41] Atomic force microscopy (AFM) topography data in Figure 3.3a and 3.3b indicate that on Si(111) electrodes – a crystal cut commonly used by electrochemists and surface scientists^[42,43] – these vertical steps tend to have preferred orientations. Commercial Si(111) wafers have a major flat indicating the [110] direction (a stereographic view of a Si(111) wafer is in Figure B3 Appendix B). Surface topography data obtained by AFM reveal that these vertical steps form angles of either approximately 0° or 30° with respect to the direction of the major flat (Figure 3.3a and 3.3b). Steps separating Si(111) terraces are therefore principally exposing (110) and (211) planes. An analysis of step heights and terrace widths in the AFM topography images (e.g. Figure 3.3a) revealed that even in high quality samples, such as those in Figure 3.3, the surface area ratio of Si(110) to Si(111) is 0.19 ± 0.05 to 100. This percentage is in striking accord with the 0.1% surface coverage, estimated above by cyclic voltammetry, for the adventitious redox couple appearing upon oxidation to the silicon electrode (Figure 3.1). Representative AFM height profiles,

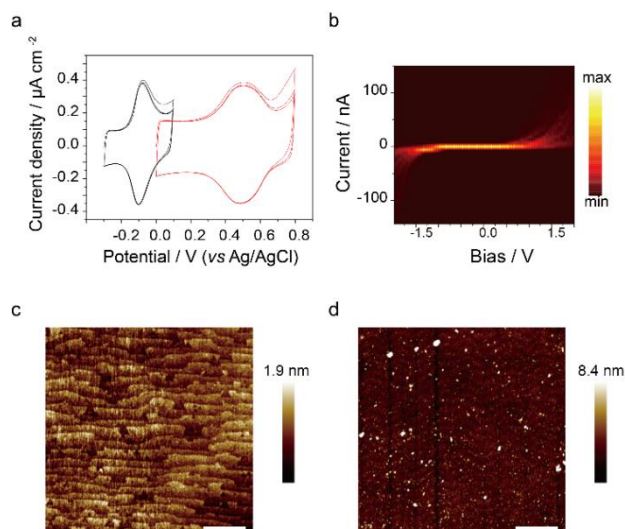


Figure 3.4. (a) Cyclic voltammograms of Si(111) electrodes indicating an anodic shift with progressive potential cycling (three cycles, black curves; 100 cycles, red curves) of the apparent formal potential of the silica/silicon redox couple. The scan rate is 0.1 V/s, and the electrolyte is 1.0 M HClO₄. (b) I–V curves (AFM) of platinum–silicon junctions recorded on anodically damaged Si(111) electrodes, showing a significant increase in the leakage current (positive quadrant) compared to fresh samples (Figure 2c). (c,d) Changes to surface topography before (c) and after (d) three potential sweeps between –0.5 V and 1.0 V (0.1 V/s, 1.0 M HClO₄). Scale bars in (c) and (d) are 1 μm

acquired along a direction normal to the predominant step direction and used to estimate the area ratio of (110) and (211) facets to (111) terraces in nominal Si(111) wafers, are in Figure B4 (Appendix B).

It was therefore relevant to test the relative conductivity of Si(110) and Si(111) facets. Current–potential data (I–V hereafter), acquired by conductive AFM (Figure 3.3c and 3.3d, and Figures B5 and B6 Appendix B), indicate that the conductivity of Si(110) wafers is significantly larger than that of Si(111). For example, at a forward bias of –1.5 V, the current of platinum–Si(110) junctions is on average 21 times larger (–48 nA versus only –2.20 nA) than that of junctions made to Si(111). Silicon has no conductive bulk oxide phases,^[34] and the electro-reduction of silica has only been demonstrated in CaCl₂ melts.^[36, 44] By ensuring good mobility of O^{2–} anions the high-temperature melt aids the de-oxidation of SiO₂.^[34, 44] However, under an electric field, oxygenated anions (O^{2–} and OH[–]) are known to migrate across a thin silica layer, even at room temperature.^[45, 46] Inward migration of anionic species is therefore likely be

favoured if the silicon bands are bent upwards, as shown by control experiments on substrates of different doping type and level (Figure B1 Appendix B). Further, the growth of silica over an oxide-free substrate introduces energy levels in the band gap,^[47] demonstrated indirectly by a sharp drop of the anodization voltage observed as soon as silica adlayers form over a silicon electrode.^[47-50]

We therefore propose that despite the low electrical conductivity of bulk silica,^[34, 36, 51] its electrochemical reduction at the silica–silicon interface becomes apparently reversible at highly conductive facets, and manifests in both aqueous (Figure 3.1 and Figure B7a–c Appendix B) as well as non-aqueous electrolytes (Figure B7d–e, Appdenix B). It has been suggested that the mobile species migrating across the thickening oxide film are mainly anions.^[52] Water molecules enter the first layers of the oxide and dissociate into ionic species, which then migrate toward the silicon/oxide interface under the effect of the electrical field in the oxide.^[47, 53] The apparent formal potential of this parasitic redox couple shifts anodically with progressive oxidation (Figure 3.4a), which reflects a similar shift for the electrode open circuit potential. These shifts are caused by an increase, with oxidation, of the dark leakage current.^[5, 6] I–V curves shown in Figure 3.4b (and in Figure B8 Appendix B) confirm a substantial increase in leakage current upon initial substrate oxidation. Our oxidation-induced redox background couple is therefore in series with a “leaky” silica-rich diode. As expected, the sharp and regular terraced structure of the etched and monolayer-coated Si(111) surface (Figure 3.4c) disappears upon its oxidation: the highly conductive (110) and (211) step edges have been covered by an oxide layer (Figure 3.4d, Figure B9 appendix B).

To further confirm that the surprising silica/silicon redox reversibility arises from the silica adlayer sitting on highly conductive silicon sites, we performed electrochemical experiments on macroscopic samples cleaved to expose mainly (110) planes. This was done by cutting a Si(111) wafer along a direction parallel to the supplier-marked lap (Figure 3.5c). The wafer was then etched and chemically passivated, before dipping it in the electrolyte to wet only the (110) face. As shown in Figure 3.5, voltammograms

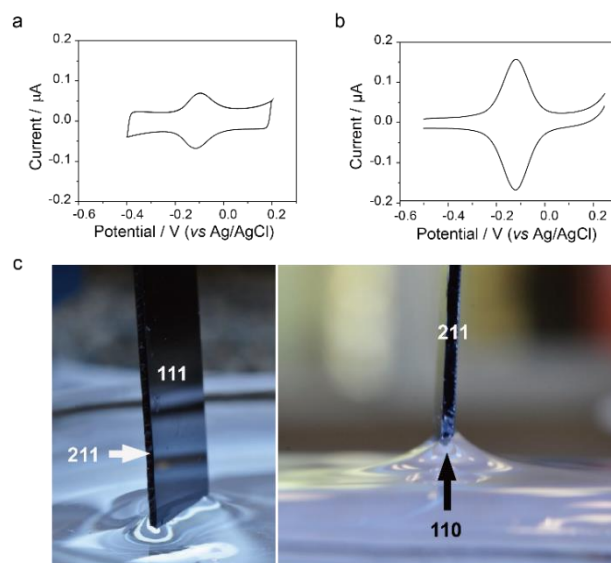


Figure 3.5. (a,b) Cyclic voltammograms of anodically damaged Si(111) and Si(110). The surface coverage of the redox background signal observed on Si(110) is $12.73 \times 10^{-12} \text{ mol cm}^{-2}$, which is 6.9 times larger than on Si(111). The geometric area ratio of the two electrodes is approximately 1.9 ((111) to (110), estimated by capacitance measurements). Voltammograms were recorded at a scan rate of 0.1 V/s, in aqueous 1.0 M HClO₄, after three potential sweeps (0.1 V/s) between -0.5 V and 1.0 V . (c) Optical images of the hanging-meniscus configuration used to wet the (110) facet in a three-electrode experiment used to record the voltammograms in (b). A graphical depiction of the (211) and (110) crystal directions in commercial Si(111) wafer is in Figure B12 Appendix B.

acquired on anodically damaged Si(110) leads to redox waves significantly larger (ca. 6.9-fold) than on Si(111).

We note that bias-driven adsorption of ions,^[19] as a potential contributor to the parasitic redox signal, was ruled out (Figure B7 Appendix B). Furthermore, surface coverages and peak positions do not change with pH, indicating that the new couple formed after anodic damaging of the surface is the result of a charge transfer not coupled to proton transfer (Figure B10 Appendix B). Controls with amorphous silicon,^[40] as well as with non-silicon conductors (Figure B11 Appendix B), indicated no appearance of redox signals after an anodic over-oxidation process, reinforcing that this new surface-confined redox couple relates to the crystalline structure of the silicon surface.

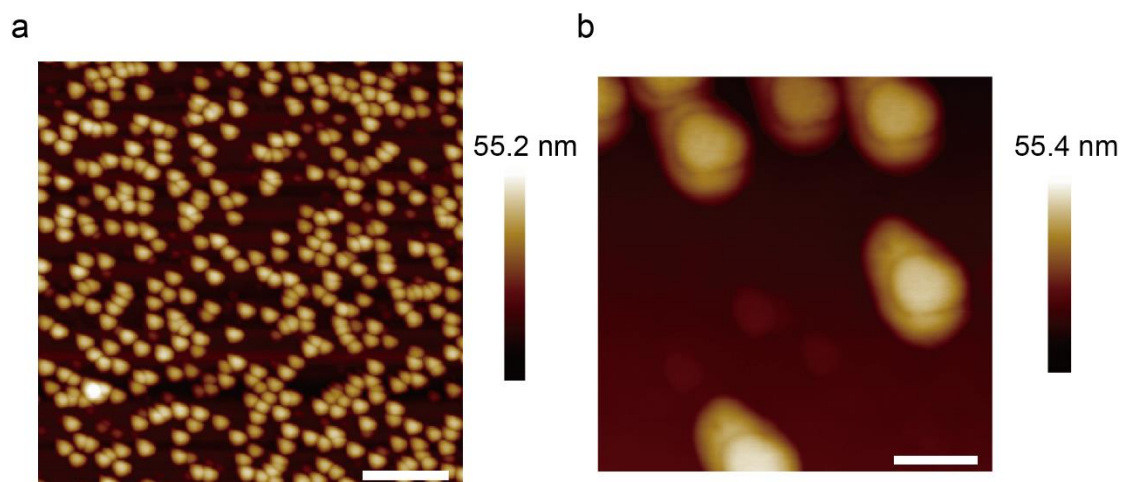


Figure 3.6. AFM topography images of Si(100) samples etched with ammonium fluoride to expose Si(111) pyramids on the surface. Scale bars are 400 nm in (a), and 100 nm in (b).

3.5 Conclusions

In conclusion, we have explored the origin of a recurrent cyclic voltammetry background signal found in a widespread semiconductor laboratory system – Si(111) electrodes. An oxidative damage, deliberate or not, of common single crystal silicon Si(111) and Si(100) electrodes (Figure 3.6) leads to the appearance of a specific set of voltammetric waves. This current signal is the reversible silica/silicon redox process, occurring on highly conductive steps separating (111) terraces. This finding has immediate implications in the electrochemistry, and surface chemistry, of silicon, effectively restricting the potential window that is free from parasitic signals and therefore permitting the study of surface reactions by means of electroanalytical methods.

3.6 Reference

- [1]. Heinze, J., Cyclic Voltammetry—“Electrochemical Spectroscopy”. *New Analytical Methods* (25). *Angew. Chem. Int. Ed.* **1984**, 23, (11), 831–847.
- [2]. Nicholson, R. S., Theory and Application of Cyclic Voltammetry for Measurement of Electrode Reaction Kinetics. *Anal. Chem.* **1965**, 37, (11), 1351-1355.

- [3]. Santangelo, P. G.; Miskelly, G. M.; Lewis, N. S., Cyclic Voltammetry at Semiconductor Photoelectrodes. 1. Ideal Surface-Attached Redox Couples with Ideal Semiconductor Behavior. *J. Phys. Chem.* **1988**, *92*, (22), 6359-6367.
- [4]. Weber, K.; Creager, S. E., Voltammetry of Redox-Active Groups Irreversibly Adsorbed onto Electrodes. Treatment Using the Marcus Relation between Rate and Overpotential. *Anal. Chem.* **1994**, *66*, (19), 3164-3172.
- [5]. Vogel, Y. B.; Zhang, L.; Darwish, N.; Gonçalves, V. R.; Le Brun, A.; Gooding, J. J.; Molina, A.; Wallace, G. G.; Coote, M. L.; Gonzalez, J.; Ciampi, S., Reproducible flaws unveil electrostatic aspects of semiconductor electrochemistry. *Nat. Commun.* **2017**, *8*, (1), 2066.
- [6]. Vogel, Y. B.; Molina, A.; Gonzalez, J.; Ciampi, S., Quantitative Analysis of Cyclic Voltammetry of Redox Monolayers Adsorbed on Semiconductors: Isolating Electrode Kinetics, Lateral Interactions, and Diode Currents. *Anal. Chem.* **2019**, *91*, (9), 5929-5937.
- [7]. Laviron, E., The use of linear potential sweep voltammetry and of a.c. voltammetry for the study of the surface electrochemical reaction of strongly adsorbed systems and of redox modified electrodes. *J. Electroanal. Chem.* **1979**, *100*, (1-2), 263-270.
- [8]. Laviron, E., Surface linear potential sweep voltammetry: Equation of the peaks for a reversible reaction when interactions between the adsorbed molecules are taken into account. *J. Electroanal. Chem. Interf. Electrochem.* **1974**, *52*, (3), 395-402.
- [9]. Zhang, L.; Laborda, E.; Darwish, N.; Noble, B. B.; Tyrell, J.; Pluczyk, S.; Brun, A. P. L.; Wallace, G. G.; Gonzalez, J.; Coote, M. L.; Ciampi, S., Electrochemical and Electrostatic Cleavage of Alkoxyamines. *J. Am. Chem. Soc.* **2018**, *140*, (2), 766-774.
- [10]. Compton, R. G.; Banks, E. C., *Understanding Voltammetry*. Imperial College Press: Covent Garden, London, UK, 2011.
- [11]. Kwon, Y.; Mrksich, M., Dependence of the Rate of an Interfacial Diels-Alder Reaction on the Steric Environment of the Immobilized Dienophile: An Example of Enthalpy-Entropy Compensation. *J. Am. Chem. Soc.* **2002**, *124*, (5), 806-812.
- [12]. Yeap, W. S.; Murib, M. S.; Cuypers, W.; Liu, X.; van Grinsven, B.; Ameloot, M.; Fahlman, M.; Wagner, P.; Maes, W.; Haenen, K., Boron-Doped Diamond Functionalization by an Electrografting/Alkyne-Azide Click Chemistry Sequence. *Chemelectrochem* **2014**, *1*, (7), 1145-1154.
- [13]. Hu, Q.; Deng, X.; Kong, J.; Dong, Y.; Liu, Q.; Zhang, X., Simple and fast electrochemical detection of sequence-specific DNA via click chemistry-mediated labeling of hairpin DNA probes with ethynylferrocene. *Analyst* **2015**, *140*, (12), 4154-4161.
- [14]. Fabre, B., Functionalization of Oxide-Free Silicon Surfaces with Redox-Active Assemblies. *Chem. Rev.* **2016**, *116*, (8), 4808-4849.
- [15]. Peiris, C. R.; Vogel, Y. B.; Le Brun, A. P.; Aragones, A. C.; Coote, M. L.; Diez-Perez, I.; Ciampi, S.; Darwish, N., Metal-Single-Molecule-

- Semiconductor Junctions Formed by a Radical Reaction Bridging Gold and Silicon Electrodes. *J. Am. Chem. Soc.* **2019**, *141*, (37), 14788–14797.
- [16]. Wei, J.; Liu, H.; Dick, A. R.; Yamamoto, H.; He, Y.; Waldeck, D. H., Direct Wiring of Cytochrome c's Heme Unit to an Electrode: Electrochemical Studies. *J. Am. Chem. Soc.* **2002**, *124*, (32), 9591-9599.
- [17]. Rohde, R. D.; Agnew, H. D.; Yeo, W. S.; Bailey, R. C.; Heath, J. R., A Non-Oxidative Approach Toward Chemically and Electrochemically Functionalizing Si(111). *J. Am. Chem. Soc.* **2006**, *128*, (29), 9518–9525.
- [18]. Ciampi, S.; James, M.; Le Saux, G.; Gaus, K.; Gooding, J. J., Electrochemical "Switching" of Si(100) Modular Assemblies. *J. Am. Chem. Soc.* **2012**, *134*, (2), 844–847.
- [19]. Gileadi, E., *Electrode Kinetics for Chemists, Chemical Engineers, and Materials Scientists*. Wiley-VCH Verlag GmbH: New York, 1993, p 52.
- [20]. Ciampi, S.; Harper, J. B.; Gooding, J. J., Wet Chemical Routes to the Assembly of Organic Monolayers on Silicon Surfaces via the Formation of Si–C Bonds: Surface Preparation, Passivation and Functionalization. *Chem. Soc. Rev.* **2010**, *39*, 2158-2183.
- [21]. Toledano, T.; Biller, A.; Bendikov, T.; Cohen, H.; Vilan, A.; Cahen, D., Controlling Space Charge of Oxide-Free Si by in Situ Modification of Dipolar Alkyl Monolayers. *J. Phys. Chem. C* **2012**, *116*, (21), 11434-11443.
- [22]. Lai, B.-C.; Wu, J.-G.; Luo, S.-C., Revisiting Background Signals and the Electrochemical Windows of Au, Pt, and GC Electrodes in Biological Buffers. *ACS Appl. Energy Mater.* **2019**, *2*, (9), 6808–6816.
- [23]. Chatterjee, S.; Carter, R.; Oakes, L.; Erwin, W. R.; Bardhan, R.; Pint, C. L., Electrochemical and Corrosion Stability of Nanostructured Silicon by Graphene Coatings: Toward High Power Porous Silicon Supercapacitors. *J. Phys. Chem. C* **2014**, *118*, (20), 10893–10902.
- [24]. Wu, Y. F.; Kashi, M. B.; Yang, Y.; Goncales, V. R.; Ciampi, S.; Tilley, R. D.; Gooding, J. J., Light-activated electrochemistry on alkyne-terminated Si(100) surfaces towards solution-based redox probes. *Electrochim. Acta* **2016**, *213*, 540–546.
- [25]. Cattaruzza, F.; Llanes-Pallas, A.; Marrani, A. G.; Dalchiele, E. A.; Decker, F.; Zanoni, R.; Prato, M.; Bonifazi, D., Redox-active Si(100) surfaces covalently functionalised with [60]fullerene conjugates: new hybrid materials for molecular-based devices. *Journal of Materials Chemistry* **2008**, *18*, (13), 1570-1581.
- [26]. Zhang, L.; Vogel, Y. B.; Noble, B. B.; Goncales, V. R.; Darwish, N.; Brun, A. L.; Gooding, J. J.; Wallace, G. G.; Coote, M. L.; Ciampi, S., TEMPO Monolayers on Si(100) Electrodes: Electrostatic Effects by the Electrolyte and Semiconductor Space-Charge on the Electroactivity of a Persistent Radical. *J. Am. Chem. Soc.* **2016**, *138*, (30), 9611-9.
- [27]. Ferrie, S.; Darwish, N.; Gooding, J. J.; Ciampi, S., Harnessing silicon facet-dependent conductivity to enhance the direct-current produced by a sliding Schottky diode triboelectric nanogenerator. *Nano Energy* **2020**, *78*, 105210.

- [28]. Webb, L. J.; Lewis, N. S., Comparison of the Electrical Properties and Chemical Stability of Crystalline Silicon(111) Surfaces Alkylated Using Grignard Reagents or Olefins with Lewis Acid Catalysts. *J. Phys. Chem. B* **2003**, *107*, (23), 5404-5412.
- [29]. Cerofolini, G. F.; Galati, C.; Renna, L., Accounting for anomalous oxidation states of silicon at the Si/SiO₂ interface. *Surf. Interface Anal.* **2002**, *33*, (7), 583–590.
- [30]. Norman, L. L.; Badia, A., Redox Actuation of a Microcantilever Driven by a Self-Assembled Ferrocenylundecanethiolate Monolayer: An Investigation of the Origin of the Micromechanical Motion and Surface Stress. *J. Am. Chem. Soc.* **2009**, *131*, (6), 2328–2337.
- [31]. Yang, Y.; Ciampi, S.; Choudhury, M. H.; Gooding, J. J., Light Activated Electrochemistry: Light Intensity and pH Dependence on Electrochemical Performance of Anthraquinone Derivatized Silicon. *J. Phys. Chem. C* **2016**, *120*, (5), 2874-2882.
- [32]. Devaraj, N. K.; Dinolfo, P. H.; Chidsey, C. E. D.; Collman, J. P., Selective Functionalization of Independently Addressed Microelectrodes by Electrochemical Activation and Deactivation of a Coupling Catalyst. *J. Am. Chem. Soc.* **2006**, *128*, (6), 1794-1795.
- [33]. Himpsel, F. J.; McFeely, F. R.; Taleb-Ibrahimi, A.; Yarmoff, J. A.; Hollinger, G., Microscopic structure of the SiO₂/Si interface. *Phys. Rev. B* **1988**, *38*, (9), 6084-6096.
- [34]. Nohira, T.; Yasuda, K.; Ito, Y., Pinpoint and bulk electrochemical reduction of insulating silicon dioxide to silicon. *Nat. Mater.* **2003**, *2*, (6), 397–401.
- [35]. Yasuda, K.; Nohira, T.; Takahashi, K.; Hagiwara, R.; Ogata, Y. H., Electrolytic Reduction of a Powder-Molded SiO₂ Pellet in Molten CaCl₂ and Acceleration of Reduction by Si Addition to the Pellet. *J. Electrochem. Soc.* **2005**, *152*, (12), D232–D237.
- [36]. Yasuda, K.; Nohira, T.; Hagiwara, R.; Ogata, Y. H., Direct electrolytic reduction of solid SiO₂ in molten CaCl₂ for the production of solar grade silicon. *Electrochim. Acta* **2007**, *53*, (1), 106–110.
- [37]. Yang, J. M.; Park, J. C.; Park, Y. B.; Kim, J. J.; Back, T. S.; Lee, H. S.; Lee, S. Y.; Park, S. W., Analytical Electron Microscopy Study of Nanometre-Scale Oxide Formed in Contact-Hole-Bottom Si Surfaces. *J. Electron. Microsc.* **2003**, *52*, (3), 305–308.
- [38]. Inoue, S.; Ichinohe, M.; Sekiguchi, A., The Isolable Cation Radical of Disilene: Synthesis, Characterization, and a Reversible One-Electron Redox System. *J. Am. Chem. Soc.* **2008**, *130*, (19), 6078–6079.
- [39]. Tan, C.-S.; Hsieh, P.-L.; Chen, L.-J.; Huang, M. H., Silicon Wafers with Facet-Dependent Electrical Conductivity Properties. *Angew. Chem. Int. Ed.* **2017**, *56*, (48), 15339-15343.
- [40]. Vogel, Y. B.; Zhang, J.; Darwish, N.; Ciampi, S., Switching of Current Rectification Ratios within a Single Nanocrystal by Facet-Resolved Electrical Wiring. *ACS Nano* **2018**, *12*, (8), 8071-8080.

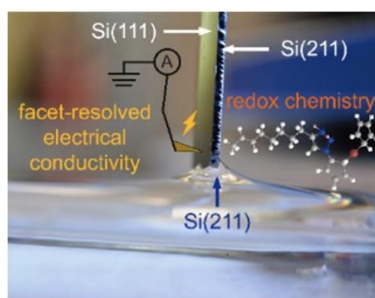
- [41]. Allongue, P.; Henry de Villeneuve, C.; Morin, S.; Boukherroub, R.; Wayner, D. D. M., The preparation of flat H-Si(111) surfaces in 40% NH₄F revisited. *Electrochim. Acta* **2000**, *45*, (28), 4591–4598.
- [42]. Rijksen, B.; Pujari, S. P.; Scheres, L.; van Rijn, C. J. M.; Baio, J. E.; Weidner, T.; Zuilhof, H., Hexadecadienyl Monolayers on Hydrogen-Terminated Si(111): Faster Monolayer Formation and Improved Surface Coverage Using the Enyne Moiety. *Langmuir* **2012**, *28*, (16), 6577–6588.
- [43]. O’Leary, L. E.; Rose, M. J.; Ding, T. X.; Johansson, E.; Brunschwig, B. S.; Lewis, N. S., Heck Coupling of Olefins to Mixed Methyl/Thienyl Monolayers on Si(111) Surfaces. *J. Am. Chem. Soc.* **2013**, *135*, (27), 10081–10090.
- [44]. Cho, S. K.; Fan, F.-R. F.; Bard, A. J., Formation of a silicon layer by electroreduction of SiO₂ nanoparticles in CaCl₂ molten salt. *Electrochim. Acta* **2012**, *65*, 57–63.
- [45]. Bardwell, J. A.; Clark, K. B.; Mitchell, D. F.; Bisailion, D. A.; Sproule, G. I.; MacDougall, B.; Graham, M. J., Growth and Characterization of Room Temperature Anodic SiO₂ Films. *J. Electrochem. Soc.* **1993**, *140*, (8), 2135–2138.
- [46]. Schmuki, P.; Böhni, H.; Bardwell, J. A., In Situ Characterization of Anodic Silicon Oxide Films by AC Impedance Measurements. *J. Electrochem. Soc.* **1995**, *142*, (5), 1705–1712.
- [47]. Zhang, X. G., *Electrochemistry of Silicon and Its Oxide*. Kluwer Academic, New York,: 2001, <https://doi.org/10.1007/b100331p> 111.
- [48]. Uritsky, V. X., Role of Electron / Hole Processes in the Initial Stage of Silicon Anodization. *Mater. Sci. Forum* **1995**, *185–188*, 115–118.
- [49]. Young, L.; Zobel, F. G. R., An Ellipsometric Study of Steady-State High Field Ionic Conduction in Anodic Oxide Films on Tantalum, Niobium, and Silicon. *J. Electrochem. Soc.* **1966**, *113*, (3), 277.
- [50]. Jakubowicz, J., Study of surface morphology of electrochemically etched n-Si (111) electrodes at different anodic potentials. *Cryst. Res. Technol.* **2003**, *38*, (3-5), 313–319.
- [51]. Lee, J. Y.; Lee, J. G.; Lee, S. H.; Seo, M.; Piao, L.; Bae, J. H.; Lim, S. Y.; Park, Y. J.; Chung, T. D., Hydrogen-Atom-Mediated Electrochemistry. *Nat. Commun.* **2013**, *4*, 2766.
- [52]. Mackintosh, W. D.; Plattner, H. H., The Identification of the Mobile Ion during the Anodic Oxidation of Silicon. *J. Electrochem. Soc.* **1977**, *124*, (3), 396–400.
- [53]. Schmidt, P. F.; Ashner, J. D., Tracer Investigation of Hydroxyls in SiO₂ Films on Silicon. *J. Electrochem. Soc.* **1971**, *118*, (2), 325.

Every reasonable effort has been made to acknowledge the owners of copyright material. I would be pleased to hear from any copyright owner who has been omitted or incorrectly acknowledged.

Chapter 4. On the relationship between Surface Conductivity and Electrochemical Rates

This chapter is adapted from the article published by the American Chemical Society, published in *J. Phys. Chem. C.* 2021, 125, 18197–18203, titled “Absence of a Relationship between Surface Conductivity and Electrochemical Rates: Redox-Active Monolayers on Si(211), Si(111), and Si(110)”.

The paper is modified with minor changes in order to fit the general layout of this dissertation. Copyright permissions for the use of this published material in the doctoral thesis is found in the appendix section (Appendix C).



Inspired by the unexpected facet-dependent electrochemical effects of Chapter 3, this chapter focuses on investigating the relationship (or lack of any) between surface conductivity and electrochemical kinetics in silicon-based monolayers. Employing covalent Si–C-bound organic monolayers – both to protect the substrate from anodic decomposition as well as to tether a conventional redox probe, ferrocene – data of this chapter demonstrate that conductivity decrease drastically as the surface crystal cut is changed from Si(211), to Si(110), and finally to Si(111). Despite a remarkable difference in surface conductivity, rates of redox reactions of surface tethers (estimated by electrochemical impedance spectroscopy) are indistinguishable.

4.1 Abstract

Optimizing the kinetics of an electrode reaction is central to the design of devices whose function spans from sensing to energy conversion. Electrode kinetics depends strongly on electrode surface properties, but the search for optimal materials is often a trial-and-error process. Recent research has revealed a pronounced facet-dependent electrical conductivity for silicon, implicitly suggesting that rarely used crystallographic cuts of this technologically relevant material had been entirely overlooked for the fabrication of electrodes. By first protecting silicon from anodic decomposition through Si–C-bound organic monolayers, conductive atomic force microscopy demonstrates that conductivity decreases in the order (211) \gg (110) $>$ (111). However, charge-transfer rates for a model electrochemical reaction are similar on all these crystal orientations. These findings reveal the absence of a relationship between surface conductivity and kinetics of a surface-confined redox reaction and expand the range of silicon crystallographic orientations viable as electrode materials.

4.2 Introduction

Starting from the seminal work of Sagiv in 1980,^[1] fundamental and applied research on self-assembly of organic molecules onto electrode surfaces has continued gaining momentum.^[2] While most of the research on self-assembly to date has focused on gold surfaces by exploiting alkanethiol chemistry,^[3] the 1990s reports by Chidsey and co-workers of Si–C-bound monolayers have helped to expand this research from metals to semiconductors.^[4-10] Silicon remains the technologically most relevant semiconducting material,^[11-15] and silicon electrodes that are functionalized with organic monolayers have broad application prospect in the fields of microscopy,^[16, 17] sensing,^[18-21] chemical catalysis,^[22] (bio)molecular electronics,^[6, 23, 24] and information storage.^[2, 25, 26]

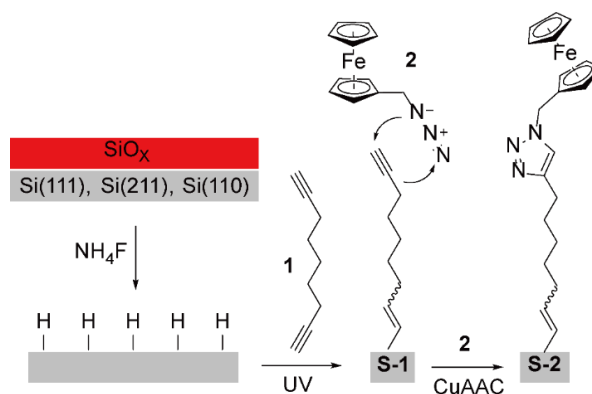
Scientists and engineers working with silicon electrodes routinely rely on dynamic electrochemical measurements – principally cyclic voltammetry^[27] – to extract kinetic information on electrode reactions.^[28, 29] However, published data of redox kinetics on

silicon are highly scattered.^[2] Some of the experimental factors contributing to this irreproducibility issue are known,^[30] others less so. Firstly, it is now generally agreed that common mathematical models used in the kinetic analysis of electrochemical data fall short of capturing all important descriptors of an electrified interface.^[29-32] Second, minor changes to surface coverage of the redox molecule,^[33] monolayer order^[34] and intermolecular interactions^[32, 35] are known to have dramatic kinetic effects.^[32, 36, 37] It remains less clear to what extent the chemical nature of the interfacial bond – between the organic monolayer and electrode – affects the rates of surface-confined electrochemical reactions.^[38, 39] An important step in the direction of clarifying on this overlooked factor was recently published. Dief and Darwish reported that for monolayers grafted on either indium–tin oxide (ITO) or silicon or carbon electrodes there is a link between changes in molecular conductivities – ascribed unambiguously to different interfacial bonds – and differences in electrochemical rates.^[40]

The origin of a putative link between electrical conductivity and electrochemical rates still lacks a conclusive explanation,^[39] but its existence and manifestation would have immediate implications in silicon electrochemistry applied to sensing and catalysis. This is because an atomically flat silicon electrode is an idealization, and even well-prepared surfaces are a continuous of flat terraces separated by small vertical steps.^[9, 29, 41] As a result, a silicon electrode of a given nominal orientation, such as commonly used Si(111) substrates, will inevitably expose a range of crystal facets, such as Si(110) and Si(211), of different surface conductivity. For example, data from Huang and co-workers indicate that the conductivity of silicon surfaces, measured with microscopic tungsten probes, decreases in the order (211) >> (111),^[42] platinum–silicon junctions are more conductive when made on Si(110) rather than on Si(111),^[9] and similar trends of facet-dependent conductivity have been reported for polyhedral Cu₂O particles.^[43]

The purpose of this paper is to clarify the presence or absence of a relationship between surface conductivity and electrochemical rates on oxide-free silicon electrodes. This is important since, to date, the vast majority of monolayer research on silicon has focused on Si(111) and Si(100) substrates,^[44-47] and highly conductive crystal facets such as

Si(110) and Si(211), which are readily available, have been entirely overlooked as potential electrode materials.



Scheme 4.1. Passivation of hydrogen-terminated silicon electrodes on Si(111), Si(211), and Si(110), followed by UV-assisted hydrosilylation of 1,8-nonadiyne (**1**) to yield an alkyne-terminated silicon surface (**S-1**), and its reaction with azidomethylferrocene (**2**) via CuAAC “click” reactions generated a redox-active monolayer (**S-2**).

4.3 Methods

4.3.1 Silicon surface modification

Unless otherwise specified, all chemical reagents were of analytical grade and used as received. Aqueous hydrogen peroxide solution (30 wt % in water, Sigma-Aldrich), sulfuric acid (Puranal, 95–97%, Sigma-Aldrich), and aqueous ammonium fluoride (40 wt%, Sigma-Aldrich) were of semiconductor grade. Redistilled solvents and Milli-Q water (>18 MΩ cm) were used for substrate cleaning procedures and to prepare electrolytic solutions. Azidomethylferrocene (**2**) was synthesized following literature procedures.^[48] Boron-doped (0.007–0.013 Ω cm), 500–550 μm thick, prime-grade and single-side polished Si(111), Si(110), and Si(211) wafers (Czochralski process, $\langle 111 \rangle \pm 0.5^\circ$, $\langle 110 \rangle > \pm 0.5^\circ$, $\langle 211 \rangle \pm 0.5^\circ$) were purchased from Siltronix S.A.S. (Archamps, France). Prior to monolayer assembly (Scheme 4.1), silicon samples were cut into squares of 1 × 1 cm, and rinsed sequentially with dichloromethane, isopropanol, and water. The samples were then immersed for 20 min in hot piranha solution (100 °C, [the solution is a 3:1 mixture (v/v) of concentrated sulfuric acid (95–97%) and hydrogen

peroxide (30%]), washed with water and immediately transferred to a degassed etching solution of 40% ammonium fluoride (the solution was degassed by means of a 30 min argon bubbling). A trace amount of ammonium sulphite was added to the fluoride solution as an oxygen scavenger, and after 9 min in the etching bath the hydrogen-terminated wafers were rinsed with copious water, dichloromethane, and then immediately reacted with a degassed sample of 1,8-nonadiyne. The liquid sample of 1,8-nonadiyne (**1**, Scheme 4.1, ~50 μ l) was then dropped on the silicon surface, and the wet sample rested for 2 h under UV light under a nitrogen atmosphere. The source of 312 nm UV radiation (Vilber, VL-215.M, nominal power output of 30 W) was placed approximately 20 cm away from the sample.^[29] Alkyne-terminated silicon samples (**S-1**) were then rinsed with isopropanol and kept under dichloromethane in a sealed reaction vial until analyzed or further reacted. Covalent attachment of azidomethylferrocene (**2**) on **S-1** surfaces followed a previously reported procedure.^[29] In brief, to a sample vial containing the alkyne-terminated sample (**S-1**), were added 5 mL of a 0.5 mM solution of **2** in an isopropanol and water mixture (1:1, v/v), copper(II) sulphate pentahydrate (20 mol% relative to the azide), and sodium ascorbate (ca. 100 mol% relative to the azide). The copper(I)-catalyzed azide–alkyne cycloaddition (CuAAC) reaction was carried out at room temperature, shielded from ambient light. After 40 min, the reaction was quenched by removing the ferrocene-modified electrode (**S-2**) from the sample vial. The samples were rinsed with copious isopropanol, water, aqueous hydrochloric acid (0.5 M), water, isopropanol, dichloromethane, and then blown dry under nitrogen before analysis.

4.3.2 Electrochemical measurements

Cyclic voltammetry (CV) was performed on a CHI650D electrochemical workstation (CH Instruments, Austin, TX) using a three-electrode and single-compartment polytetrafluoroethylene (PTFE) custom cell. The modified silicon substrate served as the working electrode, a platinum mesh as the counter electrode, and a Ag/AgCl (3.0 M NaCl) electrode as the reference electrode. All electrochemical measurements were

performed in aqueous 1.0 M perchloric acid (HClO₄) in air at room temperature (22 ± 2 °C), and under dark inside a light-proof and grounded Faraday cage. All potentials are reported against the reference electrode. A circular Viton gasket defined the geometric area of the working electrode to 0.28 cm², and ohmic contact between the back of the silicon sample and a copper plate was achieved by gently scribing the back of the electrode with emery paper before applying on it a small amount of gallium–indium eutectic. Surface coverages (Γ) of ferrocene molecules are reported in mol cm⁻² and calculated from the Faradaic charge taken as the background-subtracted integrated current from the anodic scan of the voltammograms. A minimum of seven independently prepared samples was analyzed. The 99% confidence limit of the Γ mean was calculated as $t_{n-1}s/n^{1/2}$, where t_{n-1} is 3.71, s is the standard deviation, and n the number of measurements.^[49] The apparent electron-transfer rate constants, k_{et} , for the electron-transfer reaction between tethered ferrocenes and the substrate was estimated from electrochemical impedance spectroscopy (EIS) measurements following the formalism developed by Laviron.^[50, 51] EIS data were collected between 10⁵ Hz and 10⁻¹ Hz, and both the in-phase (Z') and out-of-phase impedance (Z'') were extracted at the same time from the data and analyzed with the ZView and ZPlot software (Scribner Associates, Inc.). The k_{et} was calculated as $1/(2 R_{ct}C_{ads})$.^[50] All EIS data were obtained at an applied working electrode DC potential, E_{dc} , equal to $E_{1/2}$ ($E_{1/2}$ is the mid-point between the potential of the anodic and cathodic CV current peaks), and by setting the potential amplitude of the AC perturbation to 15 mV. Samples for EIS measurements were prepared in quadruplicates and first analyzed by three consecutive CV cycles to estimate $E_{1/2}$. The 99% confidence limit of the k_{et} mean was calculated as $t_{n-1}s/n^{1/2}$, with t_{n-1} set to 5.84.^[49]

4.3.3 Surface topography and electrical measurements

Both topography and electrical conductivity data for monolayer-modified silicon samples were obtained by atomic force microscopy (AFM) in air and at room temperature. Topography measurements were conducted on a Park NX10 atomic force

microscope operated in the tapping mode. The topography data were analyzed with XEI

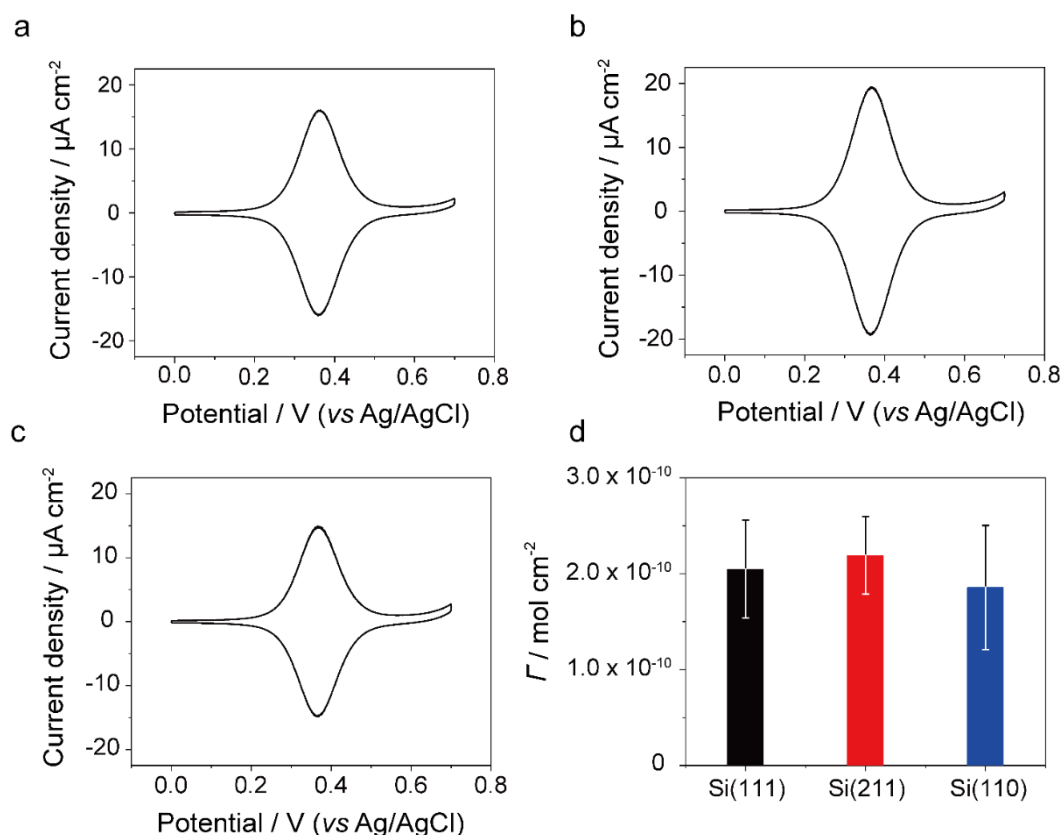


Figure 4.1. Representative cyclic voltammograms (CVs) for ferrocene monolayers (**S-2**) prepared on silicon substrates of different crystalline orientation [(a), Si(111); (b), Si(211); (c), Si(110)]. The potential sweep was started at 0 V (cathodic vertex). The voltage scan rate was 0.1 V/s, and the electrolyte was aqueous 1.0 M HClO₄. (d) CV-derived surface ferrocene coverage (Γ) for **S-2** samples prepared on Si(111), Si(211) and Si(110) electrodes. Error bars indicate the 99% confidence limit of the mean.

software (Park Systems Corp.). The scan area was set to $2 \times 2 \mu\text{m}$, the resolution to 256 points/line, and the scan rate to 1.0 Hz. Antimony (n) doped silicon AFM tips (TESPAV2-Bruker) with a spring constant of 42 N/m and resonance frequency of 320 kHz were used for the measurements. The electrical AFM experiments were conducted on a Bruker Dimension microscope with platinum AFM tips from Rocky Mountain Nanotechnology (25Pt300B, spring constant of 18 N m^{-1}). The Bruker Peak Force Tunneling AFM (PF-TUNA) module was used to acquire current–voltage (I – V) data. I – V curves were acquired with the peak force set to 2.5 μN , a current gain of either 10

nA/V or 100 nA/V, and a voltage sweep rate of 8.26 V/s. On each sample, individual I - V curves were sampled at 100 evenly spaced points, and a minimum of four samples

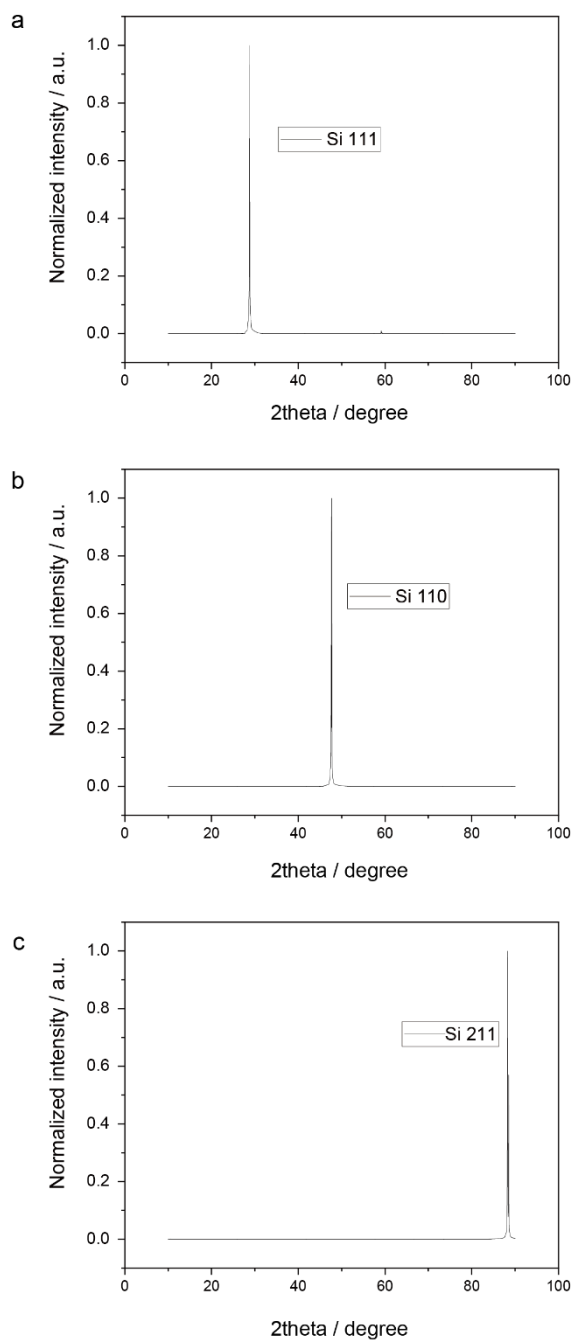


Figure 4.2. XRD patterns for Si(111), Si(110) and Si(211) substrates. Samples exposing a Si- H_x surface after NH_4F etching and stored in dichloromethane prior to XRD measurements. Note: The Si(111)-H surface is known to be a close to ideal, Si-monohydride terminated surface. However, even this near-ideal surface has dihydride edge sites. At present the average number of hydride terminations on NH_4F etched Si(211) and Si(110) is unknown.

for each silicon orientation was prepared and analyzed. All electrical AFM data were analyzed with Nano Scope 1.9.

4.3.4 X-ray diffraction measurements (XRD)

X-ray diffraction (XRD) patterns were acquired on hydrogen-terminated silicon samples using a Bruker D2 PHASER X-ray diffractometer using a Cu K α X-ray source ($\lambda = 1.54 \text{ \AA}$).

4.3.5 X-ray photoelectron spectroscopy (XPS)

X-ray photoelectron spectroscopy (XPS) surface analysis was conducted using monochromatic Al K α radiation with an Axis Supra (Kratos Analytical Ltd) instrument at 225 W. The instrument work function was calibrated to give a binding energy (BE) of 83.96 eV for the 4f_{7/2} core level of gold, and the spectrometer dispersion was adjusted to give a BE of 932.62 eV for the 2p_{3/2} core level of copper. The pass energy was set to 160 eV for survey spectra and 20 eV for high resolution spectra. All measurements were acquired in a hybrid lens mode which covers an analysis area of 210,000 μm^2 (700 \times 300 μm). Spectra were charge corrected to bring the main line of the C 1s core level spectrum to 285.0 eV.

4.4 Results and discussion

All silicon samples in this work were hydrogen-terminated surfaces^[52] modified by a hydrosilylation reaction (**1**, Scheme 4.1) to form a silicon-carbon-bound monolayer that minimizes anodic damaging of the substrate.^[48] X-Ray diffraction (XRD) patterns are shown in Figure 4.2, and a stereographic projections indicating the relative orientation of the three crystal facets are in Figure C1 (Appendix C). High-resolution X-ray photoelectron spectroscopy (XPS) scans of the Si 2p region (Figure C2, Appendix) demonstrates the monolayer ability (**S-1**) to prevent appreciable oxidation of the underlying silicon substrate. XPS data indicate that for all three facets, the

amount of silicon oxide was below the spectrometer detection limit, and the deconvolution of the C 1s XPS narrow region (Figure C2 Appendix C) shows spectral features analogous to that of 1-alkynes monolayers prepared on either H-Si(111) or H-Si(100) surfaces.^[53]

The acetylene functionality of **S-1** samples allows tethering a redox-active molecule, and as shown in Scheme 4.1, ferrocene units (**2**) were grafted on the electrodes via a copper(I)-catalyzed azide-alkyne cycloaddition (CuAAC) reaction.^[54, 55] As the rate constant for a redox reaction involving a surface-bound redox molecule depends on the molecule surface density,^[33] it was important to ensure a consistent ferrocene coverage before attempting a comparison between samples prepared on different silicon facets. Cyclic voltammetry (CV) experiments were therefore conducted to establish yields of the CuAAC reaction leading to **S-2**. Representative CV curves are shown in Figure 4.1a–c, with the coverage analysis shown in Figure 4.1d. Coverages calculated from the Faradaic charge, taken as the background-subtracted integrated current from the anodic scan, are comparable on Si(111), Si(211), and Si(110), being $(2.05 \pm 0.51) \times 10^{-10}$, $(2.19 \pm 0.40) \times 10^{-10}$, and $(1.86 \pm 0.65) \times 10^{-10}$ mol cm⁻², respectively. It is therefore unlikely that unequal surface coverages would lead to differences in k_{et} values, if any, between these three surface systems. This coverage is approximately 50% of that expected for a hexagonally close-packed full monolayer of ferrocene molecules, if the ferrocene molecules are assumed to be spherical with a diameter of 0.66 nm.^[56]

Further, the ferrocene films exhibit CV waves with full width at half maximum (fwhm hereafter) of 113 ± 2 mV in all the three substrates. The ideal fwhm from the Langmuir isotherm of a Nernstian process is 90.6 mV, and theoretical models are available to explain a non-ideal fwhm as a consequence of attractive/repulsive interactions experienced by the surface-tethered molecule.^[29] Fwhms larger than 90.6 mV are often reported in literature^[57] and can be explained as repulsive interactions between the electroactive species.^[30] The magnitude of these unavoidable interactions are therefore comparable in all three surface systems. Electrostatic attractive forces between the positive ferricenium tethers and the substrate, which would manifest as a fwhm < 90.6

mV,^[29] were not observed as they were prevented by the choice of highly doped p-type substrates.

Next, the electrical conductivity of the Si(211), Si(111) and Si(100) surfaces was

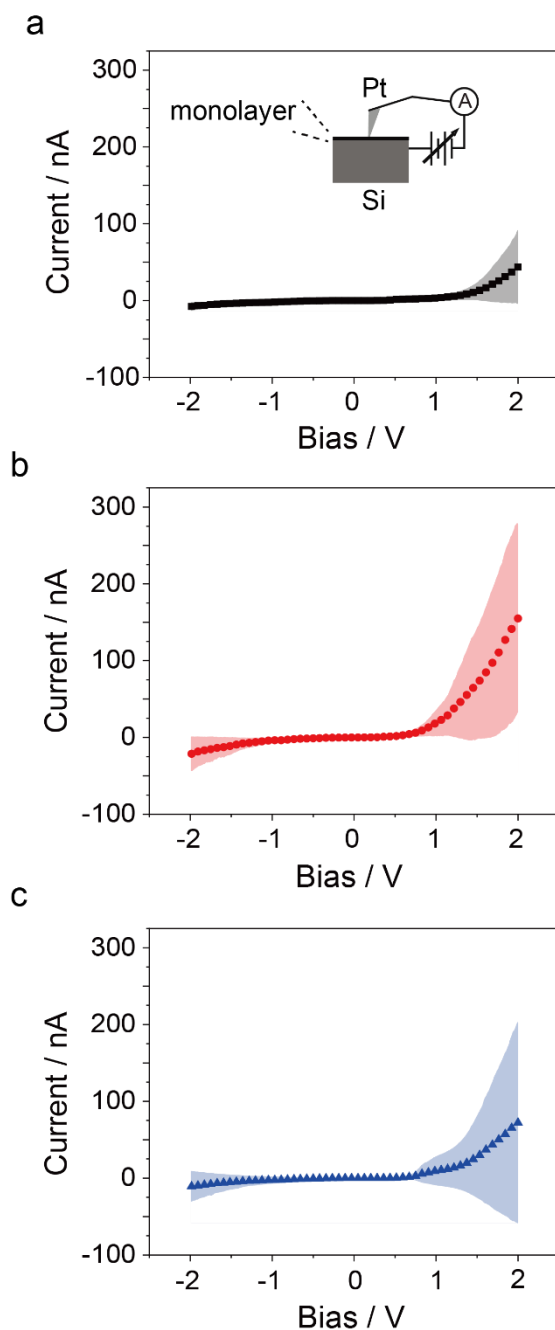


Figure 4.3. Measurement schematic and current–potential (I – V) data for platinum–silicon junctions obtained by conductive mode (PF-TUNA) atomic force microscopy (AFM) on monolayer-modified (*S-1*) Si(111) (a), Si(211) (b), and Si(110) (c). Solid symbols indicate the mean value of 400 I – V sweeps obtained on four independently prepared and analyzed samples. The color-shaded areas represent the data standard deviation.

probed by conductive atomic force microscopy (cAFM, PF-TUNA) using solid platinum AFM tips as the top metal contact. Current–voltage measurements (I–Vs) of the platinum–monolayer–silicon junctions (**S-1** samples) are shown in Figure 4.3, and the bias routing is from the substrate to the tip, so that the forward current of the junction appears in the positive quadrant (positive current, positive bias). The I–V characteristics indicate that, regardless of the bias magnitude, the electrical junction conductivity is considerably larger on Si(211) than on Si(110), and that the least conductive systems are those prepared on Si(111) crystals. For instance, at a positive sample–tip bias of 1500 mV, which is approximately 300 mV more positive than the system flat-band potential (approximated as the bias at which forward currents begin to rise exponentially), the mean relative conductivities of Si(211), Si(110), and Si(111) are in the ratio 5.9:2.3:1.0. These mean conductivities are statistically different, as inferred by an independent samples *t*-test. For example comparing Si(211) against Si(111), the experimental *t* value at 1500 mV is 7.22, which is significantly greater than the critical *t* value of 2.58 (99% confidence).^[49]

Measuring impedances over a broad range of frequencies allows to estimate individual element of an electrical circuit that can model the kinetics of a redox reaction.^[33] Representative electrochemical impedance spectroscopy (EIS) data, obtained on **S-2** samples with the aim to estimate differences in k_{et} between Si(111), Si(211) and Si(110) are shown in Figure 4.4a–c. EIS data are displayed as Bode plots, which can visually highlight variations in electrochemical kinetics. As the AC frequency becomes comparable to the time constant of the redox reaction, the slope of *Z* versus frequency plot moves towards zero, and simultaneously the value of phase angle reaches its minimum. From the EIS plots in Figure 4.4 it is apparent that the three surface systems have very similar redox kinetics. A more detailed and quantitative treatment of the kinetic properties of **S-2** samples relied on an established formalism that describes the relationship between circuit elements (C_{ads} , adsorption pseudo-capacitance; R_{ct} , charge-transfer resistance; shown in the equivalent circuit of Figure C3, Appendix C) and the kinetic parameters of strongly adsorbed redox species.^[58-60] C_{ads} , as well as the double-

layer capacitance (C_{dl}), showed frequency-dependent behavior and were therefore treated as constant-phase elements (CPEs). A CPE defines an inhomogeneity in the electrochemical system, such as kinetic dispersion.^[61] However, in our redox monolayer systems the CPEs behave very similar to a capacitor, as the power-law modifiers have values between 0.95 and 0.99, where unity indicates an ideal capacitor. From the refined C_{ads} and R_{ct} values, electron-transfer rate constants, k_{et} , were estimated as $(4.63 \pm 0.65) \times 10^2 \text{ s}^{-1}$ for Si(111), $(3.67 \pm 1.24) \times 10^2 \text{ s}^{-1}$ for Si(211) and $(4.81 \pm 1.38) \times 10^2 \text{ s}^{-1}$ for Si(110), thus indistinguishable within the experimental error (Figure 4.4d). Further, for all the three systems, at low frequencies – where the impedance is dominated by double layer charging – the phase angle approaches -90° , indicating that all samples are extremely smooth. The sigmoid shape that starts near 0° at high frequency and shifts close to -90° at low frequencies is often diagnostic of monolayer

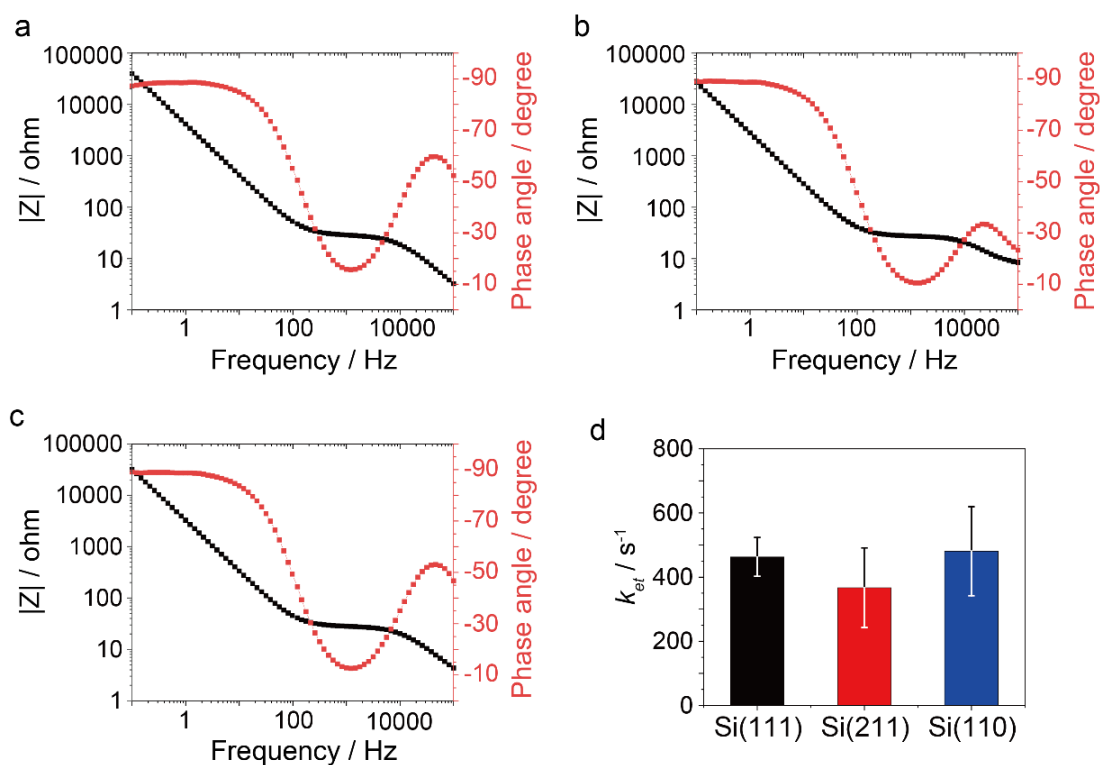


Figure 4.4. Representative EIS Bode plots for S-2 samples prepared on silicon crystals of different orientation ((a), Si(111); (b), Si(211); (c) Si(110)). The DC bias of the EIS measurement was set to the $E_{1/2}$ value obtained from CV measurements, and the amplitude of the AC perturbation was set to 15 mV. All experiments were performed in aqueous 1.0 M HClO₄. (d) Plot of the EIS-derived k_{et} values.

imperfections and surface roughness, but in our experiments a minor dispersion is only observed for the more commonly used Si(111). The EIS-inferred superior smoothness of both Si(211) and Si(110) agrees with AFM topographic data (Figure C4, Appendix C). This is an important finding, as it suggests that high quality monolayers can be prepared on a range of previously neglected low indexes silicon facets, such as Si(110) and Si(211).

4.5 Conclusions

We have explored a model electrochemical reaction, the oxidation and reduction of ferrocene, in diffusionless monolayer systems prepared on Si(111), Si(211) and Si(110) surfaces. In all three cases the redox system behaves close to ideality, suggesting that highly conductive (211) and (110) silicon crystals are an excellent alternative to conventional and widespread Si(111) substrates. Current–potential characteristics acquired by conductive atomic force microscopy reveals that surface conductivity decreases in the order Si(211)>>Si(110)>Si(111). Unlike systems where differences in electrical conductivity are imparted by changes to the chemical nature of the monolayer anchoring group,^[40] and unlike the inverse relationship between electron transfer rate constants and the length of alkyl spacers separating electrode and redox unit,^[62, 63] we found that identical surface chemistry on Si(211), Si(110), and Si(111) leads to comparable kinetics of a redox reaction occurring at the monolayer distal end. While other higher index substrates, such as Si(311) and Si(411), remain to be investigated, the current findings demonstrate a pronounced facet-dependent electrical conductivity,^[64] expand the range of silicon orientations viable as electrode material, and suggest literature discrepancies in electrochemical rate constants not to be linked to substrate defects, such as ubiquitous surface miscuts.

4.6 References

- [1]. Sagiv, J., Organized Monolayers by Adsorption. 1. Formation and Structure of Oleophobic Mixed Monolayers on Solid Surfaces. *J. Am. Chem. Soc.* **1980**, *102*,

- (1), 92–98.
- [2]. Fabre, B., Functionalization of Oxide-Free Silicon Surfaces with Redox-Active Assemblies. *Chem. Rev.* **2016**, *116*, (8), 4808–4849.
- [3]. Vericat, C.; Vela, M. E.; Benitez, G.; Carro, P.; Salvarezza, R. C., Self-Assembled Monolayers of Thiols and Dithiols on Gold: New Challenges for a Well-Known System. *Chem. Soc. Rev.* **2010**, *39*, (5), 1805–1834.
- [4]. Linford, M. R.; Chidsey, C. E. D., Alkyl Monolayers Covalently Bonded to Silicon Surfaces. *J. Am. Chem. Soc.* **1993**, *115*, (26), 12631–12632.
- [5]. Linford, M. R.; Fenter, P.; Eisenberger, P. M.; Chidsey, C. E. D., Alkyl Monolayers on Silicon Prepared from 1-Alkenes and Hydrogen-Terminated Silicon. *J. Am. Chem. Soc.* **1995**, *117*, (11), 3145–3155.
- [6]. Aragonès, A. C.; Darwish, N.; Ciampi, S.; Sanz, F.; Gooding, J. J.; Díez-Pérez, I., Single-Molecule Electrical Contacts on Silicon Electrodes under Ambient Conditions. *Nat. Commun.* **2017**, *8*, 15056.
- [7]. Peiris, C. R.; Vogel, Y. B.; Le Brun, A. P.; Aragonés, A. C.; Coote, M. L.; Díez-Pérez, I.; Ciampi, S.; Darwish, N., Metal-Single-Molecule-Semiconductor Junctions Formed by a Radical Reaction Bridging Gold and Silicon Electrodes. *J. Am. Chem. Soc.* **2019**, *141*, (37), 14788–14797.
- [8]. Vasquez, R. M.; Hlynchuk, S.; Maldonado, S., Effect of Covalent Surface Functionalization of Si on the Activity of Trifluoromethanesulfonic Anhydride for Suppressing Surface Recombination. *ACS Appl. Mater. Interfaces* **2020**, *12*, (51), 57560–57568.
- [9]. Zhang, S.; Ferrie, S.; Peiris, C. R.; Lyu, X.; Vogel, Y. B.; Darwish, N.; Ciampi, S., Common Background Signals in Voltammograms of Crystalline Silicon Electrodes are Reversible Silica–Silicon Redox Chemistry at Highly Conductive Surface Sites. *J. Am. Chem. Soc.* **2021**, *143*, (3), 1267–1272.
- [10]. Downes, N.; Cheek, Q.; Maldonado, S., Electroreduction of Perchlorinated Silanes for Si Electrodeposition. *J. Electrochem. Soc.* **2021**, *168*, (2), 022503.
- [11]. Landman, U.; Barnett, R. N.; Scherbakov, A. G.; Avouris, P., Metal-Semiconductor Nanocontacts: Silicon Nanowires. *Phys. Rev. Lett.* **2000**, *85*, (9), 1958–1961.
- [12]. Schmehl, A.; Vaithyanathan, V.; Herrnberger, A.; Thiel, S.; Richter, C.; Liberati, M.; Heeg, T.; Rokerath, M.; Kourkoutis, L. F.; Muhlbauer, S.; Boni, P.; Muller, D. A.; Barash, Y.; Schubert, J.; Idzerda, Y.; Mannhart, J.; Schlom, D. G., Epitaxial Integration of the Highly Spin-Polarized Ferromagnetic Semiconductor EuO with Silicon and GaN. *Nat. Mater.* **2007**, *6*, (11), 882–887.
- [13]. Zhang, H.; Liu, H.; Wei, K.; Kurakevych, O. O.; Le Godec, Y.; Liu, Z.; Martin, J.; Guerrette, M.; Nolas, G. S.; Strobel, T. A., BC8 Silicon (Si-III) is a Narrow-Gap Semiconductor. *Phys. Rev. Lett.* **2017**, *118*, (14), 146601.
- [14]. Lapano, J.; Brahle, M.; Zhang, L.; Roth, J.; Pogrebnyakov, A.; Engel-Herbert, R., Scaling Growth Rates for Perovskite Oxide Virtual Substrates on Silicon. *Nat. Commun.* **2019**, *10*, (1), 2464.
- [15]. Wang, J.; Yang, Z.; Chen, W.; Du, L.; Jiao, B.; Krause, S.; Wang, P.; Wei, Q.; Zhang, D.-W.; Wu, C., Modulated Light-Activated Electrochemistry at

- Silicon Functionalized with Metal-Organic Frameworks Towards Addressable DNA Chips. *Biosens. Bioelectron.* **2019**, *146*, 111750.
- [16]. Vogel, Y. B.; Darwish, N.; Ciampi, S., Spatiotemporal Control of Electrochemiluminescence Guided by a Visible Light Stimulus. *Cell Rep. Phys. Sci.* **2020**, *1*, (7), 100107.
- [17]. Ciampi, S.; James, M.; Le Saux, G.; Gaus, K.; Justin Gooding, J., Electrochemical "Switching" of Si(100) Modular Assemblies. *J. Am. Chem. Soc.* **2012**, *134*, (2), 844–847.
- [18]. Qin, G.; Santos, C.; Zhang, W.; Li, Y.; Kumar, A.; Erasquin, U. J.; Liu, K.; Muradov, P.; Trautner, B. W.; Cai, C., Biofunctionalization on Alkylated Silicon Substrate Surfaces via "Click" Chemistry. *J. Am. Chem. Soc.* **2010**, *132*, (46), 16432–16441.
- [19]. Chen, L.; Zhou, Y.; Jiang, S.; Kunze, J.; Schmuki, P.; Krause, S., High resolution LAPS and SPIM. *Electrochem. Commun.* **2010**, *12*, (6), 758–760
- [20]. Juan-Colás, J.; Parkin, A.; Dunn, K. E.; Scullion, M. G.; Krauss, T. F.; Johnson, S. D., The Electrophotonic Silicon Biosensor. *Nat. Commun.* **2016**, *7*, (1), 12769.
- [21]. Terrero Rodríguez, I. M.; Borrill, A. J.; Schaffer, K. J.; Hernandez, J. B.; O'Neil, G. D., Light-Addressable Electrochemical Sensing with Electrodeposited n-Silicon/Gold Nanoparticle Schottky Junctions. *Anal. Chem.* **2020**, *92*, (16), 11444–11452.
- [22]. Pekarek, R. T.; Kearney, K.; Simon, B. M.; Ertekin, E.; Rockett, A. A.; Rose, M. J., Identifying Charge Transfer Mechanisms across Semiconductor Heterostructures via Surface Dipole Modulation and Multiscale Modeling. *J. Am. Chem. Soc.* **2018**, *140*, (41), 13223-13232.
- [23]. Ciampi, S.; Gooding, J. J., Direct Electrochemistry of Cytochrome c at Modified Si(100) Electrodes. *Chem. Eur. J.* **2010**, *16*, (20), 5961–5968.
- [24]. Chen, X.; Park, Y. J.; Kang, M.; Kang, S.-K.; Koo, J.; Shinde, S. M.; Shin, J.; Jeon, S.; Park, G.; Yan, Y.; MacEwan, M. R.; Ray, W. Z.; Lee, K.-M.; Rogers, J. A.; Ahn, J.-H., CVD-grown monolayer MoS₂ in bioabsorbable electronics and biosensors. *Nat. Commun.* **2018**, *9*, (1), 1690.
- [25]. Fabre, B., Ferrocene-Terminated Monolayers Covalently Bound to Hydrogen-Terminated Silicon Surfaces. Toward the Development of Charge Storage and Communication Devices. *Acc. Chem. Res.* **2010**, *43*, (12), 1509–1518.
- [26]. Fabre, B.; Pujari, S. P.; Scheres, L.; Zuilhof, H., Micropatterned Ferrocenyl Monolayers Covalently Bound to Hydrogen-Terminated Silicon Surfaces: Effects of Pattern Size on the Cyclic Voltammetry and Capacitance Characteristics. *Langmuir* **2014**, *30*, (24), 7235–7243.
- [27]. Heinze, J., Cyclic Voltammetry—"Electrochemical Spectroscopy". *New Analytical Methods* (25). *Angew. Chem. Int. Ed.* **1984**, *23*, (11), 831–847.
- [28]. Santangelo, P. G.; Miskelly, G. M.; Lewis, N. S., Cyclic Voltammetry at Semiconductor Photoelectrodes. 1. Ideal Surface-Attached Redox Couples with Ideal Semiconductor Behavior. *J. Phys. Chem.* **1988**, *92*, (22), 6359–6367.
- [29]. Vogel, Y. B.; Zhang, L.; Darwish, N.; Gonçalves, V. R.; Le Brun, A.; Gooding,

- J. J.; Molina, A.; Wallace, G. G.; Coote, M. L.; Gonzalez, J.; Ciampi, S., Reproducible flaws unveil electrostatic aspects of semiconductor electrochemistry. *Nat. Commun.* **2017**, *8*, (1), 2066.
- [30]. Vogel, Y. B.; Molina, A.; Gonzalez, J.; Ciampi, S., Quantitative Analysis of Cyclic Voltammetry of Redox Monolayers Adsorbed on Semiconductors: Isolating Electrode Kinetics, Lateral Interactions, and Diode Currents. *Anal. Chem.* **2019**, *91*, (9), 5929–5937.
- [31]. Vogel, Y. B.; Molina, A.; Gonzalez, J.; Ciampi, S., Microelectrode Arrays with Active-Area Geometries Defined by Spatial Light Modulation. *Electrochim. Acta* **2020**, *356*, 136849.
- [32]. Gonzalez, J.; Sequí-Castellano, J. A., Electrochemical determination of kinetic parameters of surface confined redox probes in presence of intermolecular interactions by means of Cyclic Voltammetry. Application to TEMPO monolayers in gold and platinum electrodes. *Electrochim. Acta* **2021**, *365*, 137331.
- [33]. Ciampi, S.; Choudhury, M. H.; Ahmad, S. A. B. A.; Darwish, N.; Brun, A. L.; Gooding, J. J., The Impact of Surface Coverage on the Kinetics of Electron Transfer Through Redox Monolayers on a Silicon Electrode Surface. *Electrochim. Acta* **2015**, *186*, 216–222.
- [34]. Laborda, E.; González, J.; Molina, A., Analytical Theory for Ion Transfer–Electron Transfer Coupled Reactions at Redox Layer–Modified/Thick Film–Modified Electrodes. *Curr. Opin. Electrochem.* **2020**, *19*, 78–87.
- [35]. Gonzalez, J.; Sequí, J.-A., Kinetic Implications of the Presence of Intermolecular Interactions in the Response of Binary Self-Assembled Electroactive Monolayers. *ACS Omega* **2018**, *3*, (1), 1276–1292.
- [36]. Dhar, D.; McKenas, C. G.; Huang, C.-W.; Atkin, J. M.; Dempsey, J. L.; Lockett, M. R., Quantitative Effects of Disorder on Chemically Modified Amorphous Carbon Electrodes. *ACS Appl. Energy Mater.* **2020**, *3*, (8), 8038–8047.
- [37]. Patel, D. A.; Chevalier, R. B.; Weller, A. M.; Shakespeare, C. C.; Soares, E. J.; Landis, E. C., Porosity Effects on the Ordering and Stability of Self-Assembled Monolayers on Nanoporous Gold. *J. Phys. Chem. C* **2020**, *124*, (49), 26851–26863.
- [38]. Chen, F.; Li, X.; Hihath, J.; Huang, Z.; Tao, N., Effect of Anchoring Groups on Single-Molecule Conductance: Comparative Study of Thiol-, Amine-, and Carboxylic-Acid-Terminated Molecules. *J. Am. Chem. Soc.* **2006**, *128*, (49), 15874–15881.
- [39]. Wierzbinski, E.; Venkatramani, R.; Davis, K. L.; Bezer, S.; Kong, J.; Xing, Y.; Borguet, E.; Achim, C.; Beratan, D. N.; Waldeck, D. H., The Single-Molecule Conductance and Electrochemical Electron-Transfer Rate Are Related by a Power Law. *ACS Nano* **2013**, *7*, (6), 5391–5401.
- [40]. Dief, E. M.; Darwish, N., Ultrasonic Generation of Thiyl Radicals: A General Method of Rapidly Connecting Molecules to a Range of Electrodes for Electrochemical and Molecular Electronics Applications. *ACS Sens.* **2021**, *6*,

- (2), 573–580.
- [41]. Allongue, P.; Henry de Villeneuve, C.; Morin, S.; Boukherroub, R.; Wayner, D. D. M., The preparation of flat H-Si(111) surfaces in 40% NH₄F revisited. *Electrochim. Acta* **2000**, *45*, (28), 4591–4598.
- [42]. Tan, C.-S.; Hsieh, P.-L.; Chen, L.-J.; Huang, M. H., Silicon Wafers with Facet-Dependent Electrical Conductivity Properties. *Angew. Chem. Int. Ed.* **2017**, *56*, (48), 15339–15343.
- [43]. Vogel, Y. B.; Zhang, J.; Darwish, N.; Ciampi, S., Switching of Current Rectification Ratios within a Single Nanocrystal by Facet-Resolved Electrical Wiring. *Acs Nano* **2018**, *12*, (8), 8071–8080.
- [44]. Rohde, R. D.; Agnew, H. D.; Yeo, W.-S.; Bailey, R. C.; Heath, J. R., A Non-Oxidative Approach toward Chemically and Electrochemically Functionalizing Si(111). *J. Am. Chem. Soc.* **2006**, *128*, (29), 9518–9525.
- [45]. O’Leary, L. E.; Rose, M. J.; Ding, T. X.; Johansson, E.; Brunschwig, B. S.; Lewis, N. S., Heck Coupling of Olefins to Mixed Methyl/Thienyl Monolayers on Si(111) Surfaces. *J. Am. Chem. Soc.* **2013**, *135*, (27), 10081–10090.
- [46]. Zhang, L.; Vogel, Y. B.; Noble, B. B.; Goncales, V. R.; Darwish, N.; Brun, A. L.; Gooding, J. J.; Wallace, G. G.; Coote, M. L.; Ciampi, S., TEMPO Monolayers on Si(100) Electrodes: Electrostatic Effects by the Electrolyte and Semiconductor Space-Charge on the Electroactivity of a Persistent Radical. *J. Am. Chem. Soc.* **2016**, *138*, (30), 9611–9619.
- [47]. Yang, Y.; Ciampi, S.; Gooding, J. J., Coupled Thermodynamic and Kinetic Changes in the Electrochemistry of Ferrocenyl Monolayers Induced by Light. *Langmuir* **2017**, *33*, (10), 2497–2503.
- [48]. Ciampi, S.; Eggers, P. K.; Le Saux, G.; James, M.; Harper, J. B.; Gooding, J. J., Silicon (100) electrodes resistant to oxidation in aqueous solutions: an unexpected benefit of surface acetylene moieties. *Langmuir* **2009**, *25*, (4), 2530–2539.
- [49]. Miller, J. N.; Miller, J. C., *Statistics and Chemometrics for Analytical Chemistry*. 5th ed. Pearson education: Essex, England, 2005.
- [50]. Laviron, E., A.C. polarography and faradaic impedance of strongly adsorbed electroactive species: Part II. Theoretical study of a quasi-reversible reaction in the case of a Frumkin isotherm. *J. Electroanal. Chem. Interfacial Electrochem.* **1979**, *105*, (1), 25-34.
- [51]. Laviron, E., A.C. Polarography and faradaic impedance of strongly adsorbed electroactive species: Part III. Theoretical complex plane analysis for a surface redox reaction. *Journal of Electroanalytical Chemistry and Interfacial Electrochemistry* **1979**, *105*, (1), 35-42.
- [52]. Higashi, G. S.; Becker, R. S.; Chabal, Y. J.; Becker, A. J., Comparison of Si(111) Surfaces Prepared Using Aqueous Solutions of NH₄F versus HF. *Appl. Phys. Lett.* **1991**, *58*, (15), 1656–1658.
- [53]. Kondo, M.; Mates, T. E.; Fischer, D. A.; Wudl, F.; Kramer, E. J., Bonding Structure of Phenylacetylene on Hydrogen-Terminated Si(111) and Si(100): Surface Photoelectron Spectroscopy Analysis and Ab Initio Calculations.

- Langmuir* **2010**, *26*, (22), 17000–17012.
- [54]. Ciampi, S.; Bocking, T.; Kilian, K. A.; James, M.; Harper, J. B.; Gooding, J. J., Functionalization of Acetylene-Terminated Monolayers on Si(100) Surfaces: A Click Chemistry Approach. *Langmuir* **2007**, *23*, (18), 9320–9329.
- [55]. Ciampi, S.; Harper, J. B.; Gooding, J. J., Wet Chemical Routes to the Assembly of Organic Monolayers on Silicon Surfaces via the Formation of Si-C Bonds: Surface Preparation, Passivation and Functionalization. *Chem. Soc. Rev.* **2010**, *39*, (6), 2158–2183.
- [56]. Rowe, G. K.; Creager, S. E., Redox and Ion-Pairing Thermodynamics in Self-Assembled Monolayers. *Langmuir* **1991**, *7*, (10), 2307–2312.
- [57]. Paxton, W. F.; Kleinman, S. L.; Basuray, A. N.; Stoddart, J. F.; Van Duyne, R. P., Surface-Enhanced Raman Spectroelectrochemistry of TTF-Modified Self-Assembled Monolayers. *J. Phys. Chem. Lett.* **2011**, *2*, (10), 1145–1149.
- [58]. Laviron, E., A.C. Polarography and Faradaic Impedance of Strongly Adsorbed Electroactive Species: Part I. Theoretical and Experimental Study of a Quasi-Reversible Reaction in the Case of a Langmuir Isotherm. *J. Electroanal. Chem. Interf. Electrochem.* **1979**, *97*, (2), 135–149.
- [59]. Creager, S. E.; Wooster, T. T., A New Way of Using ac Voltammetry To Study Redox Kinetics in Electroactive Monolayers. *Anal. Chem.* **1998**, *70*, (20), 4257–4263.
- [60]. Abhayawardhana, A. D.; Sutherland, T. C., Heterogeneous Proton-Coupled Electron Transfer of an Aminoanthraquinone Self-Assembled Monolayer. *J. Phys. Chem. C* **2009**, *113*, (12), 4915–4924.
- [61]. Brevnov, D. A.; Finklea, H. O.; Van Ryswyk, H., AC Voltammetry Studies of Electron Transfer Kinetics for a Redox Couple Attached via Short Alkanethiols to a Gold Electrode. *J. Electroanal. Chem.* **2001**, *500*, (1), 100–107.
- [62]. Eckermann, A. L.; Feld, D. J.; Shaw, J. A.; Meade, T. J., Electrochemistry of Redox-Active Self-Assembled Monolayers. *Coord. Chem. Rev.* **2010**, *254*, (15), 1769–1802.
- [63]. Eggers, P. K.; Darwish, N.; Paddon-Row, M. N.; Gooding, J. J., Surface-Bound Molecular Rulers for Probing the Electrical Double Layer. *J. Am. Chem. Soc.* **2012**, *134*, (17), 7539–7544.
- [64]. Tan, C.-S.; Huang, M. H., Metal-like Band Structures of Ultrathin Si {111} and {112} Surface Layers Revealed through Density Functional Theory Calculations. *Chem. - Eur. J.* **2017**, *23*, (49), 11866–11871.

Every reasonable effort has been made to acknowledge the owners of copyright material. I would be pleased to hear from any copyright owner who has been omitted or incorrectly acknowledged.

Chapter 5. Summary and conclusions

This dissertation presented surface chemistry, electrochemistry and AFM research about facet-resolved electrochemical effects in silicon. The electrodes were chemically modified with organic monolayers through hydrosilylation reactions, for the purpose of surface passivation, functionalization and most importantly, to access diffusionless redox systems. In summary, what the experiments presented in the previous chapters, and their analysis, have explored and demonstrated are: 1) photocurrent effects explains the origin of voltammetric peak multiplicity as heterogeneous leakage instead of what is normally explained as disorder; 2) facet-dependent conductivity effects to be linked to unexpected silica–silicon reversible redox chemistry, 3) lack of a relationship between surface conductivity and charge transfer rates of electroactive species adsorbed on monolayers.

Chapter 1 introduced the fundamental electrochemistry, electrochemistry and surface chemistry common to the all the results chapters. It was partially based on our recently published review on facet-dependent electrochemistry of semiconductors. (*Curr. Opin. Electrochem.* 2022, 35, 101085) The results presented in **Chapter 2** have successfully demonstrated that peak multiplicity in cyclic voltammograms (CV) – arguably the most common electroanalytical technique – is caused by heterogeneous photocurrent effects on the silicon electrode rather than disordered domains in the monolayers. The “disorder” hypothesis still prevail in literature while heterogeneity of photoeffects is rarely considered. Conductive atomic force microscopy (C-AFM) confirmed a heterogeneous leakage current resulting, therefore causing local differences in open circuit potential of silicon electrode, which eventually appeared as peak shifts and hence multiplicity in CVs.

Chapter 3 (*J. Am. Chem. Soc.* 2021;143(3), 1267–1272) unveils and exploits facet-dependent conductivity effects leading to the reversible silica–silicon redox reaction on some specific silicon crystal defects. CVs and C-AFM data were collected and analyzed

to conclude that highly conductive Si(110) facets, which existed in the edges of Si(111) terraces, are sites where the silica–silicon redox conversion becomes electrochemically reversible even at room temperature. The data of this chapter constitute the first example of reversible silica–silicon redox reaction in simple electrolyte rather than in molten salts. The scale is however “nanoscale”. But not occurring on a practical scale, it is a key step in advancing silica electrochemical reduction. Moreover, the results highlight an unexpected aspect of facet-resolved semiconductor electrochemistry. Most significantly, the result of this chapter redefines the electrochemical potential window accessible for studying the electrochemistry of silicon through electroanalytical approaches without interference from parasitic signals.

Chapter 4 presents data concluding that disparities in conductivity between different facets of silicon crystals don't affect measurably the redox electrochemical kinetics at the distal end of an electroactive organic monolayer adsorbed on these crystals. This chapter set a model system to estimate the electrochemical kinetics. In the experiments, surface densities of substrates with different facets [Si(111), Si(110), Si(211) modified with ferrocene SAMs] were constrained at the same level by estimating surface coverages from CVs. After ruling out the impact of surface densities on the electrochemical kinetics, the results of C-AFM experiments demonstrated that the conductivity is decreasing dramatically in the order Si(211)>Si(110)>Si(111). Despite the conspicuous difference (facet-dependent) in electrical conductivity (no free-energy changes involved), rates of redox reactions [estimated by electrochemical impedance spectroscopy (EIS)] proceeding at the distal end of SAMs attached on different facets were indistinguishable. This chapter carries also the message that highly conductive Si(110) and Si(211) substrates can be good replacement for traditional and extensively explored Si(111) substrates.

In conclusion, substantial achievements have been obtained in the emerging field of facet-resolved electrochemistry. The contribution of this thesis is to expand the field on semiconductor electrochemistry. The ultimate goal of semiconductor electrochemistry is to understand (and eventually predictably manipulate) the thermodynamics and

kinetics of redox processes taking place at the semiconductor electrode. Facet-resolved silicon electrochemistry aids in the search for the optimal electrode material which has so far remained largely a trial-and-error process. This research will play a vital role in incorporating novel material into the digitized world of the future.

Chapter 6. Perspective and outlook

The results of this thesis have redefined the potential window which can be employed to follow the progress of surface reactions. The initial aim of this doctoral project is to catalyze click reaction by the electric field, while in the investigating process we found that the electrochemistry of the surface facet defects was unknown. The facet resolved electrochemistry has great potential in designing novel catalysts for the redox electrochemical reaction to optimize the thermodynamics and electrochemical kinetics process.^[1] Chemical or electrochemical reactions always proceed by reorganizing the chemical bonds or redistributing the electron density of the reactants.^[2, 3] Therefore, controlling the direction of electronic movement is the key step in a catalytic process of a reaction. Conventionally, catalysis is employing special chemical molecules (which are not consumed in the procedure) to accelerate/inhibit the rate of a reaction. Recently, electric field catalysis has attracted scientists' interests as a "general and smart" catalyst increasingly,^[4-8] since the first electrostatic catalysis of the Diels–Alder reaction was reported in *Nature* as a proof-of-concept experimental survey of a specific bimolecular reaction in 2016.^[9] The *Nature* paper demonstrated that the external electric field can address exceptional and inevitable interaction towards the formation of C–C bonds and the orientation of chemical bonds along the reaction axis. It experimentally proved to align an electric field appropriately can manipulate the dipole direction of reactant molecule and regulate the active energetical barrier of reaction at the transition state. It is known that the above-mentioned features are facet-dependent, therefore combining facet-resolved electrochemistry with electrostatics (internal or external electric field) can pave a new path for the catalysis of organic synthesis at will in the future.

6.1 Outlook

Nucleophilic substitutions are one of the most important reactions in organic synthesis,

such as S_N1 (unimolecular nucleophilic substitution) and S_N2 (bimolecular nucleophilic substitution). It is known that electric fields (EF) from solvent and polar groups can accelerate or slow down the dissociation of chemical bonds involved in S_N1 reactions. On the contrary, it has not been proven experimentally that S_N2 reactions (some of them) can be catalyzed by exogenous electric fields. So far there are only theoretical calculations, not actual experiments.^[10, 11] For example, Yu et al. reported that when there is a competition between S_N1 and S_N2 paths, this competition can be tweaked by the electric field or charged functionalities.^[11] The S_N2 process proceeded prone while reactants were with the neutral nucleophiles and anion-leaving groups. One of the foreseen applications of molecular surface systems such as those described in this thesis is to validate (or falsify) such predictions. In this perspective chapter I therefore define a model reaction that could be used to design such experiment. The reaction is the Menshutkin reaction, which is a model S_N2 reaction. Shaik et al. reported that flipping the orientation of the electric field along the reaction axis can catalyze this reaction because the electric field could lower transition states hence have a catalytic effect towards the products.^[10] In order to ensure alignment between reaction axis and external field the reactants can be immobilized on different facets of silicon electrodes as outlined in the thesis. For example, tethering the monolayer on different facet substrates with halide derivatives (i.e., Br-, Cl-) at distal end as a nucleophile, the model Menshutkin reaction will perform with tert-aminomethyl ferrocene derivative as electrolyte (as electrochemical active label) under electric field. Another future application of facet resolved electrochemistry and may be down the line of electrochemical enantioselective synthesis, which is of great importance in the pharmaceutical industry. It is known that the feature of S_N2 reaction is chiral reversion (i.e., Walden inversion), and chirality is a primarily optical geometrical concept that refers to an object that is mirror asymmetry. The facet differences at the nanoscale have the potential to develop chiral amplification of surface crystal structure at a larger scale.^[12] Chirality exists extensively in living organisms, which are composed hierarchically from the asymmetrical molecular level to larger supramolecular

assembled aggregates. In the enzyme catalysis process, there exists a nanoscale electrostatics field which has been demonstrated by Boxer et al.^[13] By proper design, the different facets of crystal nanoparticles have the potential to address different asymmetric steric effects, which may aid chiral facet catalysis.

Moreover, different facet crystal structures can show different adsorption abilities at the catalyst surface. For instances, palladium is always employed in catalysis of hydrogen adsorption, it is reported that the electrochemical hydrogen adsorption was dependent on the surface structure of polycrystalline Pd.^[14] The microstructure of the Pd surface at the grain boundary can facilitate the adsorption rate. At low index facets (as grains close to (100), (101), and (111)), the hydrogen adsorption rates were lower compared to the high index facet such as grains close to (411). It addresses the potential to generate different electric field at different facet, as results of the chapter 3 demonstrating the different facet crystal showing different conductivities.

Overall, facet resolved electrochemistry will have significant potential in the engineering of chemical catalysis. A comprehension of how facet electric field governs chemical bond redistributing and controlling the reaction rate will benefit the design of novel catalysts. Also, facet-resolved electrochemistry can apply in many devices design fields, such as 1) in making the molecular transistor, it can regulate the rectification behavior by orienting the molecule direction in the circuits to be used as molecule memory devices; 2) in studying electrostatics function in the cell, it can understand the facet dependent effects in enzyme functions; 3) in optimizing the new semiconductor material, it can benefit the modern digitized world.

6.2 References

- [1]. Zhang, S.; Ciampi, S., Facet-resolved electrochemistry: from single particles to macroscopic crystals. *Curr. Opin. Electrochem.* **2022**, *35*, 101085.
- [2]. Shaik, S.; Mandal, D.; Ramanan, R., Oriented electric fields as future smart reagents in chemistry. *Nat Chem* **2016**, *8*, (12), 1091-1098.
- [3]. Dutta Dubey, K.; Stuyver, T.; Kalita, S.; Shaik, S., Solvent Organization and Rate Regulation of a Menshutkin Reaction by Oriented External Electric Fields are Revealed by Combined MD and QM/MM Calculations. *J. Am. Chem. Soc.*

- 2020**, *142*, (22), 9955-9965.
- [4]. Zhang, L.; Laborda, E.; Darwish, N.; Noble, B. B.; Tyrell, J.; Pluczyk, S.; Brun, A. P. L.; Wallace, G. G.; Gonzalez, J.; Coote, M. L.; Ciampi, S., Electrochemical and Electrostatic Cleavage of Alkoxyamines. *J. Am. Chem. Soc.* **2018**, *140*, (2), 766–774.
- [5]. Zhang, L.; Vogel, Y. B.; Noble, B. B.; Goncales, V. R.; Darwish, N.; Brun, A. L.; Gooding, J. J.; Wallace, G. G.; Coote, M. L.; Ciampi, S., TEMPO Monolayers on Si(100) Electrodes: Electrostatic Effects by the Electrolyte and Semiconductor Space-Charge on the Electroactivity of a Persistent Radical. *J. Am. Chem. Soc.* **2016**, *138*, (30), 9611–9619.
- [6]. Akamatsu, M.; Sakai, N.; Matile, S., Electric-Field-Assisted Anion- π Catalysis. *J Am Chem Soc* **2017**, *139*, (19), 6558-6561.
- [7]. Huang, X.; Tang, C.; Li, J.; Chen, L.-C.; Zheng, J.; Zhang, P.; Le, J.; Li, R.; Li, X.; Liu, J.; Yang, Y.; Shi, J.; Chen, Z.; Bai, M.; Zhang, H.-L.; Xia, H.; Cheng, J.; Tian, Z.-Q.; Hong, W., Electric field–induced selective catalysis of single-molecule reaction. *Sci Adv* **2019**, *5*, (6), eaaw3072.
- [8]. Heo, J.; Ahn, H.; Won, J.; Son, J. G.; Shon, H. K.; Lee, T. G.; Han, S. W.; Baik, M.-H., Electro-inductive effect: Electrodes as functional groups with tunable electronic properties. *Science* **2020**, *370*, (6513), 214-219.
- [9]. Aragonés, A. C.; Haworth, N. L.; Darwish, N.; Ciampi, S.; Bloomfield, N. J.; Wallace, G. G.; Diez-Perez, I.; Coote, M. L., Electrostatic catalysis of a Diels-Alder reaction. *Nature* **2016**, *531*, (7592), 88-91.
- [10]. Ramanan, R.; Danovich, D.; Mandal, D.; Shaik, S., Catalysis of Methyl Transfer Reactions by Oriented External Electric Fields: Are Gold-Thiolate Linkers Innocent? *J. Am. Chem. Soc.* **2018**, *140*, (12), 4354-4362.
- [11]. Yu, L. J.; Coote, M. L., Electrostatic Switching between S_N1 and S_N2 Pathways. *J Phys Chem A* **2019**, *123*, (2), 582-589.
- [12]. Im, S. W.; Ahn, H.-Y.; Kim, R. M.; Cho, N. H.; Kim, H.; Lim, Y.-C.; Lee, H.-E.; Nam, K. T., Chiral Surface and Geometry of Metal Nanocrystals. *Adv. Mater.* **2020**, *32*, (41), 1905758.
- [13]. Fried, S. D.; Bagchi, S.; Boxer, S. G., Extreme electric fields power catalysis in the active site of ketosteroid isomerase. *Science* **2014**, *346*, (6216), 1510-1514.
- [14]. Yule, L. C.; Daviddi, E.; West, G.; Bentley, C. L.; Unwin, P. R., Surface microstructural controls on electrochemical hydrogen absorption at polycrystalline palladium. *J. Electroanal. Chem.* **2020**, *872*, 114047.

Every reasonable effort has been made to acknowledge the owners of copyright material. I would be pleased to hear from any copyright owner who has been omitted or incorrectly acknowledged.

Appendix A

This material is adapted from the Supporting Information of the paper published by the American Chemical Society, in *Langmuir* 2022, 38, (2), 743–750 , “Non-ideal cyclic voltammetry of redox monolayers on silicon electrodes: peak splitting is caused by heterogeneous photocurrents and not by molecular disorder”. It is modified with minor changes in order to fit the general layout of this dissertation. This paper constitutes **Chapter 2**.

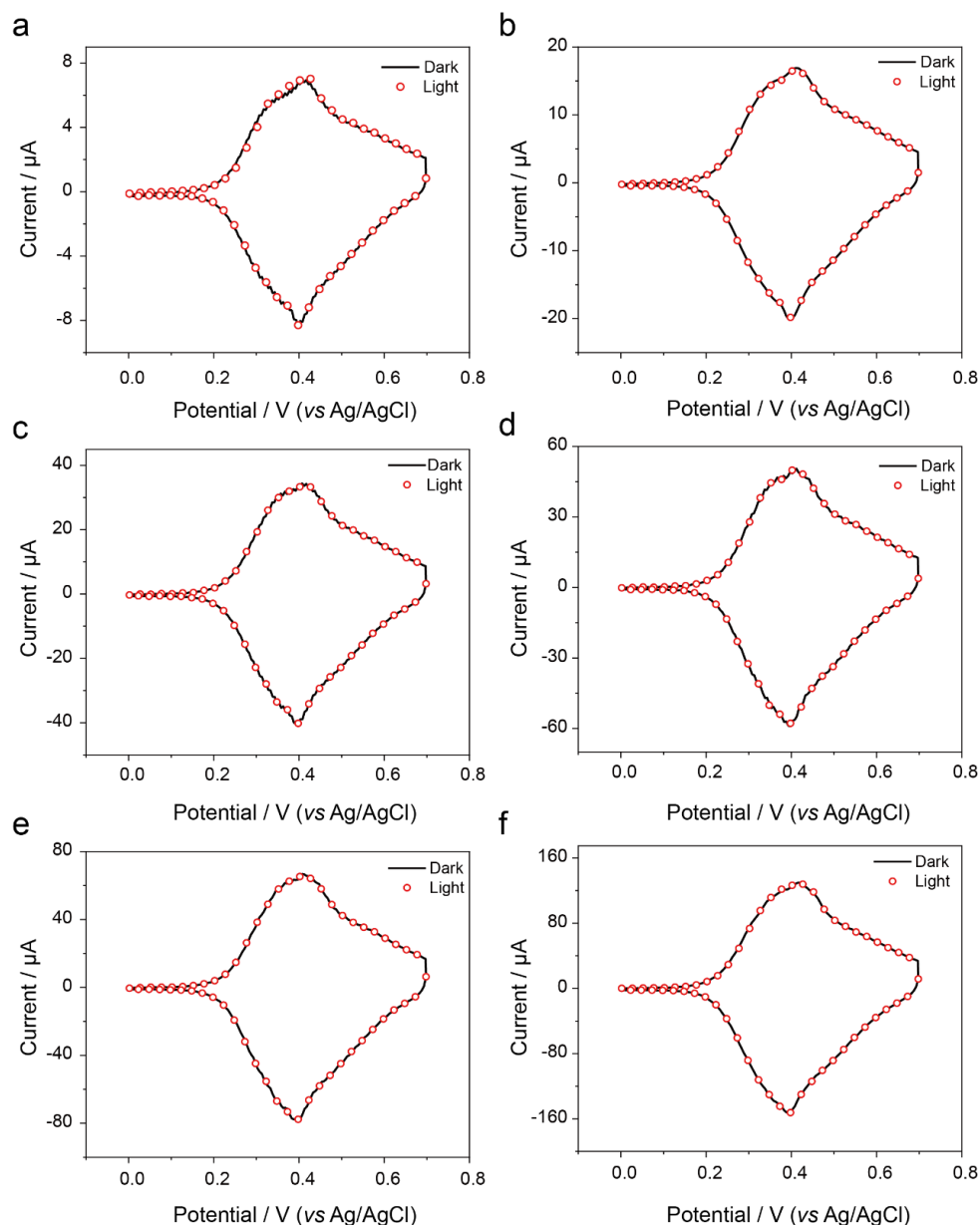


Figure A1. Representative CVs of a monolayer-modified gold electrode (11-ferrocenyl-1-undecanethiol monolayers self-assembled on Au(111)). The voltage sweep rate was changed between 100 and 2000 mV s^{-1} and the data acquired in 1.0 M HClO_4 , either under dark or under electrode illumination (solid line, dark; state, red empty symbols, light). Electrode illumination had no effect on the CV traces. (100 mV s^{-1} , dark coverage = $5.22 \times 10^{-10} \text{ mol cm}^{-2}$, coverage under light = $5.17 \times 10^{-10} \text{ mol cm}^{-2}$; b) 250 mV s^{-1} , dark coverage = $5.19 \times 10^{-10} \text{ mol cm}^{-2}$, coverage under light = $5.22 \times 10^{-10} \text{ mol cm}^{-2}$; c) 500 mV s^{-1} , dark coverage = $5.22 \times 10^{-10} \text{ mol cm}^{-2}$, coverage under light = $5.17 \times 10^{-10} \text{ mol cm}^{-2}$; d) 750 mV s^{-1} , dark coverage = $5.06 \times 10^{-10} \text{ mol cm}^{-2}$, coverage under light = $5.08 \times 10^{-10} \text{ mol cm}^{-2}$; e) 1000 mV s^{-1} , dark coverage = $5.12 \times 10^{-10} \text{ mol cm}^{-2}$, v $5.11 \times 10^{-10} \text{ mol cm}^{-2}$; f) 2000 mV s^{-1} , dark coverage = $4.99 \times 10^{-10} \text{ mol cm}^{-2}$, coverage under light = $4.97 \times 10^{-10} \text{ mol cm}^{-2}$)

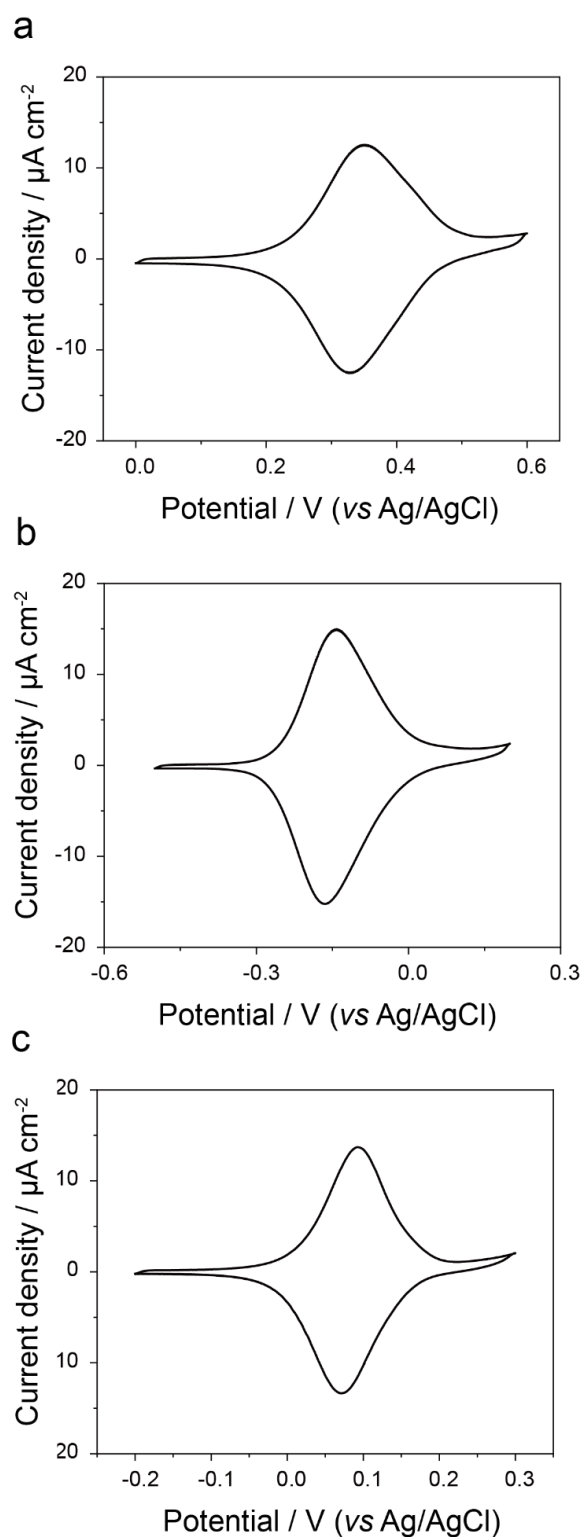


Figure A2. Representative CVs of M-2 samples prepared on either (a) HD p-type Si(111), dark, and indicating a ferrocene coverage of $1.94 \pm 0.26 \times 10^{-10} \text{ mol cm}^{-2}$, (b) LD n-type Si(111) under light intensity 24.1 mW cm^{-2} , with a coverage of $1.99 \pm 0.84 \times 10^{-10} \text{ mol cm}^{-2}$, and (c) LD n-type Si(100) under light intensity 24.1 W cm^{-2} , showing a coverage of $1.44 \pm 0.23 \times 10 \text{ mol cm}^{-2}$. The electrolyte was aqueous 1.0 M HClO_4 and the scan rate 100 mV s^{-1} .

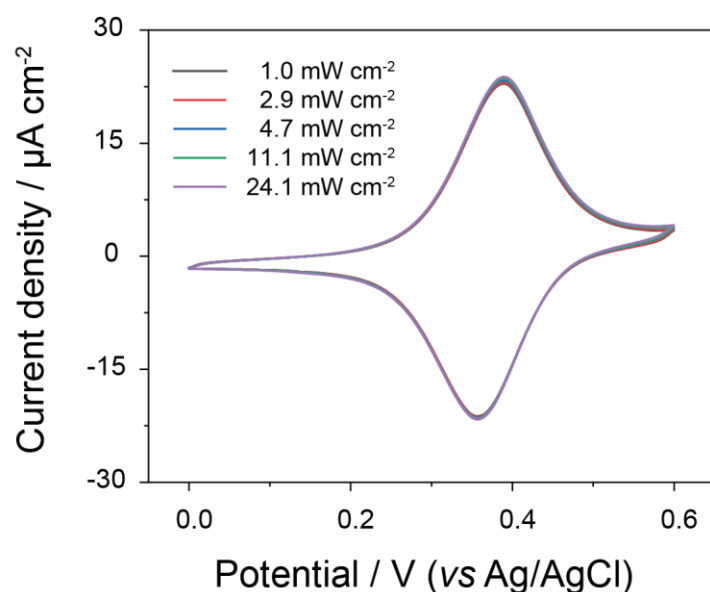


Figure A3. Representative CVs of *M-2* monolayers prepared on HD *p*-type Si(111) recorded under different light intensity (indicated in figure). The electrolyte was aqueous 1.0 M HClO₄ and the scan rate 100 mV s⁻¹.

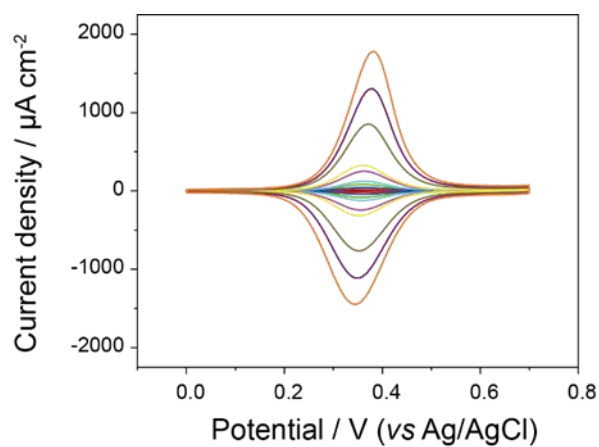


Figure A4. Representative CVs of *M-2* samples prepared on HD *p*-type Si(111) under dark at different voltage scan rate (50 mV s⁻¹, 100 mV s⁻¹, 250 mV s⁻¹, 500 mV s⁻¹, 750 mV s⁻¹, 1.0 V s⁻¹, 2.0 V s⁻¹, 5.0 V s⁻¹, 7.5 V s⁻¹, 10.0 V s⁻¹). The electrolyte was aqueous 1.0 M HClO₄.

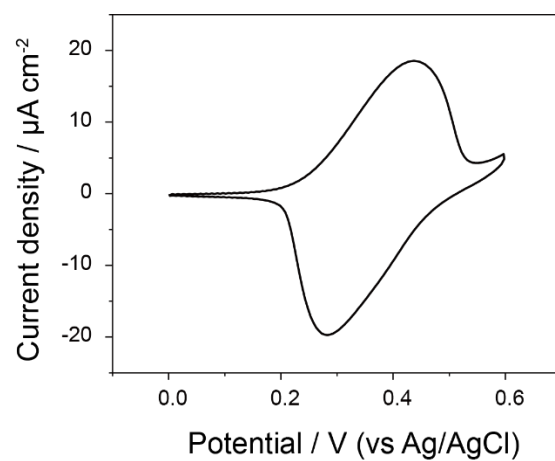


Figure A5. Representative CV of a M-2 sample prepared on LD n-type Si(111) and recorded under dark. The electrolyte was aqueous 1.0 M HClO₄ and the scan rate 100 mV s⁻¹.

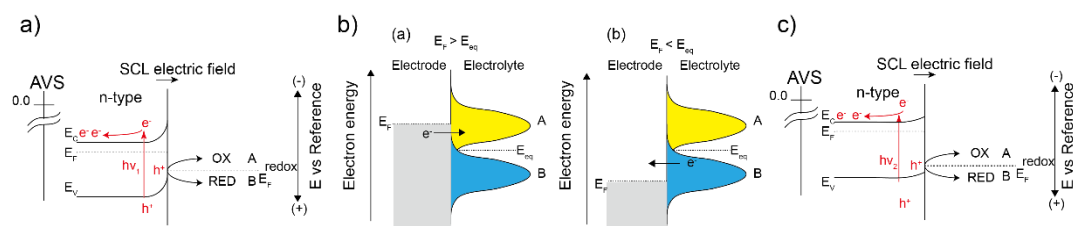


Figure A6. a) In n-type electrodes, at potentials more positive than EFB, the Fermi level is lowered (i.e. further away from the zero AVS) and electrons are forced away from the space charge region and leave behind ionized positively charged donor centers. In depletion, and under illumination, holes generated in the valence band will migrate toward the interface under an electric field pointing outward (i.e. bands pointing upward) where this vacant state at the top of the valence band will consume available electrons. Depleted n-type electrodes under illumination can therefore act as photoanodes. In summary, the blocking effect of depleted dark silicon electrodes is efficiently reversed upon illumination with light of a frequency greater than 2.7×10^{14} Hz provided that inversion is not reached and electron-hole recombination events are minimized. Generated electron-hole (e^-/h^+) pairs at depleted n-electrodes under illumination. Minority charge carriers migrate under the space-charge region electric field toward the electrolyte and participate in redox reactions (i.e. photooxidations at n-type electrodes). Since valence band holes mediate the oxidation of surface species, the potential at which the rate of change of surface concentrations peaks (i.e. a peak in the CV of non-diffusive species) is less positive (i.e. closer to the zero of the AVS scale), or in other words contra-thermodynamic relative to the situation in a metal electrode. The situation of a metal electrode is depicted in b). Here The applied potential lifting or lowering EF above or below E_{eq} corresponds to electro-reduction (a) and electro-oxidation (b). c) The effect of increasing the light intensity is that of flattening the bands (i.e. shifting upward the E_F)

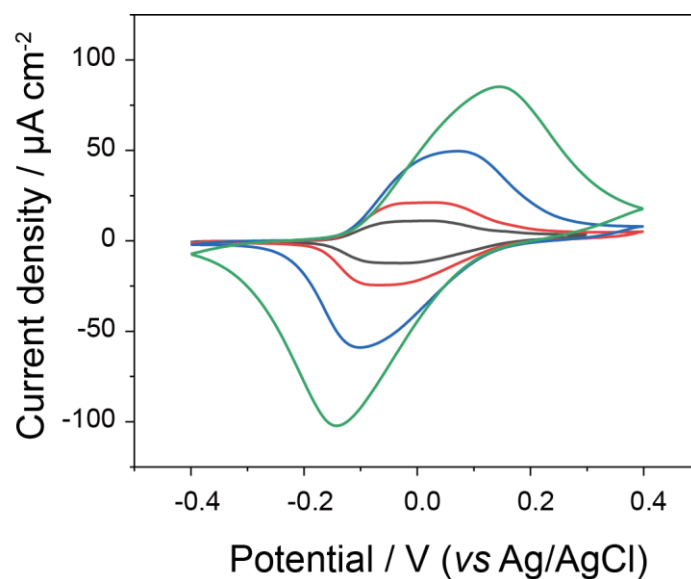


Figure A7 . Representative CVs of **M-2** samples prepared LD *n*-type Si(111) recorded under light intensity of 1.0 mW cm^{-2} by varying the voltage scan rate (0.1, 0.2, 0.5 and 1.0 V/s; $\Gamma = 2.34 \times 10^{-10} \text{ mol cm}^{-2}$). The electrolyte was aqueous 1.0 M HClO_4 .

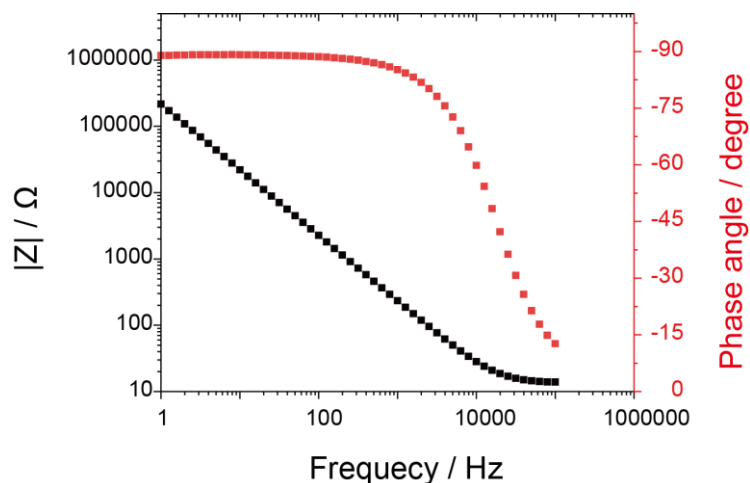


Figure A8. Electrochemical impedance spectroscopy (EIS) data for **M-2** monolayers (*n*-type, Si(111) dark) acquired between 10^5 Hz and 1 Hz , at an applied working electrode DC potential of 0.0 V versus Ag/AgCl and with an AC perturbation of 15 mV.

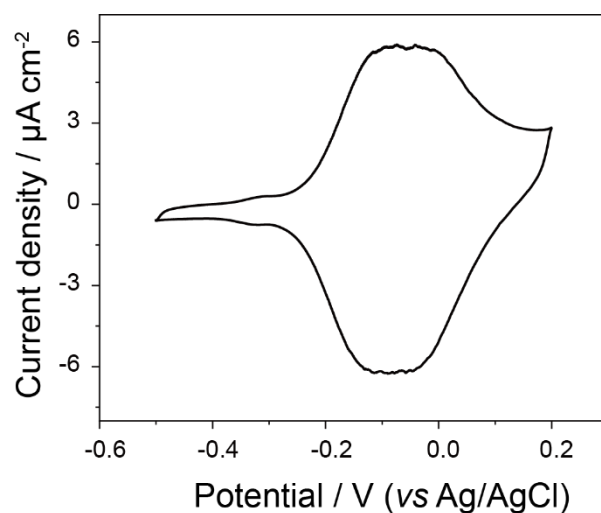


Figure A9. Representative CV of **M-2** sample prepared by LD n-type Si(111) photoanodes under light intensity 1.0 mW cm^{-2} in aqueous 1.0 M HClO_4 . The scan rate is 0.1 V/s , and the ferrocene coverage (Γ) is $1.07 \times 10^{-10} \text{ mol cm}^{-2}$. Click reaction quenched after 5 min

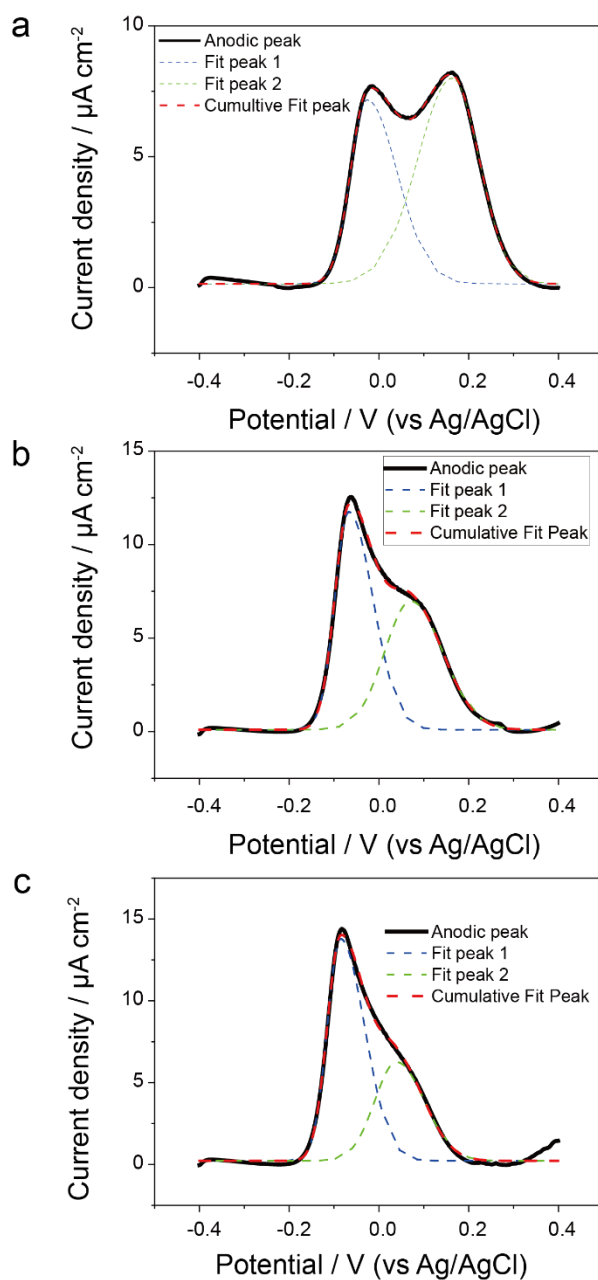


Figure A10. Deconvolution of the anodic peaks from representative CVs of **M-2** monolayers prepared on *n*-type LD, Si(111), recorded under variable light intensity. a) 1.0 mW cm^{-2} , cumulative coverage $2.40 \times 10^{-10} \text{ mol cm}^{-2}$, fwhm of peak 1 = 122.2 mV, fwhm peak 2 = 161.7 mV; b) 2.9 mW cm^{-2} , cumulative coverage $2.43 \times 10^{-10} \text{ mol cm}^{-2}$, fwhm of peak 1 = 99.7 mV, fwhm peak 2 = 152.2 mV; c) 4.7 mW cm^{-2} , cumulative coverage $2.45 \times 10^{-10} \text{ mol cm}^{-2}$, fwhm of peak 1 = 97.8 mV, fwhm peak 2 = 130.3 mV. Curve refinement was done using the bi-Gaussian peak function in Origin 9.

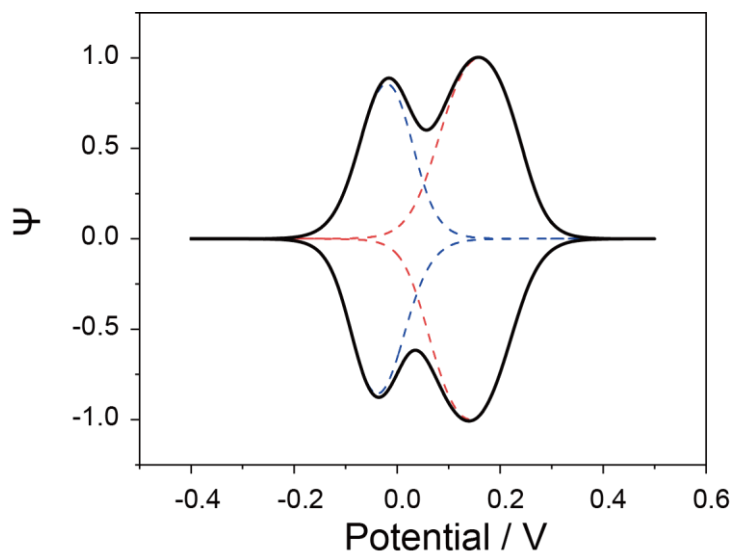


Figure A11. Simulation of the CV trace recorded at the lowest light intensity, demonstrating that the key feature of the experimental data, a ~ 190 mV peak-to-peak separation, can be accounted for as surface domains with a 1,000 fold difference in the dark leakage current (1.0×10^{-9} A for the blue dashed trace, 1.1×10^{-6} A for the red dashed trace). The self-interaction parameter, G , necessary to reproduce the experimental fwhm, is negative, indicating repulsive molecular interactions for ferrocenes in both domains (-1.4 , red trace; -0.6 , blue trace). Best fit parameters are 10 s^{-1} for the electron transfer rate constant, $750 \text{ } \mu\text{A}$ for photocurrent (both peaks), unity for the diode quality factor, and 0.5 for α .

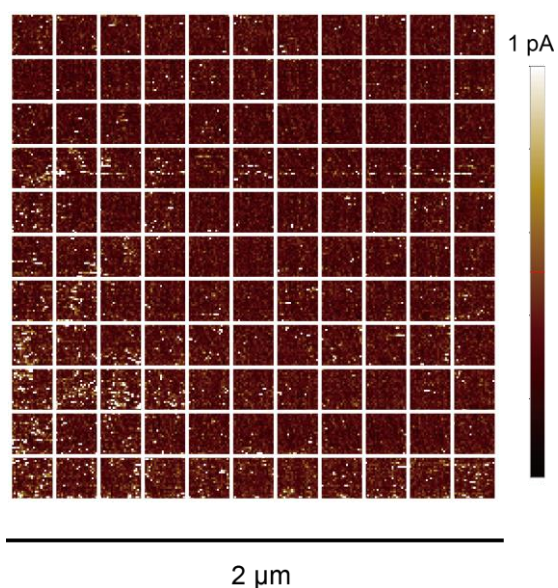


Figure A12. Representative AFM of current map at 0 V. The sampling area was of $2 \times 2 \mu\text{m}^2$. Individual I–V traces (from -2.0 V to $+2.0 \text{ V}$) were collected in the center of each square shown in figure.

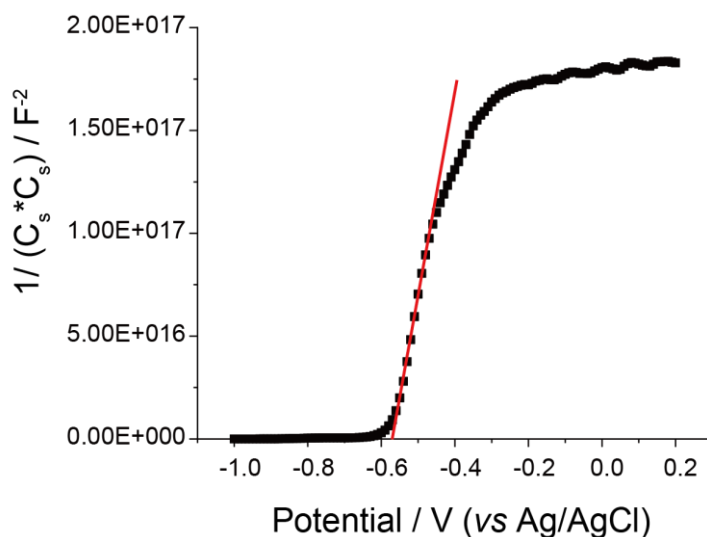


Figure A13. EIS Mott–Schottky (M–S) measurement of capacitance vs sample bias for M-2 samples prepared on LD n-type Si(111). The experiments were run in dark, with the AC frequency set to 40,000 Hz, the AC bias amplitude to 15 mV. The electrolyte was 1.0 M aqueous HClO_4 .

Appendix B

This part is adapted from the Supporting Information of the paper published by the American Chemical Society in *J. Am. Chem. Soc.* 2021, *143*, (3), 1267-1272, “Common Background Signals in Voltammograms of Crystalline Silicon Electrodes are Reversible Silica–Silicon Redox Chemistry at Highly Conductive Surface Sites”. It is modified with minor changes in order to fit the general layout of this dissertation. This paper constitutes **Chapter 3**.

B1. Control experiments on Si(111) wafers of different doping level and type

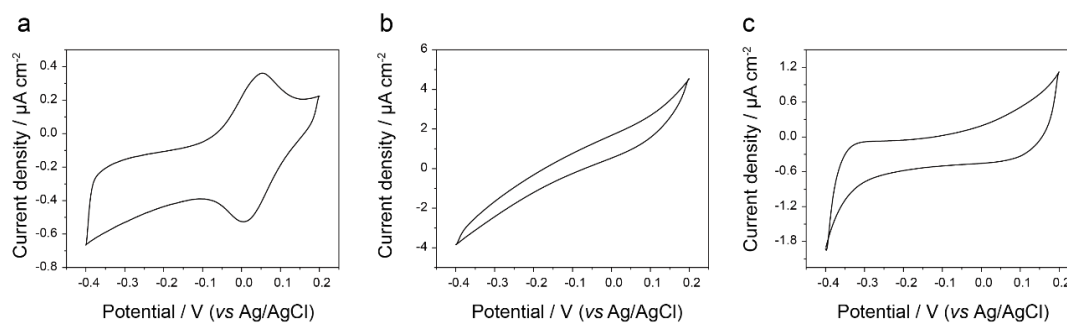


Figure B1. Representative cyclic voltammograms recorded on anodically damaged monolayer-coated Si(111) samples of different doping level and type ((a), n-type, highly doped Si(111), 0.007–0.013 Ω cm; (b) Si(111), highly doped p-type Si(111), 0.007–0.013 Ω cm; (c) Si(111), lowly doped p-type Si(111), 8–12 Ω cm). The electrode voltage was first ramped three times from an initial bias of -0.5 V to an anodic vertex set to 1.0 V, and then back to -0.5 V (not shown). Cyclic voltammograms shown in figure were then sampled, after this oxidative procedure, between -0.4 V and 0.2 V. Scan rates were set to 0.1 V/s, and all experiments were performed in aqueous 1.0 M HClO_4 as the supporting electrolyte.

B2. Stability testing

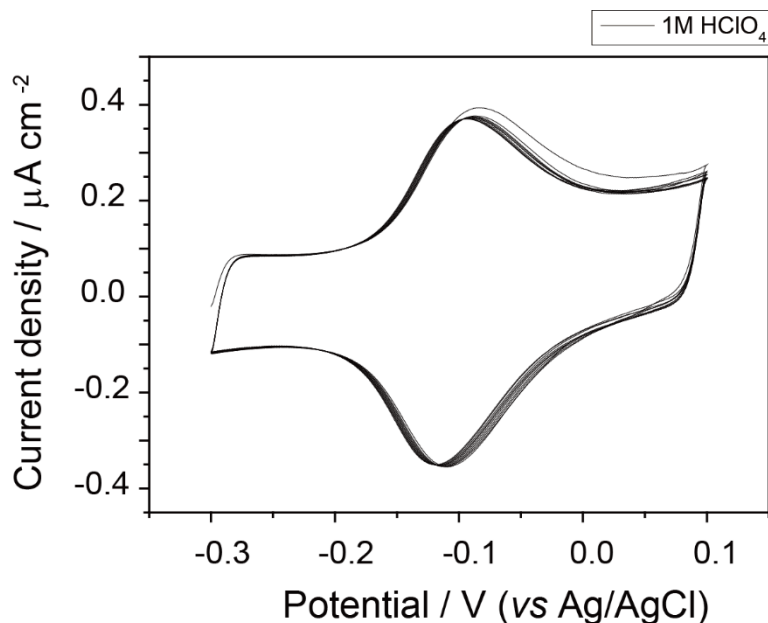


Figure B2. Representative consecutive cyclic voltammograms (ten cycles, scan rate 0.1 V/s) acquired on Si(111) electrodes previously subject to an electrochemical anodic damaging process. The electrode anodic damage was introduced by means of ramping the potential of the working silicon electrode from an initial -0.5 V bias, to an anodic vertex set to 1.0 V (3 cycles). The electrolyte was aqueous 1.0 M HClO₄. The surface coverage, estimated by integration of the first circle, was 2.50×10^{-12} mol cm⁻². From the second cycle onwards, the coverage remained approximately stable, changing from 2.33×10^{-12} mol cm⁻² (second cycle), to 2.27×10^{-12} mol cm⁻² (10th cycle, equivalent to a drop smaller than 3%).

B3. Stereographic projection of a commercial Si(111) wafer

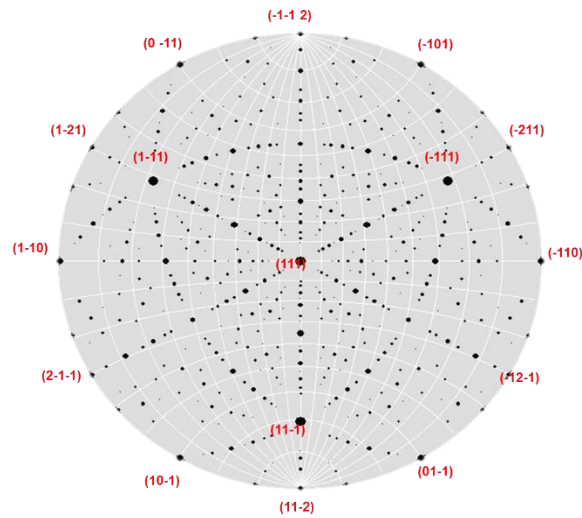


Figure B3. Stereographic projection of a Si(111) wafer. This is a graphical representation of crystal planes (3D features) in a 2D plane. The center of the circle indicates the direction of the (111), here meaning that sections parallel to the wafer will be (111) planes. The supplier marked a major lap to indicate the $\langle 110 \rangle$ direction. The stereographic projection depicts the angular relationships between crystal faces (defines the relative ϕ and ρ angles) and indicates that the terraces visible in the AFM images of Si(111), assuming they are normal to the wafer surface, are roughly either Si(110) or Si(211) facets.

B4. Estimates of the area-ratio between surface steps and Si(111) terraces

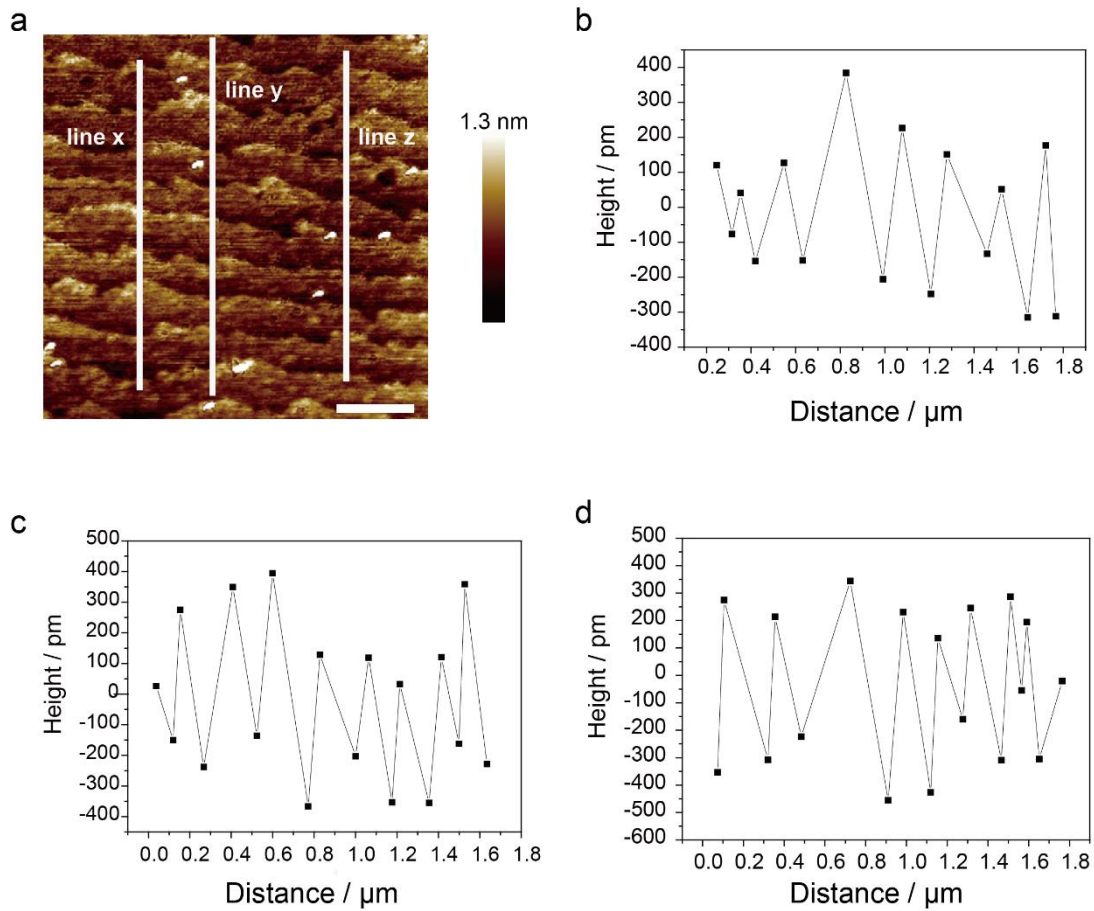


Figure B4. Estimation of the area ratio between Si(110) steps and Si(111) terraces. *a)* AFM topography image of a Si(111) sample showing a terraced structure. *b–d)* are height profiles measured along the three sampling lines (*x*, *y* and *z*) marked in panel (*a*). The three lines are drawn along a direction orthogonal to the terraces main direction, which by considering the major lap of the wafer indicates the surface of the steps is mainly Si(110). Quantitatively, data in *b*), pertinent to the line *x* drawn in (*a*) suggest a Si(111)/Si(11) area ratio of 0.18%, data in (*c*), pertinent to the line *y* in (*a*) suggest a 0.20% value, and data in (*d*), pertinent to line *z* indicate a 0.25% ratio.

B5. Facet-resolved conductivity: average current–potential (conductive AFM) data for Si(111) and Si(110)

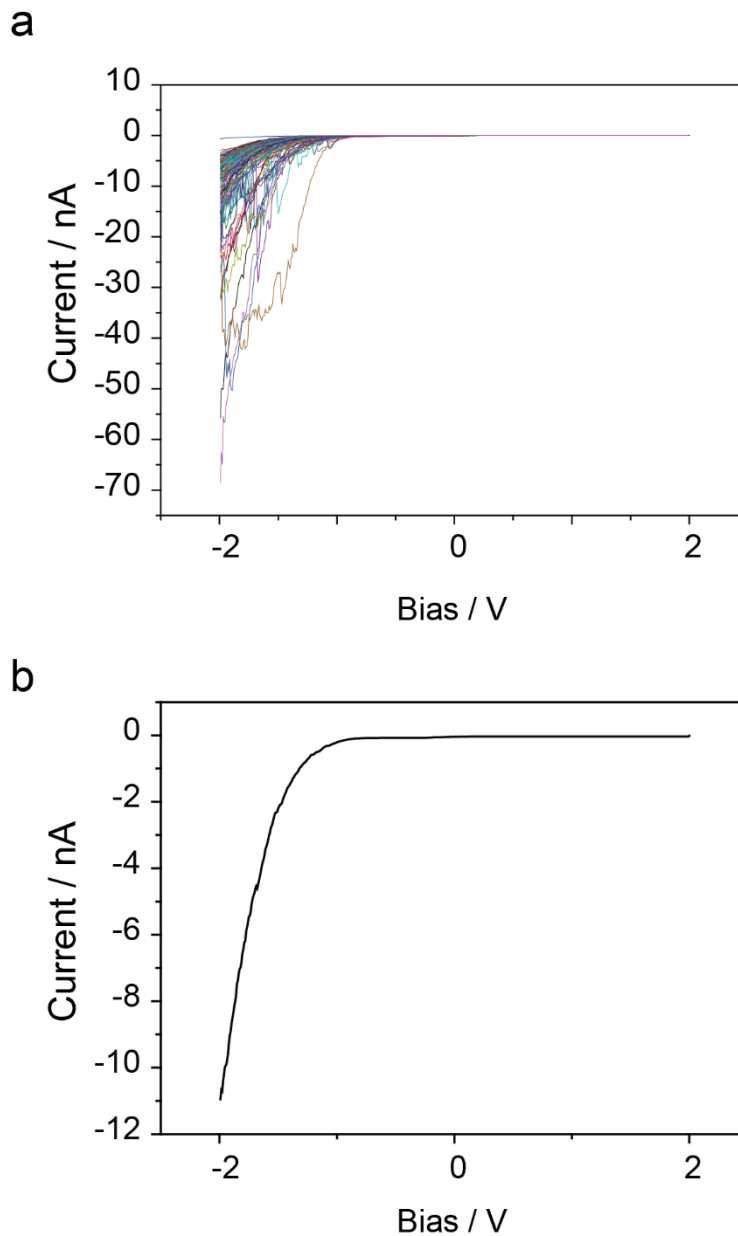


Figure B5. Current output from (Pt–Si) contacts made by conductive AFM on lowly doped (7–13 Ω cm) CZ n-type Si(111). a) Representative (ca. 100) current–potential (I – V) curves acquired on oxide-free Si(111) sample coated with a monolayer of 1,8-nonadiyne. b) Average of the individual traces shown in panel (a).

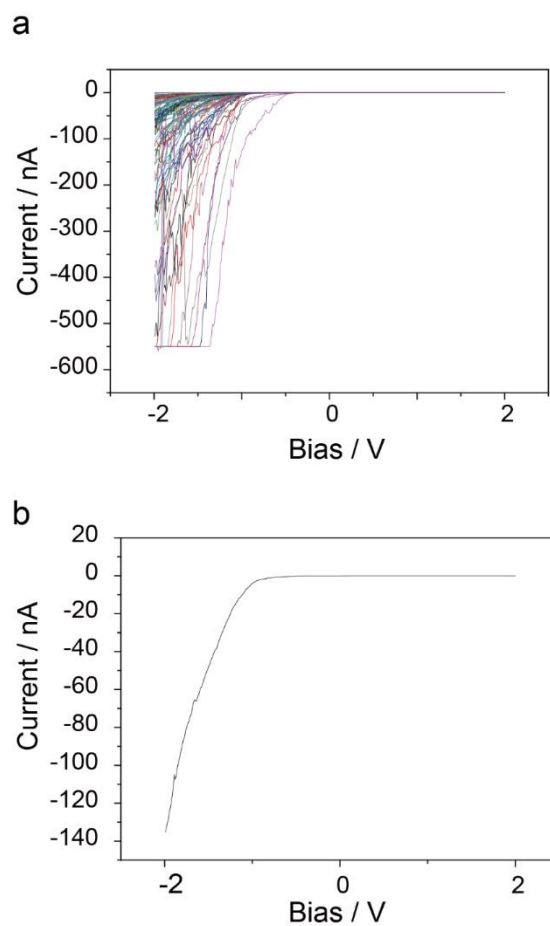


Figure B6. Current output from (Pt-Si) contacts made by conductive AFM on lowly doped (7–13 Ω cm) CZ n-type Si(110). a) Representative (ca. 100) current–potential (I–V) curves acquired on oxide-free Si(110) sample coated with a monolayer of 1,8-nonadiyne. The Si(110) surface was first exposed by cutting a Si(111) wafer along a direction parallel to the lapped edge exposing the (110) plane, as marked on commercial Si(111) wafers purchased from Siltronic. The sample was coated with a monolayer of 1,8-nonadiyne. Individual traces are in (a), and their average I–V values are in (b).

B6. Control experiments in different electrolyte systems

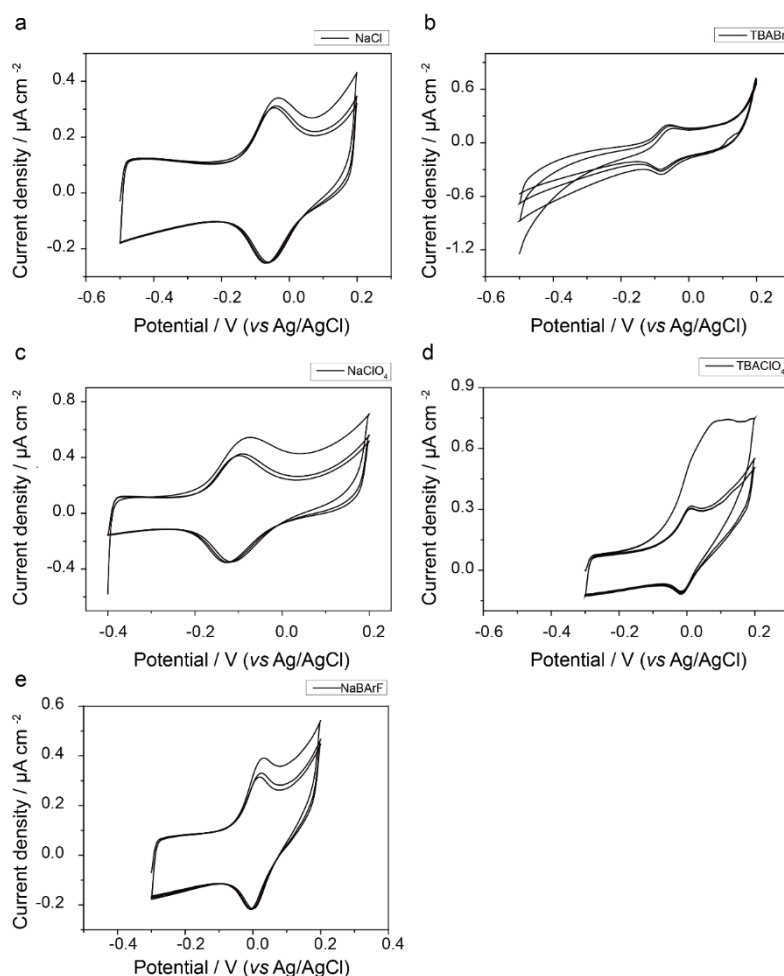


Figure B7. Cyclic voltammograms acquired on monolayer-coated Si(111) electrodes in different electrolyte systems. Data in figure show that for the entire range of electrolytes tested – from strongly coordinating sodium chloride to non-coordinating sodium tetrakis[3,5-bis(trifluoromethyl)phenyl]borate (NaBARF) – silicon anodic damage invariably leads to the appearance of the two redox waves centred at ca. -0.1 V, with no evidence of effects linked to the nature of the electrolyte anion. Experiments shown in figure were performed after having deliberately introduced an anodic damage to the electrode by means of ramping the voltage between -0.5 V and 1.0 V for three consecutive cycles. The electrolytic systems (electrolyte/solvent) are: a) 1.0 M NaCl/water, surface coverage 2.26×10^{-12} mol cm^{-2} ; b) 1.0 M TBABr/water, 1.22×10^{-12} mol cm^{-2} ; c) 1.0 M NaClO_4 /water, 2.87×10^{-12} mol cm^{-2} ; d) 0.25 M TBAClO_4 /acetonitrile, 4.60×10^{-13} mol cm^{-2} ; and e) 0.01 M NaBARF/isopropanol, 8.64×10^{-13} mol cm^{-2} . All scan rates were set to 0.1 V/s.

B7. Electrical and topographical characterization of samples upon their oxidation

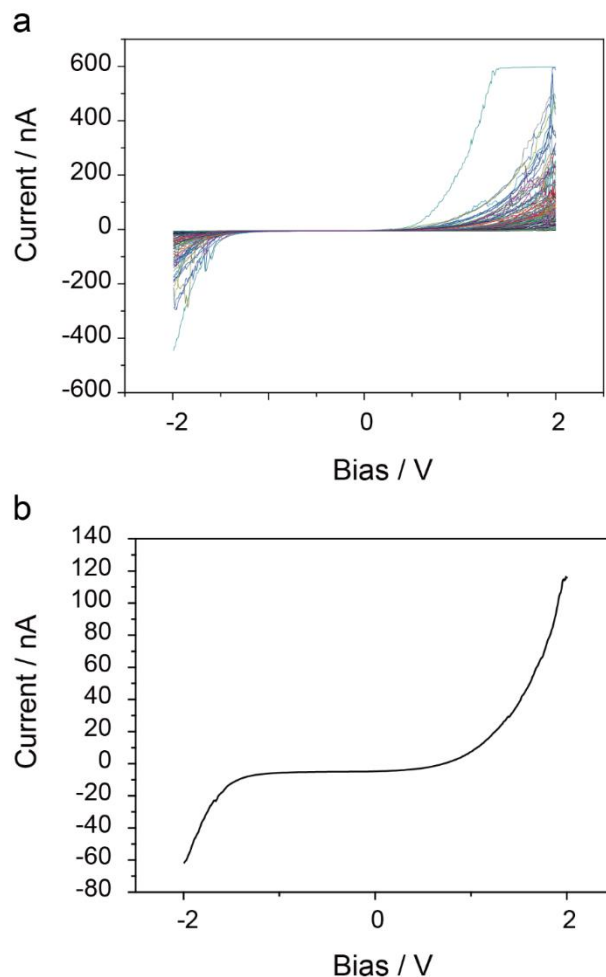


Figure B8. a) One hundred current–potential (I – V) curves (conductive AFM) acquired on anodically damaged Si(111) sample. The anodic process consisted of three cyclic voltammetry cycles between -0.5 V and 1.0 V in aqueous 1.0 M HClO_4 and at a scan rate of 0.1 V/s. b) Average of the traces shown in panel (a). The sample was monolayer-coated (1,8-nonadiyne) poorly doped (7 – 13 Ω cm) CZ n -type Si(111) wafer.

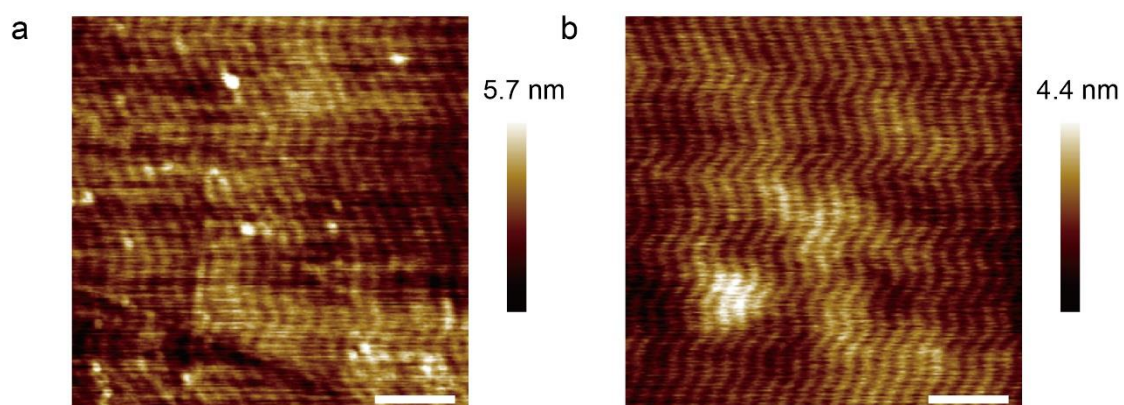


Figure B9. AFM topography images of an anodically damaged Si(111) sample. The sample was coated with a monolayer of 1,8-nonadiyne and then ramped between -0.5 V to 1.0 V (100 cycles, 1.0 M HClO_4 , scan rate 0.1 V/s). Scale bars are $2\mu\text{m}$ in (a) and 400 nm in (b).

B8. pH effects

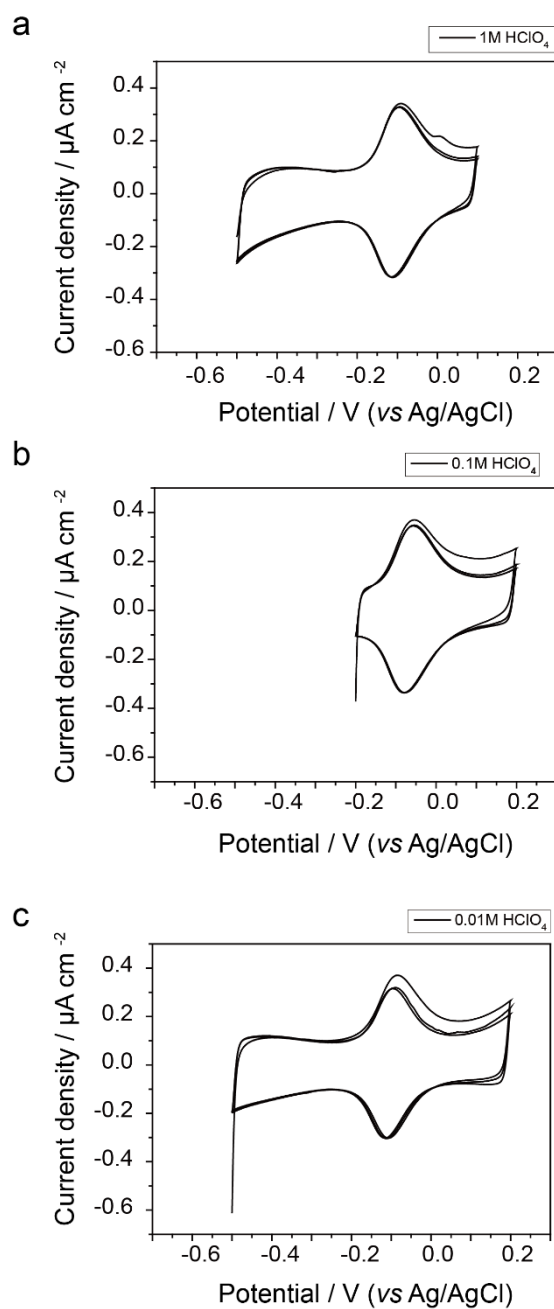


Figure B10. Representative cyclic voltammograms for anodically damaged Si(111) electrodes under acidic conditions. The electrolyte varied between a) 1.0 M HClO_4 , b) 0.1 M HClO_4 , and c) 0.01 M HClO_4 . The scan rate is 0.1 V/s. Data shown in figures are recorded after having deliberately introduced an anodic damage to the electrode by means of ramping the voltage between -0.5 V and 1.0 V for three consecutive cycles. All electrodes were initially monolayer coated.

B9. Controls with carbon and amorphous silicon electrodes

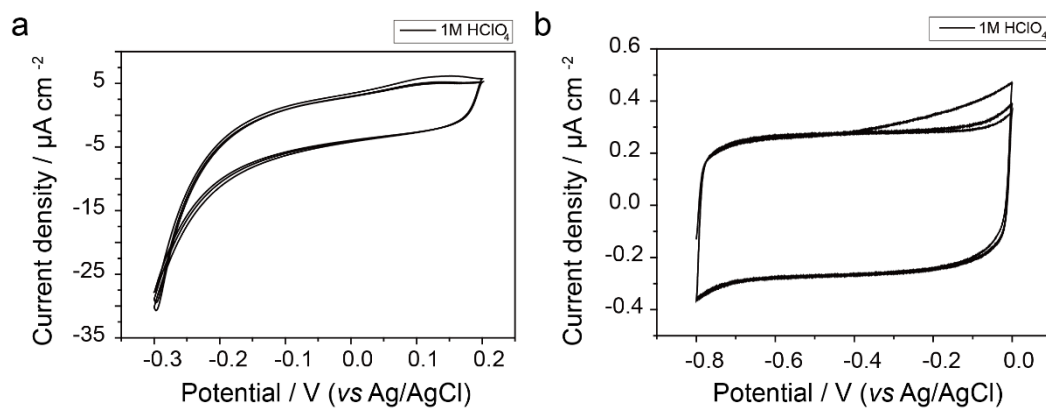


Figure B11. Cyclic voltammetry data of glassy carbon (a) and amorphous silicon electrodes (b). Both samples were analyzed after performing three voltammetric scans between -0.5 V and 1.0 V at the sweep rate of 0.1 V/s in 1.0 M HClO_4 .

B10. Exposing a Si(110) facet in a lapped Si(111) wafer

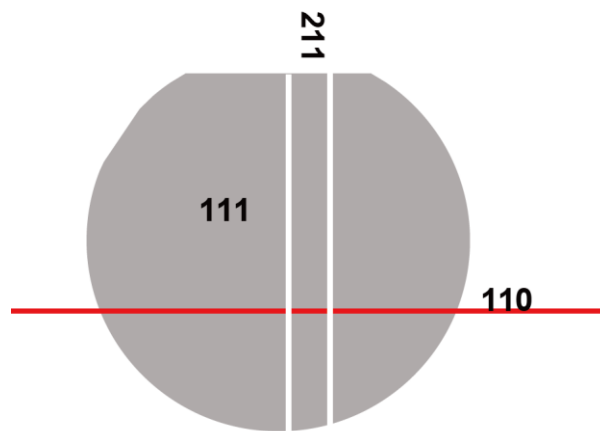


Figure B12. Schematic depiction of the Si(110) lap in a commercial Si(111) wafer.

Appendix C

This part is adapted from Supporting Information of the paper published by the American Chemical Society in *J. Phys. Chem. C* 2021, *125*, (33), 18197-18203, “Absence of a Relationship Between Surface Conductivity and Electrochemical Rates: Redox-Active Monolayers on Si(211), Si(111), and Si(110)”. It is modified with minor changes in order to fit the general layout of this dissertation. This paper constitutes **Chapter 4**.

C1. Additional results and discussions

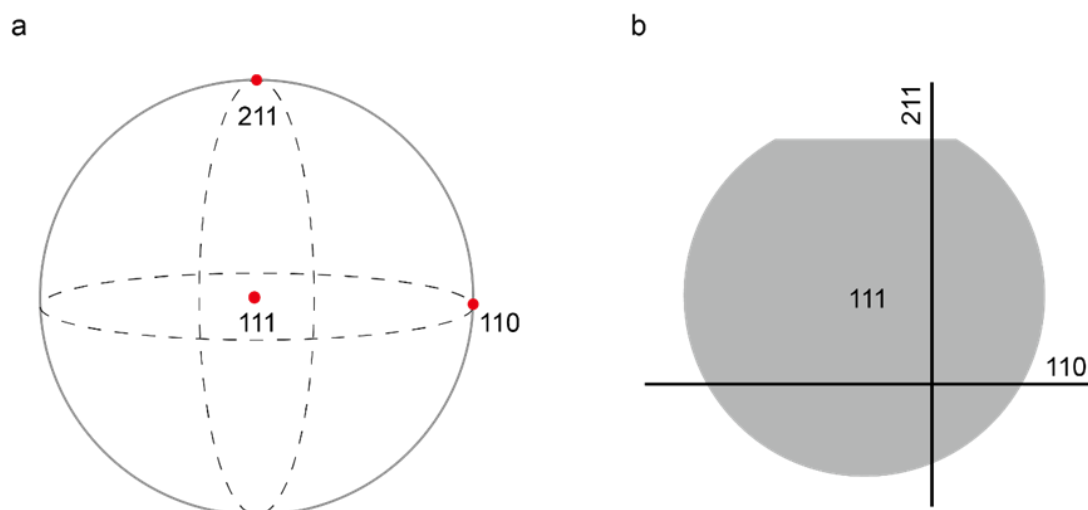


Figure C1. a) Stereographic projection of silicon representing the crystallographic orientation relationship of Si(111), Si(211), and Si(110) surfaces. These projections illustrate the relative orientation of crystal planes (a 3D feature) on a 2D plane. b) Schematic depiction of cutting directions that could be used to expose Si(110) and Si(211) facets starting from a commercial Si(111) wafer. For instance, a lapped edge in a commercial Si(111) wafer often marks the (110) surface, and can be used to perform surface chemistry and electrochemistry on this facet. Alternatively, cleaving the Si(111) wafer along a direction normal to the lapped edge will expose the Si(211) surface.

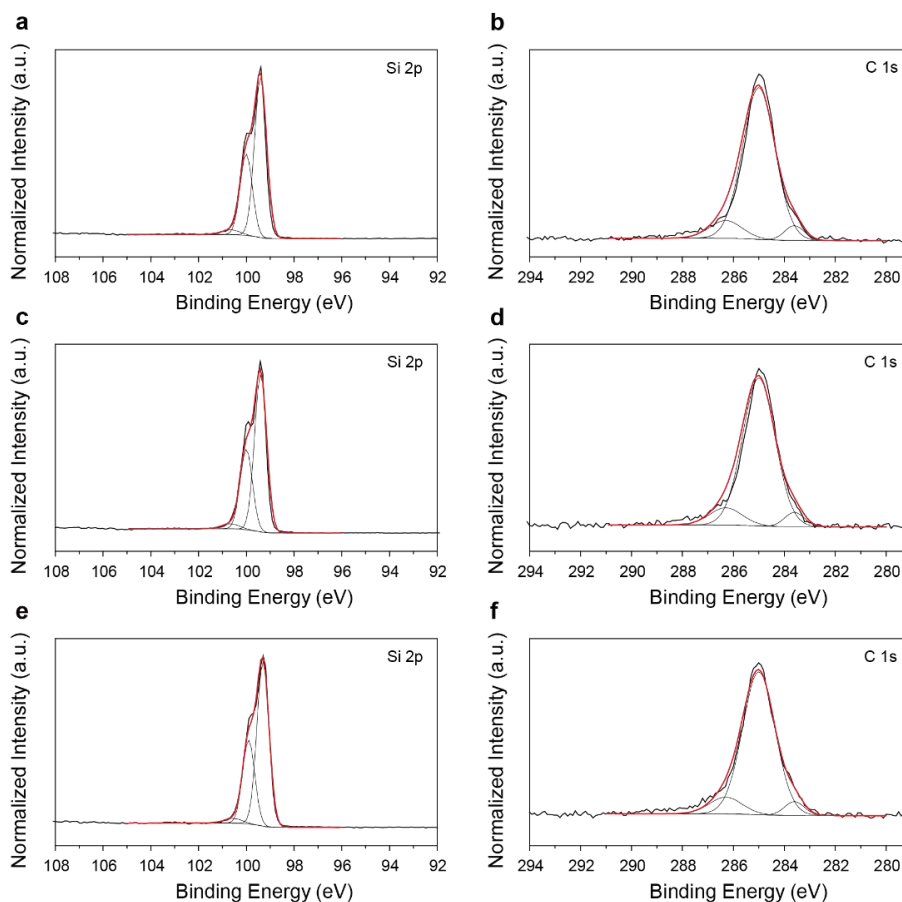


Figure C2. XPS narrow scans of the Si 2p and C 1s regions for 1,8-nonadiyne-modified samples prepared on either: Si(211), (a–b); Si(110), (c–d), and Si(111), (e–f). The substrate was p-type of 0.007–0.013 ohm cm resistivity. The black thick lines are the experimental XPS data (108–92 eV for Si 2p, and 294–279 eV for C 1s), while thinner black traces indicate the fitted contributions ascribed to Si 2p_{3/2} at 99.5 eV (0.6 eV fwhm), Si 2p_{1/2} at 100.1 eV (0.6 eV fwhm)^[1], Si-bound to hydrogen (Si–H) at 100.75 eV (0.9 eV fwhm)^[2], methylene carbons (C–C) at 285.0 eV (1.4 eV fwhm), silicon-bound olefinic carbons (Si–C=C) at 283.6 eV (0.9 eV fwhm), and oxygen bond carbon (C–O) at 286.3 eV (1.4 eV fwhm)^[3]. The structure of the adventitious C–O bond is not fully elucidated, although the contamination has been reported in several works.^[4–6]

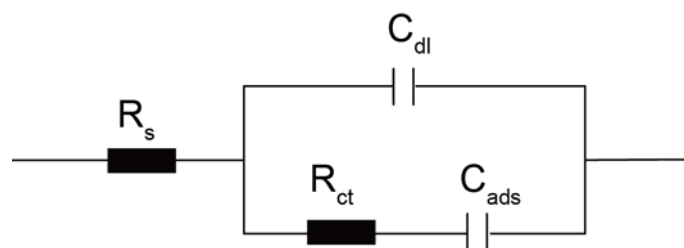


Figure C3. Equivalent electrical circuit used to fit the electrochemical impedance spectroscopy data. R_s stands for solution resistance, R_{ct} for charge transfer resistance, C_{dl} for double layer capacitance, and C_{ads} for adsorption pseudo-capacitance.

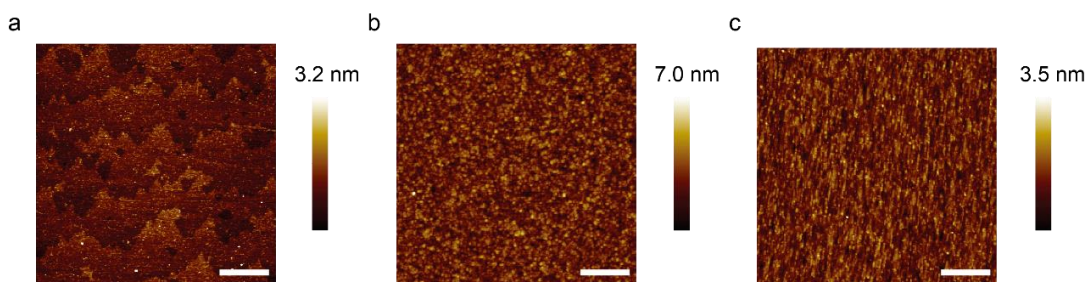


Figure C4. Atomic force microscopy topography (height sensor) data for 1,8-nonadiyne coated Si(111), Si(211), and Si(110), a–c respectively. All scale bars are 400 nm.

Surface topography. The roughness of the monolayer-coated silicon substrates was assessed by AFM. Data shown in Figure C4 indicate that samples prepared on Si(111), Si(211) and Si(110) were of the highest quality and highly smooth. Si(111) Rq values, the root mean square of the surface roughness, were 0.24 ± 0.03 nm, and Ra, which is the arithmetic roughness average of the surface, was 0.16 ± 0.01 nm. Rq for Si(211) was larger and changes in etching time were unsuccessful in further improving this. Rq was 1.40 ± 0.12 nm, and Ra was 1.06 ± 0.06 nm. For Si(110) Rq was 0.61 ± 0.02 nm and Ra 0.48 ± 0.01 nm.

C2. References

- [1]. Cerofolini, G. F.; Galati, C.; Renna, L., Accounting for anomalous oxidation states of silicon at the Si/SiO₂ interface. *Surf. Interface Anal.* **2002**, *33*, (7), 583-590.
- [2]. Zhang, S.; Ferrie, S.; Peiris, C. R.; Lyu, X.; Vogel, Y. B.; Darwish, N.; Ciampi, S., Common background signals in voltammograms of crystalline silicon electrodes are reversible silica–silicon redox chemistry at highly conductive surface sites. *J. Am. Chem. Soc.* **2021**, *143*, (3), 1267-1272.
- [3]. Ciampi, S.; James, M.; Michaels, P.; Gooding, J. J., Tandem “Click” Reactions at Acetylene-Terminated Si(100) Monolayers. *Langmuir* **2011**, *27*, (11), 6940-6949.
- [4]. Wallart, X.; Henry de Villeneuve, C.; Allongue, P., Truly quantitative xps characterization of organic monolayers on silicon: Study of alkyl and alkoxy monolayers on H–Si(111). *J. Am. Chem. Soc.* **2005**, *127*, (21), 7871-7878.
- [5]. Scheres, L.; Arafat, A.; Zuilhof, H., Self-assembly of high-quality covalently bound organic monolayers onto silicon. *Langmuir* **2007**, *23*, (16), 8343-8346.
- [6]. Cerofolini, G. F.; Galati, C.; Reina, S.; Renna, L., Quantitative XPS analysis of hydrosilated 1-alkene and 1-alkyne at terraced, dihydrogen-terminated, 1 × 1 (100) silicon. *Surf. Interface Anal.* **2006**, *38*, (3), 126-138.

Every reasonable effort has been made to acknowledge the owners of copyright material. I would be pleased to hear from any copyright owner who has been omitted or incorrectly acknowledged.

Appendix D. Statements of contributions of others

Statement of contributions for:

Song Zhang, Simone Ciampi, Facet-resolved electrochemistry: from single particles to macroscopic crystals, *Curr. Opin. Electrochem.* 2022:101085 <https://doi.org/10.1016/j.coelec.2022.101085>. Paper included in Chapter 1.

I, Song Zhang, as the first author, drafted the first version of the manuscript, prepared all figures and schemes, except for the contributions of co-authors as specified below.

Simone Ciampi edited the manuscript and conceptualized its structure.

Co-author's signature

Simone Ciampi

Statement of contributions for:

Song Zhang, Xin Lyu, Carlos Hurtado Torres, Nadim Darwish, and Simone Ciampi. Non-Ideal Cyclic Voltammetry of Redox Monolayers on Silicon Electrodes: Peak Splitting is Caused by Heterogeneous Photocurrents and Not by Molecular Disorder. *Langmuir* 2022, 38(2), 743–750, <https://doi.org/10.1021/acs.langmuir.1c02723>. Paper included in Chapter 2.

I, Song Zhang, as the first author, performed all silicon-surface modification experiments, all the electrochemical experiments, most surface characterizations, the great majority of the data analysis, drafted the first version of the manuscript, and prepared all figures and schemes, except for the contributions of co-authors as specified below.

Xin Lyu helped with the acquisition of the AFM data with sample preparation.

Carlos Hurtado Torres helped with acquisition of the contact angle data with sample preparation.

Nadim Darwish co-supervised the project and edited the manuscript.

Simone Ciampi performed the surface modification and electrochemical experiments on the gold electrodes, performed the simulations for the photoelectrodes, designed and supervised the project, edited the manuscript.

Co-authors' signatures:

Xin Lyu

Carlos Hurtado Torres

Nadim Darwish

Simone Ciampi

Statement of contributions for:

Song Zhang, Stuart Ferrie, Chandramalika R. Peiris, Xin Lyu, Yan B. Vogel, Nadim Darwish, and Simone Ciampi. Common Background Signals in Voltammograms of Crystalline Silicon Electrodes are Reversible Silica–Silicon Redox Chemistry at Highly Conductive Surface Sites. *J. Am. Chem. Soc.* 2021, 143(3), 1267–1272, <https://doi.org/10.1021/jacs.0c10713>. Paper included in Chapter 3.

I, Song Zhang, as the first author, performed all the electrochemistry experiments, most of the surface modification procedures, most of the data analysis, drafted the first version of the manuscript, and prepared all figures, except for the contributions of co-authors as specified below.

Stuart Ferrie and Chandramalika R. Peiris helped with the acquisition of the AFM data. Xin Lyu acquired the XPS data and assisted with the XPS samples preparation. Yan B. Vogel helped with the analysis of the cyclic voltammograms and sample preparation for XPS.

Nadim Darwish co-supervised the project and edited manuscript.

Simone Ciampi designed and supervised the project, performed some control experiments, and edited the manuscript.

Co-author's signatures:

Stuart Ferrie

Chandramalika R. Peiris

Xin Lyu

Yan B. Vogel

Nadim Darwish

Simone Ciampi

Statement of contributions for:

Song Zhang, Stuart Ferrie, Xin Lyu, Yunfei Xia, Nadim Darwish, Zhenbo Wang, and Simone Ciampi. Absence of a Relationship between Surface Conductivity and Electrochemical Rates: Redox-Active Monolayers on Si(211), Si(111), and Si(110). *J. Phys. Chem. C.* 2021, 125(33), 18197–18203, <https://doi.org/10.1021/acs.jpcc.1c05023>. Paper included in Chapter 4.

I, Song Zhang, as the first author, performed most of the surface modification procedures, all of the electrochemistry experiments, the majority of the data analysis, drafted the first version of manuscript, and prepared all figures and schemes, except for the contributions of co-authors as specified below.

Stuart Ferrie and Xin Lyu helped with the acquisition of the AFM data.

Xin Lyu helped with acquisition the XPS data with sample preparation.

Yunfei Xia and Zhenbo Wang helped with the XRD measurements.

Nadim Darwish co-supervised the project and edited the manuscript.

Simone Ciampi designed and supervised the project, performed some control experiments, and edited the manuscript.

Co-author's signatures:

Stuart Ferrie

Xin Lyu

Yunfei Xia

Nadim Darwish

Zhenbo Wang

Simone Ciampi

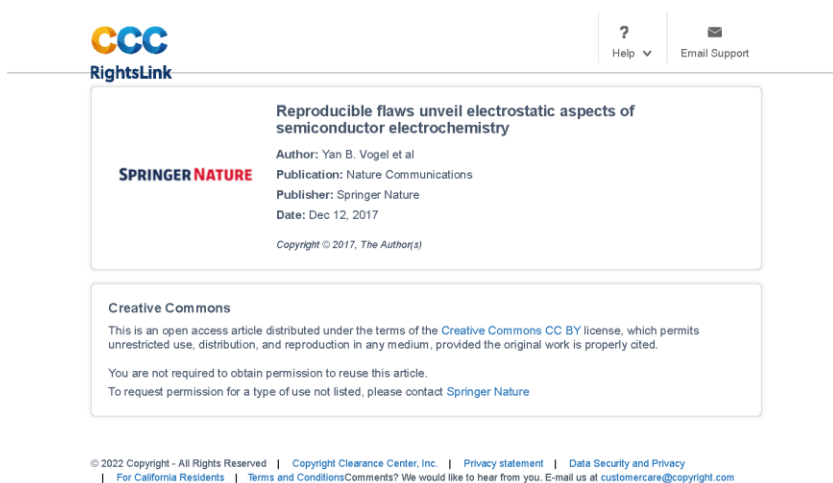
Appendix E. Rights and permissions

Rights and Permissions related to Chapter 1:

Figure 1.7 is reprinted from paper published in *Nature Communications* 2017, 8, 2066.

Vogel, Y. B.; Zhang, L.; Darwish, N.; Gonçales, V. R.; Le Brun, A.; Gooding, J. J.; Molina, A.; Wallace, G. G.; Coote, M. L.; Gonzalez, J.; Ciampi, S., Reproducible flaws unveil electrostatic aspects of semiconductor electrochemistry.

Under the terms of the CC BY 4.0 license, <http://creativecommons.org/licenses/by/4.0/>



The screenshot shows the RightsLink interface for a Springer Nature article. At the top left is the CCC RightsLink logo. On the top right, there are links for 'Help' and 'Email Support'. The main content area is divided into two sections. The first section, titled 'Reproducible flaws unveil electrostatic aspects of semiconductor electrochemistry', includes the author 'Yan B. Vogel et al', publication 'Nature Communications', publisher 'Springer Nature', and date 'Dec 12, 2017'. The second section, titled 'Creative Commons', states that the article is distributed under the CC BY license and provides information on how to request permission for reuse.

CCC
RightsLink

?
Help

Email Support

Reproducible flaws unveil electrostatic aspects of semiconductor electrochemistry

SPRINGER NATURE

Author: Yan B. Vogel et al
Publication: Nature Communications
Publisher: Springer Nature
Date: Dec 12, 2017
Copyright © 2017, The Author(s)

Creative Commons

This is an open access article distributed under the terms of the [Creative Commons CC BY](#) license, which permits unrestricted use, distribution, and reproduction in any medium, provided the original work is properly cited.

You are not required to obtain permission to reuse this article.
To request permission for a type of use not listed, please contact [Springer Nature](#)

© 2022 Copyright - All Rights Reserved | Copyright Clearance Center, Inc. | Privacy statement | Data Security and Privacy
| For California Residents | Terms and Conditions Comments? We would like to hear from you. E-mail us at customercare@copyright.com

This page is available in the following languages: 



Creative Commons License Deed

Attribution 4.0 International (CC BY 4.0)



This is a human-readable summary of (and not a substitute for) the [license](#).

You are free to:

Share — copy and redistribute the material in any medium or format

Adapt — remix, transform, and build upon the material

for any purpose, even commercially.

The licensor cannot revoke these freedoms as long as you follow the license terms.

Under the following terms:

Attribution — You must give appropriate credit, provide a link to the license, and indicate if changes were made. You may do so in any reasonable manner, but not in any way that suggests the licensor endorses you or your use.

No additional restrictions — You may not apply legal terms or technological measures that legally restrict others from doing anything the license permits.

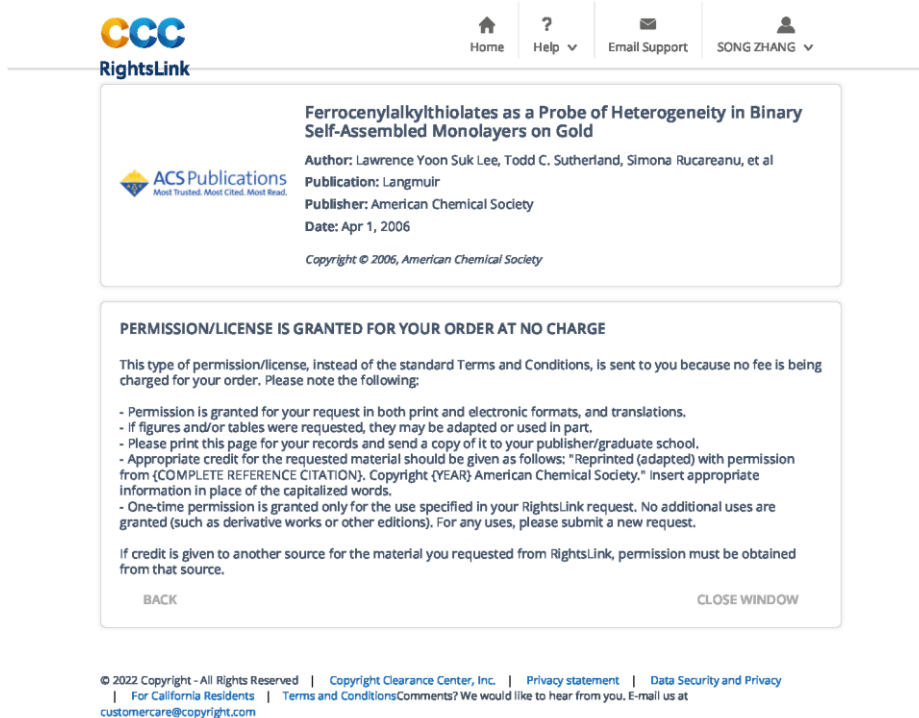
Notices:

You do not have to comply with the license for elements of the material in the public domain or where your use is permitted by an applicable exception or limitation.

No warranties are given. The license may not give you all of the permissions necessary for your intended use. For example, other rights such as publicity, privacy, or moral rights may limit how you use the material.

Figure 1.8 is adapted from the paper published in *Langmuir* 2006, 22, (9), 4438-4444.

Lee, L. Y. S.; Sutherland, T. C.; Rucareanu, S.; Lennox, R. B.,
Ferrocenylalkylthiolates as a Probe of Heterogeneity in Binary Self-Assembled
Monolayers on Gold.



CCC
RightsLink

Home ? Email Support SONG ZHANG

Ferrocenylalkylthiolates as a Probe of Heterogeneity in Binary Self-Assembled Monolayers on Gold

Author: Lawrence Yoon Suk Lee, Todd C. Sutherland, Simona Rucareanu, et al
Publication: Langmuir
Publisher: American Chemical Society
Date: Apr 1, 2006
Copyright © 2006, American Chemical Society

PERMISSION/LICENSE IS GRANTED FOR YOUR ORDER AT NO CHARGE

This type of permission/license, instead of the standard Terms and Conditions, is sent to you because no fee is being charged for your order. Please note the following:

- Permission is granted for your request in both print and electronic formats, and translations.
- If figures and/or tables were requested, they may be adapted or used in part.
- Please print this page for your records and send a copy of it to your publisher/graduate school.
- Appropriate credit for the requested material should be given as follows: "Reprinted (adapted) with permission from {COMPLETE REFERENCE CITATION}, Copyright {YEAR} American Chemical Society." Insert appropriate information in place of the capitalized words.
- One-time permission is granted only for the use specified in your RightsLink request. No additional uses are granted (such as derivative works or other editions). For any uses, please submit a new request.

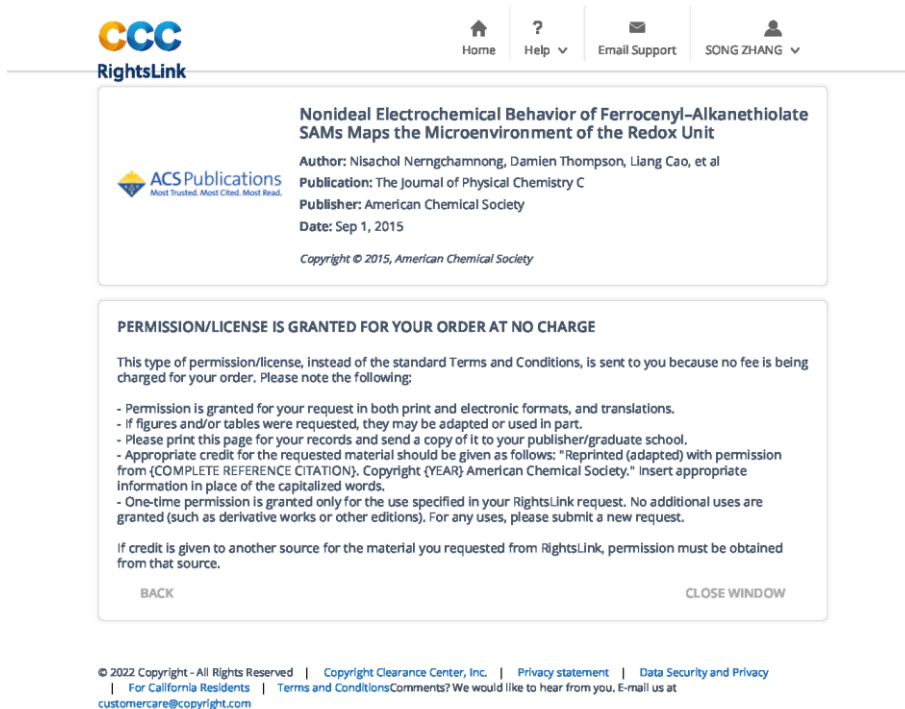
If credit is given to another source for the material you requested from RightsLink, permission must be obtained from that source.

BACK CLOSE WINDOW

© 2022 Copyright - All Rights Reserved | Copyright Clearance Center, Inc. | Privacy statement | Data Security and Privacy
| For California Residents | Terms and Conditions Comments? We would like to hear from you. E-mail us at
customercare@copyright.com

Figure 1.9 is reprinted from the paper published in *J. Phys. Chem. C* 2015, 119, (38), 21978-21991.

Nerngchamnong, N.; Thompson, D.; Cao, L.; Yuan, L.; Jiang, L.; Roemer, M.; Nijhuis, C. A., Nonideal Electrochemical Behavior of Ferrocenyl-Alkanethiolate Sams Maps the Microenvironment of the Redox Unit.



CCC
RightsLink

Home ? Help Email Support SONG ZHANG

Nonideal Electrochemical Behavior of Ferrocenyl-Alkanethiolate SAMS Maps the Microenvironment of the Redox Unit

ACS Publications
Most Trusted. Most Cited. Most Read.

Author: Nisachol Nerngchamnong, Damien Thompson, Liang Cao, et al
Publication: The Journal of Physical Chemistry C
Publisher: American Chemical Society
Date: Sep 1, 2015
Copyright © 2015, American Chemical Society

PERMISSION/LICENSE IS GRANTED FOR YOUR ORDER AT NO CHARGE

This type of permission/license, instead of the standard Terms and Conditions, is sent to you because no fee is being charged for your order. Please note the following:

- Permission is granted for your request in both print and electronic formats, and translations.
- if figures and/or tables were requested, they may be adapted or used in part.
- Please print this page for your records and send a copy of it to your publisher/graduate school.
- Appropriate credit for the requested material should be given as follows: "Reprinted (adapted) with permission from {COMPLETE REFERENCE CITATION}, Copyright {YEAR} American Chemical Society." Insert appropriate information in place of the capitalized words.
- One-time permission is granted only for the use specified in your RightsLink request. No additional uses are granted (such as derivative works or other editions). For any uses, please submit a new request.

If credit is given to another source for the material you requested from RightsLink, permission must be obtained from that source.

BACK CLOSE WINDOW

© 2022 Copyright - All Rights Reserved | Copyright Clearance Center, Inc. | Privacy statement | Data Security and Privacy
| For California Residents | Terms and Conditions Comments? We would like to hear from you. E-mail us at
customercare@copyright.com

Figure 1.10 is adapted from the paper published in *J. Am. Chem. Soc.* 2018, 140, (42), 13672-13679.

Wong, R. A.; Yokota, Y.; Wakisaka, M.; Inukai, J.; Kim, Y., Discerning the Redox-Dependent Electronic and Interfacial Structures in Electroactive Self-Assembled Monolayers.

CCC
RightsLink

Home | Help | Email Support | SONG ZHANG

Discerning the Redox-Dependent Electronic and Interfacial Structures in Electroactive Self-Assembled Monolayers

ACS Publications
Most Trusted. Most Cited. Most Read.

Author: Raymond A. Wong, Yasuyuki Yokota, Mitsuru Wakisaka, et al
Publication: Journal of the American Chemical Society
Publisher: American Chemical Society
Date: Oct 1, 2018
Copyright © 2018, American Chemical Society

PERMISSION/LICENSE IS GRANTED FOR YOUR ORDER AT NO CHARGE

This type of permission/license, instead of the standard Terms and Conditions, is sent to you because no fee is being charged for your order. Please note the following:

- Permission is granted for your request in both print and electronic formats, and translations.
- If figures and/or tables were requested, they may be adapted or used in part.
- Please print this page for your records and send a copy of it to your publisher/graduate school.
- Appropriate credit for the requested material should be given as follows: "Reprinted (adapted) with permission from {COMPLETE REFERENCE CITATION}, Copyright (YEAR) American Chemical Society." Insert appropriate information in place of the capitalized words.
- One-time permission is granted only for the use specified in your RightsLink request. No additional uses are granted (such as derivative works or other editions). For any uses, please submit a new request.

If credit is given to another source for the material you requested from RightsLink, permission must be obtained from that source.

BACK | CLOSE WINDOW

© 2022 Copyright - All Rights Reserved | Copyright Clearance Center, Inc. | Privacy statement | Data Security and Privacy
| For California Residents | Terms and Conditions Comments? We would like to hear from you. E-mail us at customercare@copyright.com

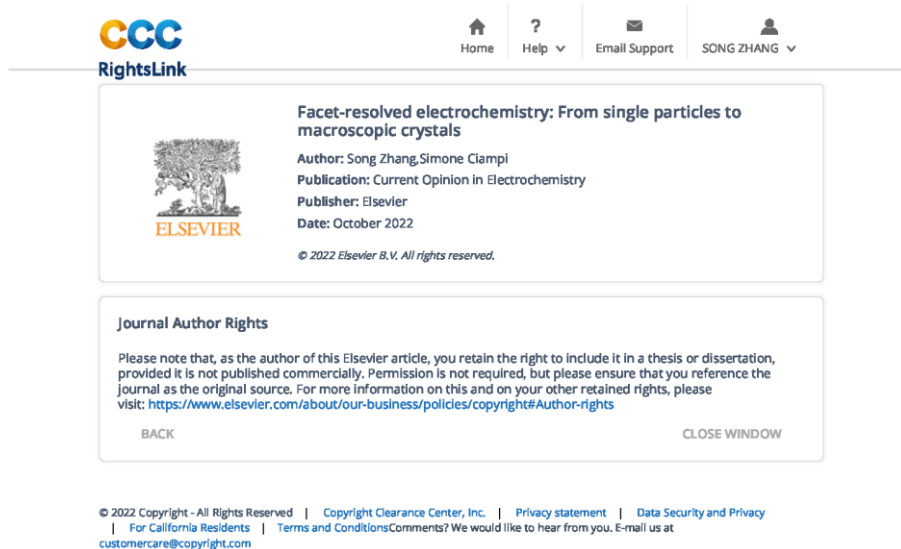
Rights and permissions related to Section 1.6.1:

Rights are retained to reuse in a thesis by the authors.

Section 1.6.1 (review paper) is adapted from the paper published in *Curr. Opin. Electrochem.* 2022, 35, 101085.


Zhang, Song., Ciampi, Simone*., Facet-Resolved Electrochemistry: From Single Particles to Macroscopic Crystals.

I am the first author of this paper.




The screenshot displays the RightsLink interface for an Elsevier article. At the top, there is a navigation bar with the CCC logo, a 'RightsLink' label, and user options: Home, Help, Email Support, and a user profile for SONG ZHANG. The main content area is divided into two sections. The first section, titled 'Facet-resolved electrochemistry: From single particles to macroscopic crystals', includes the Elsevier logo, the article title, author information (Song Zhang, Simone Ciampi), publication details (Current Opinion in Electrochemistry), publisher (Elsevier), and date (October 2022). A copyright notice for 2022 Elsevier B.V. is also present. The second section, titled 'Journal Author Rights', contains a paragraph explaining that authors retain the right to include the article in a thesis or dissertation, provided it is not published commercially. It includes a link to the Elsevier copyright policy page. At the bottom of this section are 'BACK' and 'CLOSE WINDOW' buttons. A footer at the very bottom of the page contains copyright and privacy information for 2022, including links to the Copyright Clearance Center, Inc., privacy statement, data security and privacy policy, and California residents' information.

Rights and permissions of **Figure 1.11**, **Figure 1.12**, **Figure 1.13**, **Figure 1.14**, and **Figure 1.15** have been cleared when submit the review paper to Elsevier.
 Copyright clearances are for submission to Elsevier.
Figure 1.11(submission version to Elsevier)



[Home](#) | [? Help](#) | [Email Support](#) | [SONG ZHANG](#)



Silicon Wafers with Facet-Dependent Electrical Conductivity Properties

Author: Chih-Shan Tan, Pei-Lun Hsieh, Lih-Juann Chen, et al
Publication: Angewandte Chemie International Edition
Publisher: John Wiley and Sons
Date: Nov 2, 2017

Copyright © 2017, John Wiley and Sons

Order Completed

Thank you for your order.

This Agreement between Mr. SONG ZHANG ("You") and John Wiley and Sons ("John Wiley and Sons") consists of your license details and the terms and conditions provided by John Wiley and Sons and Copyright Clearance Center.

Your confirmation email will contain your order number for future reference.

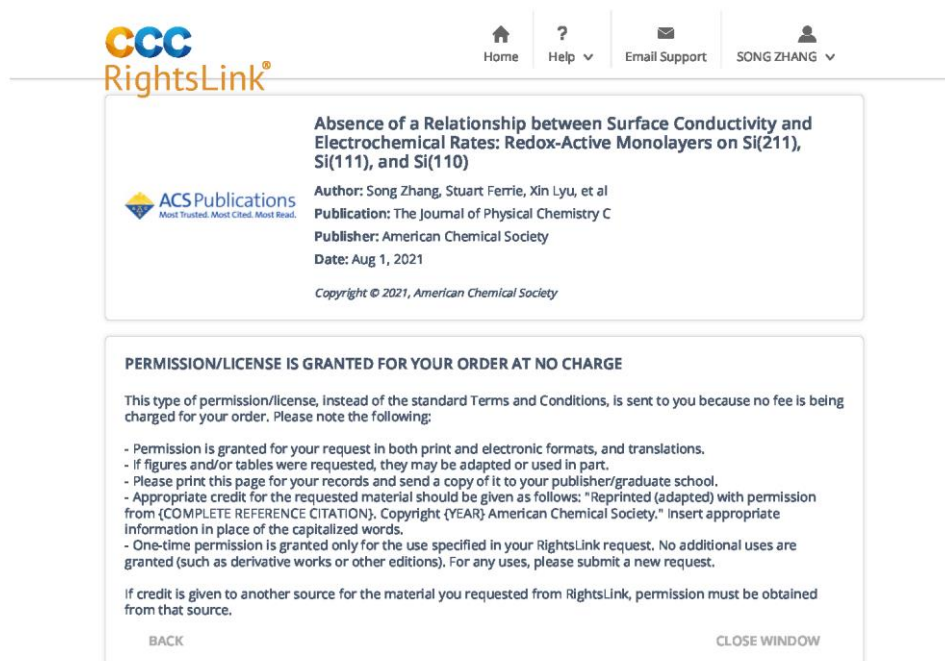
License Number	5307320609545	Printable Details
License date	May 13, 2022	

Licensed Content	Order Details
Licensed Content Publisher	John Wiley and Sons
Licensed Content Publication	Angewandte Chemie International Edition
Licensed Content Title	Silicon Wafers with Facet-Dependent Electrical Conductivity Properties
Licensed Content Author	Chih-Shan Tan, Pei-Lun Hsieh, Lih-Juann Chen, et al
Licensed Content Date	Nov 2, 2017
Licensed Content Pages	10
	Type of use
	Journal/Magazine
	Requestor type
	University/Academic
	Is the reuse sponsored by or associated with a pharmaceutical or medical products company?
	no
	Format
	Print and electronic
	Portion
	Figure/table
	Number of figures/tables
	2
	Will you be translating?
	No
	Circulation
	1 - 29

About Your Work	Additional Data
Title of new article	Facet-resolved electrochemistry: from single particles to macroscopic crystals
Lead author	SONG ZHANG
Title of targeted journal	Current Opinion in Electrochemistry
Publisher	Elsevier
Expected publication date	Jul 2022
	Portions
	figure 1 and figure 3 of Silicon Wafers with Facet-Dependent Electrical Conductivity Properties

📍 Requestor Location		📄 Tax Details	
Requestor Location	Mr. SONG ZHANG School of Molecular and Life Sciences Curtin University, Bentley, Western Australia, Perth, 6102 Australia Attn: Mr. SONG ZHANG	Publisher Tax ID	EU826007151
\$ Price			
Total	0.00 AUD		
<p>Would you like to purchase the full text of this article? If so, please continue on to the content ordering system located here: Purchase PDF If you click on the buttons below or close this window, you will not be able to return to the content ordering system.</p>			
			Total: 0.00 AUD
CLOSE WINDOW		ORDER MORE	

Figure 1.12 (submission version to Elsevier)



The screenshot displays the CCC RightsLink interface. At the top left is the logo for CCC RightsLink. To the right are navigation links: Home, Help, Email Support, and a user profile for SONG ZHANG. The main content area is divided into two sections. The first section provides details for a specific article: 'Absence of a Relationship between Surface Conductivity and Electrochemical Rates: Redox-Active Monolayers on Si(211), Si(111), and Si(110)'. It lists the author as Song Zhang, Stuart Ferrie, Xin Lyu, et al, the publication as The Journal of Physical Chemistry C, the publisher as American Chemical Society, and the date as Aug 1, 2021. The second section, titled 'PERMISSION/LICENSE IS GRANTED FOR YOUR ORDER AT NO CHARGE', explains that this type of permission is granted instead of standard terms because no fee is charged. It includes a list of conditions: permission is granted in both print and electronic formats; figures and tables may be adapted; users should print the page and send a copy to their publisher/graduate school; credit should be given as 'Reprinted (adapted) with permission from {COMPLETE REFERENCE CITATION}, Copyright {YEAR} American Chemical Society.'; and one-time permission is granted only for the specified use. A note states that if credit is given to another source, permission must be obtained from that source. At the bottom of this section are 'BACK' and 'CLOSE WINDOW' buttons.

CCC
RightsLink®

Home Help Email Support SONG ZHANG

Absence of a Relationship between Surface Conductivity and Electrochemical Rates: Redox-Active Monolayers on Si(211), Si(111), and Si(110)

ACS Publications
Most Trusted. Most Cited. Most Read.

Author: Song Zhang, Stuart Ferrie, Xin Lyu, et al
Publication: The Journal of Physical Chemistry C
Publisher: American Chemical Society
Date: Aug 1, 2021
Copyright © 2021, American Chemical Society

PERMISSION/LICENSE IS GRANTED FOR YOUR ORDER AT NO CHARGE

This type of permission/license, instead of the standard Terms and Conditions, is sent to you because no fee is being charged for your order. Please note the following:

- Permission is granted for your request in both print and electronic formats, and translations.
- If figures and/or tables were requested, they may be adapted or used in part.
- Please print this page for your records and send a copy of it to your publisher/graduate school.
- Appropriate credit for the requested material should be given as follows: "Reprinted (adapted) with permission from {COMPLETE REFERENCE CITATION}, Copyright {YEAR} American Chemical Society." Insert appropriate information in place of the capitalized words.
- One-time permission is granted only for the use specified in your RightsLink request. No additional uses are granted (such as derivative works or other editions). For any uses, please submit a new request.

If credit is given to another source for the material you requested from RightsLink, permission must be obtained from that source.

BACK CLOSE WINDOW

Common Background Signals in Voltammograms of Crystalline Silicon Electrodes are Reversible Silica-Silicon Redox Chemistry at Highly Conductive Surface Sites



Author: Song Zhang, Stuart Ferrie, Chandramallika R. Peiris, et al
Publication: Journal of the American Chemical Society
Publisher: American Chemical Society
Date: Jan 1, 2021

Copyright © 2021, American Chemical Society

PERMISSION/LICENSE IS GRANTED FOR YOUR ORDER AT NO CHARGE

This type of permission/license, instead of the standard Terms and Conditions, is sent to you because no fee is being charged for your order. Please note the following:

- Permission is granted for your request in both print and electronic formats, and translations.
- If figures and/or tables were requested, they may be adapted or used in part.
- Please print this page for your records and send a copy of it to your publisher/graduate school.
- Appropriate credit for the requested material should be given as follows: "Reprinted (adapted) with permission from {COMPLETE REFERENCE CITATION}, Copyright {YEAR} American Chemical Society." Insert appropriate information in place of the capitalized words.
- One-time permission is granted only for the use specified in your RightsLink request. No additional uses are granted (such as derivative works or other editions). For any uses, please submit a new request.

If credit is given to another source for the material you requested from RightsLink, permission must be obtained from that source.

[BACK](#)

[CLOSE WINDOW](#)


Figure 1.13 (submission version to Elsevier)

Adapted from the study by

Vogel YB, Gonçalves VR, Gooding JJ, Ciampi S: Electrochemical microscopy based on spatial light modulators: a projection system to spatially address electrochemical reactions at semiconductors. **J Electrochem Soc** 2017, 165:H3085–H3092.

<https://iopscience.iop.org/article/10.1149/2.0111804jes/meta>, under the terms of the CC BY 4.0 license, <http://creativecommons.org/licenses/by/4.0/>.

Figure 1.14 (submission version to Elsevier)



The screenshot shows the RightsLink interface. At the top left is the 'CCC RightsLink' logo. To the right are navigation icons for Home, Help, Email Support, and a user profile for 'SONG ZHANG'. The main content area displays the following information:

Switching of Current Rectification Ratios within a Single Nanocrystal by Facet-Resolved Electrical Wiring

Author: Yan B. Vogel, Jinyang Zhang, Nadim Darwish, et al
Publication: ACS Nano
Publisher: American Chemical Society
Date: Aug 1, 2018
Copyright © 2018, American Chemical Society

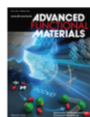
PERMISSION/LICENSE IS GRANTED FOR YOUR ORDER AT NO CHARGE

This type of permission/license, instead of the standard Terms and Conditions, is sent to you because no fee is being charged for your order. Please note the following:

- Permission is granted for your request in both print and electronic formats, and translations.
- If figures and/or tables were requested, they may be adapted or used in part.
- Please print this page for your records and send a copy of it to your publisher/graduate school.
- Appropriate credit for the requested material should be given as follows: "Reprinted (adapted) with permission from {COMPLETE REFERENCE CITATION}, Copyright {YEAR} American Chemical Society." Insert appropriate information in place of the capitalized words.
- One-time permission is granted only for the use specified in your RightsLink request. No additional uses are granted (such as derivative works or other editions). For any uses, please submit a new request.

If credit is given to another source for the material you requested from RightsLink, permission must be obtained from that source.

BACK CLOSE WINDOW



Nanocrystal Inks: Photoelectrochemical Printing of Cu₂O Nanocrystals on Silicon with 2D Control on Polyhedral Shapes

Author: Simone Ciampi, Nadim Darwish, J. Justin Gooding, et al
 Publication: Advanced Functional Materials
 Publisher: John Wiley and Sons
 Date: Nov 12, 2018

© 2018 WILEY-VCH Verlag GmbH & Co. KGaA, Weinheim

Order Completed

Thank you for your order.

This Agreement between Mr. SONG ZHANG ("You") and John Wiley and Sons ("John Wiley and Sons") consists of your license details and the terms and conditions provided by John Wiley and Sons and Copyright Clearance Center.

Your confirmation email will contain your order number for future reference.

License Number 5307331198288 [Printable Details](#)

License date May 13, 2022

Licensed Content

Licensed Content Publisher	John Wiley and Sons
Licensed Content Publication	Advanced Functional Materials
Licensed Content Title	Nanocrystal Inks: Photoelectrochemical Printing of Cu ₂ O Nanocrystals on Silicon with 2D Control on Polyhedral Shapes
Licensed Content Author	Simone Ciampi, Nadim Darwish, J. Justin Gooding, et al
Licensed Content Date	Nov 12, 2018
Licensed Content Volume	28
Licensed Content Issue	51
Licensed Content Pages	9

Order Details

Type of use	Journal/Magazine
Requestor type	University/Academic
Is the reuse sponsored by or associated with a pharmaceutical or medical products company?	no
Format	Print and electronic
Portion	Figure/table
Number of figures/tables	1
Will you be translating?	No
Circulation	1 - 29

About Your Work

Title of new article	Facet-resolved electrochemistry: from single particles to macroscopic crystals
Lead author	SONG ZHANG
Title of targeted journal	Current Opinion in Electrochemistry
Publisher	Elsevier
Expected publication date	Jul 2022

Additional Data

Portions	figure 4 of Nanocrystal Inks: Photoelectrochemical Printing of Cu ₂ O Nanocrystals on Silicon with 2D Control on Polyhedral Shapes
----------	---

Requestor Location		Tax Details	
Requestor Location	Mr. SONG ZHANG School of Molecular and Life Sciences Curtin University, Bentley, Western Australia, Perth, 6102 Australia Attn: Mr. SONG ZHANG	Publisher Tax ID	EU826007151
\$ Price			
Total	0.00 AUD		
<p>Would you like to purchase the full text of this article? If so, please continue on to the content ordering system located here: Purchase PDF If you click on the buttons below or close this window, you will not be able to return to the content ordering system.</p>			
			Total: 0.00 AUD
CLOSE WINDOW		ORDER MORE	

Figure 1.15 (submission version to Elsevier)

The screenshot displays the CCC RightsLink interface. At the top, there is a navigation bar with icons for Home, Help, Email Support, and a user profile for SONG ZHANG. The main content area is divided into two sections. The first section, titled "Metal-Single-Molecule-Semiconductor Junctions Formed by a Radical Reaction Bridging Gold and Silicon Electrodes", includes the ACS Publications logo and provides details: Author: Chandramalika R. Peiris, Yan B. Vogel, Anton P. Le Brun, et al; Publication: Journal of the American Chemical Society; Publisher: American Chemical Society; Date: Sep 1, 2019; and Copyright © 2019, American Chemical Society. The second section, titled "PERMISSION/LICENSE IS GRANTED FOR YOUR ORDER AT NO CHARGE", explains that this type of permission is granted instead of standard terms because no fee is charged. It lists several conditions: permission is granted in both print and electronic formats; figures and tables may be adapted; users should print the page for records and send a copy to their publisher; appropriate credit should be given as follows: "Reprinted (adapted) with permission from (COMPLETE REFERENCE CITATION), Copyright (YEAR) American Chemical Society."; and one-time permission is granted only for the use specified in the request. At the bottom of this section are "BACK" and "CLOSE WINDOW" links. A footer at the very bottom contains copyright information: © 2022 Copyright - All Rights Reserved | Copyright Clearance Center, Inc. | Privacy statement | Terms and Conditions, and a contact email: customercare@copyright.com.

Bidirectional Control of the Band Bending at the (201) and (010) Surfaces of β -Ga₂O₃ Using Aryldiazonium Ion and Phosphonic Acid Grafting



Author: Liam R. Carroll, Rodrigo F. Martinez-Gazoni, Nicola Gaston, et al
Publication: ACS Applied Electronic Materials
Publisher: American Chemical Society
Date: Dec 1, 2021

Copyright © 2021, American Chemical Society

PERMISSION/LICENSE IS GRANTED FOR YOUR ORDER AT NO CHARGE

This type of permission/license, instead of the standard Terms and Conditions, is sent to you because no fee is being charged for your order. Please note the following:

- Permission is granted for your request in both print and electronic formats, and translations.
- If figures and/or tables were requested, they may be adapted or used in part.
- Please print this page for your records and send a copy of it to your publisher/graduate school.
- Appropriate credit for the requested material should be given as follows: "Reprinted (adapted) with permission from (COMPLETE REFERENCE CITATION). Copyright (YEAR) American Chemical Society." Insert appropriate information in place of the capitalized words.
- One-time permission is granted only for the use specified in your RightsLink request. No additional uses are granted (such as derivative works or other editions). For any uses, please submit a new request.

If credit is given to another source for the material you requested from RightsLink, permission must be obtained from that source.


[BACK](#)


[CLOSE WINDOW](#)

Rights and Permissions related to Chapter 2:

Chapter 2 is adapted from the paper published in *Langmuir* 2022, 38, 743–750,

Song Zhang, Xin Lyu, Carlos Hurtado Torres, Nadim Darwish, and Simone Ciampi.
Non-Ideal Cyclic Voltammetry of Redox Monolayers on Silicon Electrodes: Peak Splitting is Caused by Heterogeneous Photocurrents and Not by Molecular Disorder.
I am the first author.

Home ? Help Email Support SONG ZHANG



Non-Ideal Cyclic Voltammetry of Redox Monolayers on Silicon Electrodes: Peak Splitting is Caused by Heterogeneous Photocurrents and Not by Molecular Disorder

Author: Song Zhang, Xin Lyu, Carlos Hurtado Torres, et al
Publication: Langmuir
Publisher: American Chemical Society
Date: Jan 1, 2022

Copyright © 2022, American Chemical Society

PERMISSION/LICENSE IS GRANTED FOR YOUR ORDER AT NO CHARGE

This type of permission/license, instead of the standard Terms and Conditions, is sent to you because no fee is being charged for your order. Please note the following:

- Permission is granted for your request in both print and electronic formats, and translations.
- If figures and/or tables were requested, they may be adapted or used in part.
- Please print this page for your records and send a copy of it to your publisher/graduate school.
- Appropriate credit for the requested material should be given as follows: "Reprinted (adapted) with permission from (COMPLETE REFERENCE CITATION). Copyright (YEAR) American Chemical Society." Insert appropriate information in place of the capitalized words.
- One-time permission is granted only for the use specified in your RightsLink request. No additional uses are granted (such as derivative works or other editions). For any uses, please submit a new request.

If credit is given to another source for the material you requested from RightsLink, permission must be obtained from that source.

BACK

CLOSE WINDOW

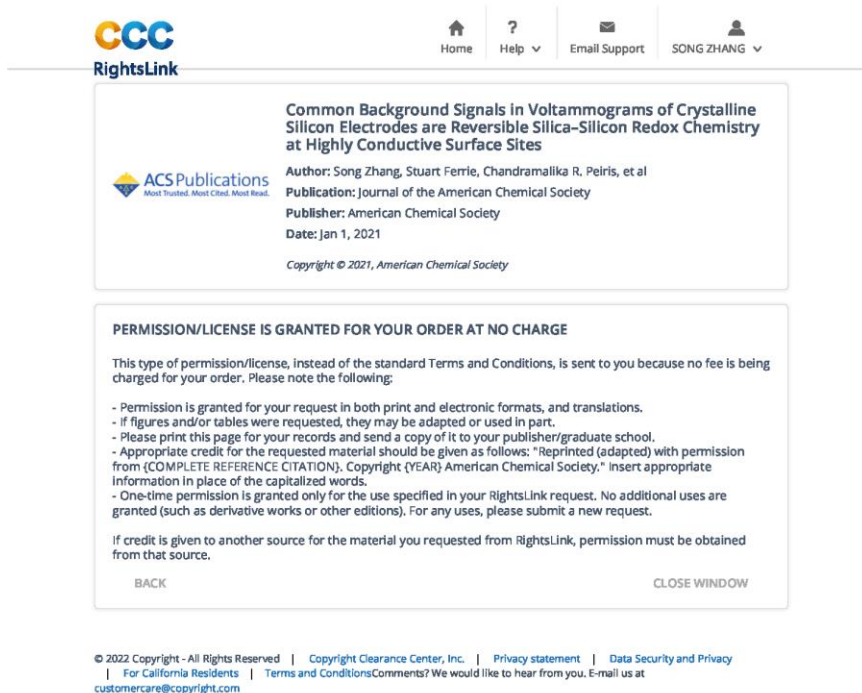
© 2022 Copyright - All Rights Reserved | Copyright Clearance Center, Inc. | Privacy statement | Data Security and Privacy
| For California Residents | Terms and Conditions Comments? We would like to hear from you. E-mail us at
customercare@copyright.com

Rights and Permissions related to Chapter 3:

Chapter 3 is adapted from the paper published in *J. Am. Chem. Soc.* 2021, 143, (3), 1267-1272.

Song Zhang, Stuart Ferrie, Chandramalika R. Peiris, Xin Lyu, Yan B. Vogel, Nadim Darwish, and Simone Ciampi. Common Background Signals in Voltammograms of Crystalline Silicon Electrodes are Reversible Silica-Silicon Redox Chemistry at Highly Conductive Surface Sites.

I am the first author.



CCC
RightsLink

Home ? Email Support SONG ZHANG

ACS Publications
Most Trusted. Most Cited. Most Read.

Common Background Signals in Voltammograms of Crystalline Silicon Electrodes are Reversible Silica-Silicon Redox Chemistry at Highly Conductive Surface Sites

Author: Song Zhang, Stuart Ferrie, Chandramalika R. Peiris, et al
Publication: Journal of the American Chemical Society
Publisher: American Chemical Society
Date: Jan 1, 2021
Copyright © 2021, American Chemical Society

PERMISSION/LICENSE IS GRANTED FOR YOUR ORDER AT NO CHARGE

This type of permission/license, instead of the standard Terms and Conditions, is sent to you because no fee is being charged for your order. Please note the following:

- Permission is granted for your request in both print and electronic formats, and translations.
- If figures and/or tables were requested, they may be adapted or used in part.
- Please print this page for your records and send a copy of it to your publisher/graduate school.
- Appropriate credit for the requested material should be given as follows: "Reprinted (adapted) with permission from {COMPLETE REFERENCE CITATION}. Copyright {YEAR} American Chemical Society." Insert appropriate information in place of the capitalized words.
- One-time permission is granted only for the use specified in your RightsLink request. No additional uses are granted (such as derivative works or other editions). For any uses, please submit a new request.

If credit is given to another source for the material you requested from RightsLink, permission must be obtained from that source.

BACK CLOSE WINDOW

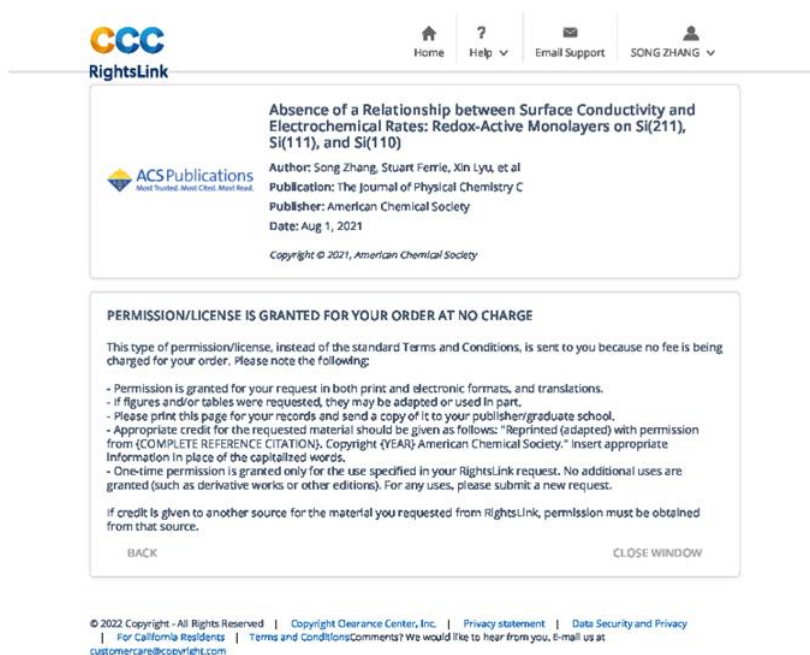
© 2022 Copyright - All Rights Reserved | Copyright Clearance Center, Inc. | Privacy statement | Data Security and Privacy
| For California Residents | Terms and Conditions Comments? We would like to hear from you. E-mail us at
customercare@copyright.com

Rights and Permissions related to Chapter 4:

Chapter 4 is adapted from the paper published in *J. Phys. Chem. C.* 2021;125(33):18197–18203.

Song Zhang, Stuart Ferrie, Xin Lyu, Yunfei Xia, Nadim Darwish, Zhenbo Wang, and Simone Ciampi* Absence of a Relationship between Surface Conductivity and Electrochemical Rates: Redox-Active Monolayers on Si(211), Si(111), and Si(110).

I am the first author.



The screenshot shows the RightsLink interface. At the top, there is a navigation bar with the CCC logo, a 'RightsLink' label, and links for Home, Help, Email Support, and a user profile for SONG ZHANG. The main content area displays the title of the paper: 'Absence of a Relationship between Surface Conductivity and Electrochemical Rates: Redox-Active Monolayers on Si(211), Si(111), and Si(110)'. Below the title, it lists the author (Song Zhang, Stuart Ferrie, Xin Lyu, et al), the publication (The Journal of Physical Chemistry C), the publisher (American Chemical Society), and the date (Aug 1, 2021). A copyright notice for 2021 by the American Chemical Society is also present. A prominent message states 'PERMISSION/LICENSE IS GRANTED FOR YOUR ORDER AT NO CHARGE'. Below this, a detailed explanation of the permission is provided, including conditions for use and citation requirements. At the bottom of the page, there is a footer with copyright information and contact details for the Copyright Clearance Center.

© 2022 Copyright - All Rights Reserved | Copyright Clearance Center, Inc. | Privacy statement | Data Security and Privacy
| For California Residents | Terms and Conditions/Comments? We would like to hear from you. E-mail us at
customercare@copyright.com